NASA Technical Memorandum 4804

A Summary of Numerous Strain-Gage Load Calibrations on Aircraft Wings and Tails in a Technology Format

Jerald M. Jenkins and V. Michael DeAngelis

July 1997

NASA Technical Memorandum 4804

A Summary of Numerous Strain-Gage Load Calibrations on Aircraft Wings and Tails in a Technology Format

Jerald M. Jenkins and V. Michael DeAngelis
Dryden Flight Research Center
Edwards, California

National Aeronautics and
Space Administration

Office of Management

Scientific and Technical
Information Program

1997

ABSTRACT

Fifteen aircraft structures that were calibrated for flight loads using strain gages are examined. The primary purpose of this paper is to document important examples of load calibrations on airplanes during the past four decades. The emphasis is placed on studying the physical procedures of calibrating strain-gaged structures and all the supporting analyses and computational techniques that have been used. The results and experiences obtained from actual data from 14 structures (on 13 airplanes and 1 laboratory test structure) are presented. This group of structures includes fins, tails, and wings with a wide variety of aspect ratios. Straight-wing, swept-wing, and delta-wing configurations are studied. Some of the structures have skin-dominant construction; others are spar-dominant. Anisotropic materials, heat shields, corrugated components, nonorthogonal primary structures, and truss-type structures are particular characteristics that are included.

NOMENCLATURE

A	area, in^2
a_{ij}	element in an array of numbers
A_{ij}	a notable element in an array of numbers
A_L	loaded area or lower area, in^2
A_T	total area, in^2
A_U	upper area, in^2
B	bending moment, in-lbf
c	distance to outer fiber from neutral axis, $h/2$, in.
C_R	relevance coefficient, nondimensional
E	modulus of elasticity, lbf/in^2
e_o	output voltage, V
E_X	excitation voltage, V
F. S.	fuselage station
G	shear modulus, lbf/in^2
GF	gage factor, nondimensional
h	distance between upper and lower centroids, in.
HiMAT	Highly Maneuverable Aircraft Technology
HWTS	Hypersonic Wing Test Structure
i	arbitrary integer
I	moment of inertia, in^4
I_{BAR}	moment of inertia of a beam element, in^4
I_C	influence coefficient, output/lbf
j	arbitrary integer
J	polar moment of inertia of cross-sectional area, in^4
K	linear constant, nondimensional
L	load or left load, lbf

M	bending moment, in-lbf
n	arbitrary integer
N	strain-gage bridge factor, nondimensional
p	cell perimeter, in.
P	load, lbf
q	shear flow, lbf/in
Q	defined as $Ah/4$, in^3
R	right load, lbf
SG	strain gage
t	skin thickness, in.
t_m	thickness of model, in.
t_w	thickness of wing, in.
TACT	Transonic Aircraft Technology
V	section shear load, lbf
x	Cartesian coordinate
y	Cartesian coordinate
y_L	distance to lower centroid, in.
y_U	distance to upper centroid, in.
z	Cartesian coordinate
β	constant, nondimensional
γ	shear strain, nondimensional
δ	deflection, in., or voltage change resulting from straining the active arms of a strain-gage bridge, V
δ_{cal}	reference voltage change resulting from shunting a calibrated resistor across one arm of a strain-gage bridge, V
ε	normal strain, nondimensional
η	span fraction
θ	angle of rotation, deg
Λ	wing sweep angle, deg
μ	nondimensional strain-gage response, δ/δ_{cal}
ξ	chord fraction
σ	normal stress, lbf/in^2
τ	shear stress, lbf/in^2
υ	Poisson's ratio, nondimensional
ϕ	angle of rotation, deg

INTRODUCTION

The idea of using calibrated strain gages through influence-coefficient formats to measure flight loads on airplane components likely evolved from similar interests in other scientific fields. The common denominator was the response of the structure at some discrete location to load, which is the well-known influence coefficient. The motivation to define the loads on lifting and stabilizing surfaces was greatly enhanced by rapidly evolving aircraft performance in the 1930 to 1950 time period. Major efforts to measure loads with strain gages were ongoing in the 1940's; however, the approach was not solidified until 1954. The idea was perpetuated by Skopinske, Aiken, and Huston[1] in their 1954 report. The linear regression approach to develop mathematical load equations from strain-gage responses obtained from physically applying loads to an airplane wing or other structural part is still the primary and only commonly used method today. Other mathematical approaches such as singular-valued decompositions[2] are being investigated and may someday prove advantageous; however, these approaches need to be demonstrated.

The complexity of load calibrations using strain gages has increased as the complexity of the structure and materials has also increased. Straight wings and tails with few and dominant spars characterized early airplane structures. Swept wings and delta wings with many spars emerged later. Complex structures such as integrated honeycomb skins and corrugated webs led to strain gages being located in less-than-optimum places. Composite materials, many of which are anisotropic, also emerged to further complicate the situation. High-speed airplanes experienced significant aerodynamic heating that affected the nature of strain-gage responses. All of these factors challenged the load-measurement engineer to adapt and create new and better approaches and tools.

The increased cost associated with conducting load calibrations on aircraft introduced an economic factor that has impacted recent aircraft programs. Aircraft developers are under extreme economic pressure to find less-expensive alternatives to the expensive strain-gage load calibrations. Advanced computer capabilities have provided new and better ways to visualize the mathematical situations, enhancing the load measurer's ability to optimize engineering judgements. All of these factors, circumstances, and tools in aggregate constitute the science of measuring loads with calibrated strain gages on aircraft.

The purpose of this paper is to document important examples of load calibrations on aircraft, many of which were flight-tested at the NASA Dryden Flight Research Facility at Edwards, California, during the past 30 years. The technical experiences and approaches leading to optimum load calibrations will be presented. The latest tools will be identified, and examples and future directions for load calibrations will be projected.

The primary emphasis of this paper will be on studying the total physical procedures of calibrating strain-gaged structures and all the supporting analyses and computational techniques that have been used. The load-calibration science will be studied using the results and experiences obtained from the actual data and from efforts involving 14 structures on 13 aircraft and 1 laboratory test structure. The structures included in the effort are as follows:

- the M2-F2 tip fin
- the X-24 tip fin
- the HL-10 center fin
- the X-24 center fin
- the X-15 horizontal tail
- the F-89 wing
- the space shuttle wing

- the T-37B wing
- the YF-12A wing
- the Highly Maneuverable Aircraft Technology (HiMAT) wing
- the Supercritical wing
- the F-111A/Transonic Aircraft Technology (TACT) wing
- the B-1 wing
- the B-2 wing
- the NASA Hypersonic Wing Test Structure (HWTS)

This group of airplane structures includes a variety of types that constitutes a typical aviation cross section. The group includes fins, tails, and wings with a wide variety of aspect ratios. The configurations range from simple configurations such as torque-tube to complex multispar delta wings. Straight-wing, swept-wing, and delta-wing configurations are also encompassed. Some of the structures have skin-dominant construction, and others are spar-dominant. Anisotropic materials, heat shields, corrugated components, nonorthogonal primary structures, and truss structures are other particular characteristics that are encountered.

THE STRUCTURAL SUBJECTS

Figure 1 shows 14 pertinent flight structures. All of these structures have strain gages installed for measuring flight loads. The structures have been loaded, and the strain responses have been documented. Figure 2 shows a structure built specifically for laboratory test activities that will also be examined. The basic approach used to calibrate structures such as these has previously been outlined.[1] A load calibration of these structures is performed by applying discrete loads in a grid pattern over the surface of the structure. The strain-sensor outputs are recorded, and linear equations are developed from which surface loads can be determined. The most common approach used with calibrated strain gages does not involve using strain measurements directly. The load equations are most commonly developed from the outputs of strain-gage bridges.[3] The load equation generally takes the following form:

$$L = [\mu_1 + \mu_2 + \mu_3 + \ldots \ \mu_j]\{\beta_{1n}\}_{n=j}^{n=1} \tag{1}$$

where L is the load, β is a constant, and μ is a nondimensional strain-gage response described as follows:

$$\mu = \frac{\delta}{\delta_{cal}} \tag{2}$$

In equation (2), δ is determined from the voltage changes of a strain-gage bridge, and δ_{cal} is a reference determined by shunting a calibrated resistor across one arm of the same strain-gage bridge. This technique was used to calibrate most of the structures shown in figures 1 and 2.

A tool that is typically used to understand the meaning of the strain-gage load calibration is the influence coefficient. The influence coefficient is defined as:

$$I_C = \frac{\mu}{L} \tag{3}$$

where μ is the strain-gage bridge output and L is the applied load. The output can be in strain, volts, or counts, depending on how the user decides to handle the data.

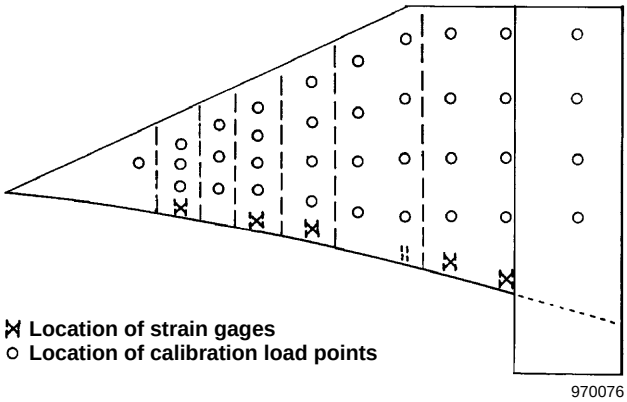

(a) M2-F2 tip fin.

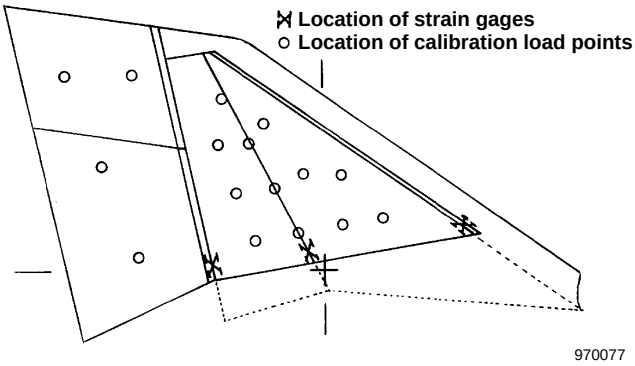

(b) X-24A tip fin.

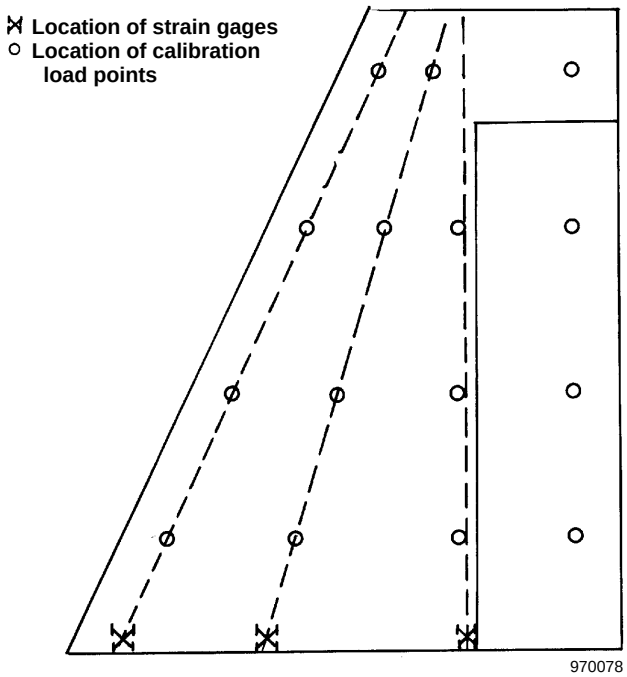

(c) HL-10 center fin.

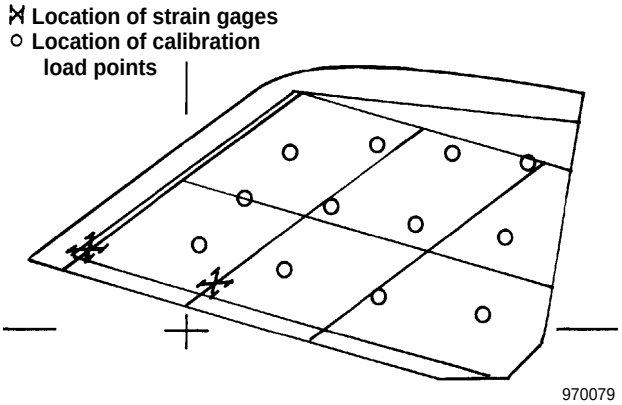

(d) X-24A center fin.

Figure 1. Lifting or stabilizing surfaces studied for load calibration characteristics.

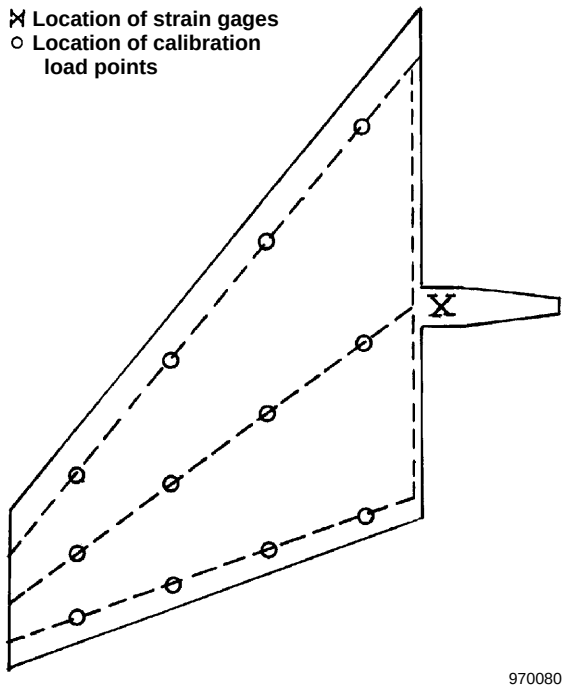

(e) X-15 horizontal tail.

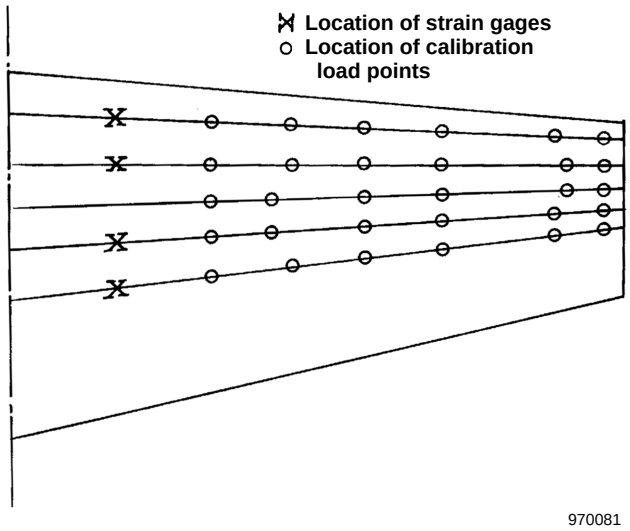

(f) F-89 wing.

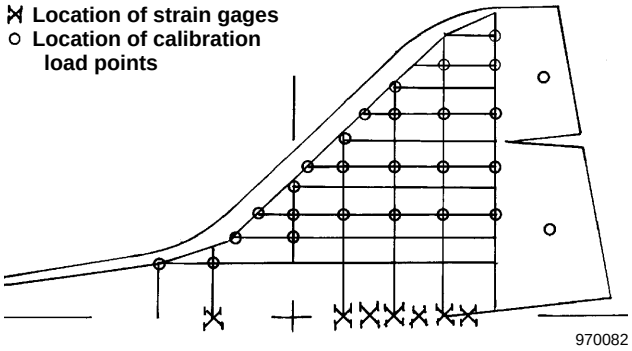

(g) Space Shuttle Orbiter wing.

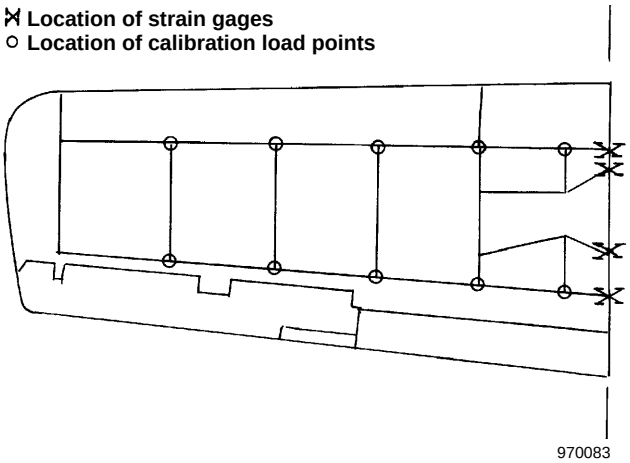

(h) T-37B wing.

Figure 1. Continued.

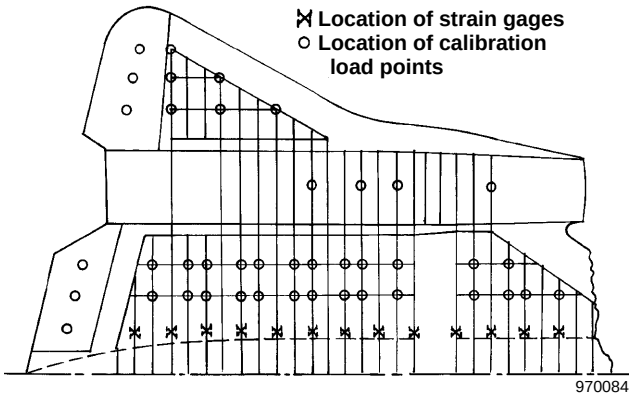

(i) YF-12A wing.

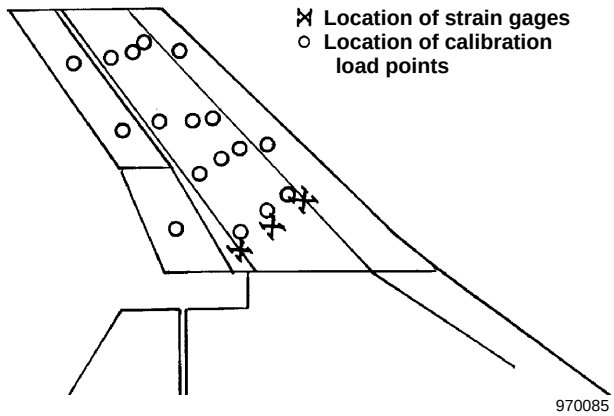

(j) HiMAT wing.

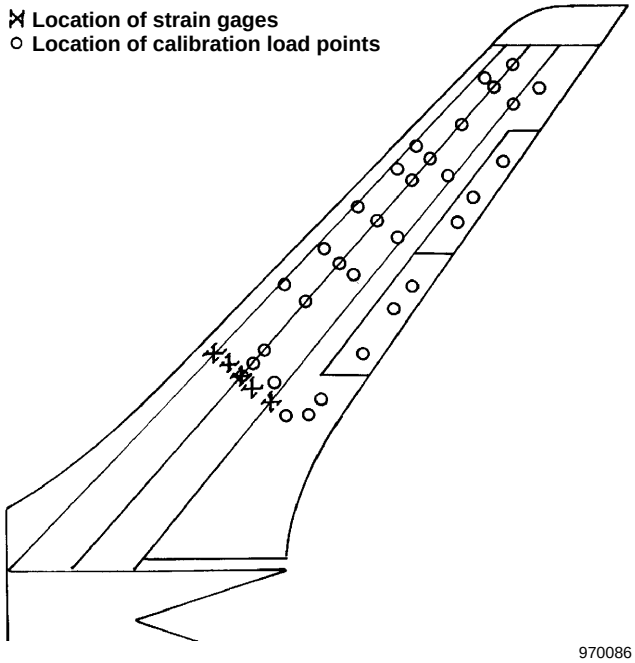

(k) Supercritical wing.

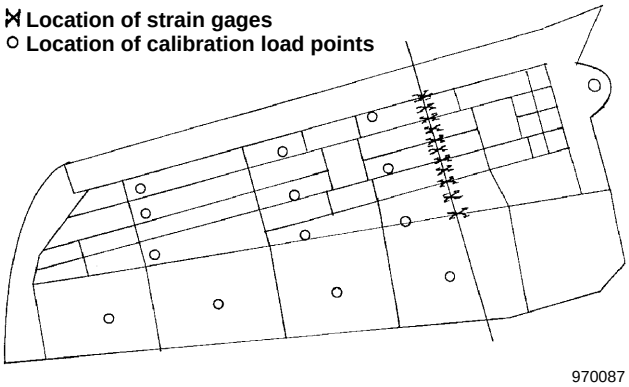

(l) F-111 TACT wing.

Figure 1. Continued.

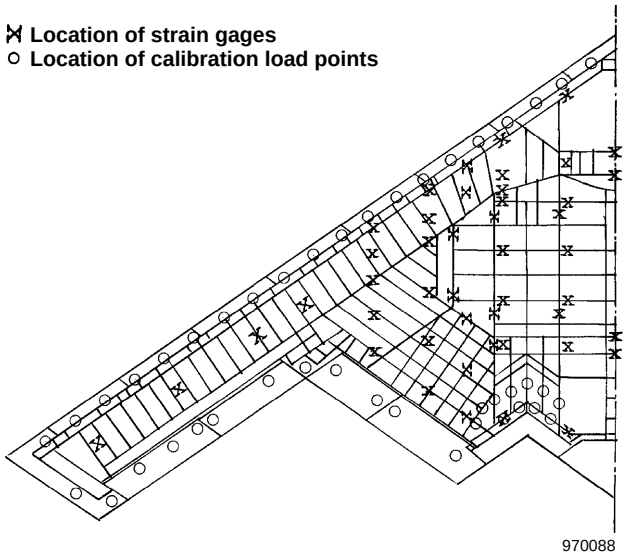

(m) B-2 wing.

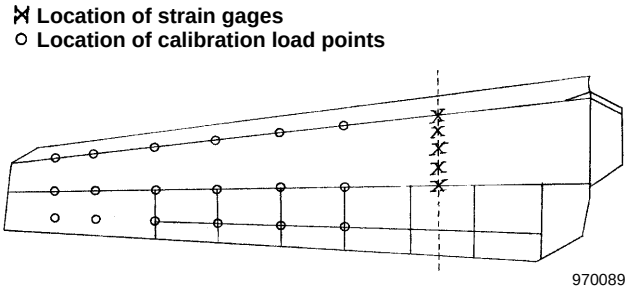

(n) B-1 wing.

Figure 1. Concluded.

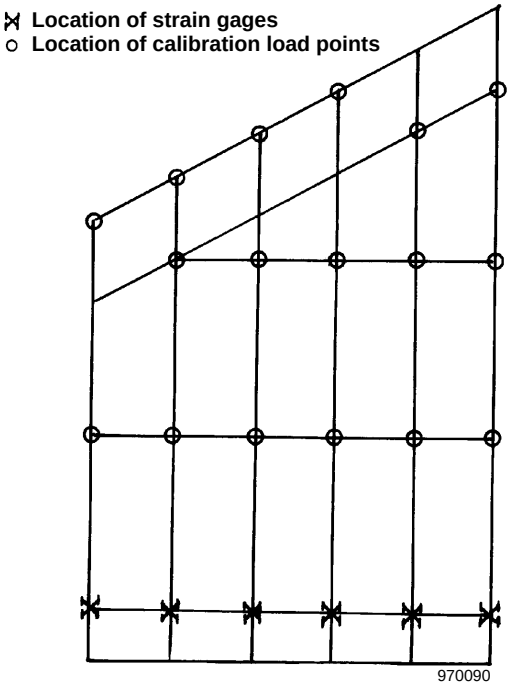

Figure 2. Hypersonic wing test structure.

From the beginning of strain-gage measurement technology,* the influence coefficient has been the primary tool to evaluate the validity of a load calibration and the primary mechanism by which strain gages are combined to obtain optimum load equations. Strain-gage bridges are specifically located to sense as uniquely as possible either shear, bending-moment, or torsional loads. The most common result is that the discrete strain-gage systems do not uniquely sense shear, bending, or torsion but sense some combination of two or all three loads. The common visual analysis mechanism is to plot the influence coefficient as a function of span and to approximate the contours of constant chord.

Figures 3(a) to 3(c) show an ideal shear, bending, and torsion response. Figures 3(d) and 3(e) show two examples of combined responses: torsion/bending and shear/torsion/bending. A perfect shear response is one in which the chord contours all fall upon each other to form a flat horizontal response (a single line) of influence coefficient in the span direction. An ideal bending response is one in which the chord lines all fall upon each other to form a single line increasing linearly in the span direction. An ideal torsion response is one in which the constant chord lines form a pattern in the span direction that has the shape of the planform of the load points of the structure being calibrated. A combined torsion/bending response is one in which the constant chord lines increase linearly in the span direction but do not fall upon each other. A combined shear/bending/torsion response is one in which the constant chord lines only slightly increase linearly in the span direction and do not fall upon each other. In reality, actual responses rarely look like any of the cases presented. Significant nonlinearity is usually present, and the best that can be done is to minimize the nonlinearity in the influence-coefficient plot to look as much as possible like these ideal cases by linearly combining several gages (eq. (1)) to form an aggregate influence-coefficient plot.

Modern computer graphics have provided additional ways of visualizing strain-gage load calibrations. Figure 3 also shows two very effective methods. The influence coefficients can be presented in three-dimensional format as ribbon plots and wire-frame plots. The influence coefficient is presented on the vertical axis, and the span and chord locations associated with the discrete influence coefficient are plotted on the other two axes. The five illustrative cases discussed in the previous paragraph appear in ribbon or wire-frame plots as linear surfaces or as warped linear surfaces. The warped linear surface occurs because the influence coefficient is presented in terms of percent-span and percent-chord location rather than as actual rectangular coordinates in the plane of the structural surface. This presentation results in a distortion or warpage for certain cases because wings are normally tapered. The advantage of the three-dimensional plots is that the degree to which discrete load points lie outside the influence-coefficient surface can be easily visualized. The relative usefulness of the various types of plots is discussed after actual examples that provide insight into the merits of various presentations have been given.

It should be noted that several approximations are present in the bulk of this report. The generation of the wire-frame and ribbon plots with personal computer software is done by inputting an array of information at equal intervals. In other words, the values of influence coefficients are determined, for example, for 5- or 10-percent increments of span or chord from 0 to 100 percent. If the actual load point occurs at 9-percent span and the 6-percent chord, then the value can be inputted as 10-percent span and 5-percent chord. The same type of data manipulation is done with the actual load calibration when influence-coefficient plots are being considered. In general, load points will primarily be discussed in terms of the closest 5- or 10-percent span or chord.

The extent to which a grid of load points can be applied to the surface of a structure is limited by the peculiar nature of the structure itself. The input for the three-dimensional plots is a matrix of influence-coefficient values for percent span and percent chord in incremental fashion. Consider a structure that is loaded at seven load points. The matrix of influence coefficients must be developed from the information developed from the seven actual load points at which data are measured. The following matrix contains uppercase values, A_{ij}, for influence coefficients that represent actual load points, and lowercase values, a_{ij}, for influence coefficients that must be interpolated from the values obtained from the actual load points:

---

*Gray, A. K. J., "Procedures Manual for Flight Test Determination and Evaluation of Load Distribution and Structural Integrity," Report No. EFT-55-1, Northrop Aircraft, Inc., June 1955.

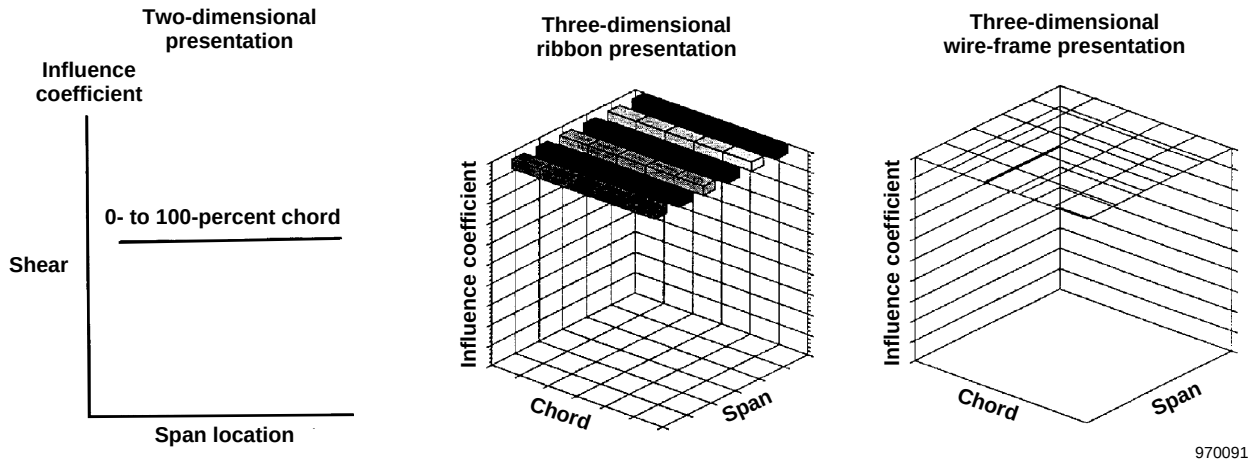

(a) Shear.

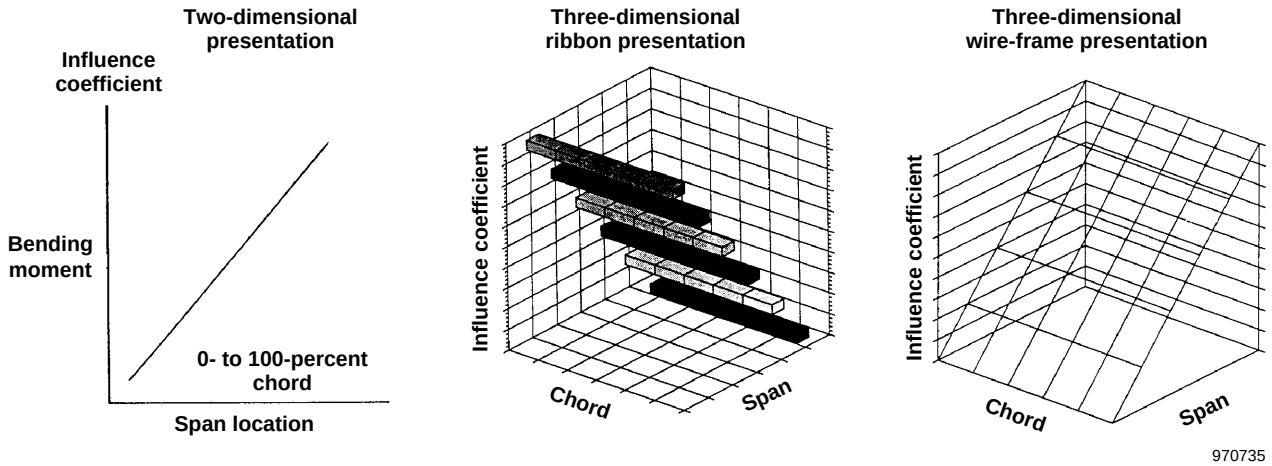

(b) Bending moment.

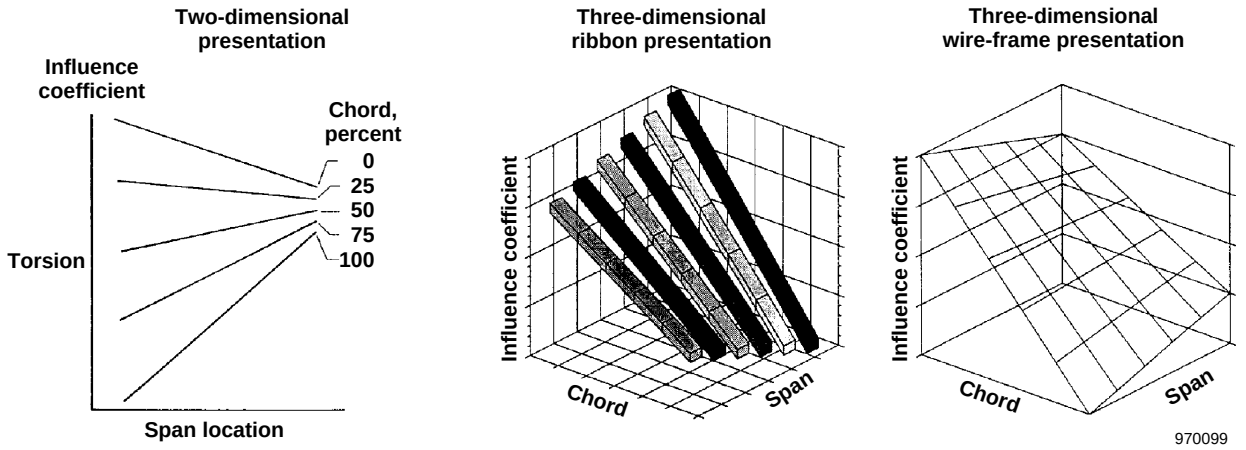

(c) Torsion.

Figure 3. Methods of presenting the common lifting-surface strain-gage responses in terms of influence-coefficient plots.

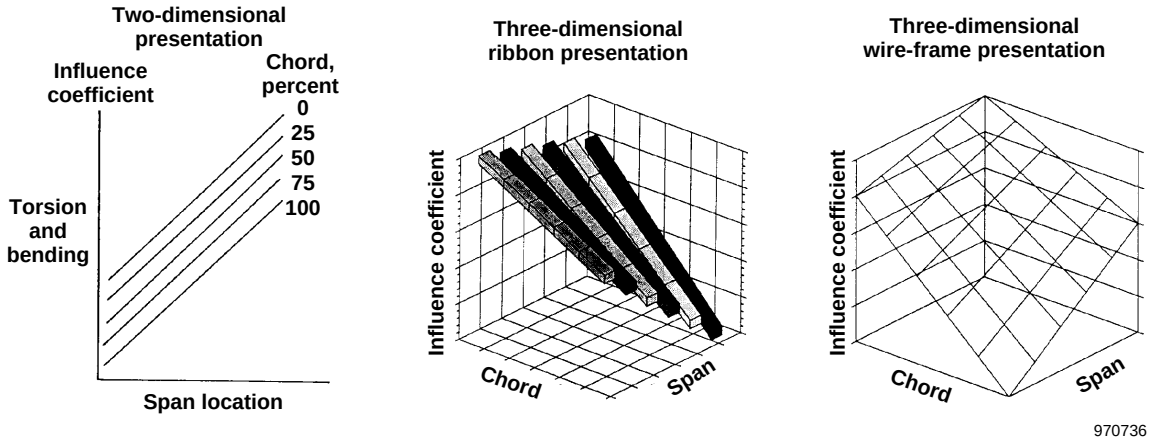

(d) Torsion and bending.

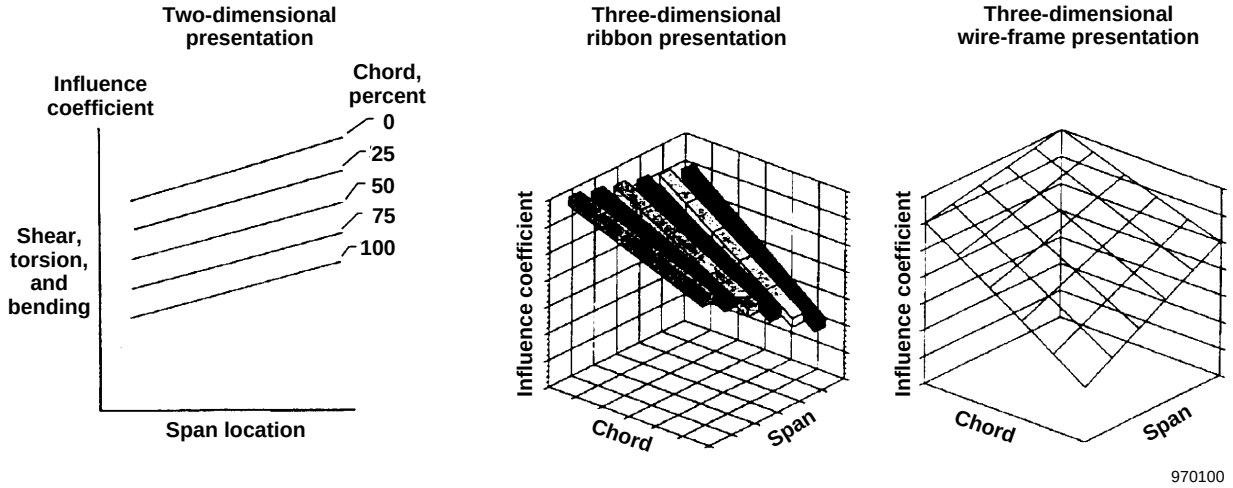

(e) Shear, torsion, and bending.

Figure 3. Concluded

$$
\begin{array}{cc}
 & \text{Percent span} \\
\text{Percent chord} & \begin{bmatrix}
a_{11} & a_{12} & a_{13} & a_{14} & a_{15} & a_{16} \\
a_{21} & A_{22} & a_{23} & a_{24} & A_{25} & a_{26} \\
a_{31} & a_{32} & a_{33} & A_{34} & a_{35} & a_{36} \\
a_{41} & A_{42} & a_{43} & a_{44} & A_{45} & a_{46} \\
a_{51} & a_{52} & A_{53} & A_{54} & a_{55} & a_{56} \\
a_{61} & a_{62} & a_{63} & a_{64} & a_{65} & a_{66}
\end{bmatrix}
\end{array}
$$

Many coefficients are obviously not defined in this array involving a seven-point load calibration. A complete array is required to present the ribbon and wire-frame plots that will be extensively used throughout this report. The array must also be developed in equal increments in both the span and chord directions; therefore, the array would typically be developed in 10- or 20-percent increments. The extrapolation and interpolation processes are extensive, and no traditional method of evaluating these processes exists. The concept of a relevance coefficient is therefore introduced to evaluate the extent of the load calibration in the remainder of the paper. A relevance coefficient, C_R, is defined as:

$$
C_R = \frac{A_L}{A_T} \tag{4}
$$

where A_L is the area loaded and A_T is the total area. The area loaded is defined as 10 percent of chord and span on either side of the specific location of the load point. Figure 4(a) shows the relevance coefficient pictorially illustrated; two cases are shown. One case has a calibration structure in which 18 load points are used, and the other case is one in which only 8 load points are used. Obviously, the case with 18 load points appears to cover more discrete areas on the surface and provide the format for a better load calibration. The total validity of this observation provides groundwork for further study in later sections. The case with 18 load points covers 72 percent of the structural planform and has a relevance coefficient of 0.72. The case with 8 load points covers 32 percent of the structural planform and has a relevance coefficient of 0.32.

Figure 4(b) graphically shows additional characteristics of the relevance coefficient. Data must be interpolated, extrapolated, and rounded off when developing influence-coefficient plots. The large number of calibration load points provides complete information to develop the influence-coefficient plots. If only two load points are available in the span and chord direction (as shown in the left part of figure 4(b)), then irregularities or interpolative discontinuities can occur. The right side of figure 4(b) shows the result of four load points in the span and chord direction. The trend of the data is easily established, and the span/chord interpolation is apparent.

The load calibrations of the various airplanes will be introduced next along with pertinent characteristics of the structural configuration. Throughout this paper, errors relating to load measurement will be stated. It should be noted that these errors may not be exactly comparable. Some of the quotations are errors of the load calibration. In other words, an error statement is presented that represents the individual calibration loads that can be calculated from the load equations derived from the load calibration. Other quotations are errors of the flight load measurement. These quotations have the equation errors factored into the error estimate, but other factors are involved.

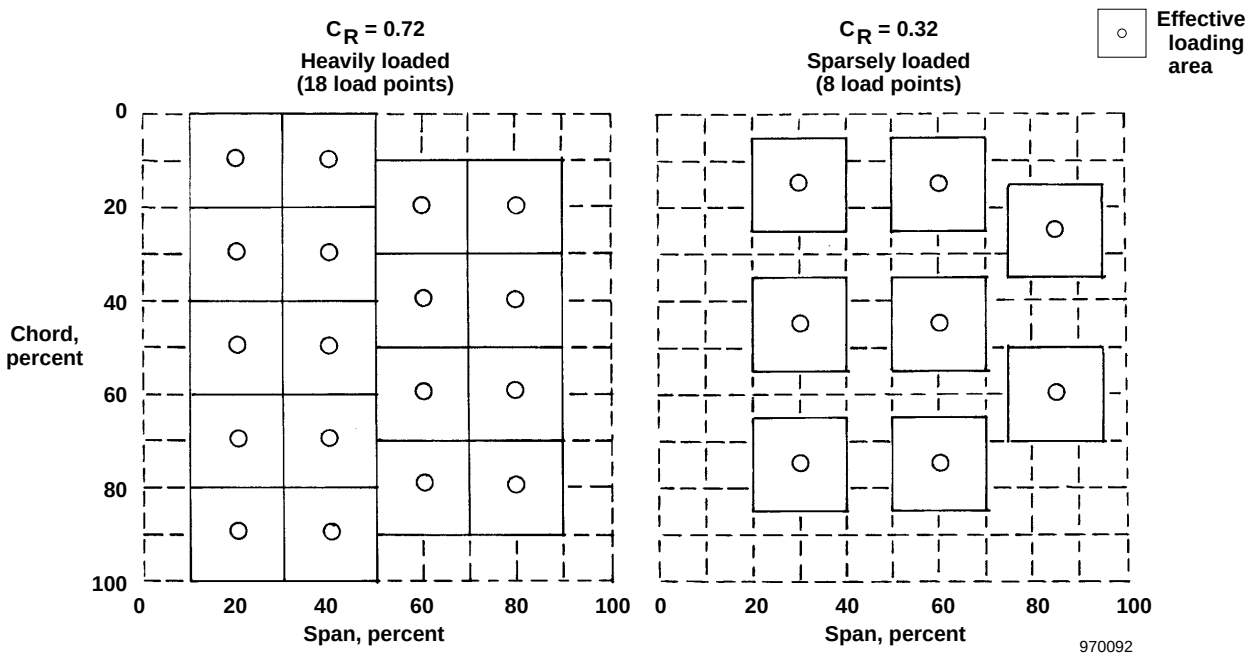

(a) Pictorial illustration of the relevance coefficient.

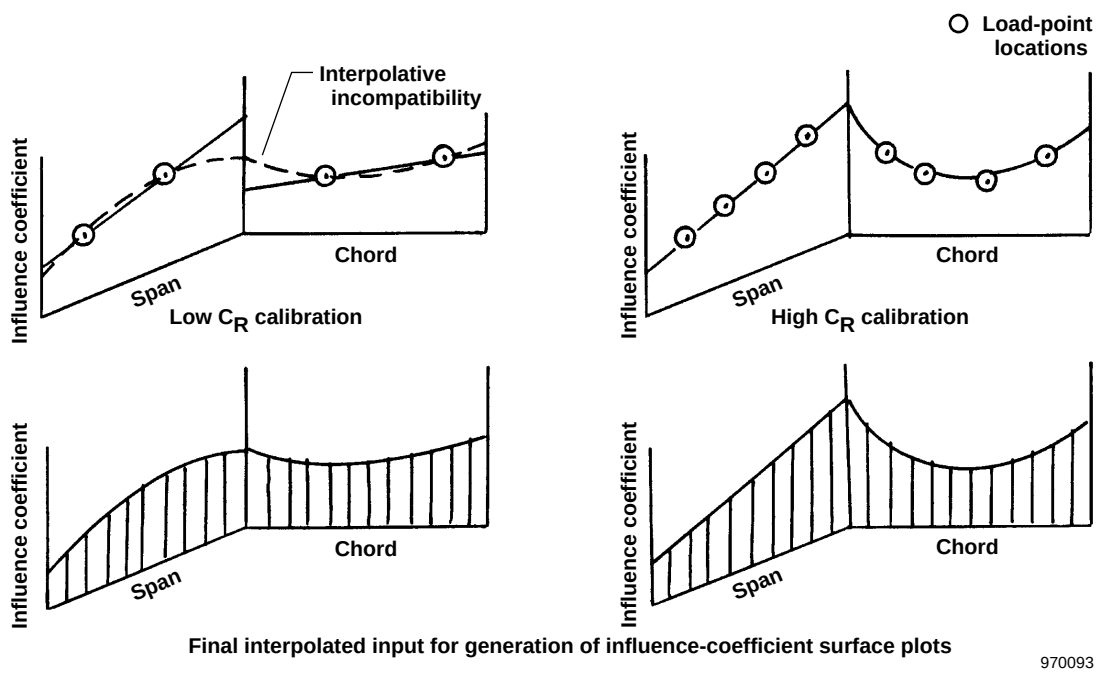

(b) Effect of the relevance coefficient on the generation of influence-coefficient input data for ribbon and wire-frame plots.

Figure 4. The relevance coefficient and how input data are generated for the ribbon and wire-frame plots.

CALIBRATION OF THE AIRCRAFT STRUCTURES

The basic purpose of this section is to present the physical load calibration of the strain gages and the characteristics of the response. The number of load points, the location of the load points, the location of the strain gages, the structural arrangement, the influence coefficients, and all other circumstances and facts pertinent to the load calibration are presented in this section.

M2-F2 Tip Fin

Appendix A shows a three-view sketch of the M2-F2 lifting body. Loads were measured on the tip fin, which figure 1(a) shows in more detail. The stabilizing surface is a low-aspect-ratio structure with multiple spars. Figure 1(a) also shows the location of strain gages and an extensive grid of calibration load points. The basic strain-gage load calibration has been documented,* and the flight results have previously been presented.[4] Thirty-five load points were used to calibrate 20 strain-gage bridges located in and around the 7 spars. The very low aspect ratio of this structure coupled with multiple short spars provided at least one unique strain-gage response characteristic. The three-dimensional ribbon plot (fig. 5) is the primary method used to present data for this structure.

Figure 5 also shows the conventional presentation of a shear bridge (120S). The bridge can be seen to be sensitive to torque and slightly sensitive to bending moment but is primarily a shear bridge. Figures 6, 7, and 8 show three

*Friend, Edward L., "M2-F2 Vertical Tail Calibration," Branch Report BR-2, NASA Flight Research Center, Aug. 1966.

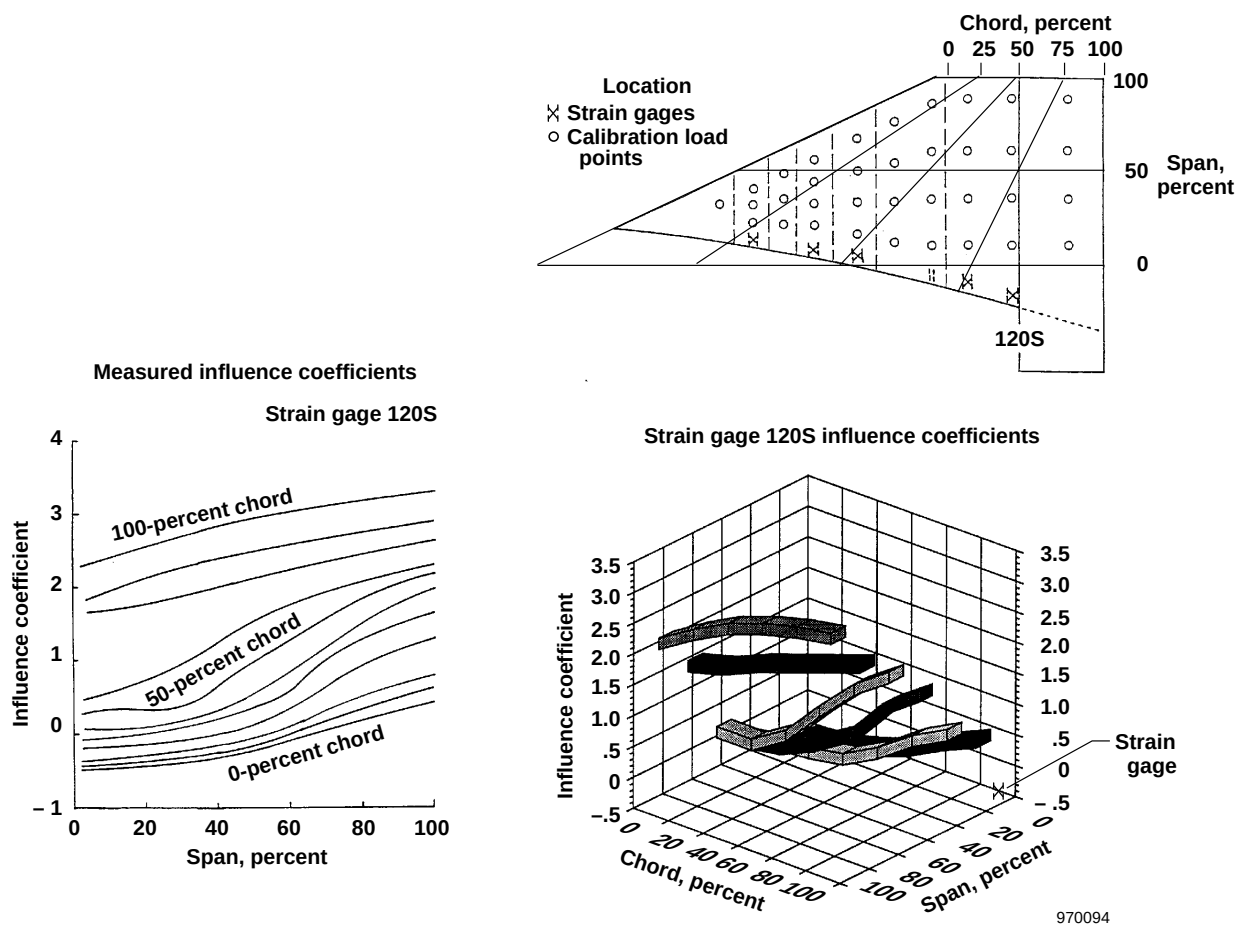

Figure 5. Contrasting methods of presenting influence-coefficient plots for the M2-F2 tip fin.

typical responses for this structure. Figure 6 also shows the shear bridge 120S. Several bridges exhibit similar characteristics. This bridge did cover shear loading near the tip with some bending contamination. Another bridge located on the same spar (fig. 7), 118S, shows another pattern where the trailing-edge and root loads result in large influence coefficients. Figure 8 shows the response of bridge 106S, which is located on one of the short spars in the forward part of the structure. This type of response was seen numerous times on other spars and represents a fairly unique structural response. The strain-gage bridge 106S responds primarily to spanwise loads located near the spar itself. Because this bridge is capable of sensing applied load in only a small local area, a large number of bridges is needed to define the load over the entire surface.

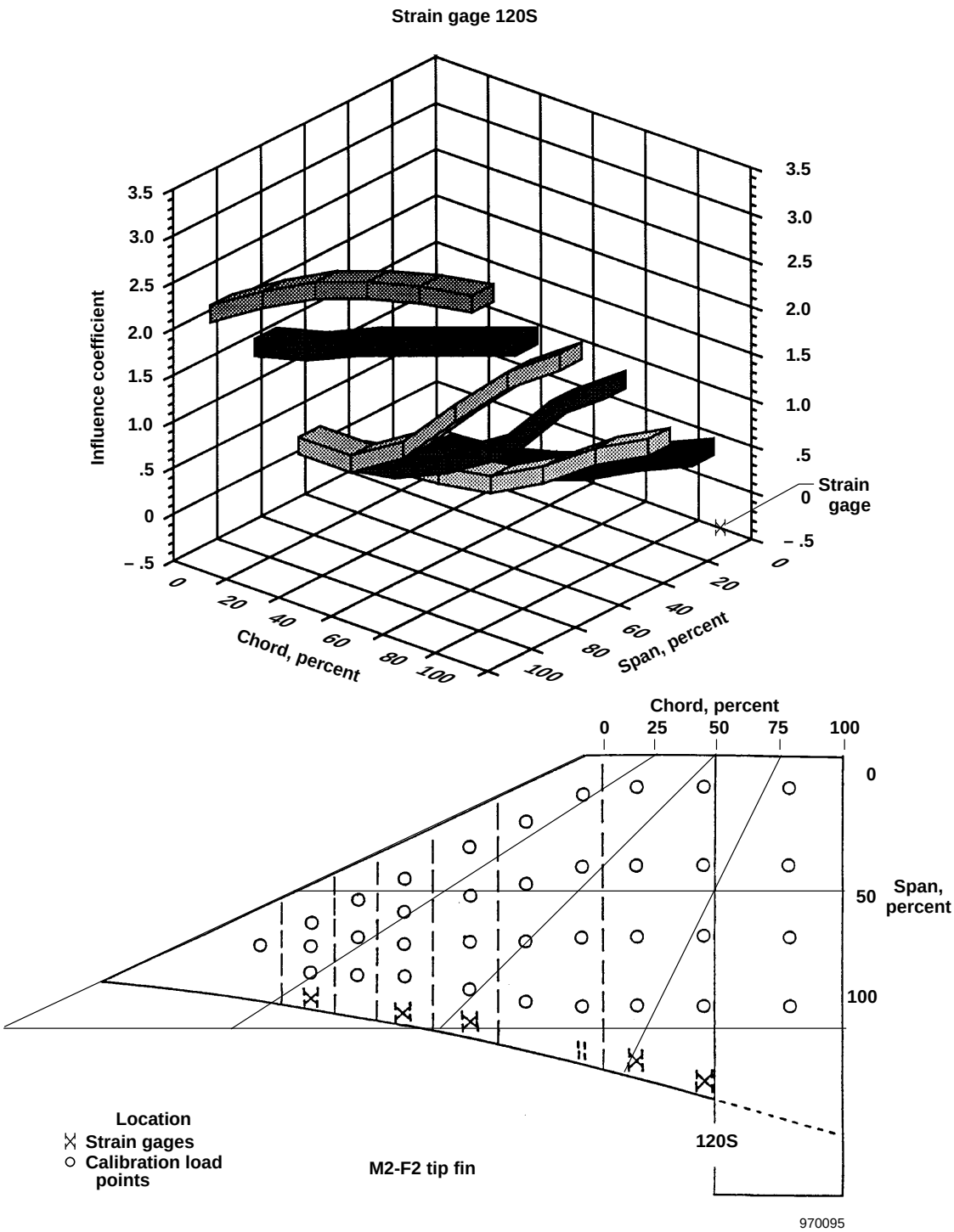

Figure 6. Influence-coefficient plot for strain gage 120S on the M2-F2 tip fin.

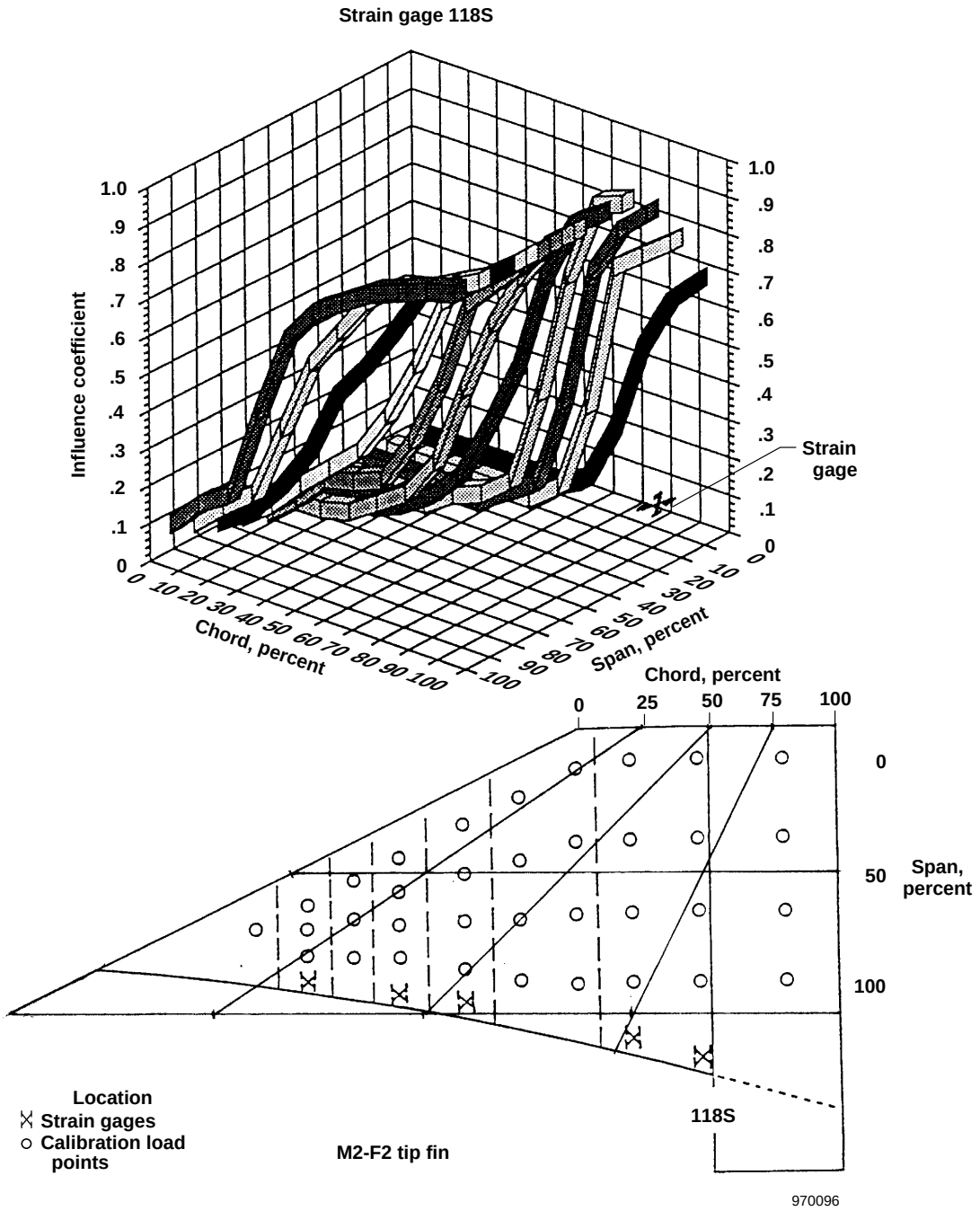

Figure 7. Influence-coefficient plot for strain gage 118S on the M2-F2 tip fin.

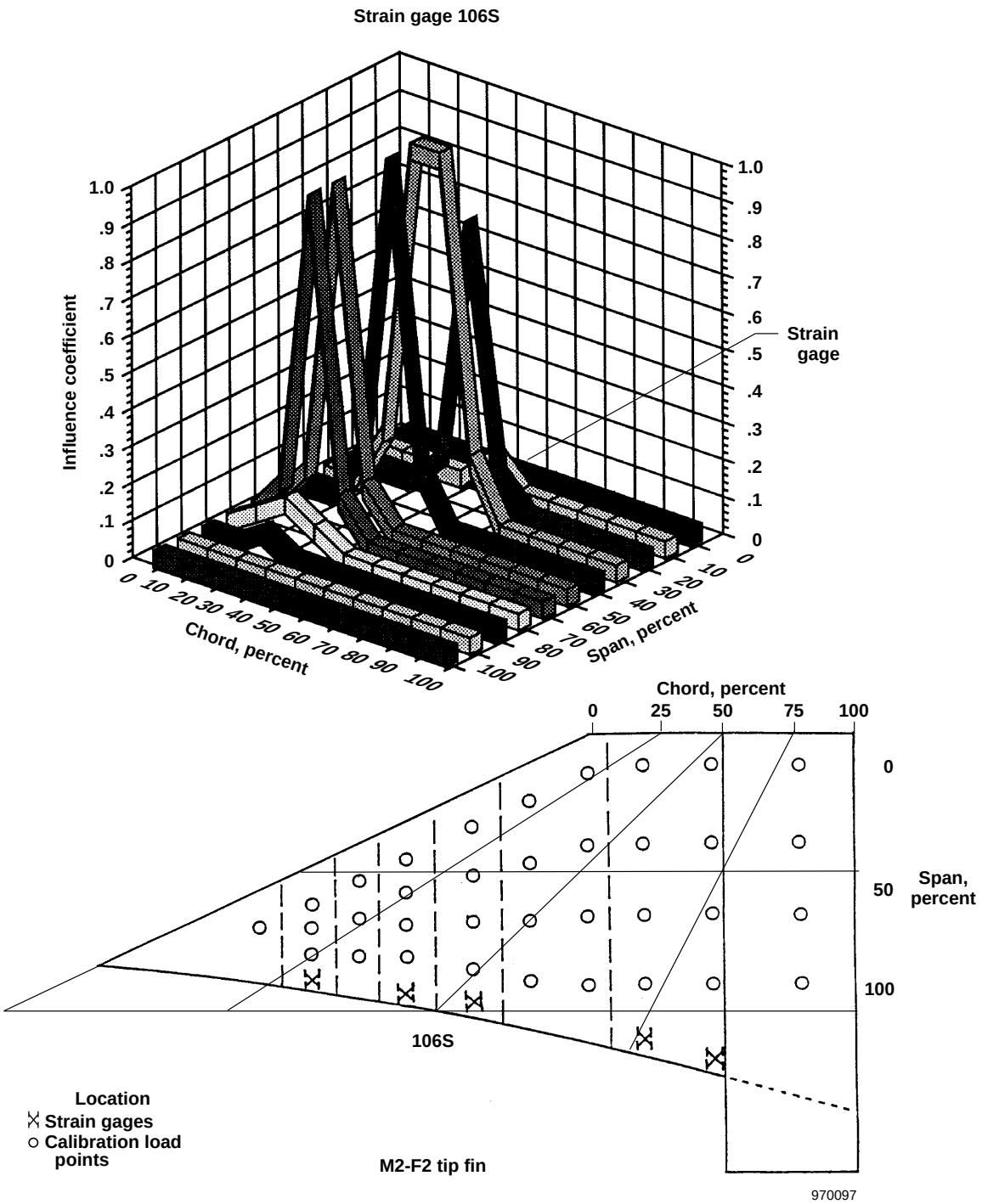

Figure 8. Influence-coefficient plot for strain gage 106S on the M2-F2 tip fin.

Figure 9 clearly shows the difficulty with measuring a discrete load such as shear on a structure that behaves like this one. Combining a reasonable number of bridge responses linearly to produce an aggregate influence-coefficient plot that appears as a flat plane is desirable and is depicted as the perfect shear response shown in figure 9. Combining the three responses shown to the left on figure 9 leaves areas that still are not covered. This lack of coverage means that many additional bridges are required to accomplish a perfect or even an acceptable

shear response. This need for additional bridges was a major problem on flight programs in the 1960's because recording channels were very scarce in the limited data acquisition systems of that era. The best equations that could be established resulted in load measurements with the following estimated errors:

Shear	7 percent
Bending Moment	14 percent
Torsion	48 percent

Because this structure was calibrated using 35 load points, the relevance coefficient was a relatively large number:

$$C_R = 0.72$$

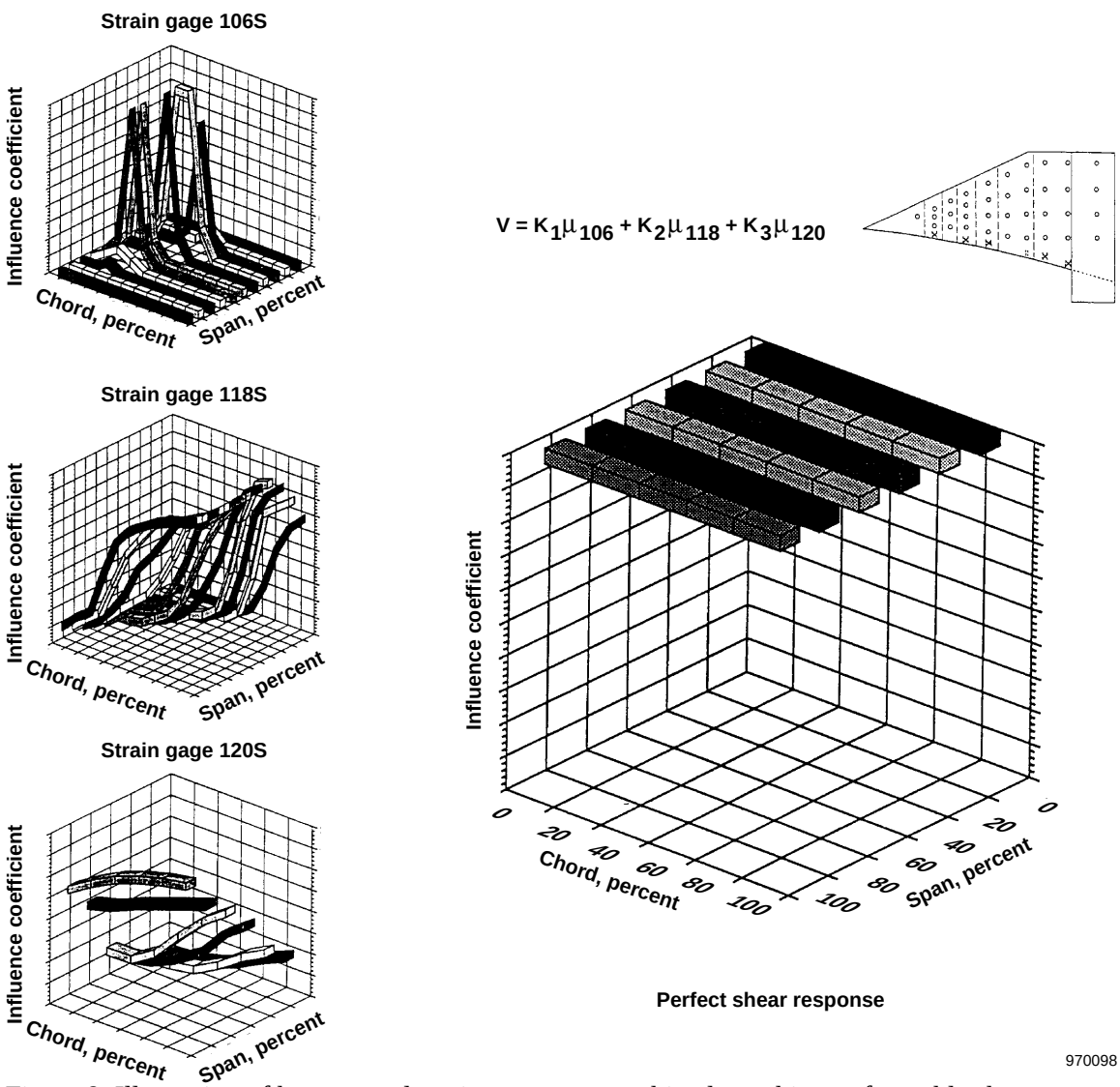

Figure 9. Illustration of how several strain gages are combined to achieve a favorable shear response.

Figure 10 shows the distribution of the calibration load points in terms of span and chord. The large number of load points provides extensive coverage that leads to the large relevance coefficient of 0.72. The large relevance coefficient logically would imply a situation where very accurate loads would be measured. This accuracy was certainly not the case for at least the bending moment and torsion. The most likely reason for the poor accuracy is the limited number of recording channels available to record flight data. More flight recording channels would allow more strain-gage bridges to be used in the equations, which would likely better define the overall response to surface loads on the structure than when limited channels are available.

X-24A Tip Fin

Appendix A shows a three-view sketch of the X-24 lifting body. Figure 1(b) shows the tip fin in more detail and where calibration load points are located along with strain gages. The stabilizing surface can be seen to be a low-aspect-ratio structure with three main spars and a large rear-located control surface. Considerably fewer load points were used to calibrate this structure than were used on the M2-F2 fin (16 as opposed to 35). Sixteen strain-gage bridges were available compared to 21 for the M2-F2 fin. The basic strain-gage calibration has been documented,* and the flight results have previously been presented.[5]

The X-24 strain-gage situation was unique in that the strain-gage instrumentation was installed to measure discrete stresses; hence, only single-active-arm strain gages were used. This choice has the drawback of having very low strain-gage outputs (around one-third to one-fourth of the output, depending on the configuration that would be obtained from a four-active-arm strain-gage bridge). This low output can be noted when X-24 tip fin influence-coefficient values are compared with values for other structures in this report. The low resolution of the calibration sensors creates a factor that could negatively impact the results of the load calibration.

Figures 11, 12, and 13 show influence-coefficient plots that cover the range of responses seen on this structure. Figure 11 shows an influence-coefficient plot that illustrates a typical shear response. Numerous strain gages respond in a similar manner. Figure 12 shows the response of the strain gage that shows a sensitivity to the loads on the control surface at the rear of the structure. Figure 13 shows a response that illustrates a very specific bending effect. Numerous sensors showed a similar dominant bending effect. By inspecting the three drastically different types of responses of the individual strain gages of figure 14, the linear combining of the gages falls short of the flat response required for a well-defined shear equation.

Figure 15 shows a strain gage that exhibits a very good characteristic in terms of sensing bending moment. The “perfect” bending response is shown as a ribbon plot along with the ribbon plot of the actual strain gage (SG 111). The wire-frame plot is introduced as another tool to look at the influence-coefficient plots. The wire-frame software plots the span values opposite to the ribbon plot, providing a reverse way of looking at the data.

The best equations that could be developed resulted in load measurements with the following estimated errors:

Shear	11 percent
Bending Moment	7 percent
Torsion	18 percent

The 16 load points used in the calibration resulted in the following relevance coefficient:

$$C_R = 0.49$$

*DeAngelis, V. Michael, “X-24A Loads Calibration,” Branch Report BR-26, NASA Flight Research Center, 1968.

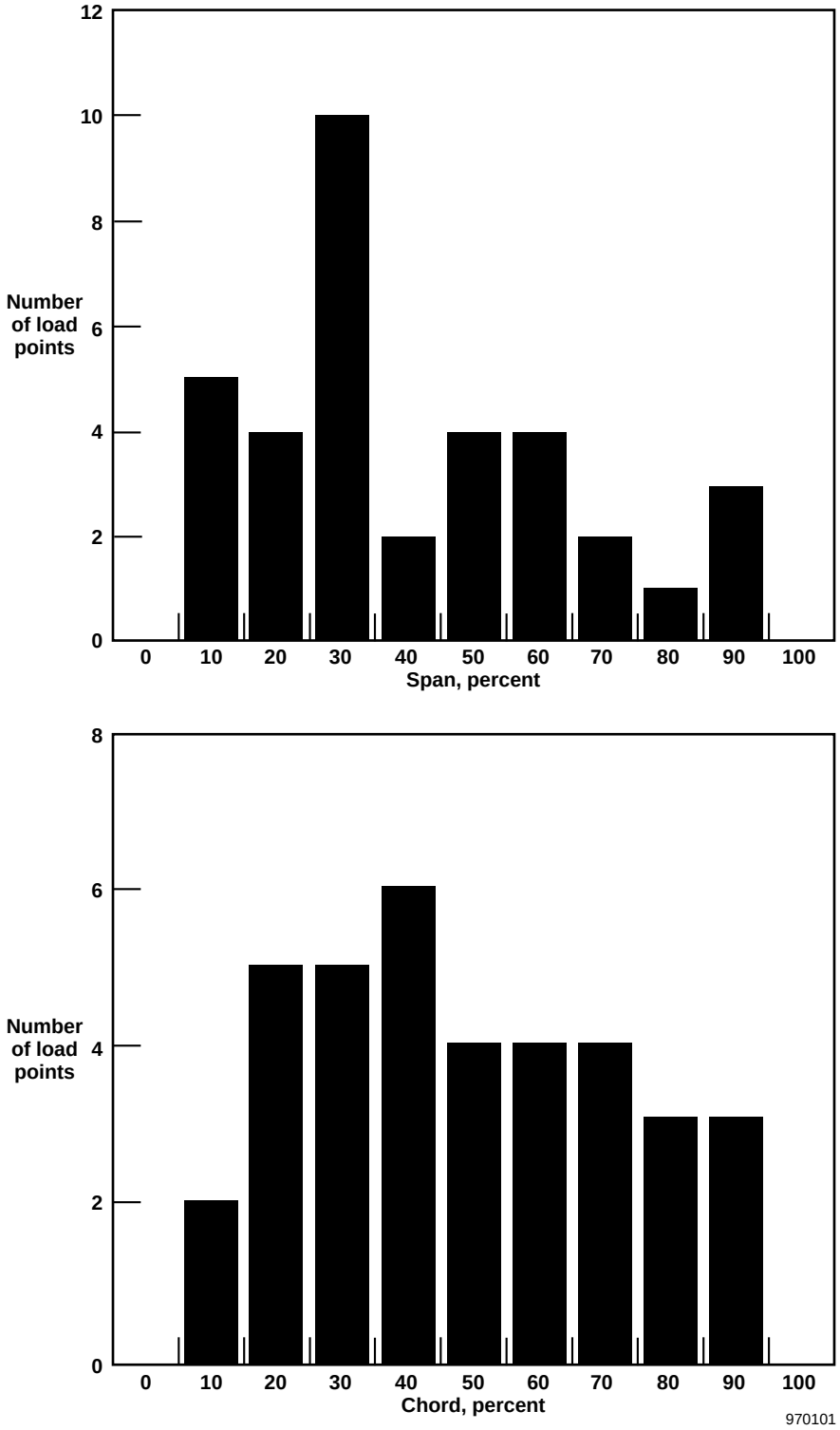

Figure 10. Distribution of load points in the span and chord directions for the M2-F2 tip fin.

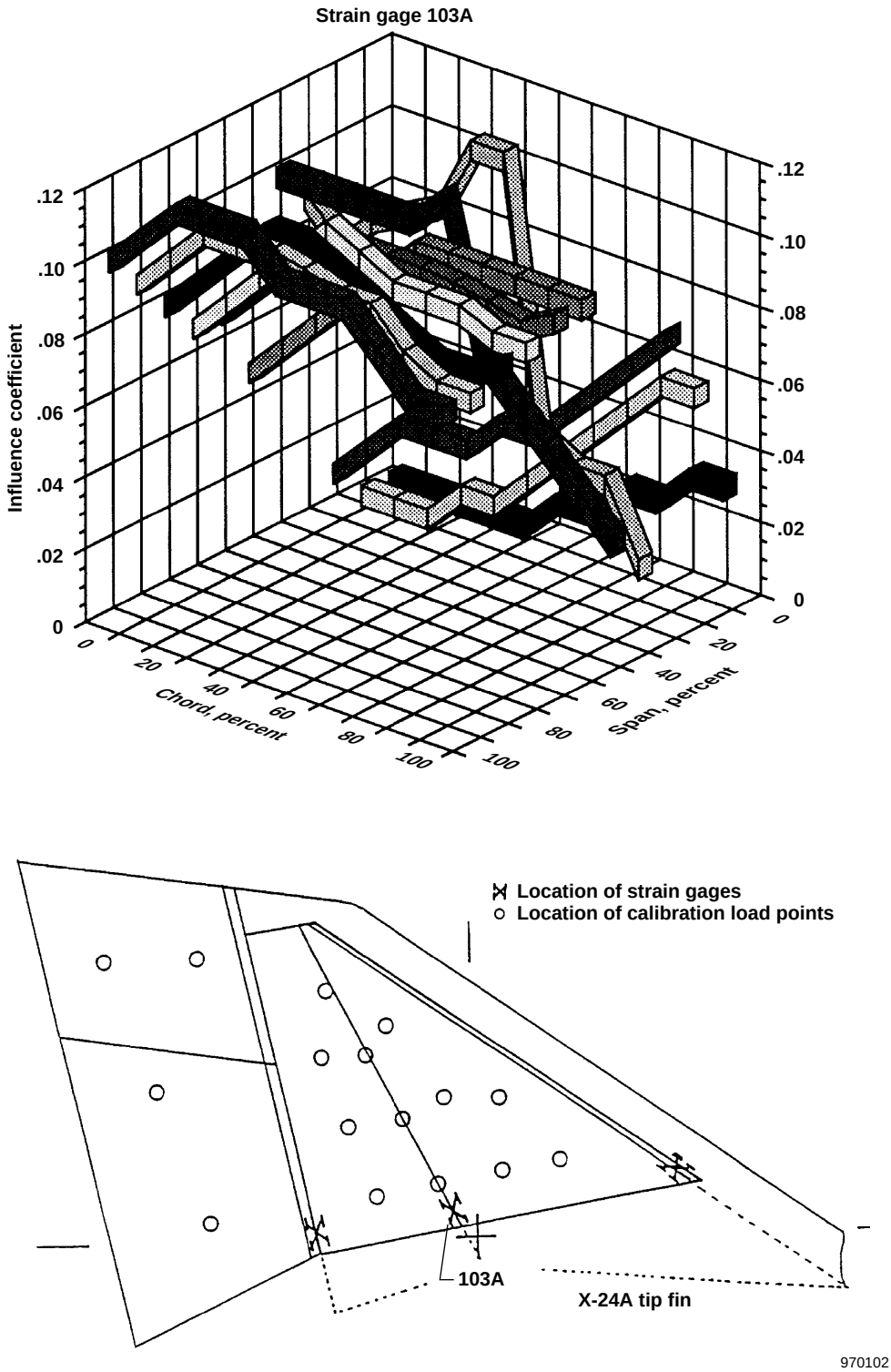

Figure 11. Influence-coefficient plot for strain gage 103A on the X-24A tip fin.

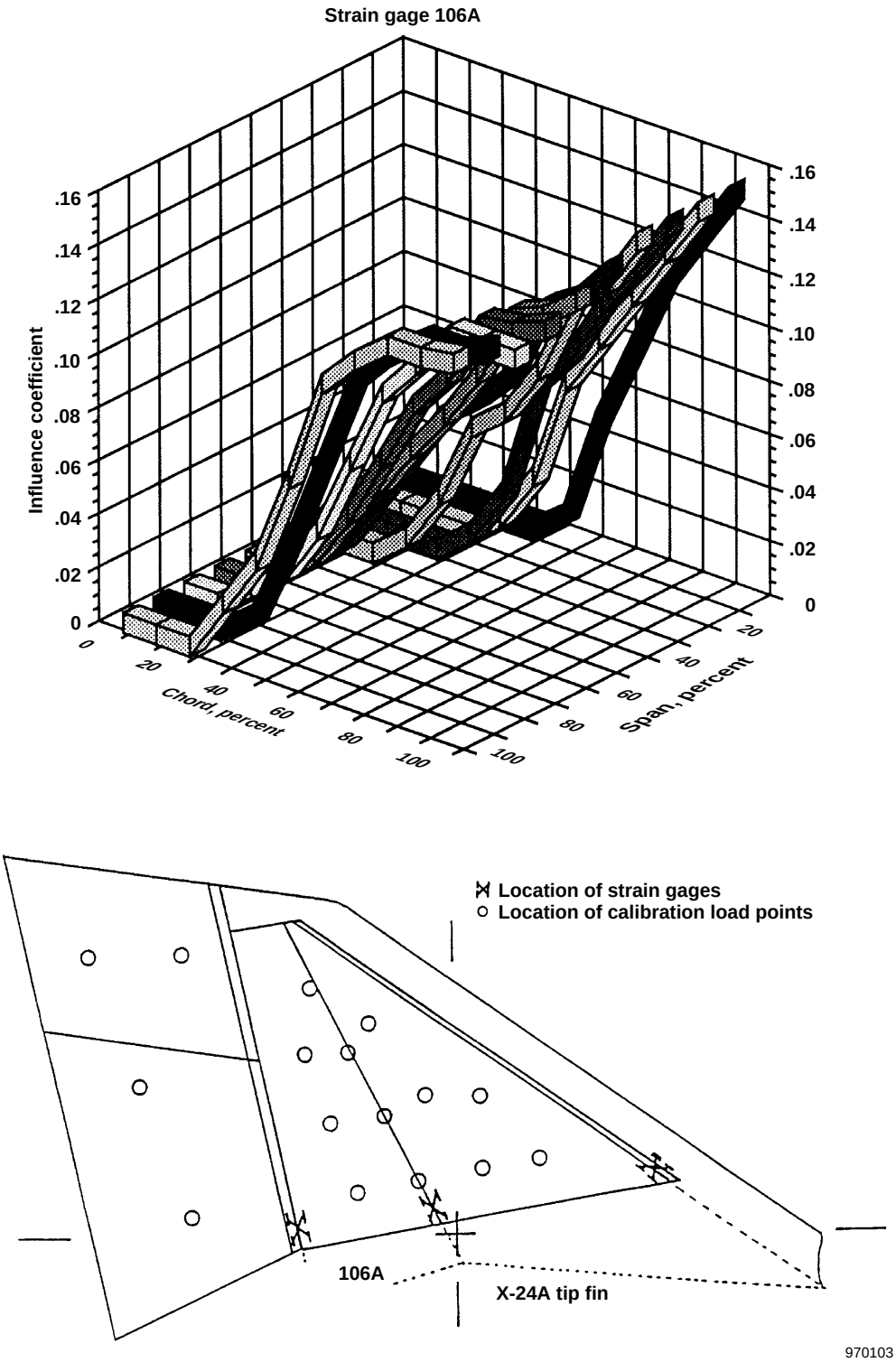

Figure 12. Influence-coefficient plot for strain gage 106A on the X-24A tip fin.

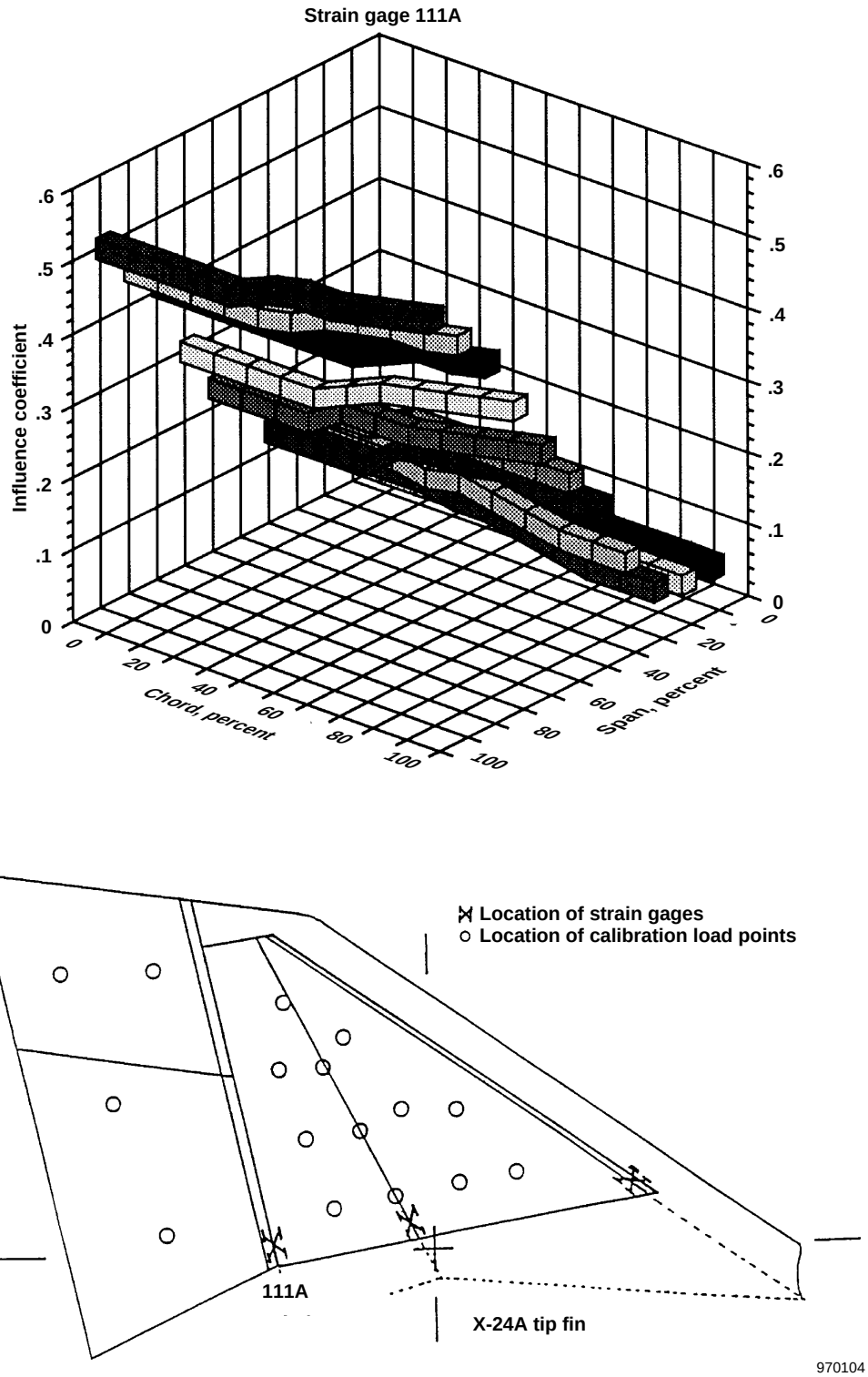

Figure 13. Influence-coefficient plot for strain gage 111A on the X-24A tip fin.

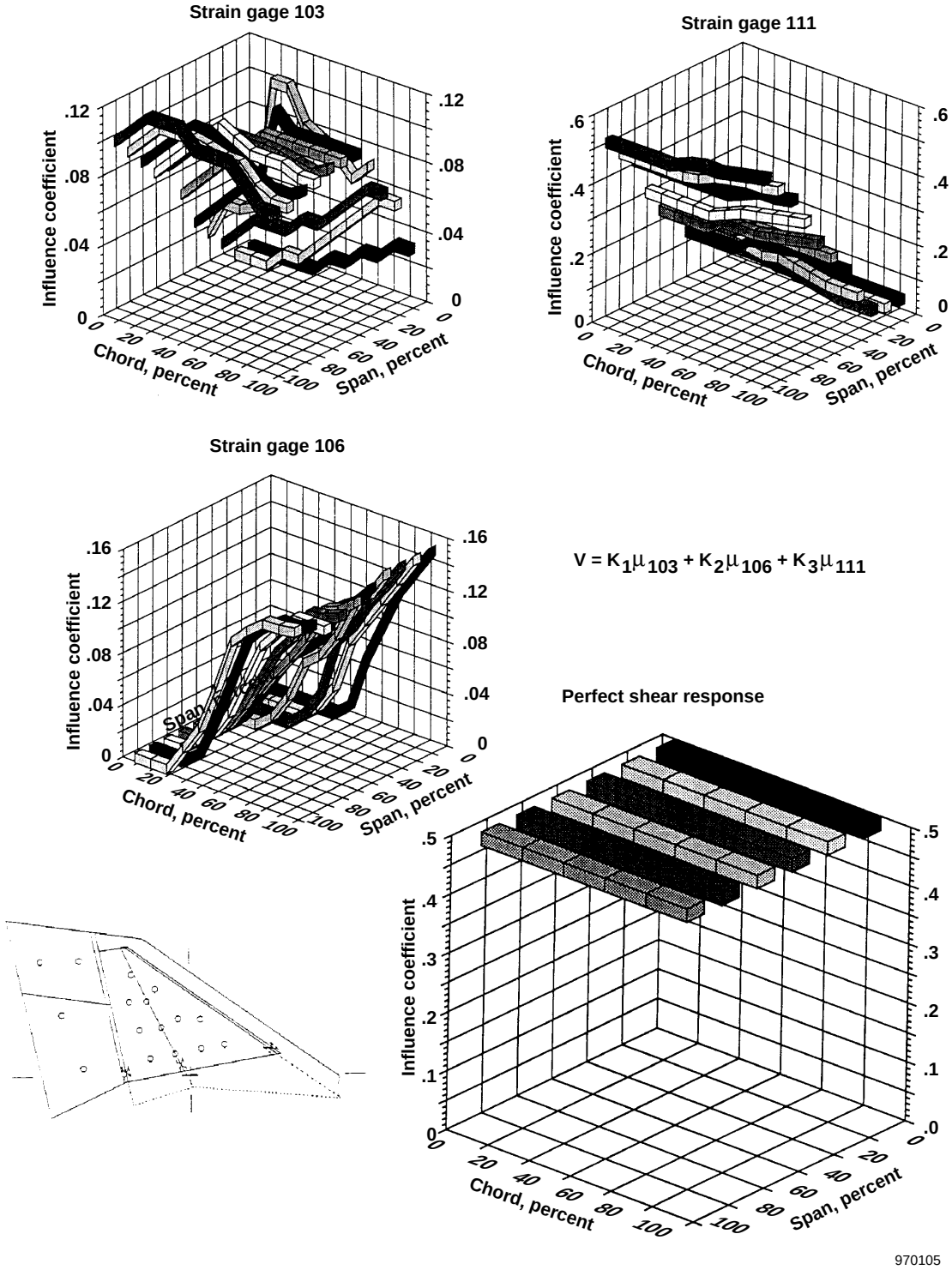

Figure 14. Illustration of how several strain gages are combined to obtain a favorable shear response.

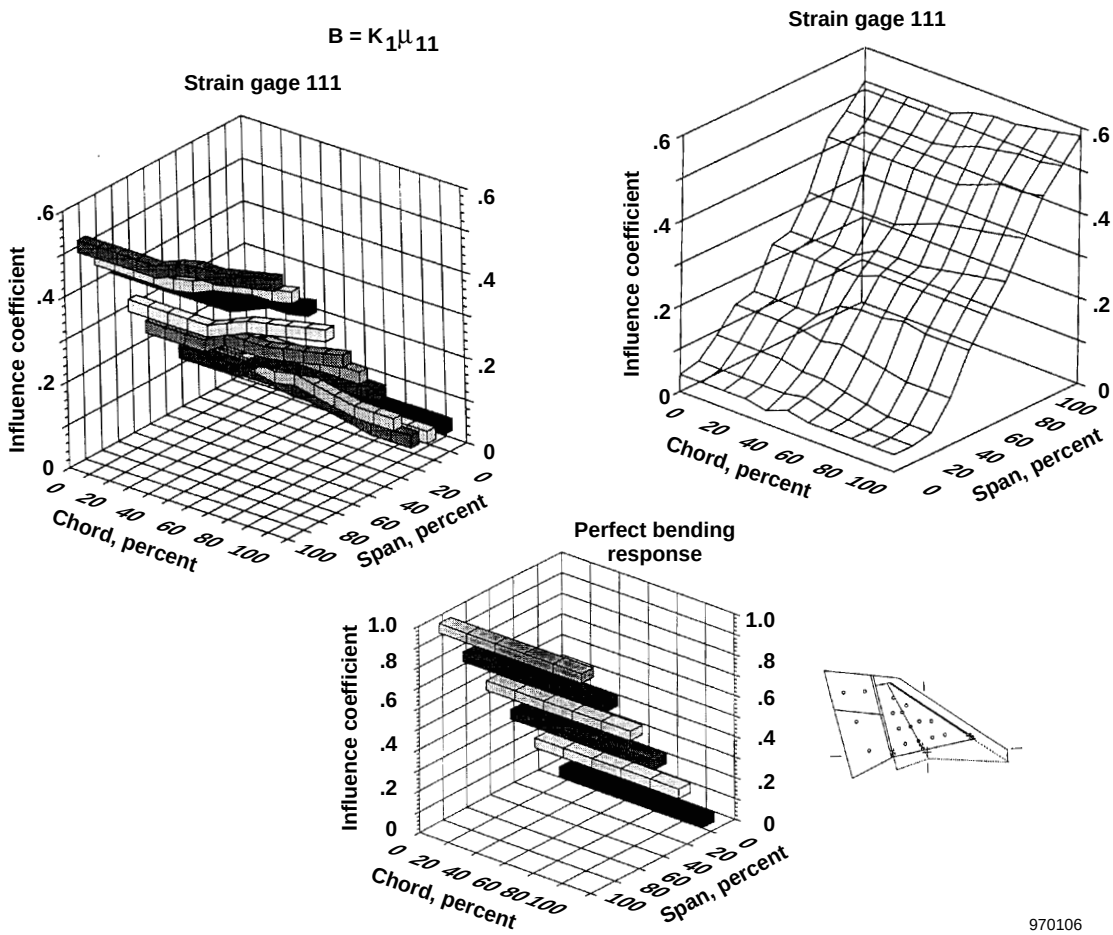

Figure 15. Illustration of a bending response.

Figure 16 shows the distribution of the calibration load points in terms of span and chord. The general ability to measure loads on the X-24 tip fin is slightly better than for the M2-F2 tip fin, although the relevance coefficient is much lower. The shear is slightly worse for the X-24 tip fin, but the bending and torsion are significantly better. The improved accuracy of the equations on the X-24 tip fin is likely attributed to the fact that fewer spars existed on the X-24 tip fin than on the M2-F2 tip fin (three as opposed to seven). It should also be recalled that the X-24 instrumentation system used single-active-arm strain gages, which tend to produce low sensor signals that can deteriorate the calibration accuracy.

HL-10 Center Fin

Appendix A shows a three-view sketch of the HL-10 lifting body. Figure 1(c) shows the center fin in more detail and where calibration load points are located along with strain gages. The planform can be seen to be a moderate-aspect-ratio structure with three main spars and a control surface covering approximately 30 percent of the chord. Fifteen load points were used to calibrate this structure. Ten four-active-arm strain-gage bridges were available to develop loads equations. The basic strain-gage load calibration has been documented.*

*Tang, Ming H., “HL-10 Vertical Tail Calibration,” Branch Report BR-4, NASA Flight Research Center, Aug. 1966.

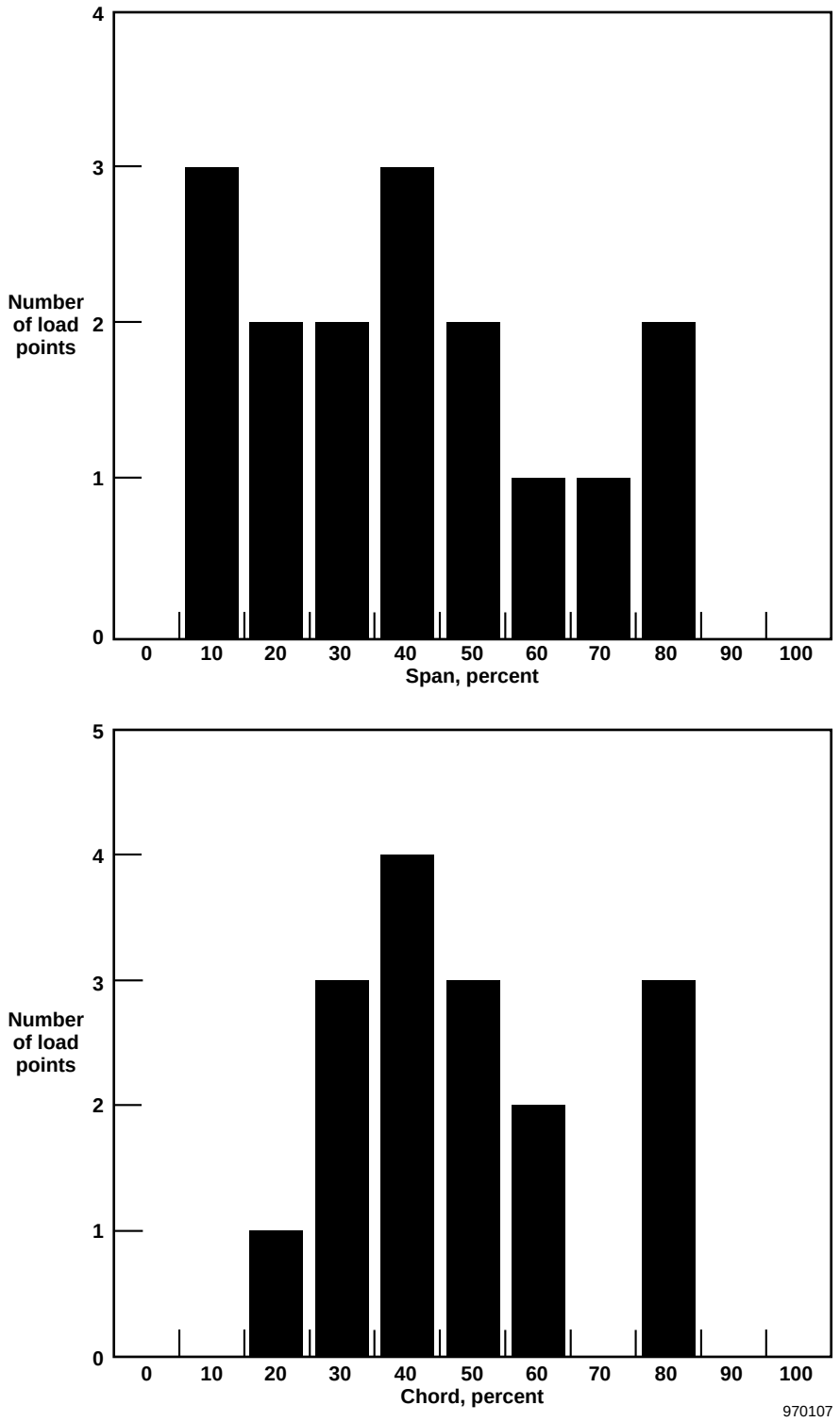

Figure 16. Distribution of load points in the span and chord directions for the X-24A tip fin.

The HL-10 center fin has a large, slim planform; hence, the problems associated with very low-aspect-ratio structures should not be present. All 10 strain-gage bridges were sensitive to some degree to both bending and torsion. Figures 17, 18, and 19 show as ribbon plots the responses of 3 strain-gage bridges that are characteristic of the group of 10. Figure 17 shows the strain-gage bridge located on the center spar, and the response is largely a bending one. Figure 18 shows a strain-gage bridge also located on the center spar. The dominant response of this bridge is shear with bending and torsion contaminants. Figure 19 shows a strain-gage bridge located on the aft spar. This bridge responds largely to torsion with some bending contamination.

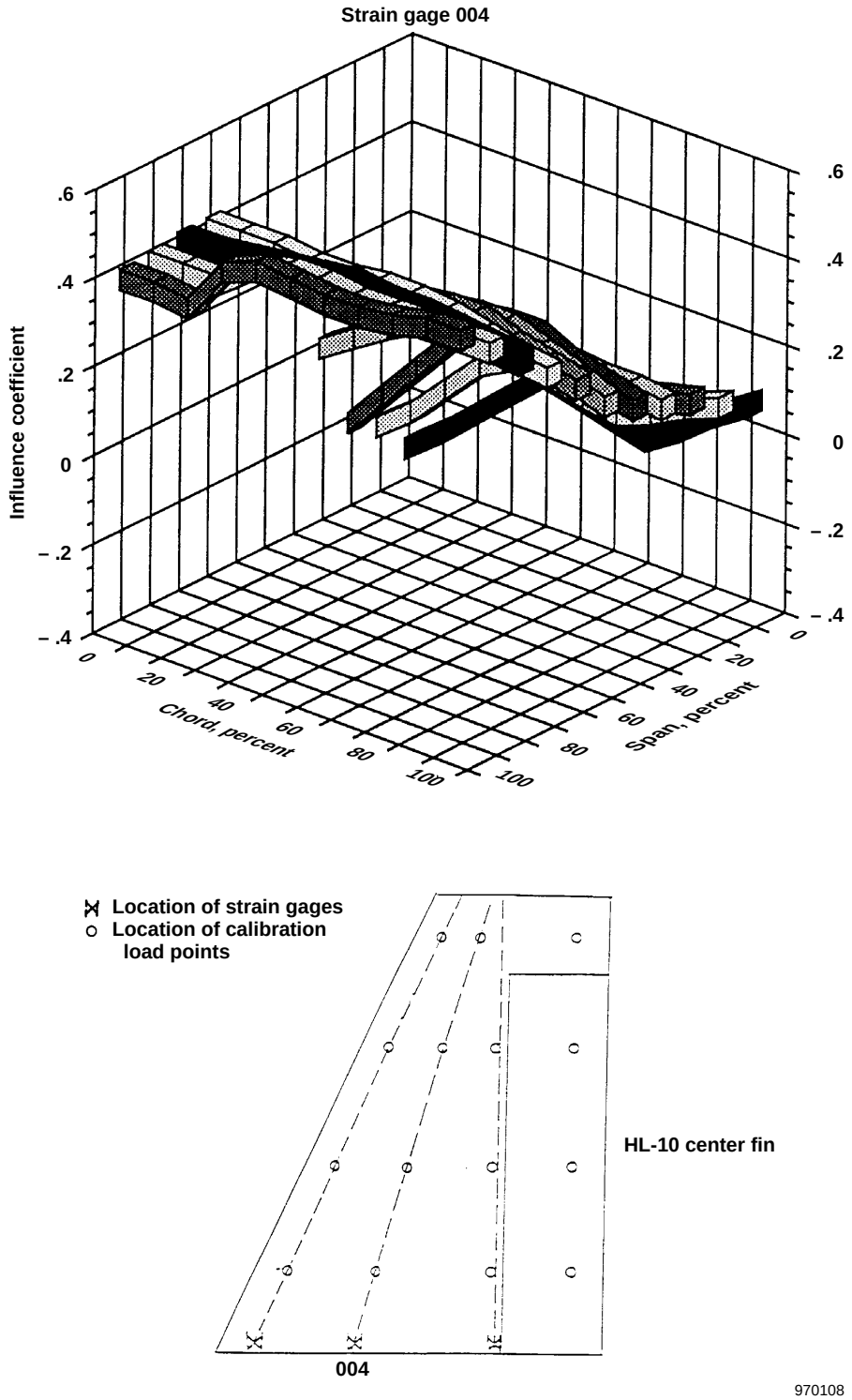

Figure 17. Influence-coefficient plot for strain gage 004 on the HL-10 center fin.

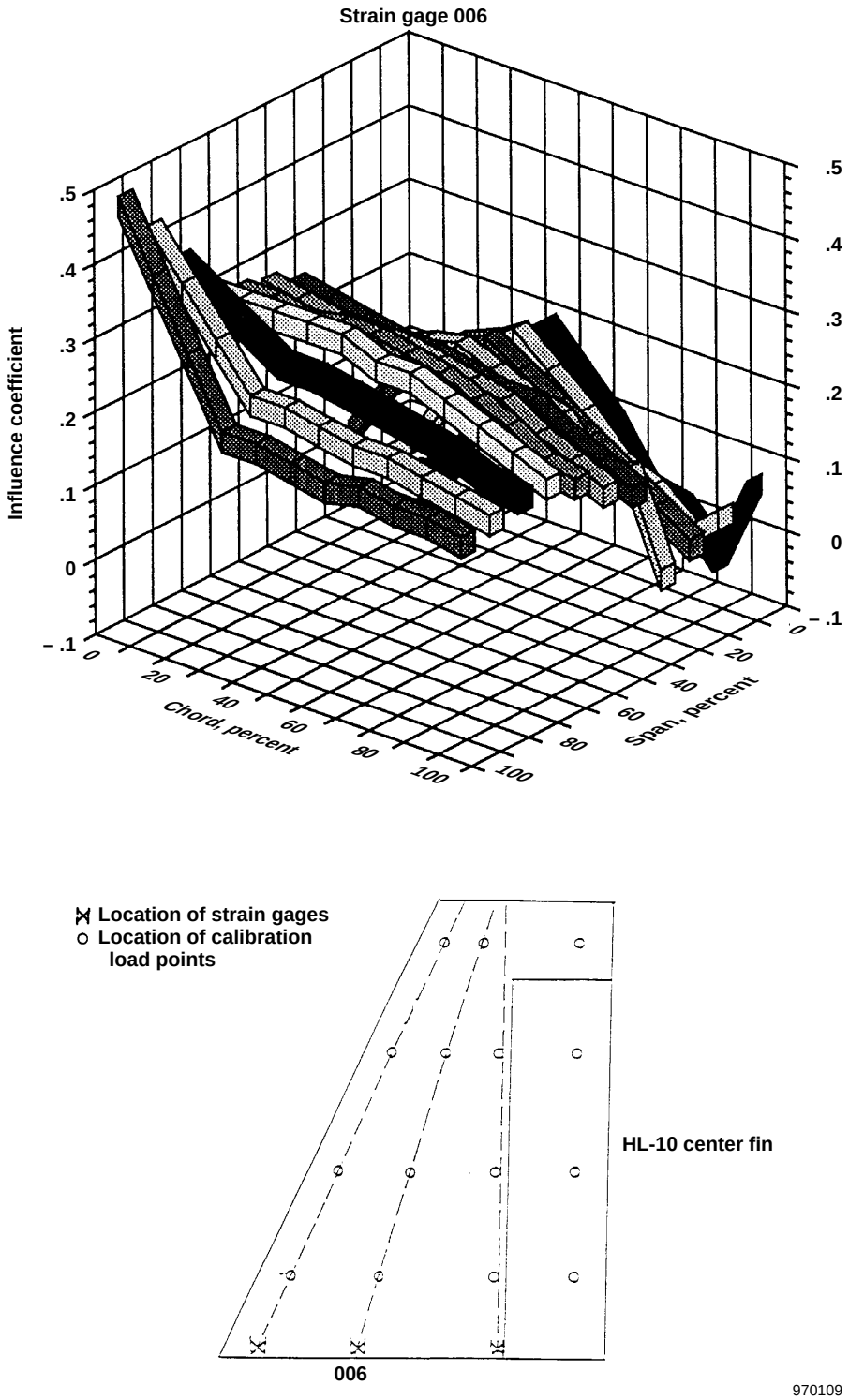

Figure 18. Influence-coefficient plot for strain gage 006 on the HL-10 center fin.

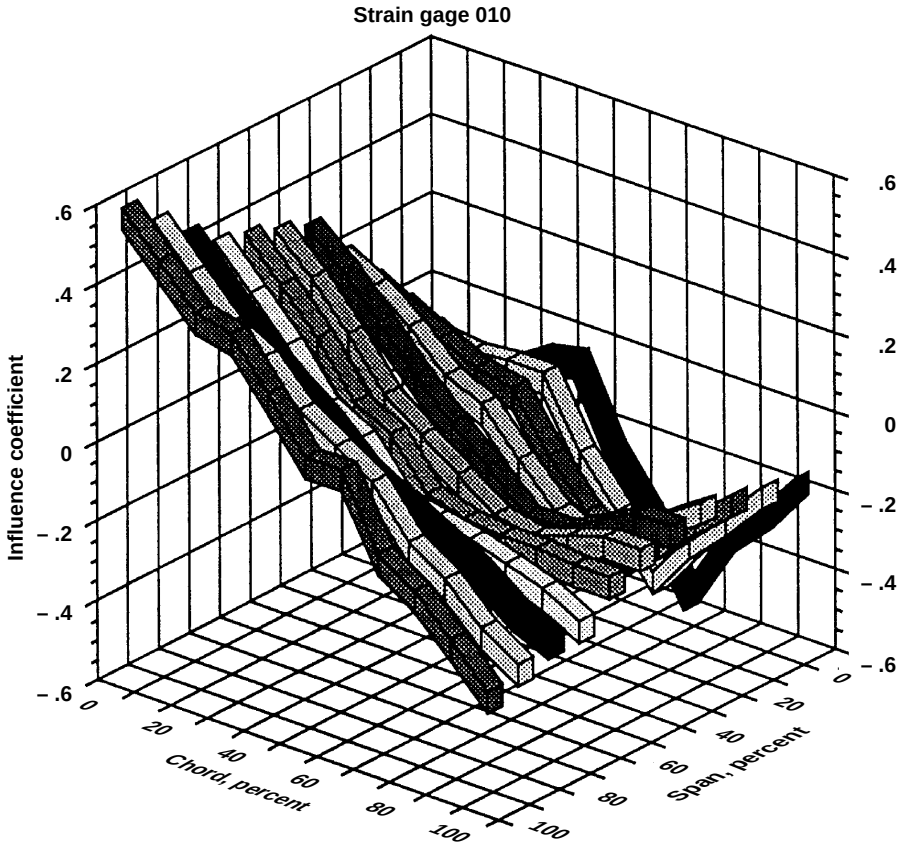

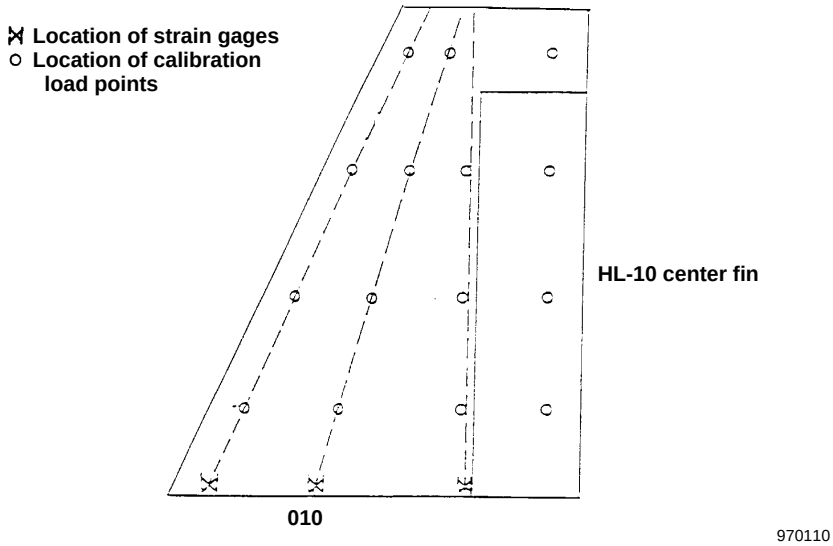

Figure 19. Influence-coefficient plot for strain gage 010 on the HL-10 center fin.

Figures 20, 21, and 22 show a better way of assimilating this information with influence-coefficient responses shown in multiple formats. A two-dimensional presentation and a wire-frame plot are shown for the individual strain-gage bridge. The ideal response most closely resembling the response for the particular bridge is also shown. The strain-gage bridge response (fig. 20) can be seen to be responding to bending (for example, influence coefficients linearly increasing in the span direction) except along the leading edge where the response is somewhat nonlinear. The bridge (fig. 21) has shear characteristics (for example, all of the influence coefficients are located on one side of the zero plane). The slight upward slope with increasing span indicates a bending effect, and the spread of the constant chord lines indicates a torsion effect. Actual influence-coefficient characteristics are quite nonplanar compared to the ideal case. The bridge shown in figure 22 indicates a large torsional influence and a definite bending input. The two-dimensional presentation shows the torsion response as a spread in the constant chord lines and the bending effect as an increasing slope with span. The three-dimensional wire-frame plot shows the combined torsion/bending complex as a plane sloping in two directions with the zero plane centrally located.

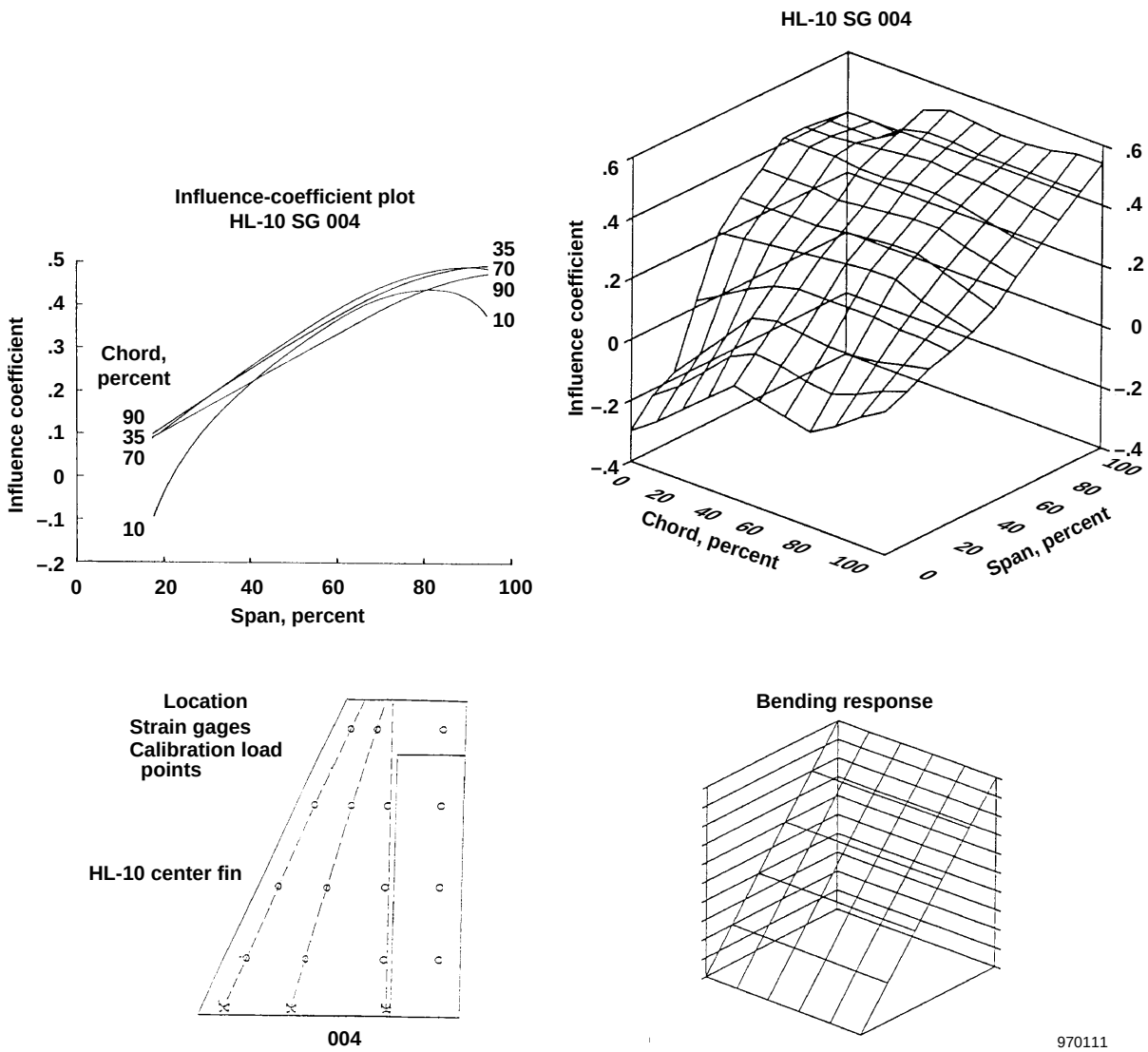

Figure 20. Examination of HL-10 center fin strain gage 004, which illustrates a dominant bending response to applied load.

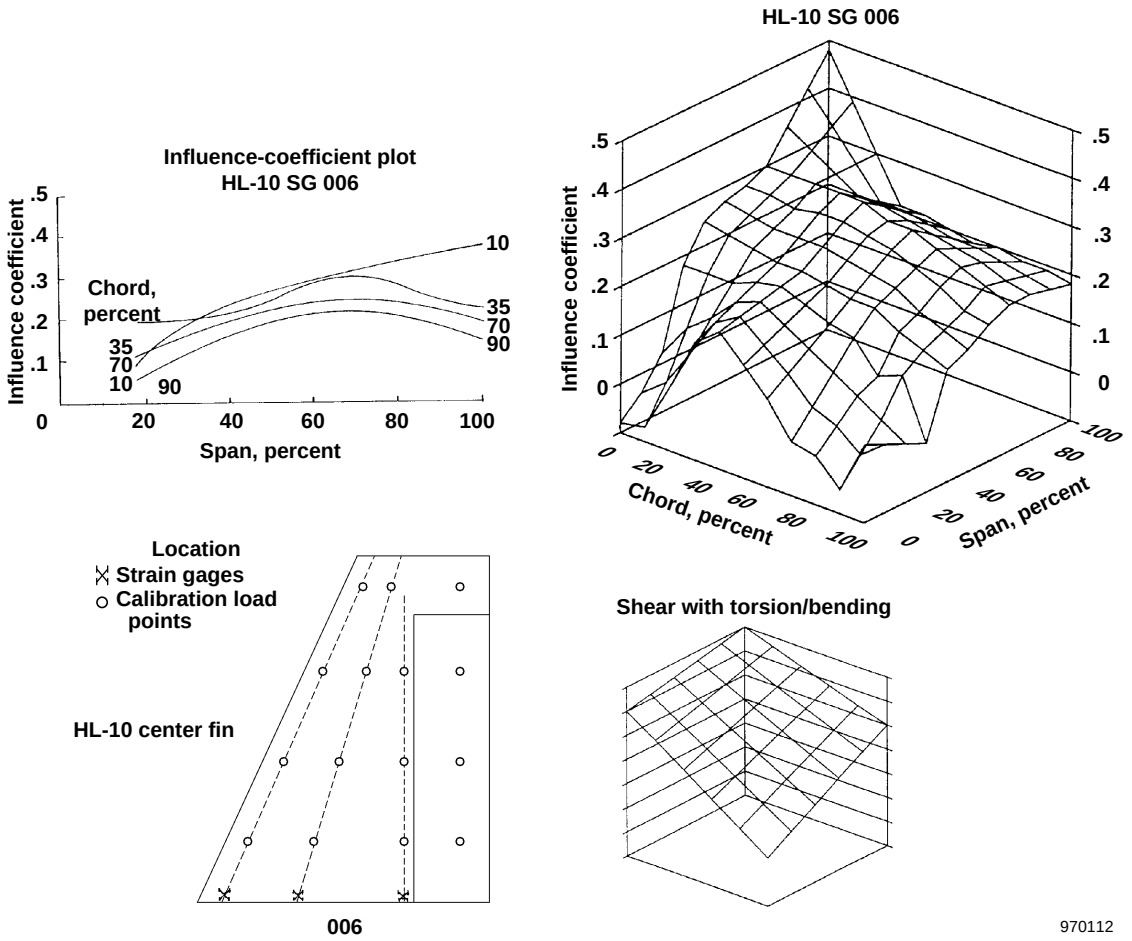

Figure 21. Examination of HL-10 center fin strain gage 006, which illustrates an example of a shear response with torsion and bending superimposed.

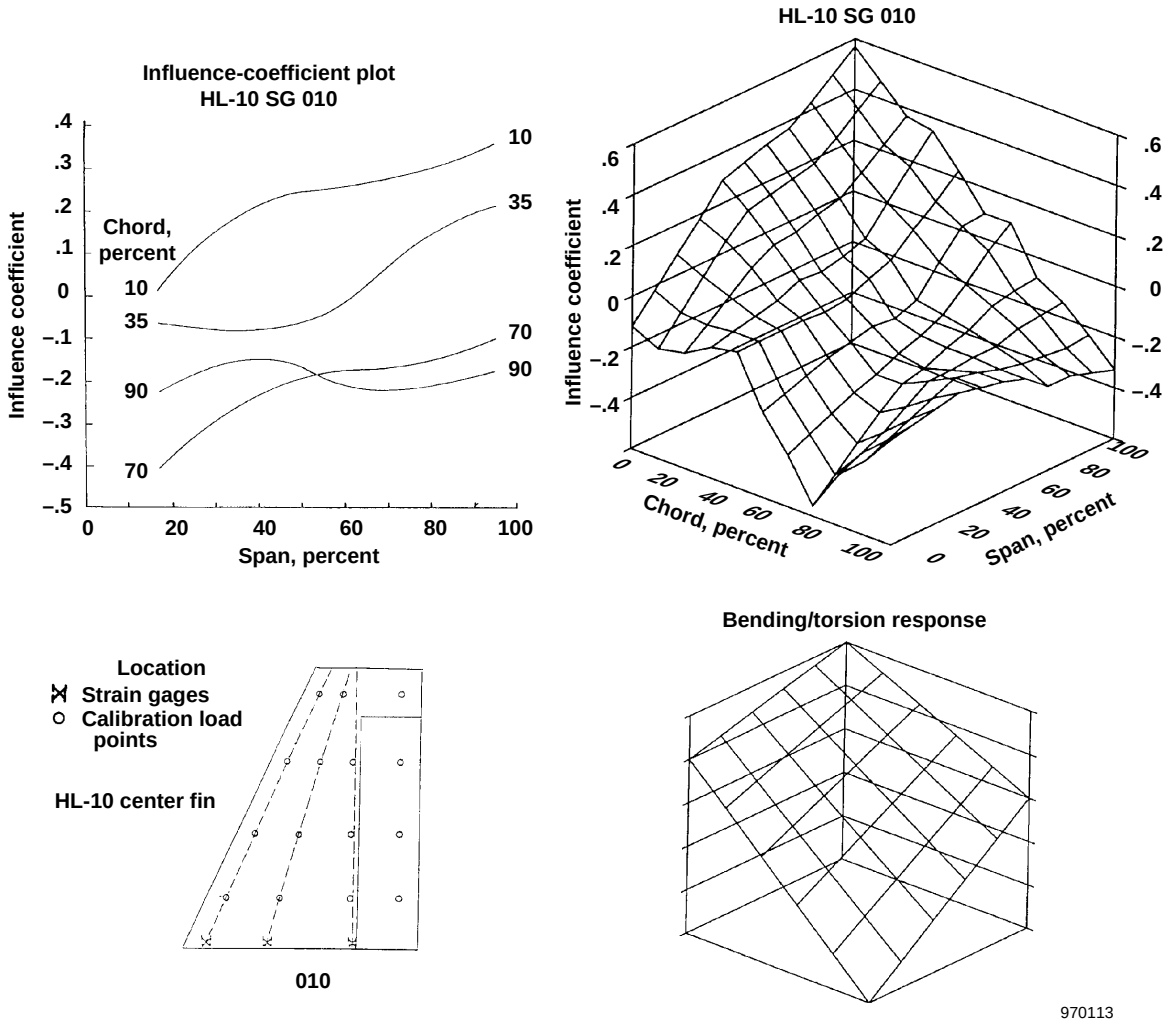

Figure 22. Examination of HL-10 center fin strain gage 010, which illustrates an example of a response with strong torsion and bending characteristics.

The best equations that could be developed resulted in load measurements with the following estimated errors:

Shear	10 percent
Bending Moment	6 percent
Torsion	16 percent

The 16 load points used in calibrating the strain-gage bridges on this structure resulted in a fairly large relevance coefficient:

$$C_R = 0.60$$

Figure 23 shows the distribution of the calibration load points in terms of span and chord. The relatively good strain-gage calibration is attributable to several favorable circumstances. The large aspect ratio of a lifting and stabilizing structure provides a favorable geometry for a good calibration. The strain-gage bridge outputs were fairly large, which eliminates resolution problems. A relevance coefficient of 0.60 results in a favorable loading distribution.

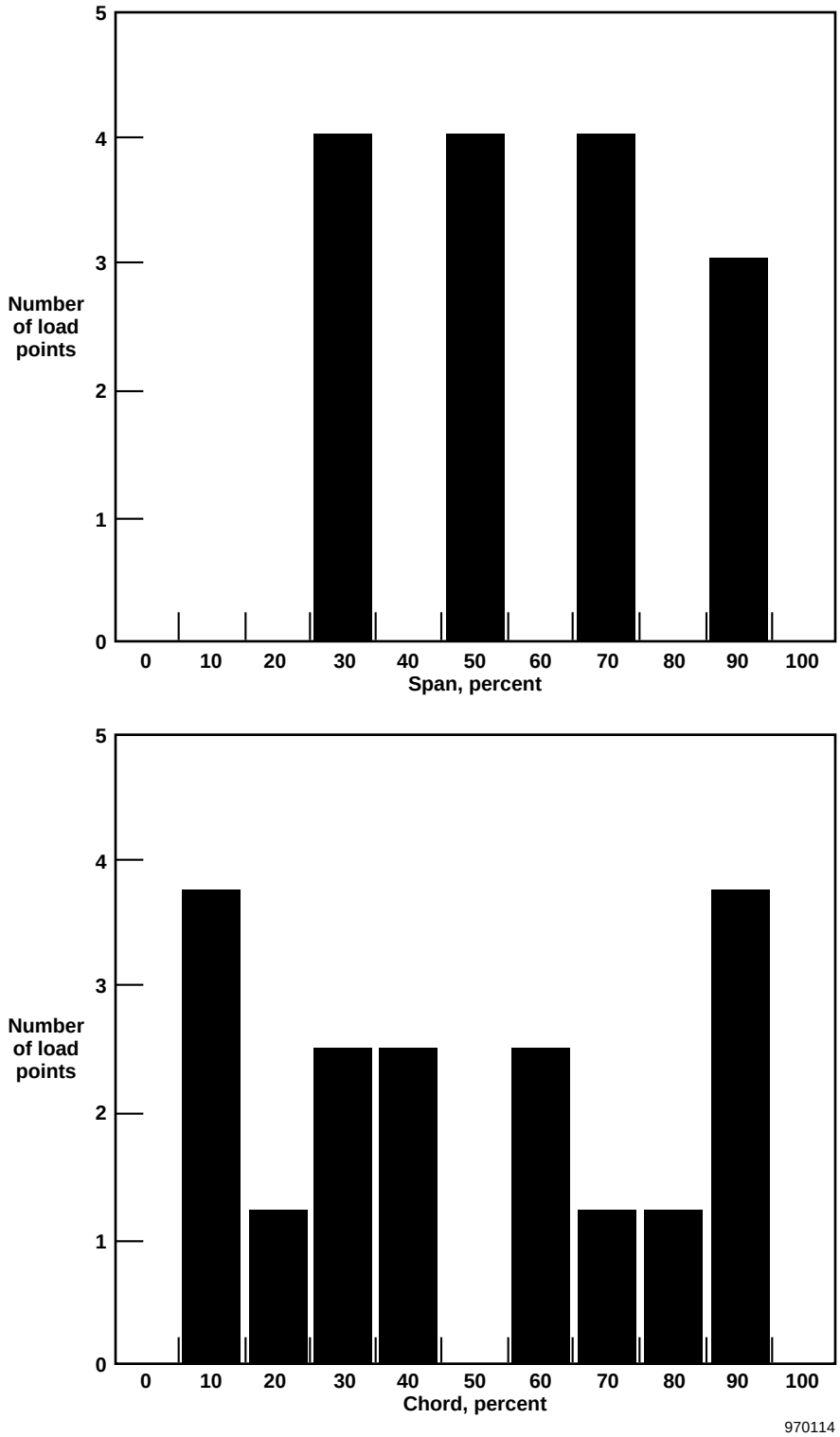

Figure 23. Distribution of load points in the span and chord directions for the HL-10 center fin.

X-24 Center Fin

Appendix A shows a three-view sketch of the X-24 lifting body. Figure 1(d) shows the center fin in more detail and where calibration load points are located along with strain gages. The planform can be seen to be a low-aspect-ratio structure with three main spars and no control surface. Twelve load points were used to perform the calibration, which was recorded from 12 strain gages located on the structure. As was the case on the X-24 tip fin, only single-active-arm strain gages were available for the load calibration. This circumstance leads to the probability that low sensor output could be a detriment to the results of this calibration.

Eight of the strain gages predominately responded in a shear sense, and four of the eight sensed some bending. The outputs were quite low for several of these bridges. The remaining four bridges responded in a combined bending/torsion complex with large outputs. Figures 24, 25, and 26 show ribbon plots of the three representative types of influence-coefficient responses. The strain-gage influence coefficient shown in figure 24 is one that largely responds to shear with a marked irregularity near the leading edge of the root chord area. The response shown in figure 25 is a torsion response that is heavily influenced by bending effects. The response shown in figure 26 is a bending response that contains major torsional effects.

Figures 27, 28, and 29 show the same three strain-gage influence coefficients in a somewhat more illustrative manner. The conventional two-dimensional manner of presenting the influence coefficient is shown in the upper left corner of the figure, and the wire-frame plot is shown in the upper right corner. The appropriate ideal or preferred shear response is shown in the bottom right of the figure. The strain gage shown in figure 27 is primarily a shear sensor with a slight elevation in the increasing span direction. A root anomaly also exists that causes a problem in the equation sense. Figure 28 shows a sensor with a strong torsional effect (for example, the spread of the chord lines is large) and a strong bending input (for example, the upward slope of all the constant chord lines in the increasing span direction). Figure 29 shows a strong bending response with a torsional spread (for example, a sharp increase in the span direction with some spread of the constant chord lines).

The calibrated sensors in this structure did not offer a wide variety of responses. All of the sensors fell into two categories: sensors that responded to shear, and sensors that responded to a bending/torsion complex. This situation does not provide a large potential for combining sensors to form an ideal response. The best equations that could be developed for this structure resulted in the following estimated errors:

Shear	17 percent
Bending Moment	15 percent
Torsion	69 percent

The 12 load points used to calibrate this structure resulted in the following relevance coefficient:

$$C_R = 0.50$$

Figure 30 shows the distribution of the calibration load points in terms of span and chord. The relatively small size of the relevance coefficient is not as important as the small strain-gage responses resulting from the single-active-arm strain gages. These small responses probably contribute in a large way to the poor accuracies of the equations. The relatively small aspect ratio is not a favorable geometric factor.

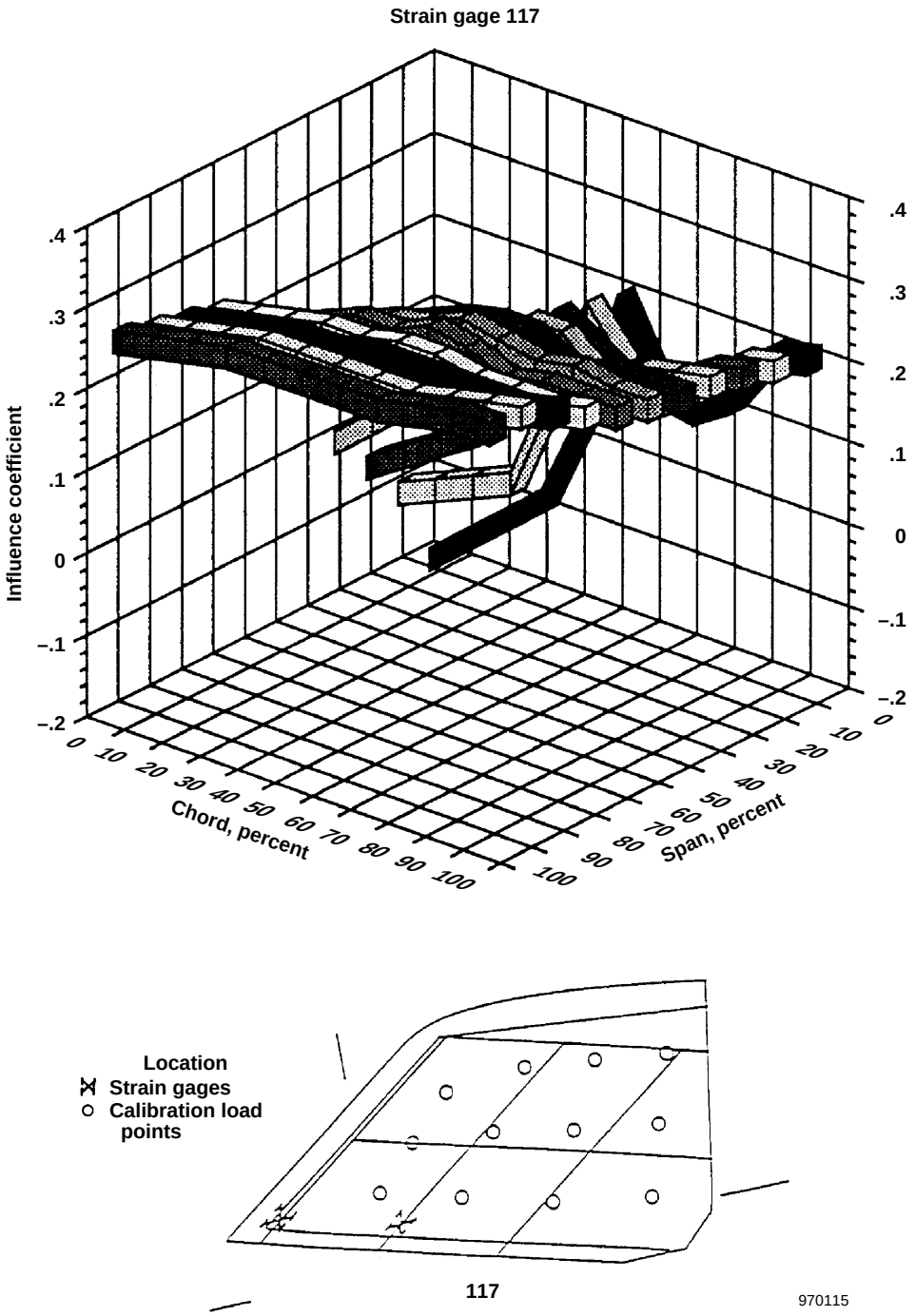

Figure 24. Influence-coefficient plot for strain gage 117 on the X-24A center fin.

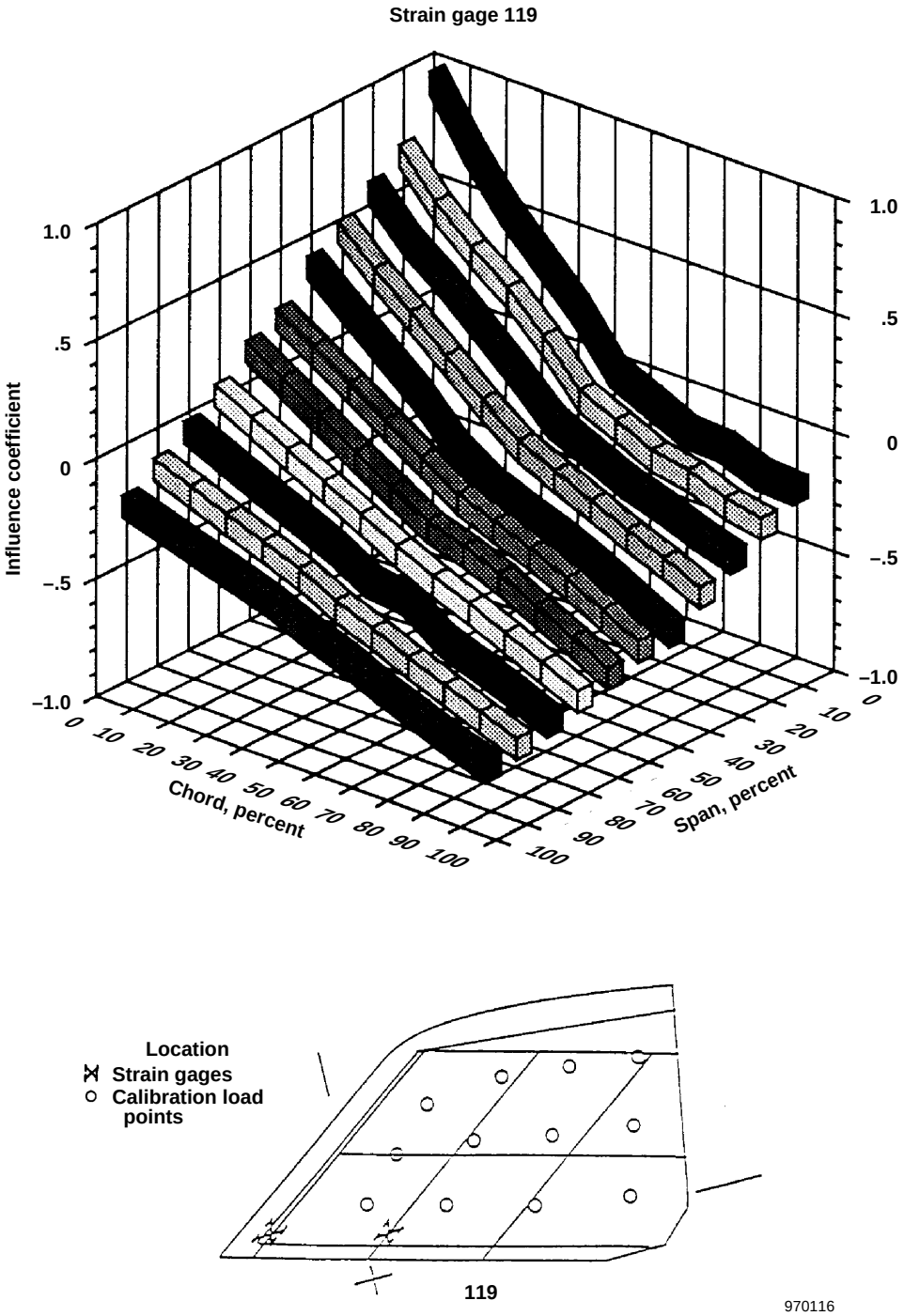

Figure 25. Influence-coefficient plot for strain gage 119 on the X-24A center fin.

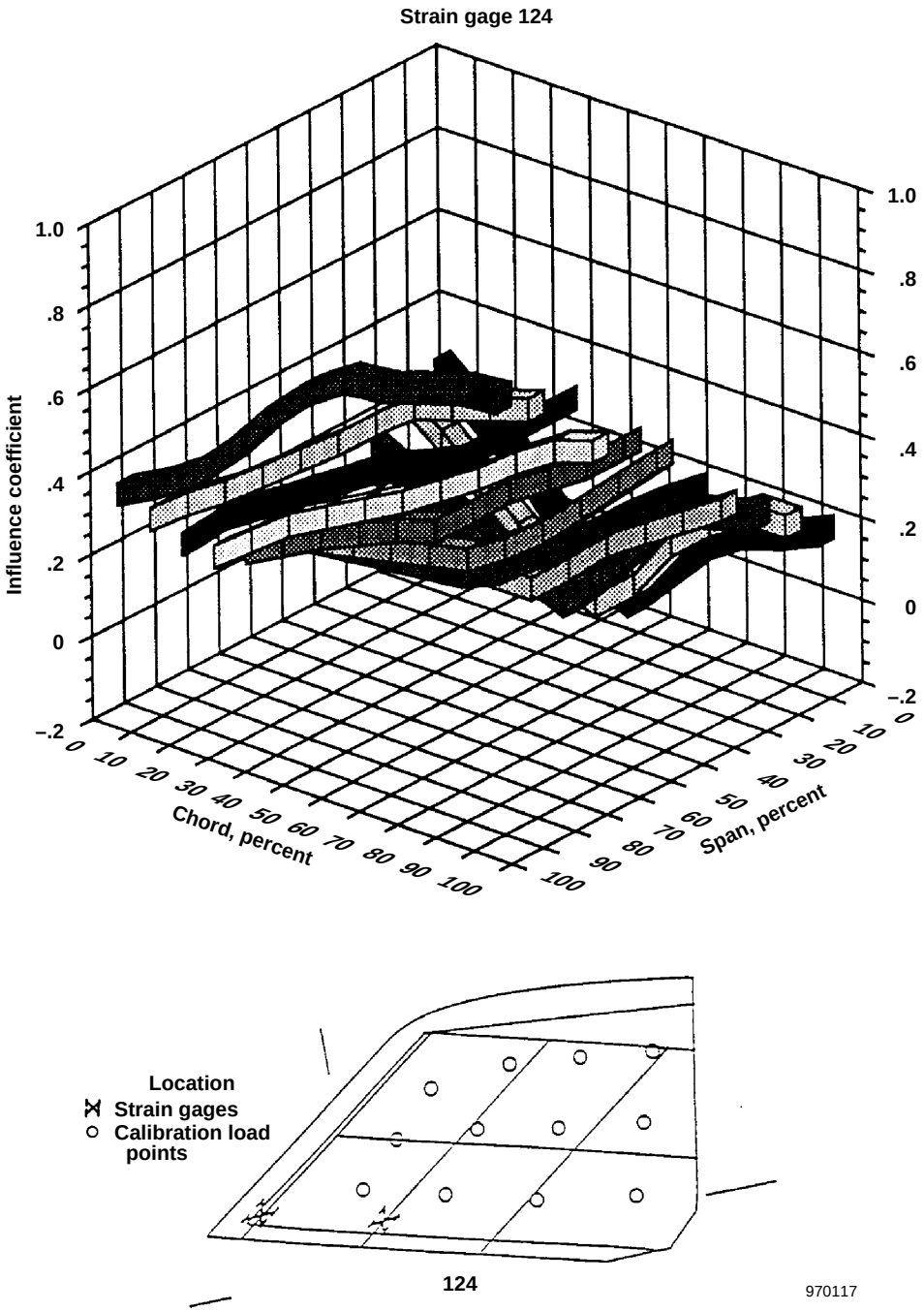

Figure 26. Influence-coefficient plot for strain gage 124 on the X-24A center fin.

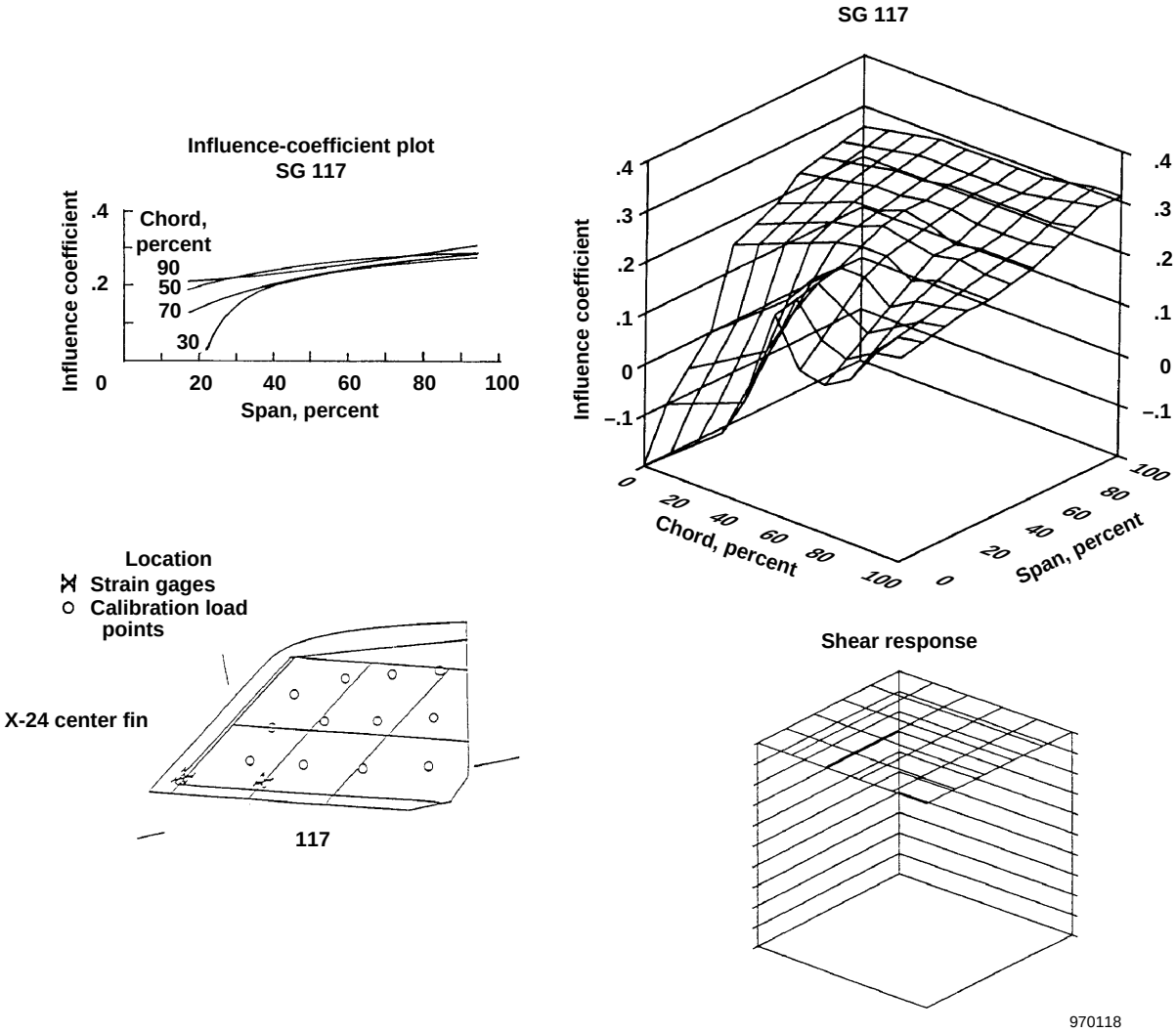

Figure 27. Examination of X-24A center fin strain gage 117, which illustrates a strong shear response.

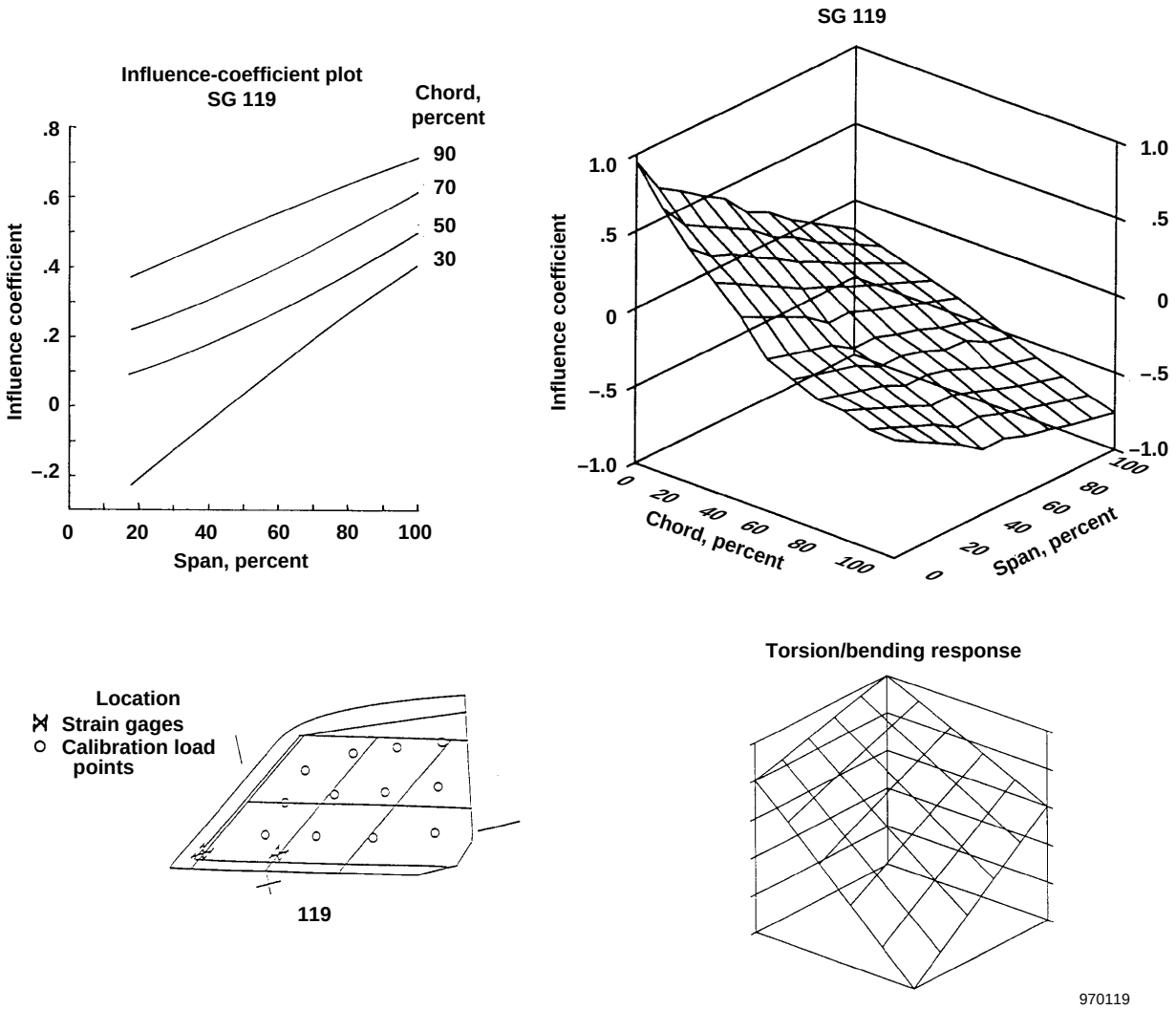

Figure 28. Examination of X-24A center fin strain gage 119, which illustrates a strong bending/torsion response.

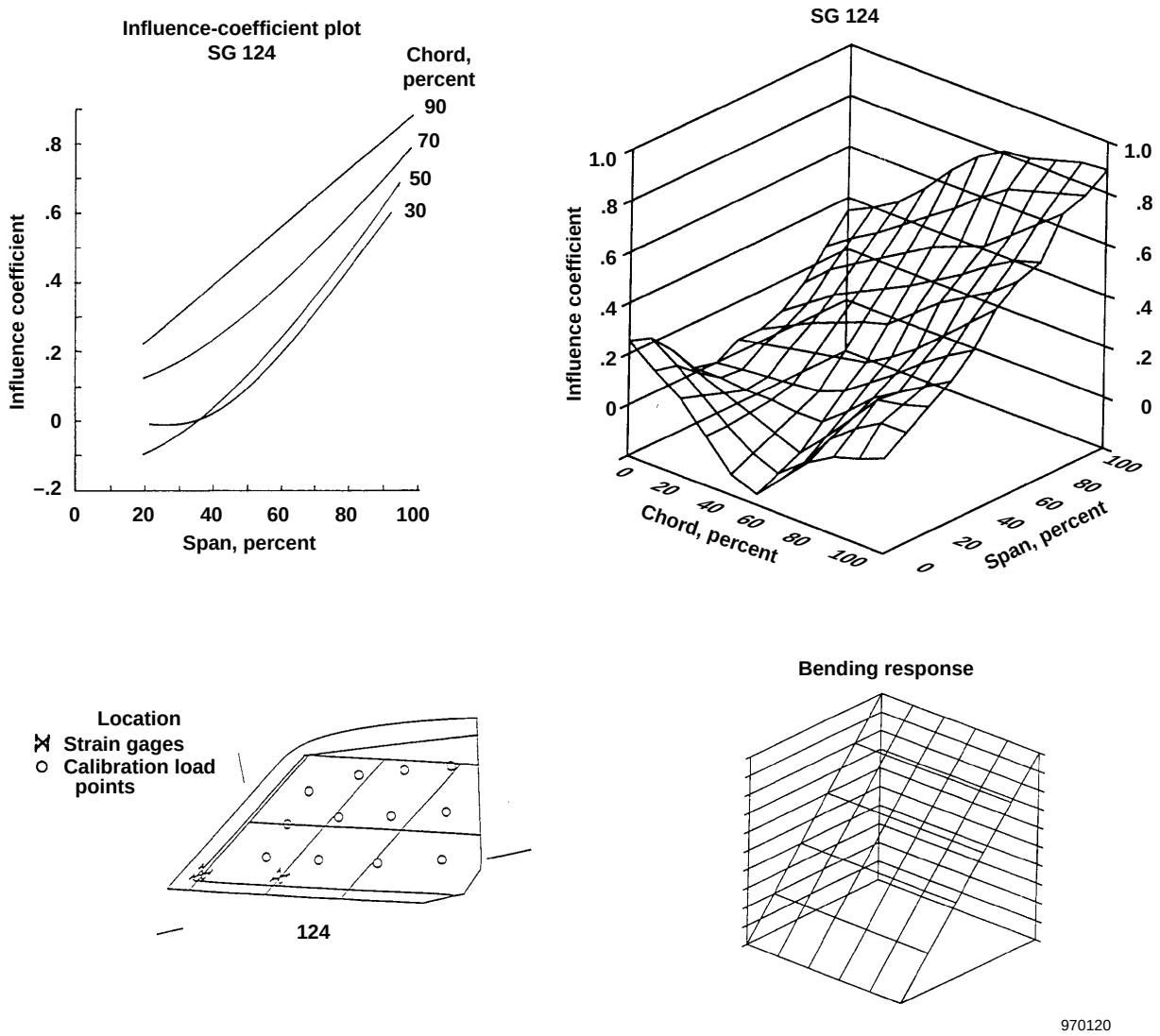

Figure 29. Examination of X-24A center fin strain gage 124, which illustrates a strong bending response.

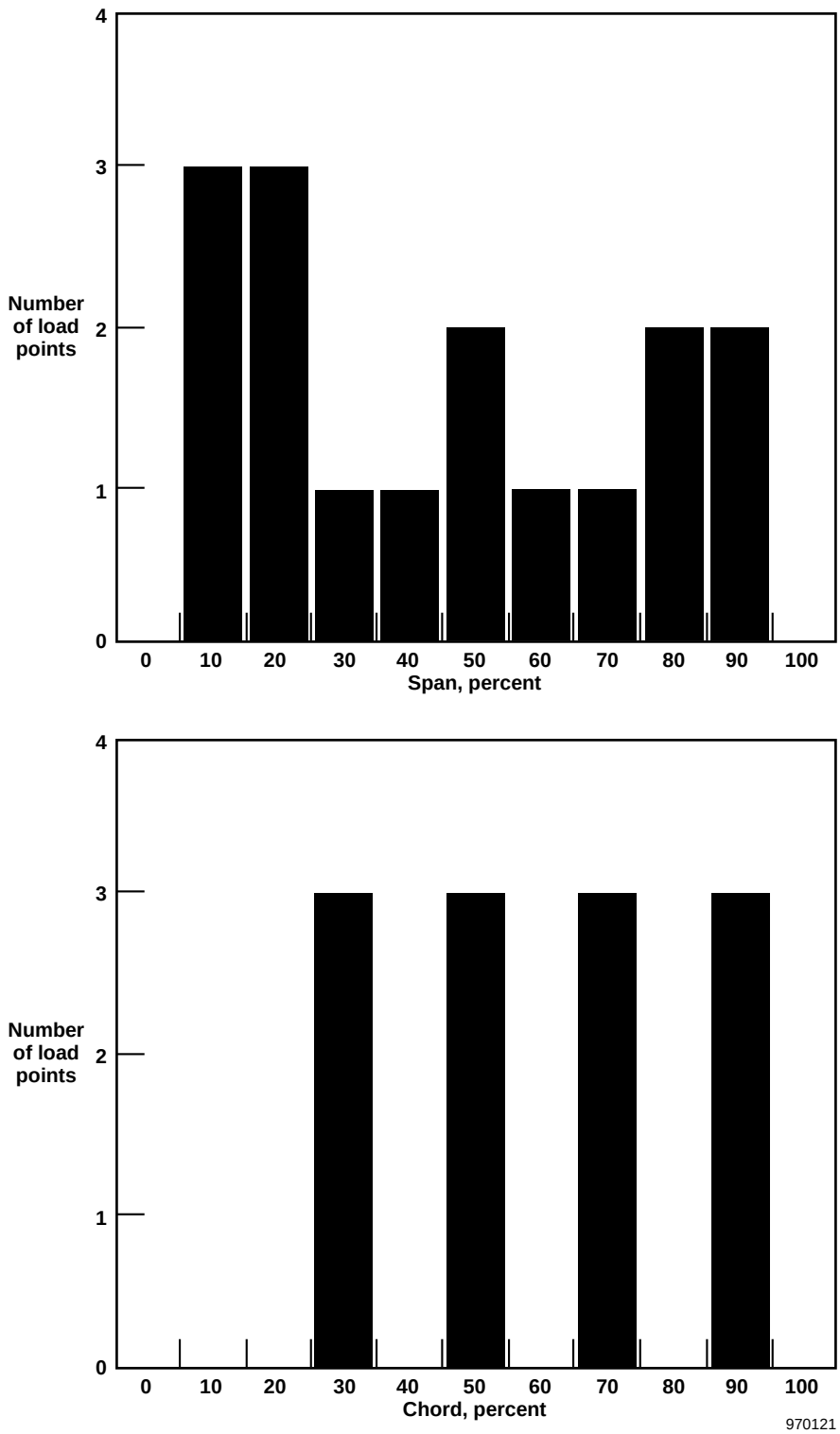

Figure 30. Distribution of load points in the span and chord directions for the X-24A center fin.

X-15 Horizontal Tail

Appendix A shows a three-view sketch of the X-15 aircraft. Figure 1(e) shows the horizontal tail in more detail and where calibration load points are located along with strain gages. The structure has a moderate-aspect-ratio planform and has three spars attached to a major root rib with all root loads passing into a torque tube. This configuration dictates that all strain-gage bridges be located on and around the torque tube. A torque tube configuration is common to many horizontal tails and represents a special class of structure with respect to calibrated strain gages for load measurement. Twelve load points were used to calibrate 14 strain-gage bridges located in the torque tube area. The basic load calibration has been documented,* and additional data have previously been given.[6]

Most of the strain-gage bridges responded in a relatively pure bending manner. The remaining bridges either responded in relatively pure torque or torque contaminated with bending. Figure 31 shows three responses that are representative of the group of strain-gage bridges. On the far left, strain-gage bridge S2 is an example of a torsion response that also senses a bending effect. In the middle, strain-gage bridge B2 has a relatively pure response to bending. On the far right, strain-gage bridge XS2 exhibits a very discrete torsional response.

Figures 32, 33, and 34 show the same three strain-gage influence-coefficient plots in a somewhat more illustrative manner. The response shown in figure 32 exhibits the chordwise spread indicating torsion, but also exhibits a slope in the span direction that means bending is present. The wire-frame plot indicates a general response that does not deviate much from the warped surface. Figure 33 shows an uncontaminated bending response. Only a very slight torsional response is seen. The actual wire-frame plot is almost identical to the ideal bending response. Figure 34 shows a pronounced torsional response. Additionally, the wire-frame plot shows a general response that deviates little from the warped plane.

This structure illustrates the fact that all movable tails having torque tube arrangements are unique in terms of strain-gage load calibrations. The most favorable equations that were developed for this structure resulted in the following estimated equations errors for the load calibration:

Shear	3 percent
Bending Moment	3 percent
Torsion	2 percent

The 12 load points used to calibrate this structure result in a relevance coefficient having the following value:

$$C_R = 0.50$$

Figure 35 shows the distribution of calibration load points in terms of span and chord loading. Several important insights are gained with this structure. Experience has led to the thought that it is difficult to obtain accurate shear equations on structures such as this one that have torque tubes, but a good argument has not been made to support this thesis. Good shear equations were obtained for this structure although no discrete responses existed that showed promising shear influence-coefficient plots. In all of the load calibration cases previously examined in this report, flight recording limitations resulted in equations with three strain-gage bridges. Five- and six-bridge equations were used for the X-15 horizontal tail. The information to obtain good shear equations is thought to exist (although not easily apparent), and the requirement is to use a large enough number of bridges in the shear equation to eliminate the bending and torsional contaminants. A very good load calibration was obtained

*Reardon, Lawrence F., “Calibration and Influence Coefficients for the X-15-3 Horizontal Stabilizers, 0104 and 0105,” Branch Report BR-10, NASA Flight Research Center, Oct. 1966.

although a relatively small relevance coefficient existed. Because a torque tube structure channels all loads into the central and singular load path, the strain response is large and resolutely defined. It is curious to note that thus far in the five load calibrations studied in this report, no universal rules or guidelines are apparent.

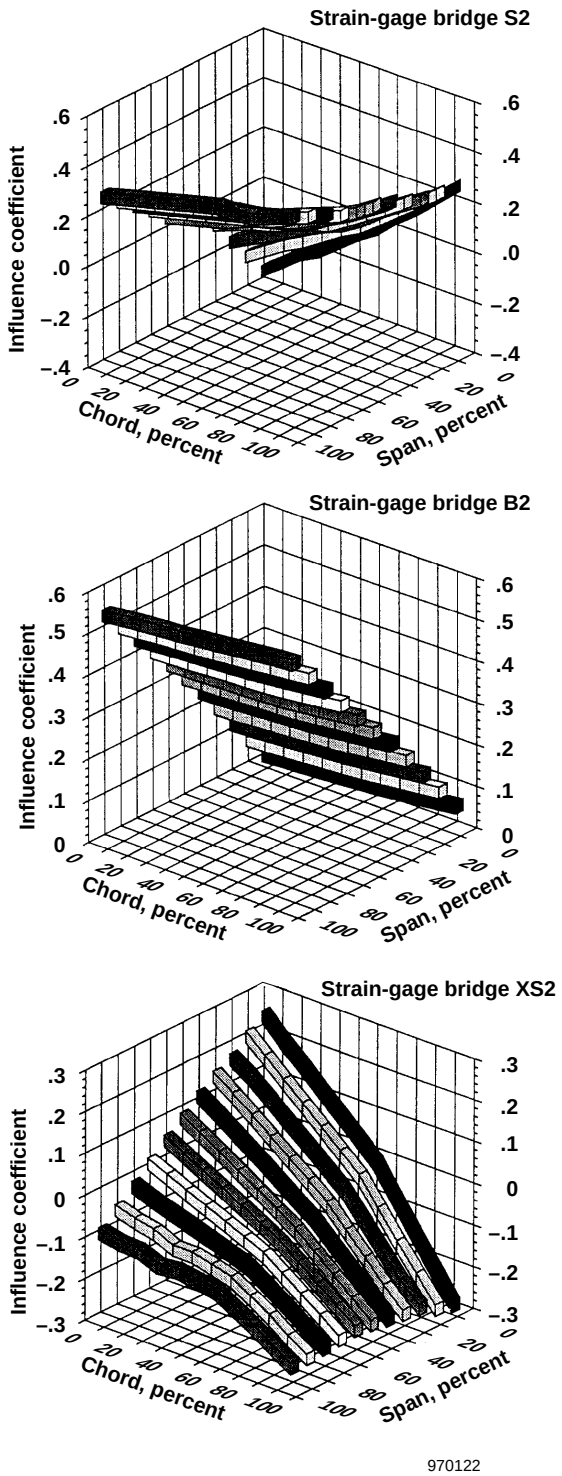

Figure 31. Spectrum of typical strain-gage bridge responses for the X-15 tail presented in three-dimensional ribbon format.

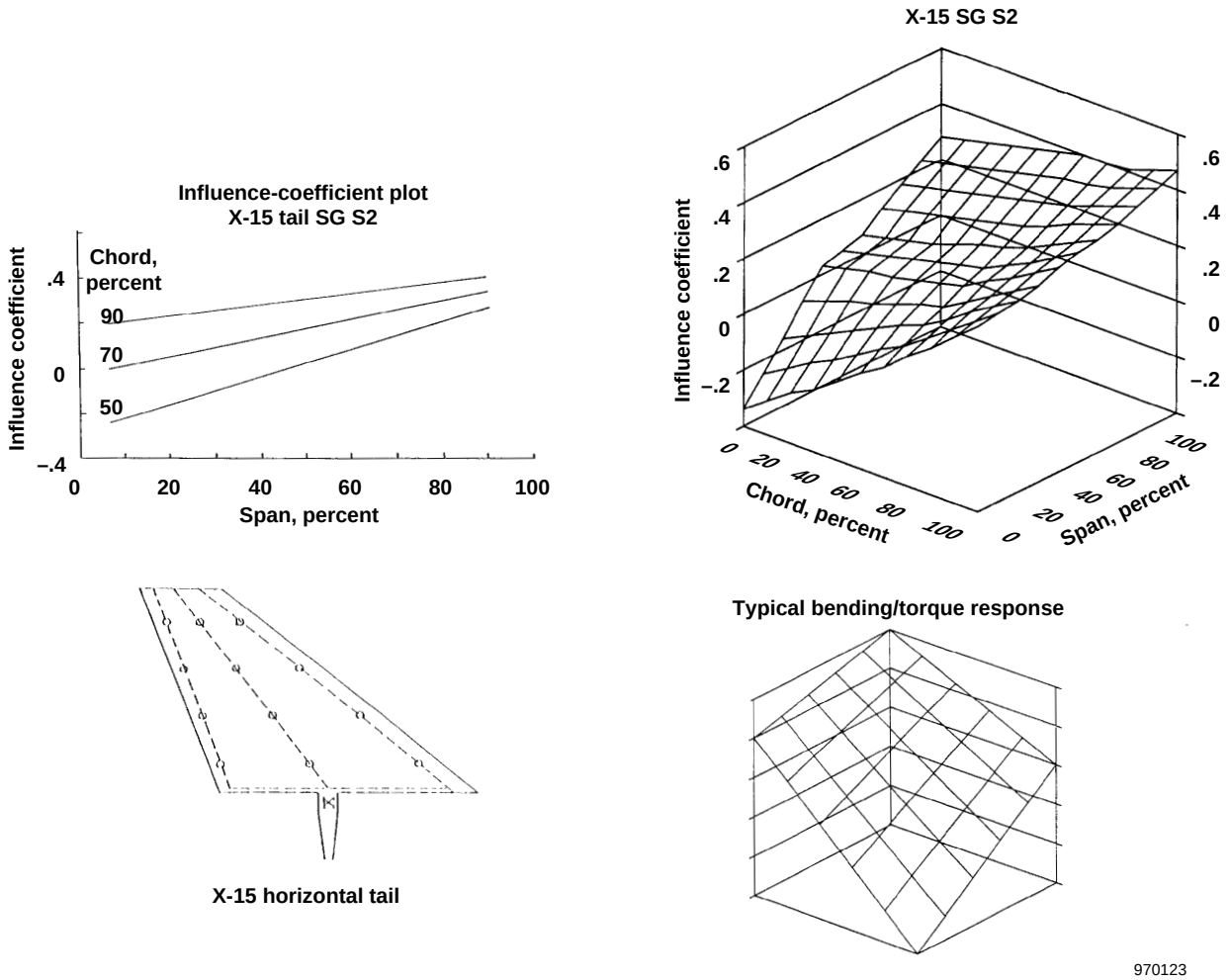

Figure 32. Examination of X-15 horizontal tail strain-gage bridge S2, which illustrates a combined bending and torsion response.

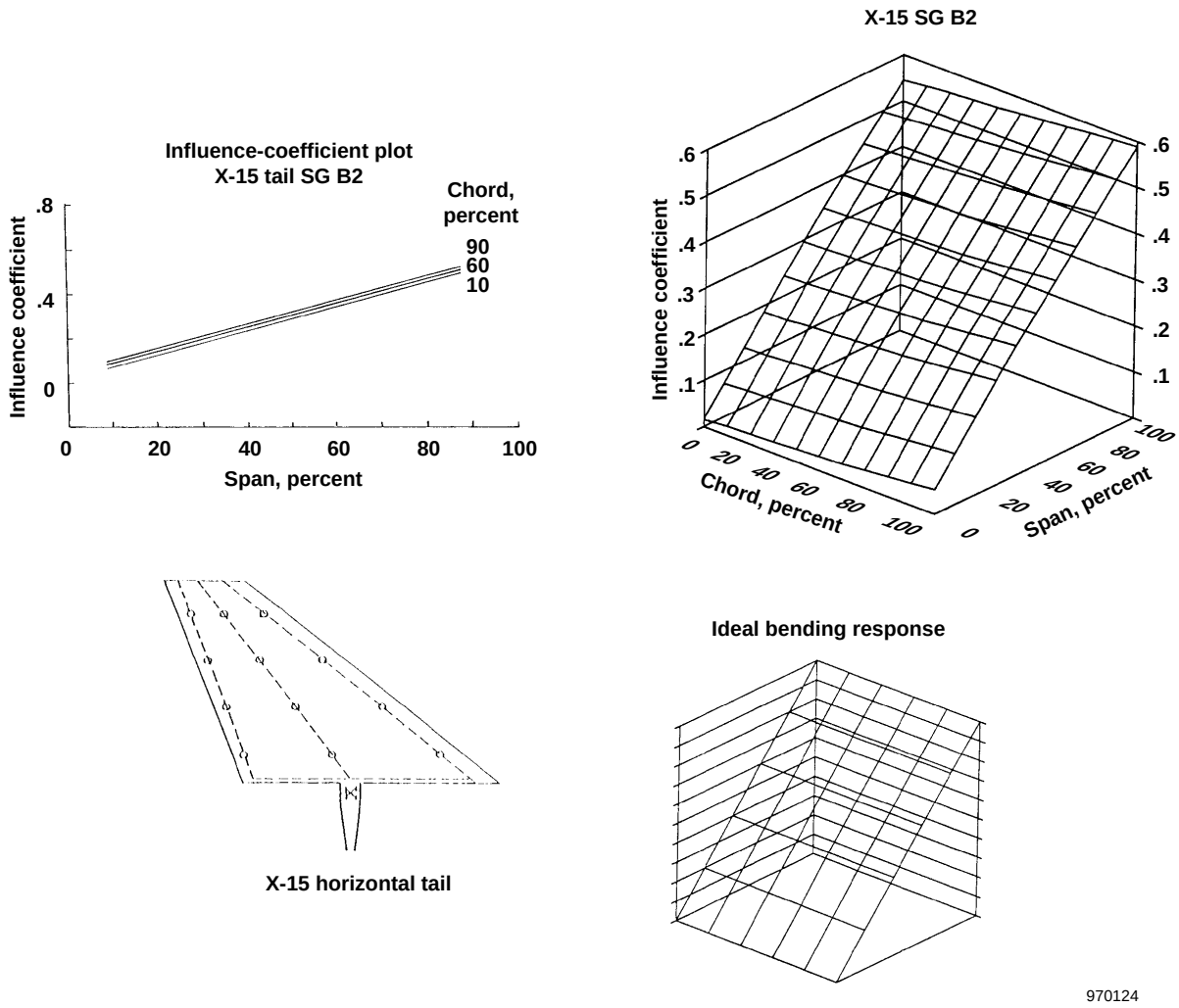

Figure 33. Examination of X-15 horizontal tail strain-gage bridge B2, which illustrates a near ideal bending response.

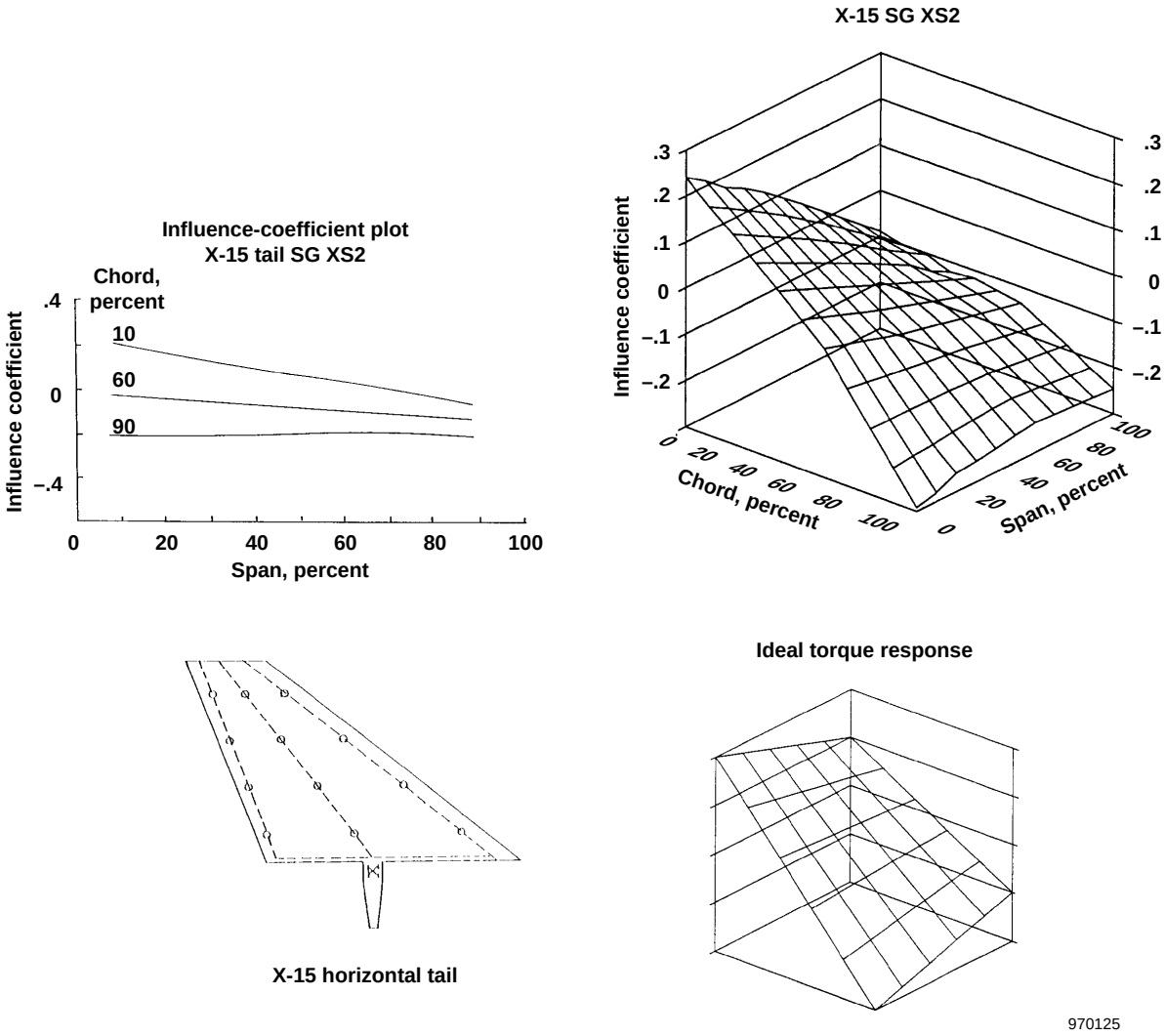

Figure 34. Examination of X-15 horizontal tail strain-gage bridge XS2, which illustrates a dominant torsional response.

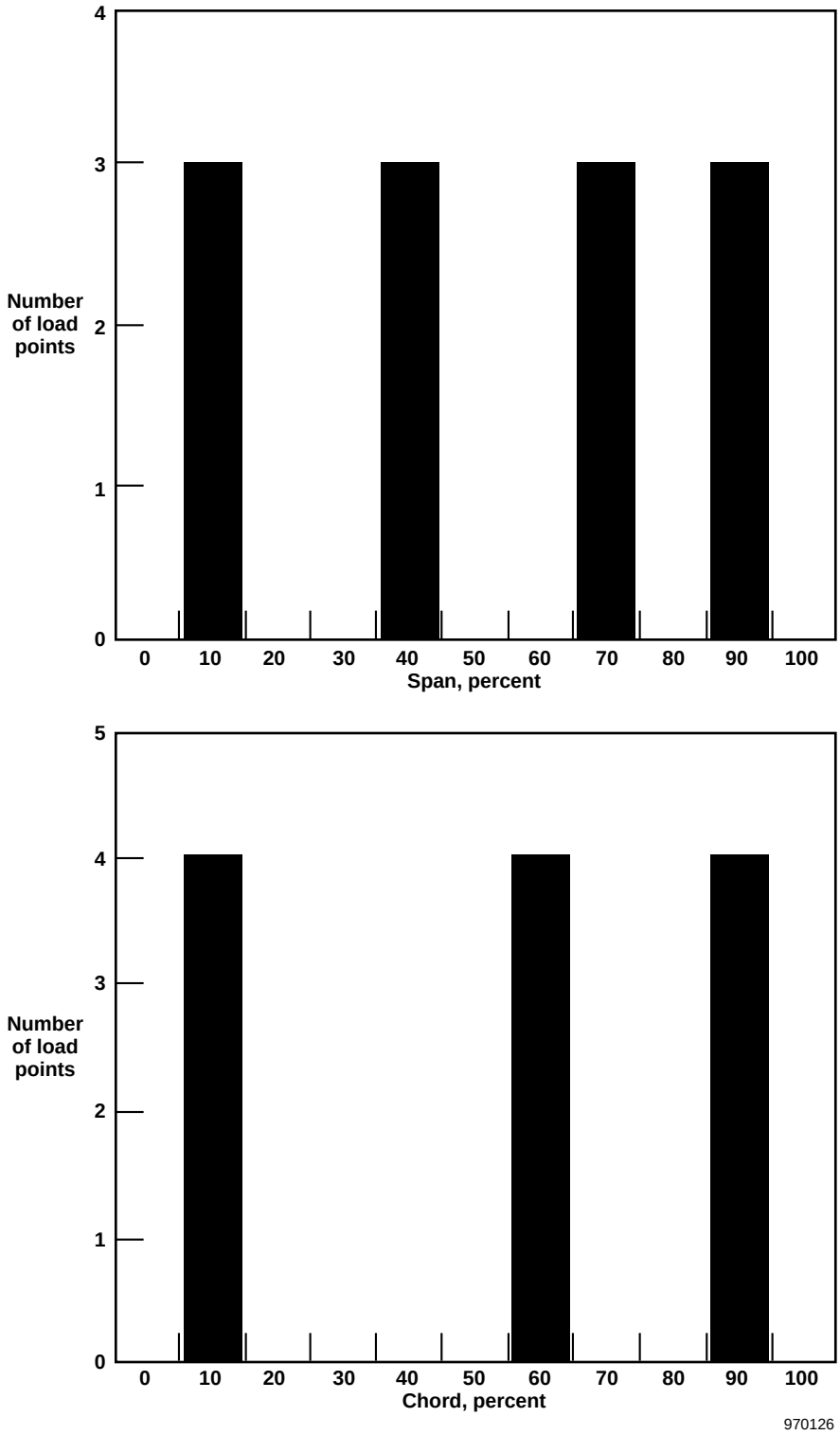

Figure 35. Distribution of load points in the span and chord directions for the X-15 horizontal tail.

F-89 Wing

Appendix A shows a three-view sketch of the F-89 aircraft. Figure 1(f) shows the wing in more detail and where calibration load points are located along with strain-gage bridges. The structure is of a straight-wing configuration with a moderate-aspect-ratio planform with five primary spars. Major control surfaces are located at the aft of the wing. Thirty load points were used to calibrate the strain gages located near the root of the five spars. This structure was not a NASA-calibrated structure but is included because it is the first example of the extensive application of reference 1. The detail has been documented in partial form.* A table of primary influence coefficients is not available.

This structure is included in this report because of the historic timing of the calibration, and because it represents a case where the subject of nonlinearity can be introduced. The influence-coefficient plot for strain gage 62 is shown in the upper left corner of figure 36. The locations of the load points and the root strain gages (including 62) are shown at the upper right. This structure was not loaded aft of the 62-percent chord; therefore, approximately the aft 40 percent of the structure was not loaded. The inboard 20 percent was also not loaded. This structure presents a case where large areas of the structure are not directly loaded. This case requires extensive extrapolation to develop a linear equation that defines the response of strain gage 62 to discrete loads over the entire wing surface. A minimum of three methods of extrapolating the load calibration were used: linear extrapolation, extrapolation of the last two points, and nonlinear curve fitting. The left bottom of figure 36 shows

*Gray, A. K. J., "Procedures Manual for Flight Test Determination and Evaluation of Load Distribution and Structural Integrity," Report No. EFT-55-1, Northrop Aircraft, Inc., June 1955.

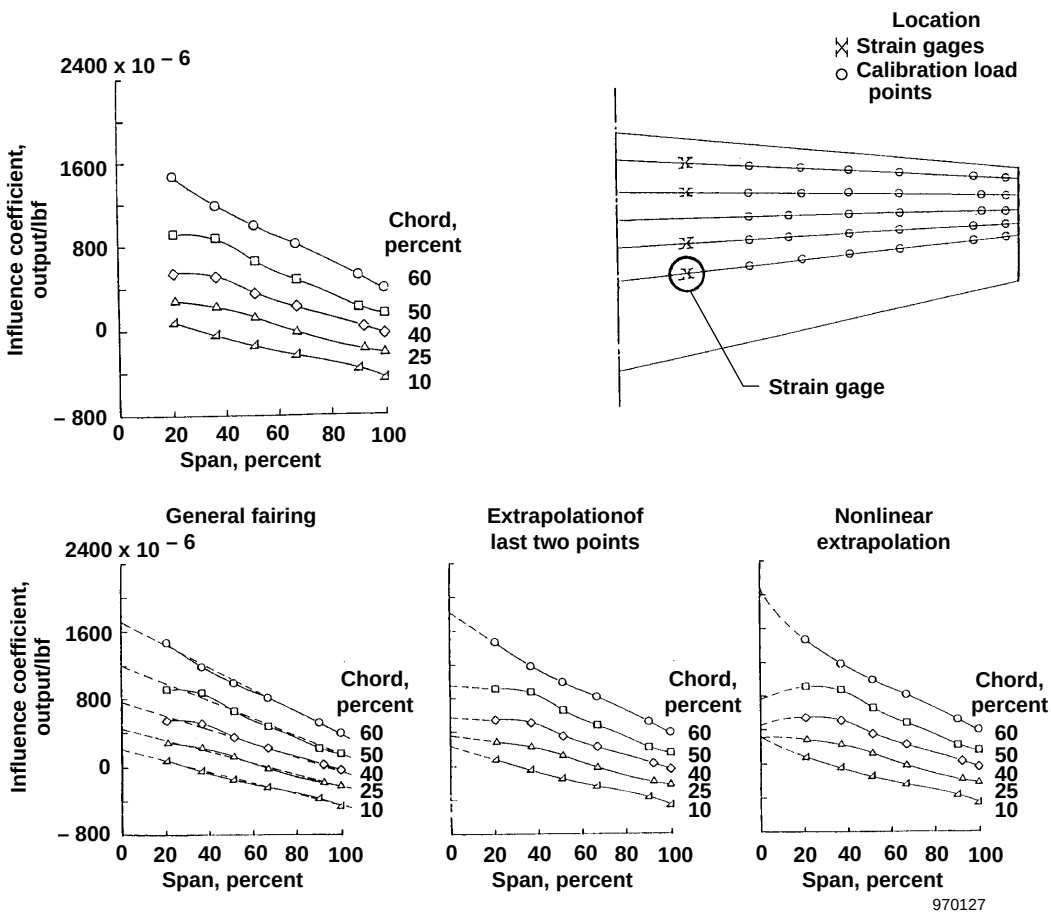

Figure 36. General load calibration characteristics of strain gage 62 on the F-89 wing.

how a linear regression would extrapolate for values to a maximum 60-percent chord. If the two inboard load calibration stations were used, then the two most inboard load points, shown in the bottom middle of the figure, would be used to project the extrapolation. The third approach, shown at the bottom right, is the full curve fit, which would be used to develop a nonlinear approximation and extrapolation.

The significance of these three comparisons is typically illustrated by examining the zero-span intercept. The load points at the 20-percent span location do not seem to follow the trend of the other load points for constant chord values. In other words, as the load points get closer to the location of the strain gages, local anomalies begin to appear in the data near the root of the lifting surface. The three methods of extrapolation shown at the bottom of figure 36 illustrate the importance of representing the extrapolation in an appropriate manner.

Figure 37 shows insight into the overall span/chord extrapolation relationship for strain gage 62. In the case with no extrapolation (top ribbon plot), the curved areas represent the basic load calibration. The values at the boundaries of the calibration loads points are extended to cover 100 percent of the wing (seen as the flat areas in the figure). In the case with extrapolation (bottom ribbon plot), the curved areas represent the basic load calibration. The extrapolation shown in the bottom right side of the figure consisted of extrapolating the data from the last two points in the chord and span directions. The extrapolation appears to minimize the actual extent of the load calibration data (fig. 37). This minimization means that the method and the extent of the extrapolation have far-reaching impact on the equations defining loads.

Figure 38 shows an even more extreme case, where the results of strain gage 12 are presented. The results can be seen to diverge at and about the 20-percent span area. The zero-span intercept varies widely, and the feasibility of applying a nonlinear curve fit as the extrapolation approach to the 50- and 60-percent chord lines seems a poor option.

This phenomenon in the area of the wing root will be seen later in the calibrations of the structures of other wings. The phenomenon is important, and the actual mechanism has a great impact on load calibrations and the resulting equations.

The F-89 wing was calibrated with 30 load points, but because of the distribution of the spars, the relevance coefficient was small:

$$C_R = 0.49$$

Figure 39 shows the distribution of the calibration load points in terms of span and chord.

Space Shuttle Orbiter

Appendix A shows a three-view sketch of the space shuttle orbiter. Figure 1(g) shows the wing in more detail and where calibration load points are located along with strain-gage bridges. The wing structure has a low-aspect-ratio planform with multiple spars that have corrugated webs and ribs that are trusses. The wing structure has large elevons at the trailing edge and a large fairing merging with the forward fuselage. Figure 40 shows the wing structure along with general strain-gage bridge locations. Twenty-seven load points were used to calibrate this structure at the locations shown (fig. 40). The shuttle orbiter wing is typical of a low-aspect-ratio delta-wing aircraft in that multiple spars and ribs are present along with a landing gear embedded in the wing. The wing also has control surfaces along the rear of the structure. Sufficient resources were available to complete a credible load calibration*† with sufficient instrumentation available. In addition, the calibration results for two shuttle orbiter aircraft (designated OV-101 and OV-102) will be presented in this section.

---

*Carter, A. L., “OV-101 Strain Gage Calibration for Flight Load Measurement,” Memorandum to Aerostructures Files, NASA Flight Research Center, Apr. 1977.

†Carter, A. L., “OV-102 Wing Calibration Results,” Memorandum to Aerostructures Branch Files, NASA Flight Research Center, Oct. 1978.

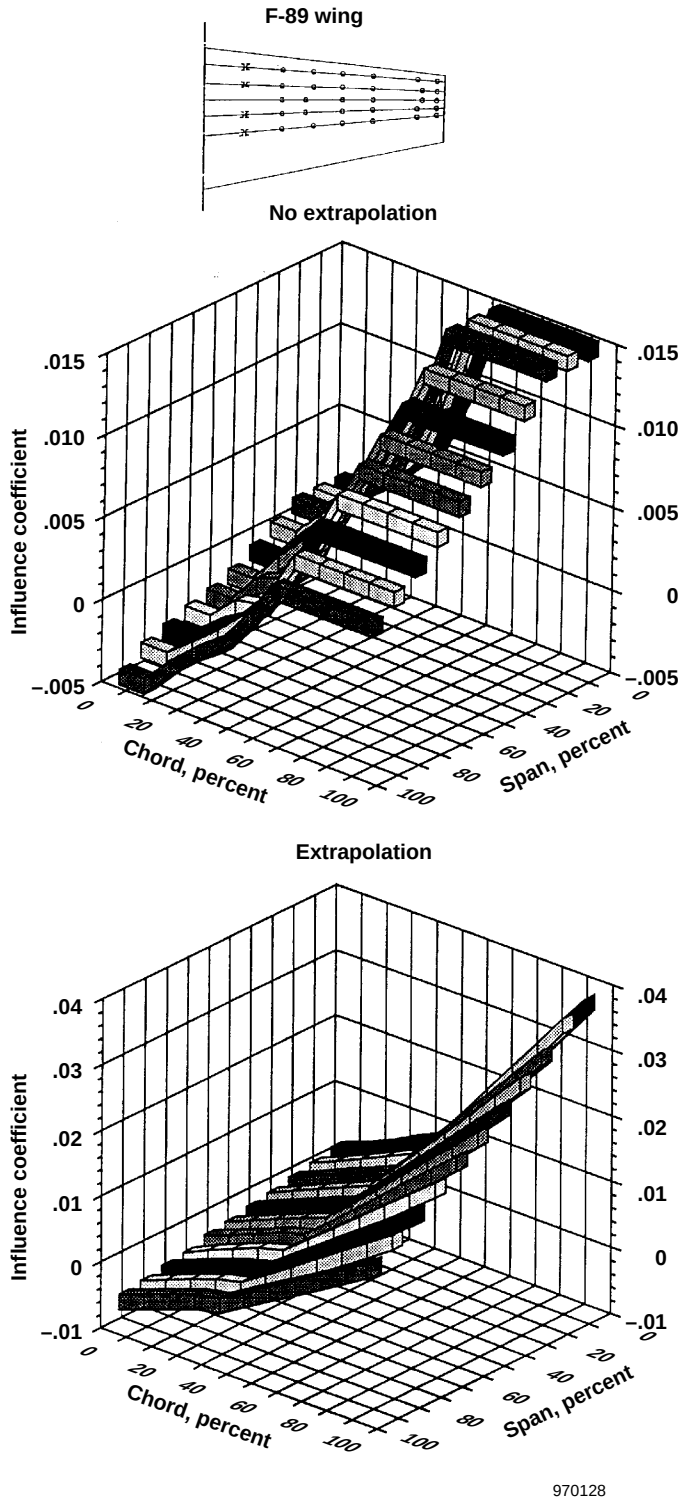

Figure 37. Basic effect of extrapolation on the influence-coefficient plot for strain gage 62 on the F-89 airplane.

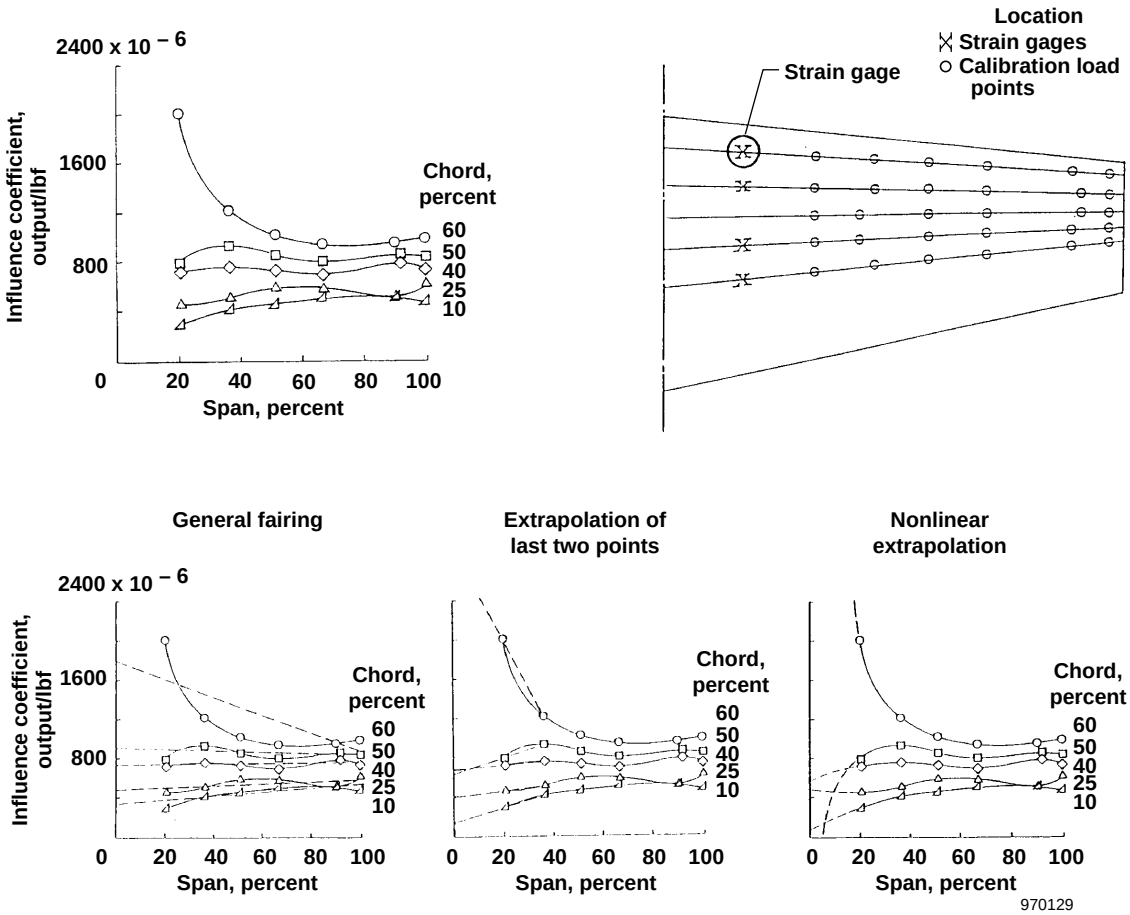

Figure 38. General load calibrations characteristics of strain gage 12 on the F-89 wing.

Figure 41 shows examples of the results of the calibration of shuttle orbiter OV-101. Figure 41(a) shows a bending response that has very little contamination in terms of torsion. Figure 41(b) shows a torsional response, and figure 41(c) shows a shear response. These three responses (figs. 41(a), (b), and (c)) give a strong indication that load equations can be developed for this wing that define the applied load well. Figure 41(d) shows an anomaly that is characteristic of delta-wing influence-coefficient plots. Strain-gage bridges that are located in the area of the leading edge/fuselage junction respond only to load points that are in that area of the wing. This irregular response results in the requirement for additional terms in the load equations to define the total load.

Figures 42 and 43 show additional examples of influence coefficients for shuttle OV-101. The responses are shown for several strain gages located at different fuselage stations. A variety of responses are seen with shear, bending, and torsion responses illustrating minor contamination by other load effects.

The data presented (figs. 44, 45, and 46) provide a unique comparison of load calibration results for several strain gages at similar locations on two different orbiter vehicles (OV-101 and OV-102). Examination of figures 44 to 46 reveals that the general distribution and shape of the influence-coefficient plots is either identical or similar. The strain-gage bridge located at fuselage station 1365 (fig. 45) is a bending-type bridge that responds almost identically on the two aircraft. The two bridge responses (fig. 46) (also at fuselage station 1365) are shear bridges that are highly sensitive to torsion. The shapes are similar, but a larger response exists for OV-101 than for OV-102.

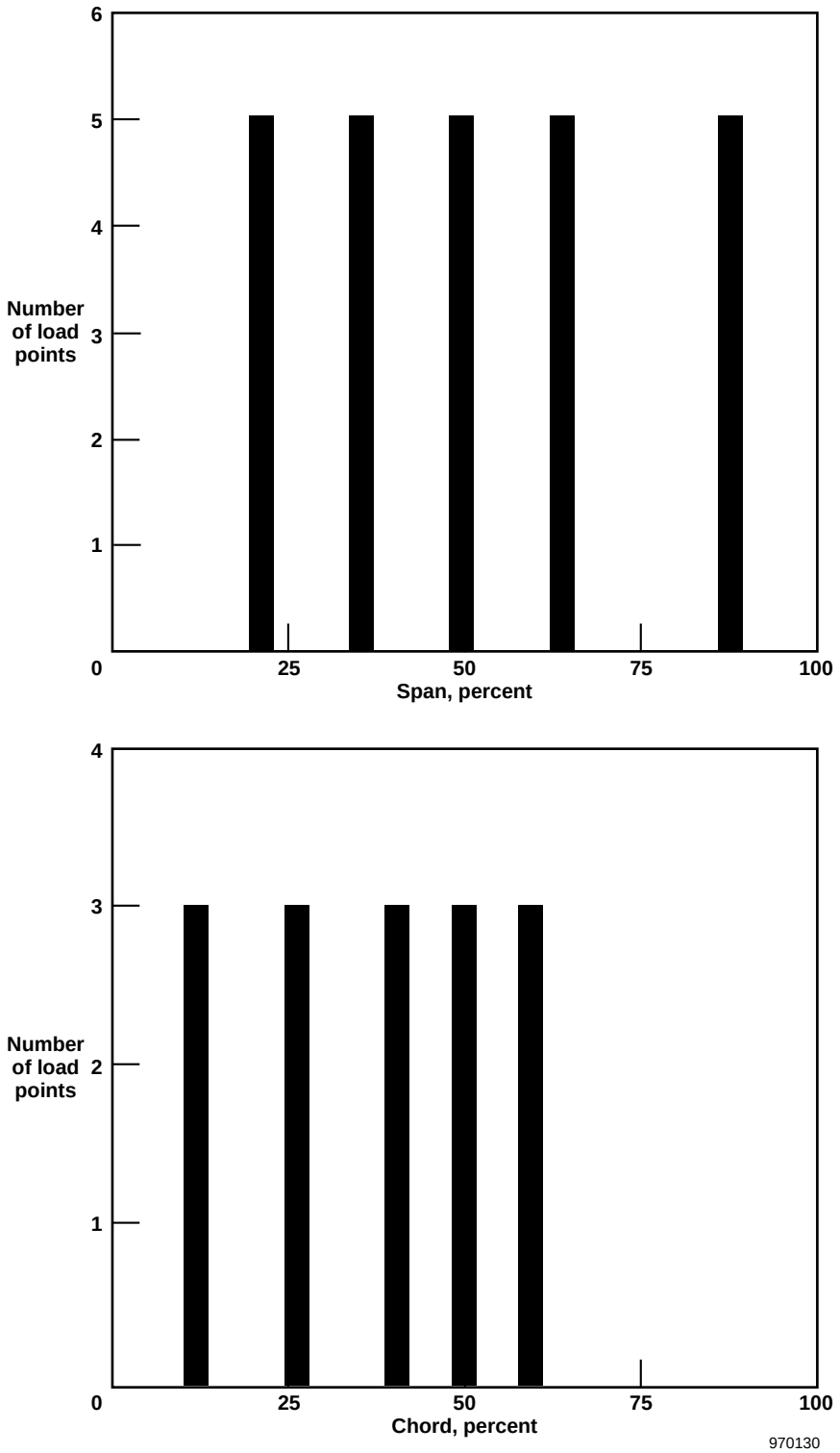

Figure 39. Distribution of load points in the span and chord directions for the F-89 wing.

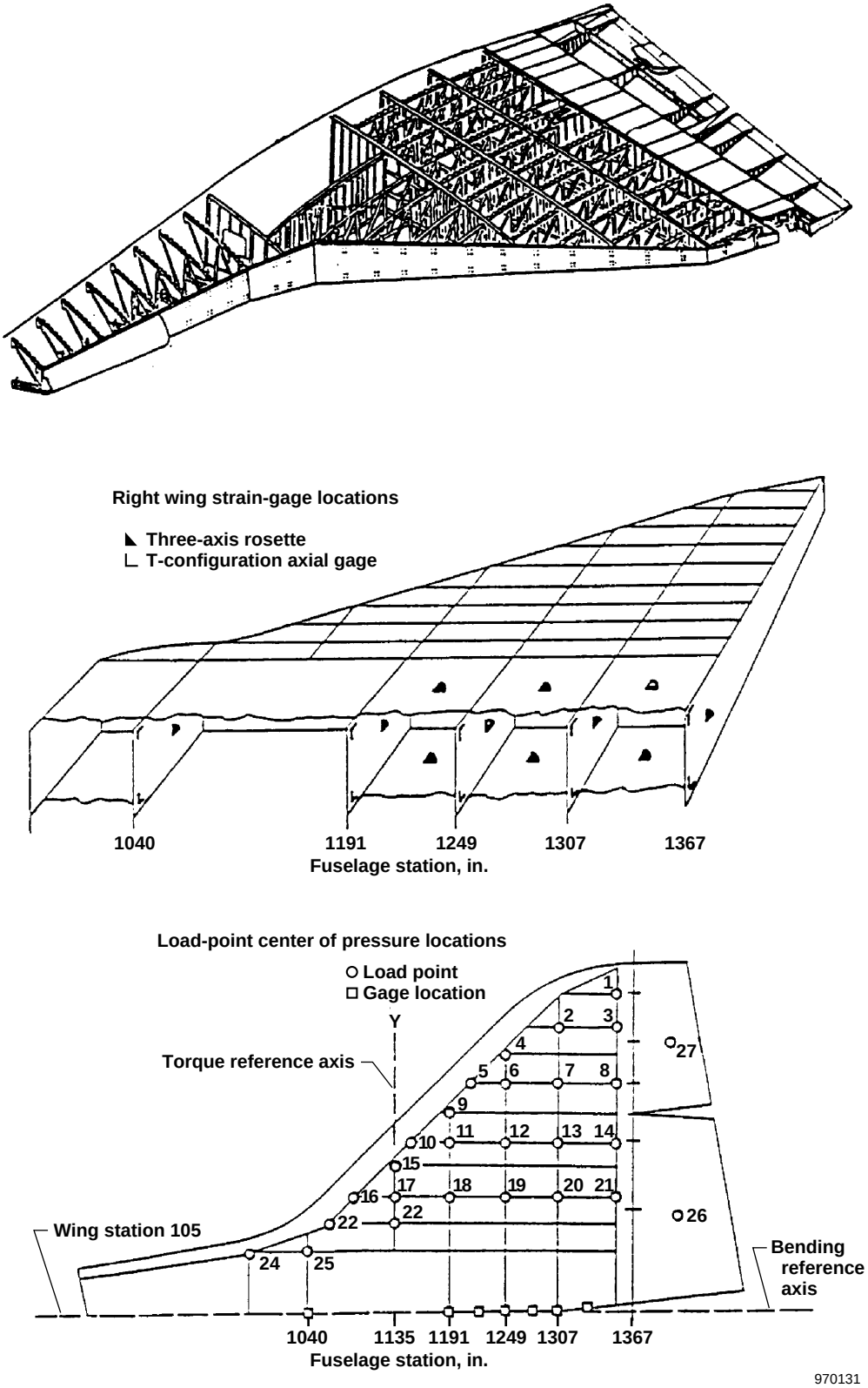

Figure 40. Basic structural arrangement, strain-gage locations, and load-point locations on the Space Shuttle Orbiter wing structure.

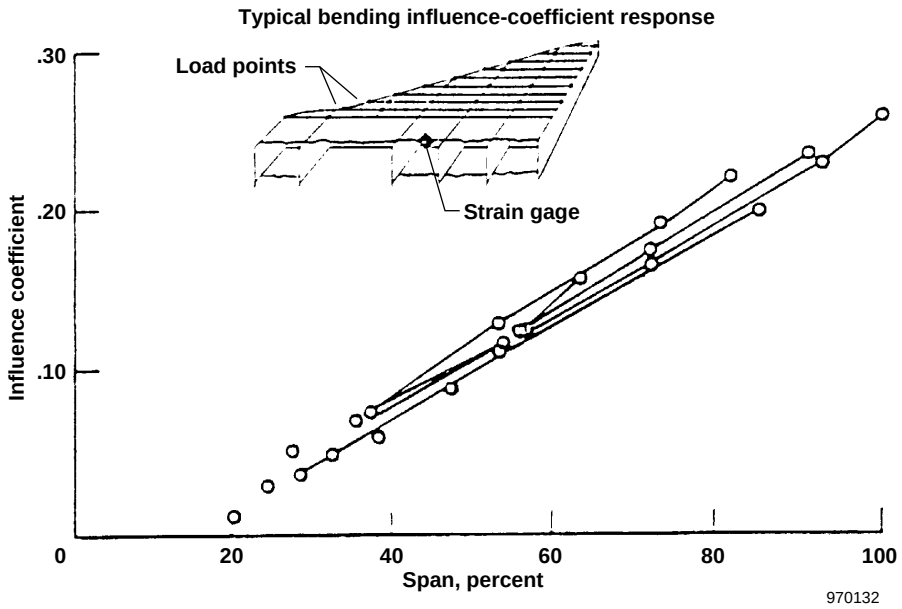

(a) Typical bending influence coefficients.

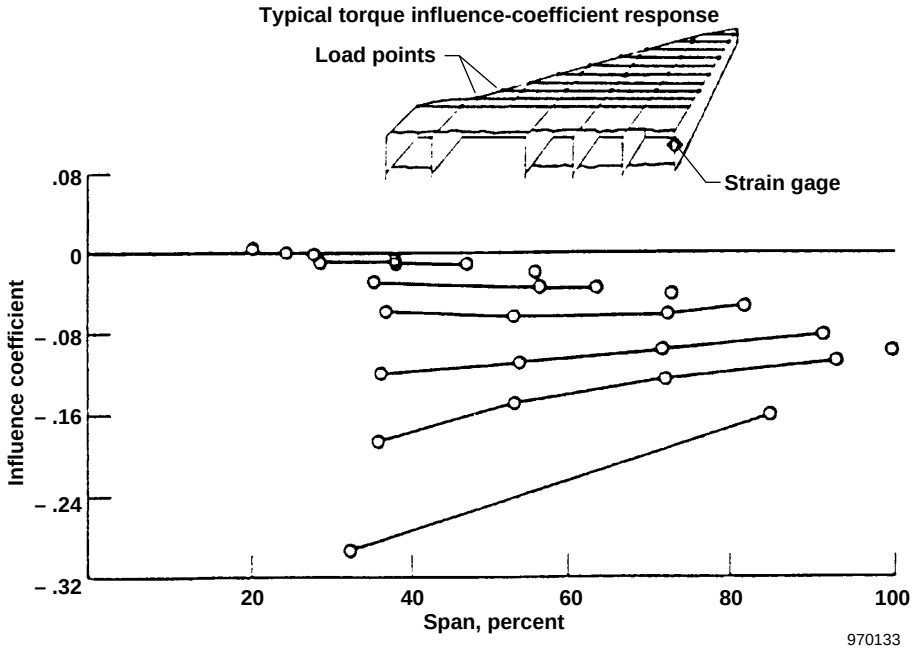

(b) Typical torsion influence coefficients.

Figure 41. Typical influence-coefficient plots for the Space Shuttle Orbiter wing.

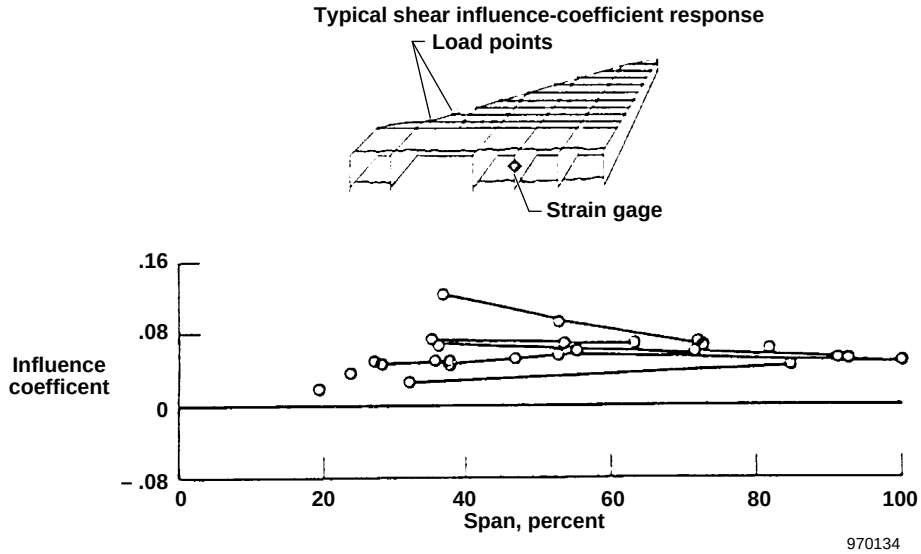

(c) Typical shear influence coefficients.

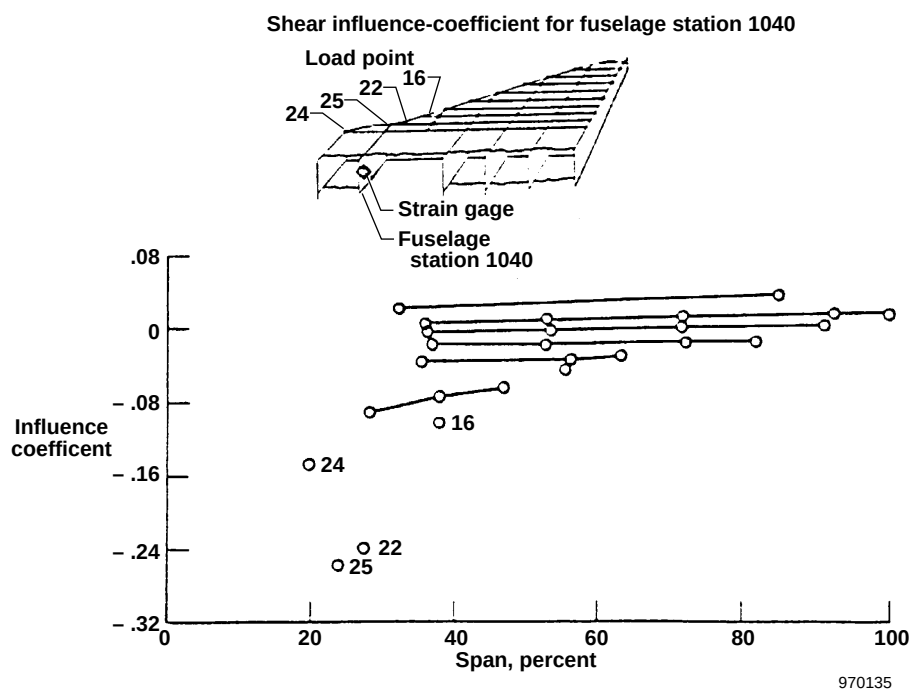

(d) Complex influence-coefficient plot.

Figure 41. Concluded.

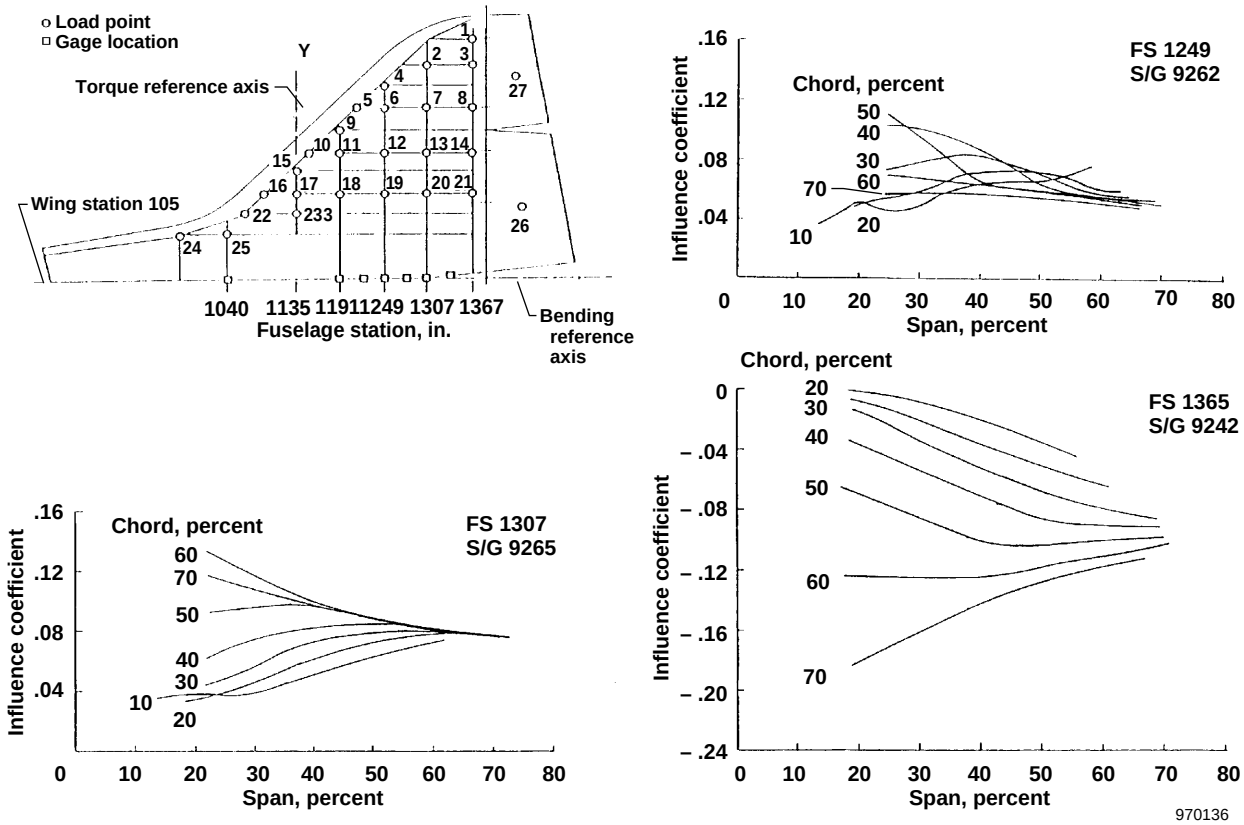

Figure 42. Influence-coefficient plots derived from the Space Shuttle Orbiter wing load calibration.

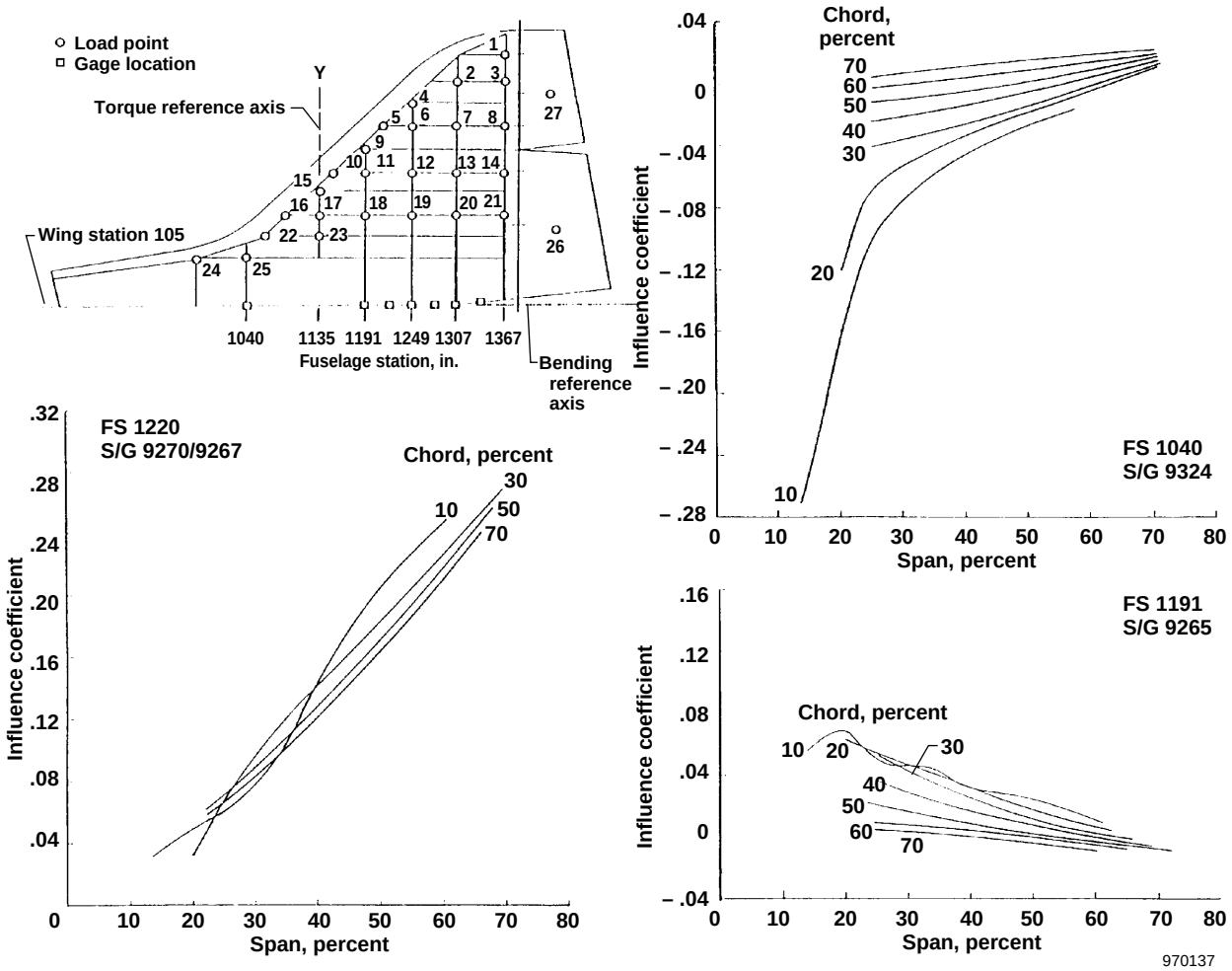

Figure 43. Influence-coefficient plots derived from the Space Shuttle Orbiter wing load calibration.

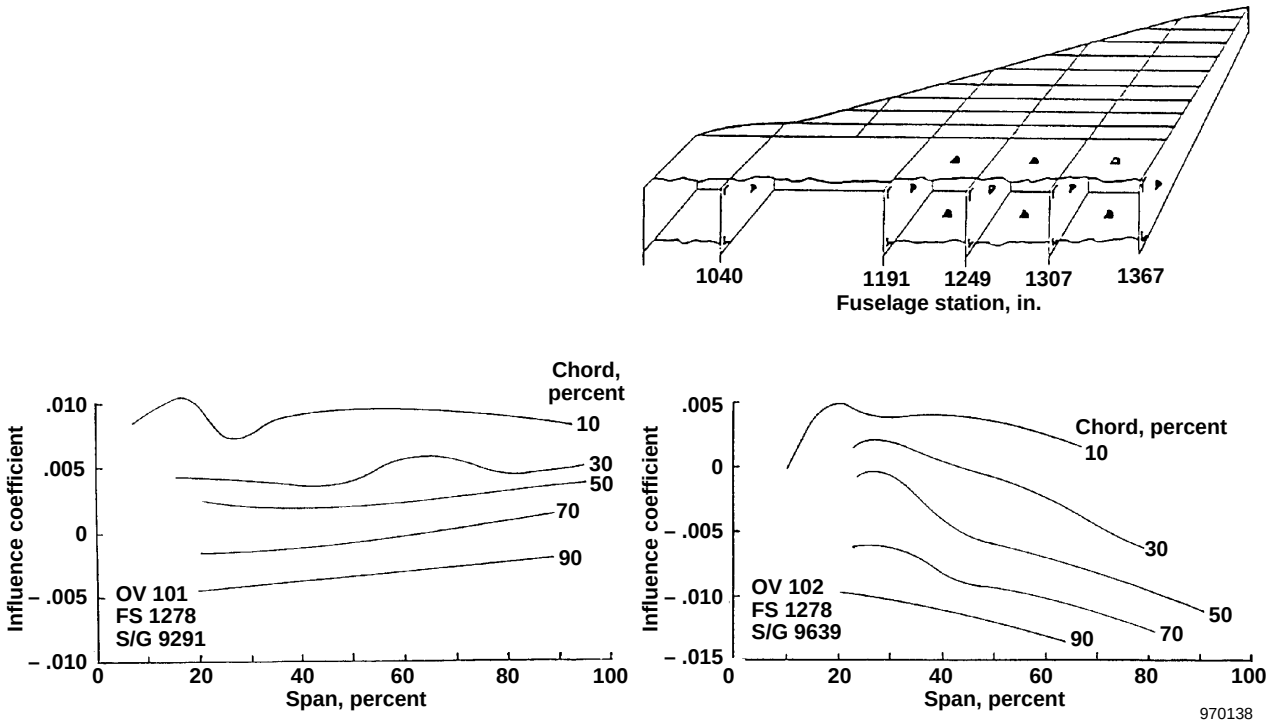

Figure 44. Comparison of shear influence-coefficient plots for comparable strain-gage bridges on Space Shuttle Orbiters OV-101 and OV-102.

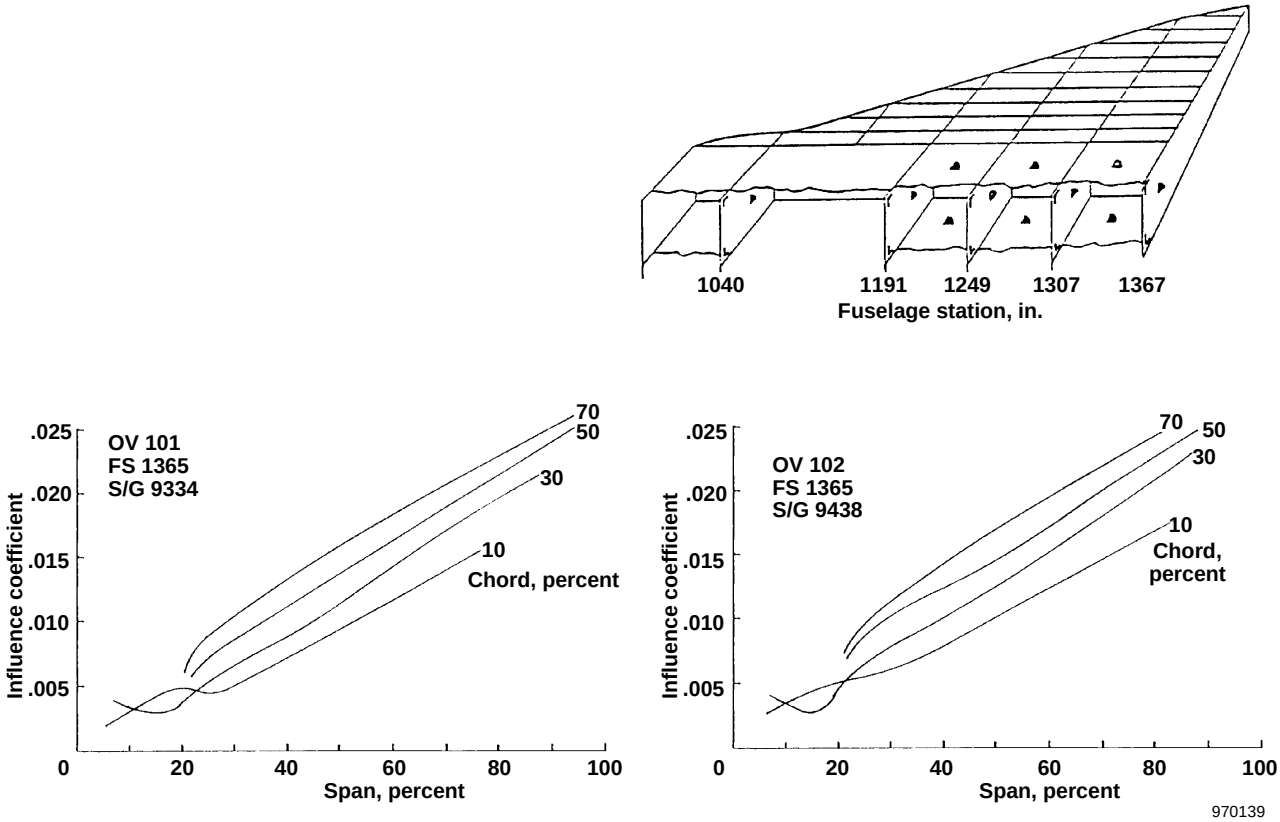

Figure 45. Comparison of bending influence-coefficient plots for comparable strain gage on Space Shuttle Orbiters OV-101 and OV-102.

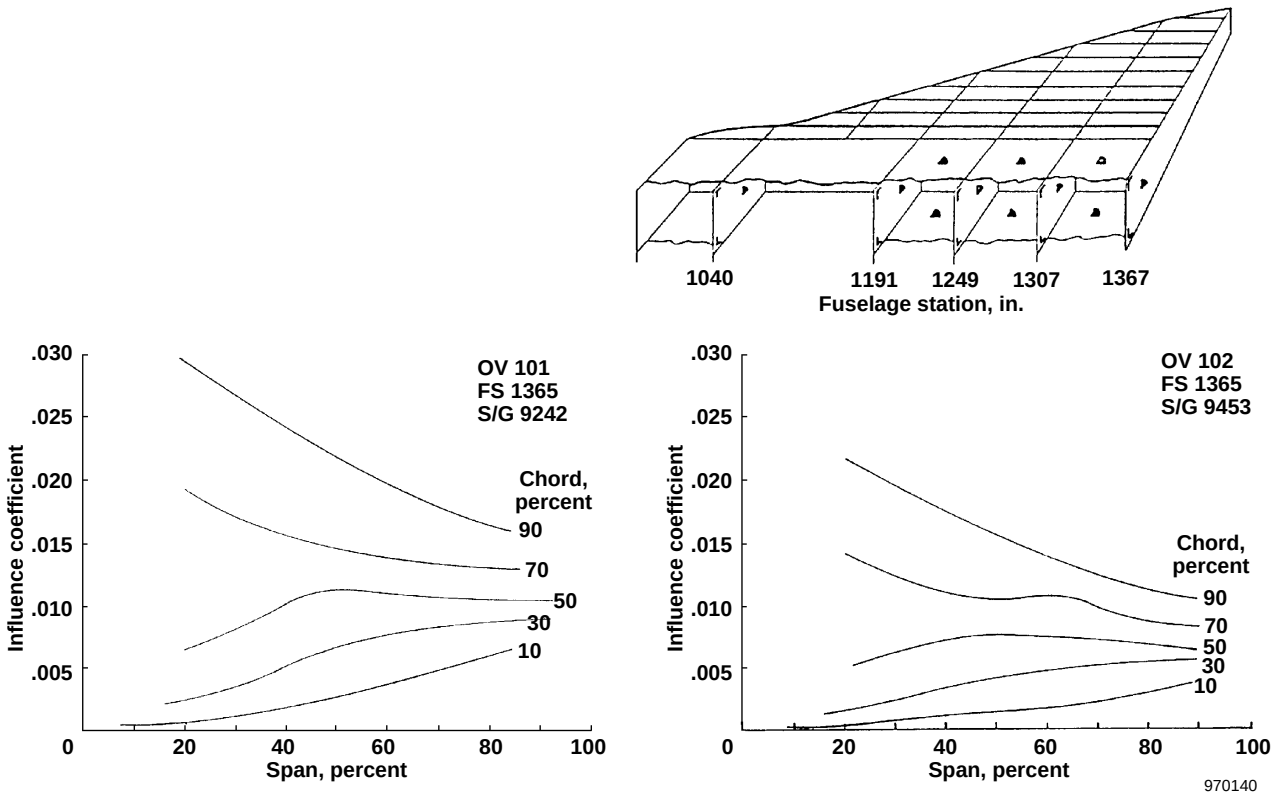

Figure 46. Comparison of torsional influence-coefficient plots for comparable strain gage on Space Shuttle Orbiters OV-101 and OV-102.

The strain-gage bridge shown in figure 44 is somewhat difficult to identify in terms of purpose. The bridge is located such that it should respond in torsion; however, the torsional effects seem to be contaminated by bending. The bending effect is more readily seen in the response for OV-102 where the constant chord lines have a definite slope. The variations in the influence-coefficient responses for the two shuttle wings could result from several sources. Some minor structural differences exist between OV-101 and OV-102 that may result in slightly altered load paths. Any minor differences in the location of the various strain gages that form the bridge could also have a significant impact on the response characteristics.

Strains were deduced from four-active-arm strain-gage bridges (appendix B) at several fuselage stations from the load instrumentation for a 30,000-lbf check load. These measured values were compared to values that were calculated for a NASTRAN[7] beam network model. Figure 47 shows a comparison of computer model strains with strains measured on the wing. The computed distribution of bending and shear strains compares closely to the values measured during the application of a 30,000-lbf check load.

Load equation accuracies based on the calibration conditions for OV-101 and OV-102 are as follows:

	OV-101	OV-102
Shear	1.0 percent	1.3 percent
Bending Moment	3.5 percent	1.3 percent
Torsion	1.6 percent	1.9 percent

These errors are based on the root-mean-square errors calculated from the individual load point results with respect to the load equations. The 27 load points used to calibrate this structure results in a relevance coefficient having the following value:

$$C_R = 0.69$$

Figure 48 shows the distribution of calibration load points in terms of span and chord loading. The load calibration of the space shuttle wing is a very complete one in terms of having a large number of load points that were well-distributed over the surface of the wing. The extent of the loading reflects adequate resources to conduct a well-conceived load calibration. The relatively large relevance coefficient reflects a generally complete coverage of the wing surface during the load calibration. The largest deficiency with the calibration of the space shuttle wings was the lack of calibration load points in the first 20 percent of the span adjacent to the root of the wing. Loading near the root of the wing or in the immediate vicinity of strain-gage instrumentation will be discussed in a later section.

T-37B Wing

Appendix A shows a three-view sketch of the T-37B aircraft. Figure 1(h) shows the wing and where the calibrated load points are located along with the strain-gage bridges. The planform is a relatively high-aspect-ratio wing with two main spars, two stub spars near the root, and a full-span control surface/flap. Ten load points were used to calibrate this wing. Twelve four-active-arm strain-gage bridges were available to develop loads equations. The basic strain-gage load calibration for this wing has previously been documented.*

*Sims, Robert L., “T-37B Strain Gage Calibration,” Branch Report BR-73, NASA Dryden Flight Research Center, Nov. 1992.

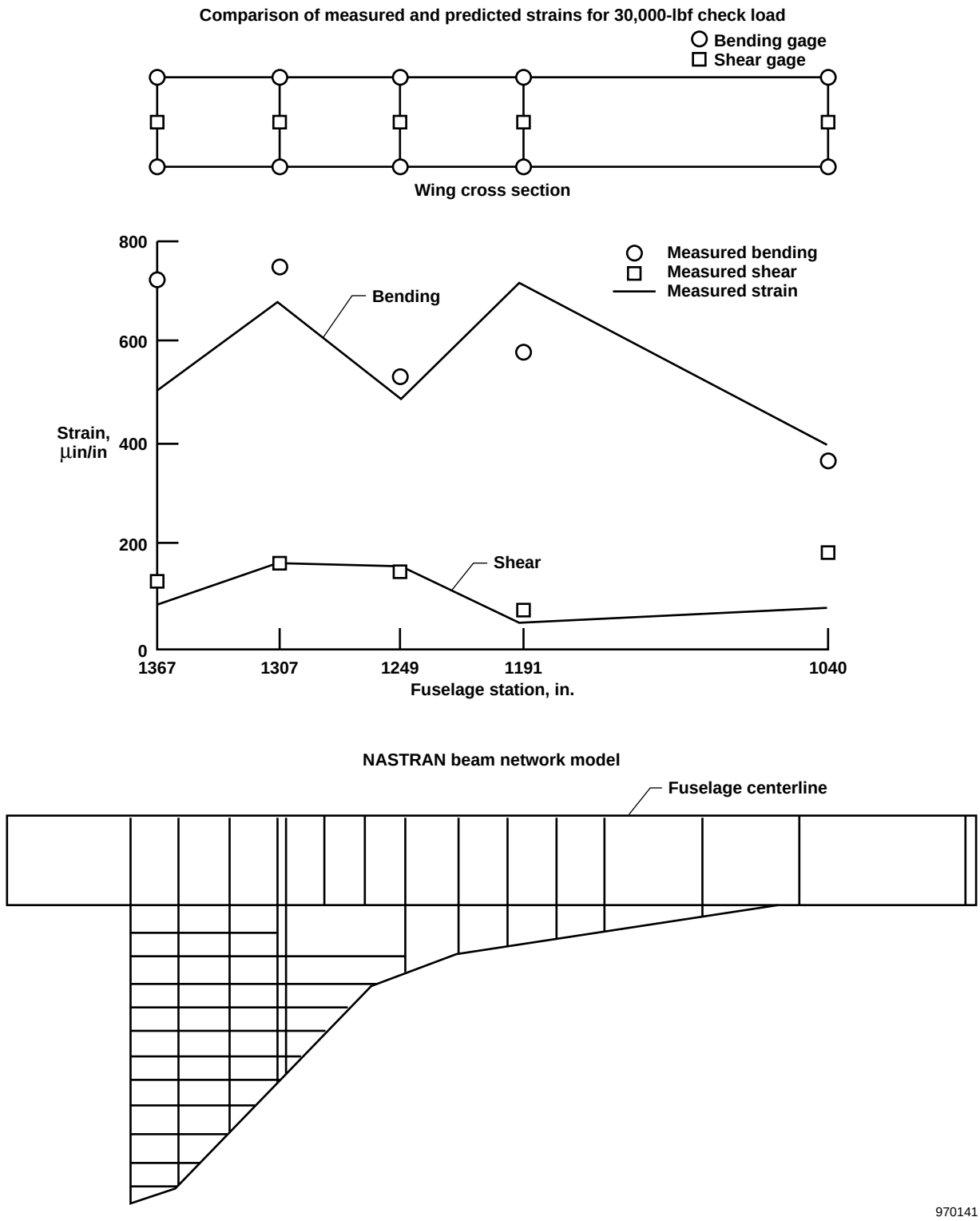

Figure 47. Comparison of measured bending and shear strains with calculated values from a finite-element structural model of the Space Shuttle Orbiter.

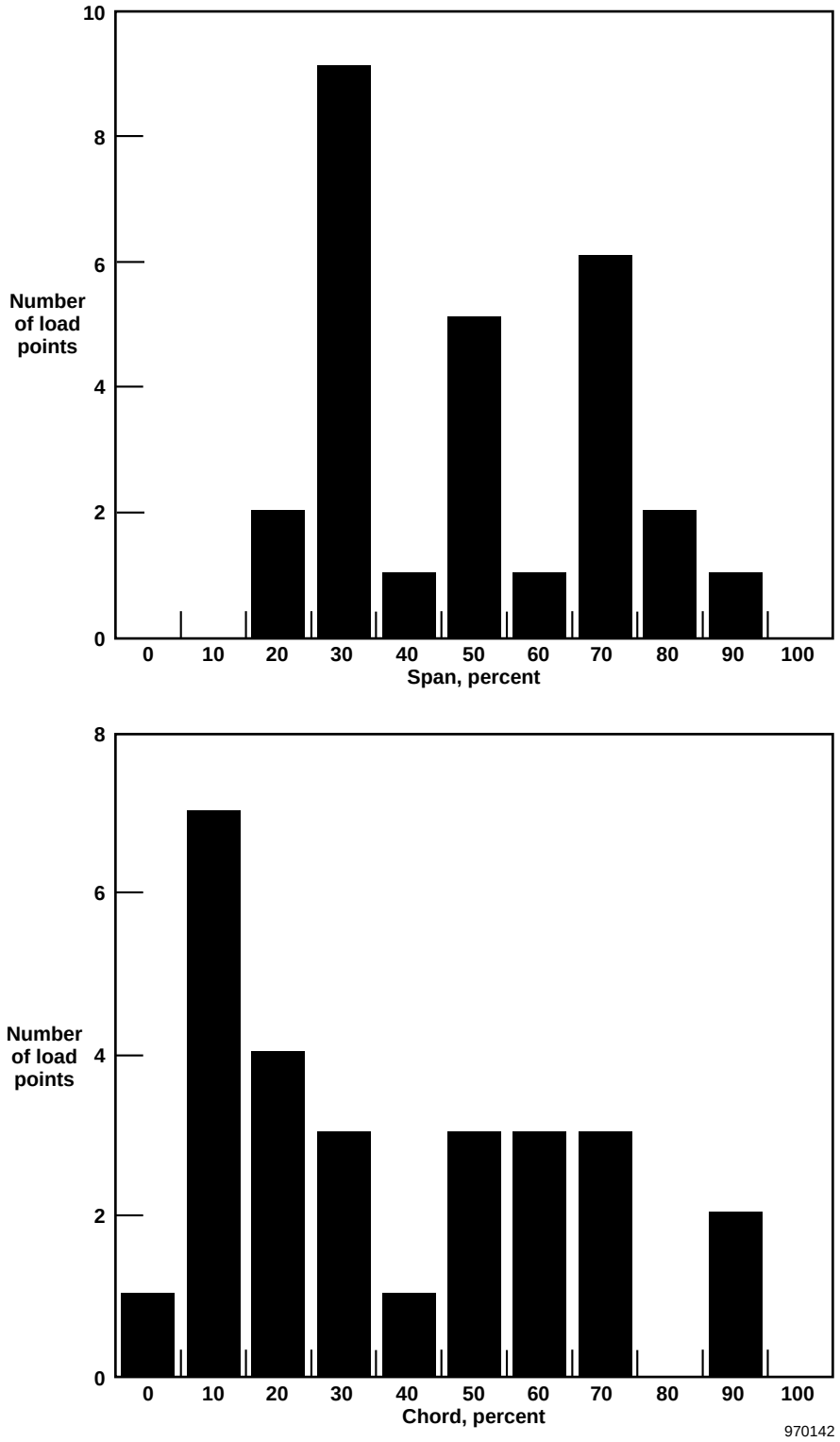

Figure 48. Span and chord distribution of load points used to calibrate the wing of the Space Shuttle Orbiter.

Figure 49 shows strain-gage bridge locations on the root spars. For the four-active-arm bending bridges, two of the strain sensors are located in the area of the top spar cap, and two are located in the area of the bottom spar cap. The four strain gages used to form the shear bridges are also seen on the webs of the spars. The individual strain gages are located in a pattern such that each of the four sensors is located at 90° intervals. The system is located 45° from the longitudinal axis of the spar near the neutral axis of the spar. The array of strain-gage bridges illustrates the general methodology associated with locating strain gages in a bridge array to maximize responses to bending, shear, and torsion. Strain gages are sometimes located on the skins in a shear configuration for greater sensitivity to torsional loads. The presentation of the strain-gage locations provides an example of a typical installation.

Figures 50 and 51 show influence-coefficient plots for the wing root. Bending responses are dominant in figure 50. The influence-coefficient plot for strain gage 11 shows an almost perfect bending response; strain gage 21 is somewhat contaminated by torsion. Figure 51 shows four shear bridge influence-coefficient plots. The net output for strain-gage bridge 43 is close to zero; hence, the bridge is not in a particularly valuable location. The remaining three responses are all sensitive to both torsion and bending, although the shear characteristics are good. Note that the front spar strain-gage bridge 13 has an influence-coefficient plot similar to the front spar response of the F-89 wing (fig. 38). In both cases, a large divergence of the influence-coefficient plot exists as the wing root is approached. The strain-gage bridge influence-coefficient plot for the rear spar (number 23) also exhibits characteristics similar to the rear spar of the F-89 wing (fig. 36). The location of the spars in the chord direction on both wings and the aspect ratios of the main spar grouping likely contribute to the similarities.

The T-37B wing was calibrated with ten load points. Because of the distribution of the primary spars and the small number of load points, the relevancy coefficient was quite small:

$$C_R = 0.32$$

Figure 52 shows the distribution of the calibration load points in terms of span and chord location for the T-37B wing load calibration.

YF-12 Wing

The load measurement program conducted with a YF-12 airplane*[8–11] is probably the most comprehensive strain-gage load measurement effort in aeronautical history by virtue of the extensive efforts in the following:

- the physical load calibration
- the studies resulting from the load calibration
- the use of advanced ground-based facilities
- the extensive instrumentation research activities
- the wide spectrum of publications
- the analytical support required to study and deal with the aerodynamic heating of the airframe

Figure 53 shows the extent of the load measurement. The loads were measured at three fuselage stations, three wing stations, the vertical tails, and the control surfaces. Only the measurements associated with the wing loads at wing station 35.0 will be included in this paper.

*Carter, Alan L., “YF-12 Strain Gage Calibration Results,” Branch Report BR-39, NASA Dryden Flight Research Center, Mar. 1972.

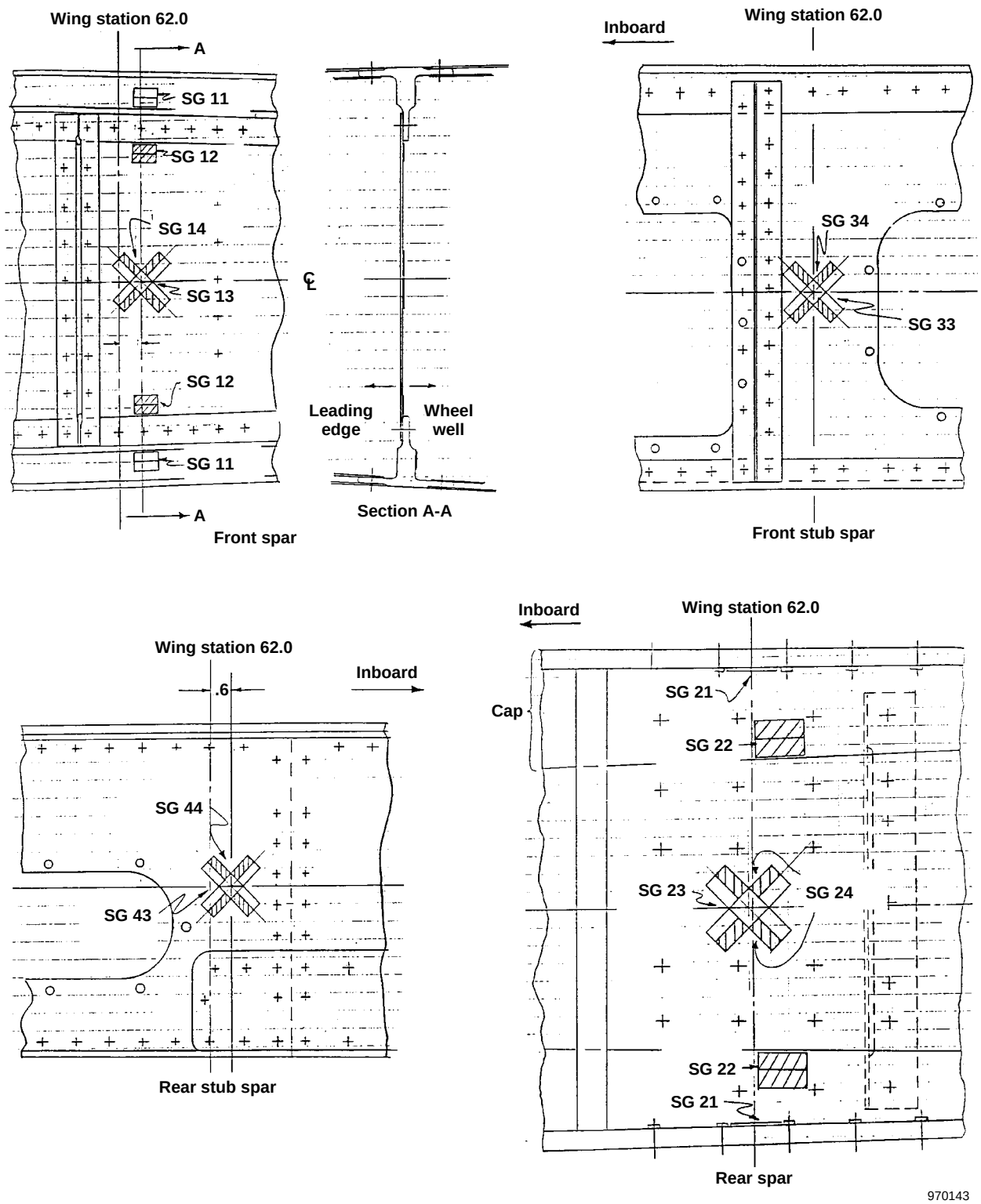

Figure 49. Location of strain-gage bridges for the T-37B wing root spars.

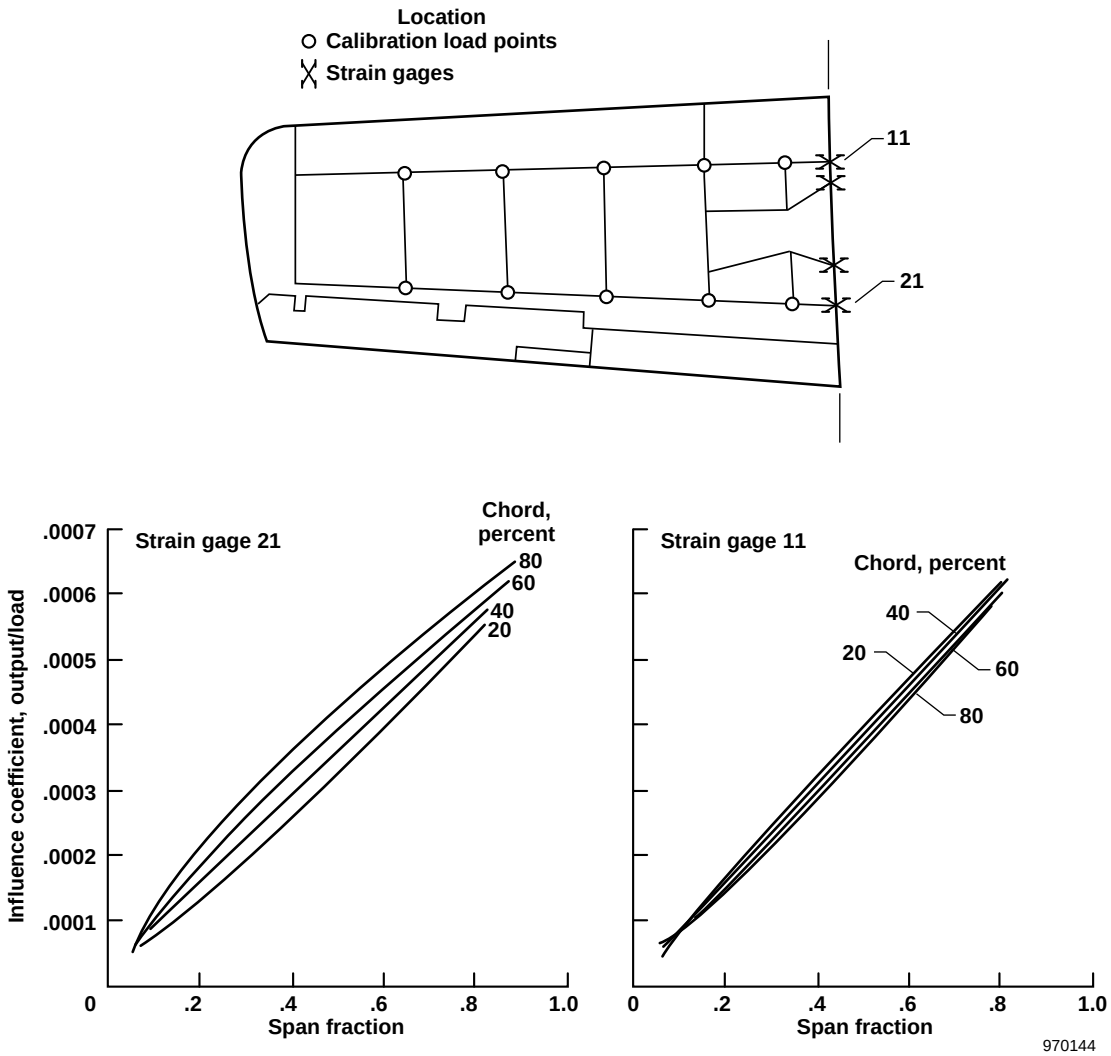

Figure 50. Influence-coefficient plots for typical bending strain-gage bridges for the T-37B wings.

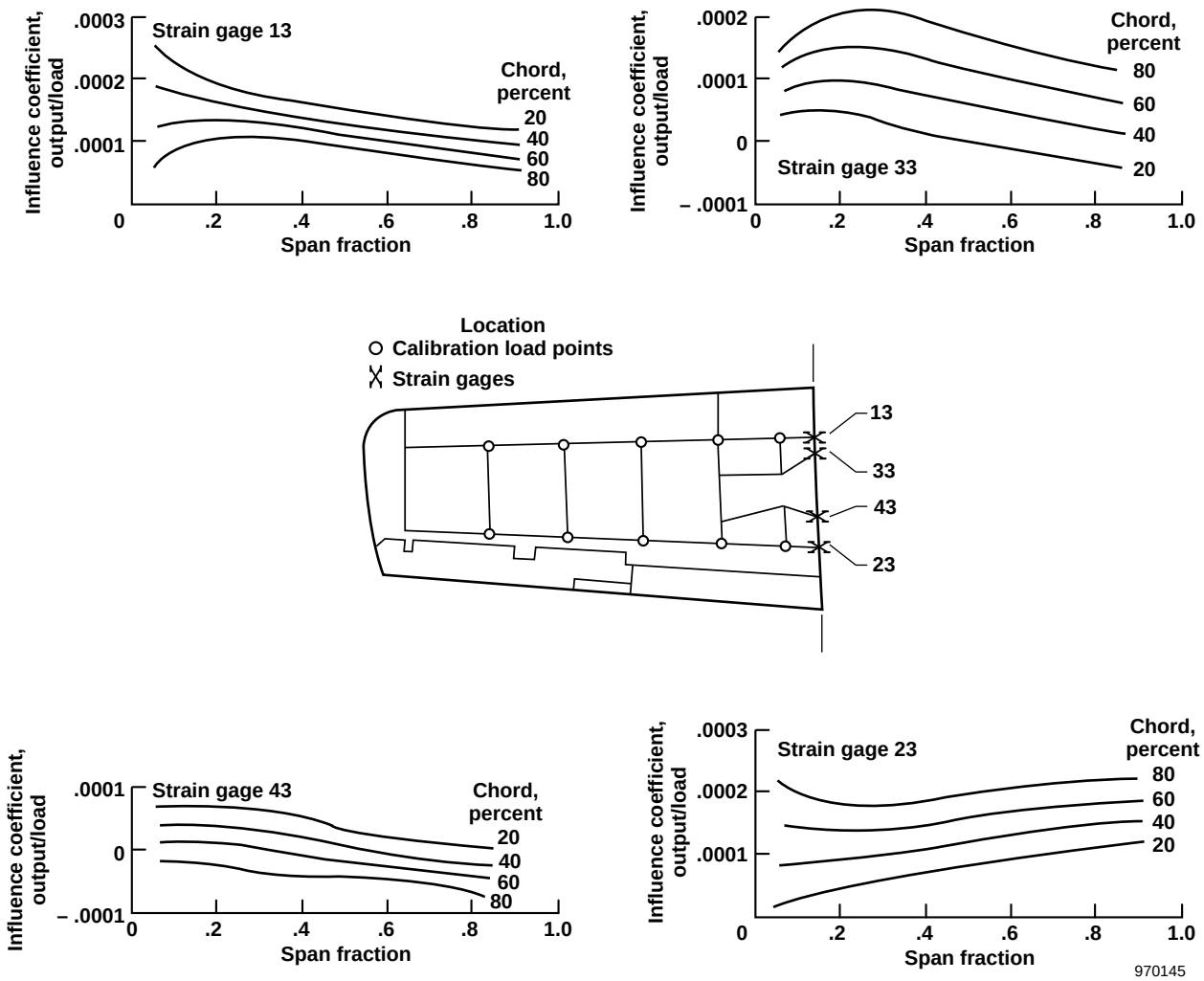

Figure 51. Influence-coefficient plots for typical shear strain-gage bridges for the T-37B wing.

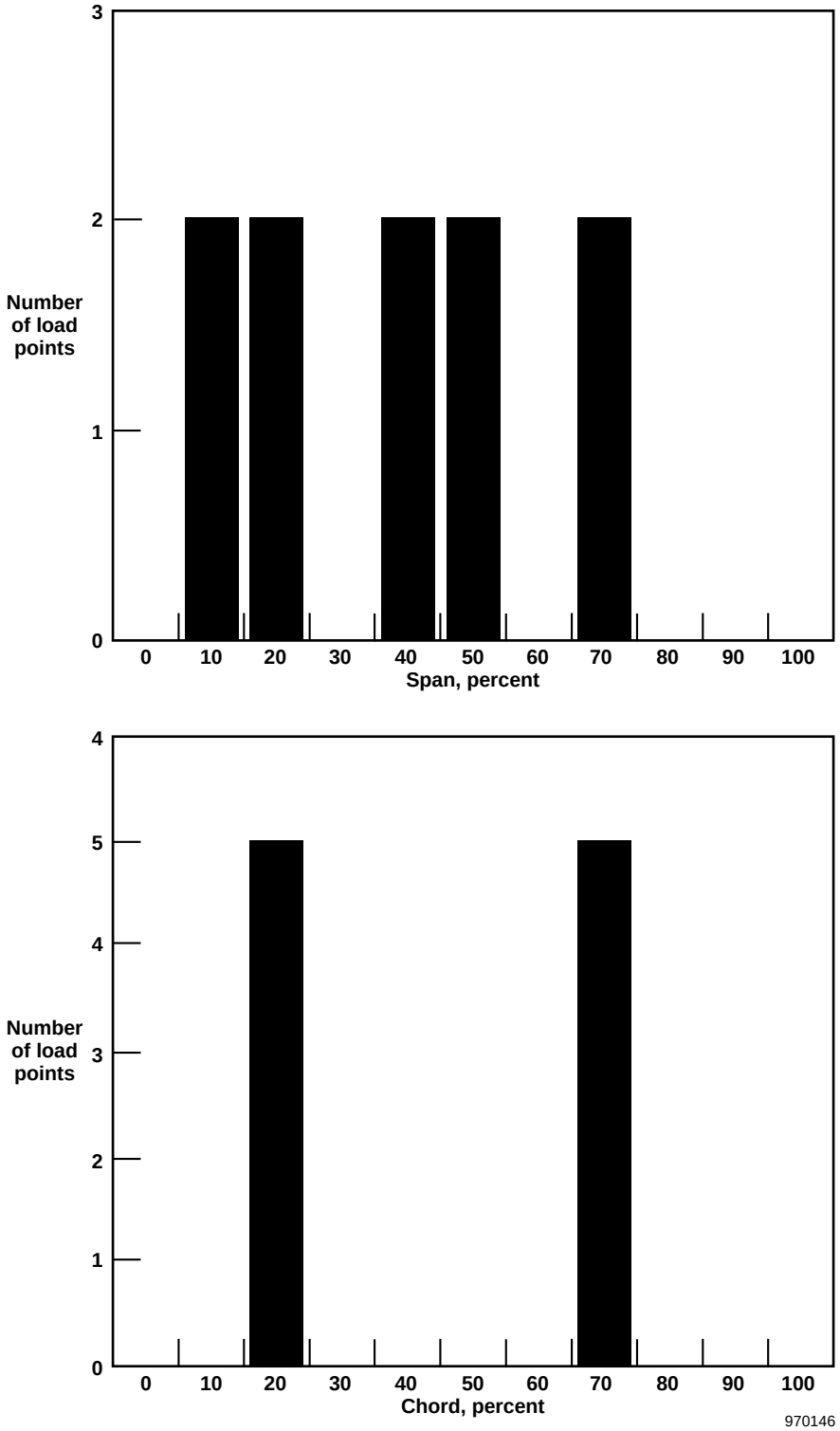

Figure 52. Distribution of load points in the span and chord directions for the T-37B wing load calibration.

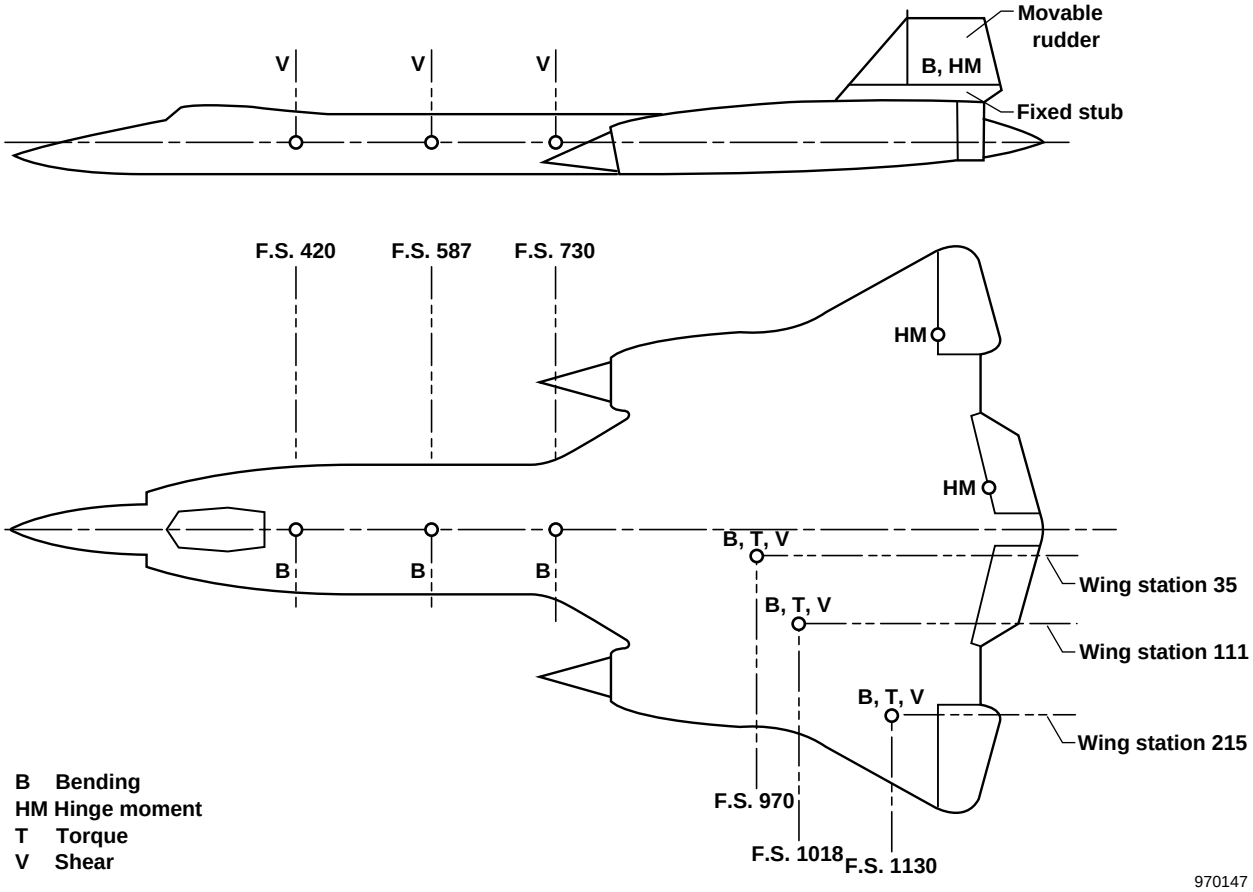

Figure 53. Load-measurement locations for the YF-12A flight loads program.[11]

Appendix A shows a three-view sketch of the YF-12 aircraft. Figure 1(i) shows the wing in more detail. The calibration load points are shown along with the strain-gage bridge locations. The instrumentation for the wing-root load measurement was quite extensive. Figures 54, 55, and 56 show numerous individual influence-coefficient plots. Additional influence-coefficient plots have previously been shown,[9] although the cross section of influence-coefficient plots shown in this report represents that which is typical of the YF-12 wing responses. Figures 54, 55, and 56 also show equation influence-coefficient plots that are derived from the constituent sensors. To the right of the equation influence coefficients are representations of the ideal case. Figure 54 shows the location of the five constituents of a primary shear equation. By incorporating a variety of responses into the shear equation, a response is created that is better than any of the constituents. This response is, of course, the purpose of using multiple terms in the equation. Figure 55 shows the same type of presentation for a primary bending-moment equation. The addition of the shear bridge to the equation would appear to contribute very little in terms of improving the overall equation. Figure 56 shows the same type of presentation for the primary torsion equation. The group of five strain-gage bridges used to formulate the torsion equation produced an equation that is much closer to the ideal than any of the individual constituents.

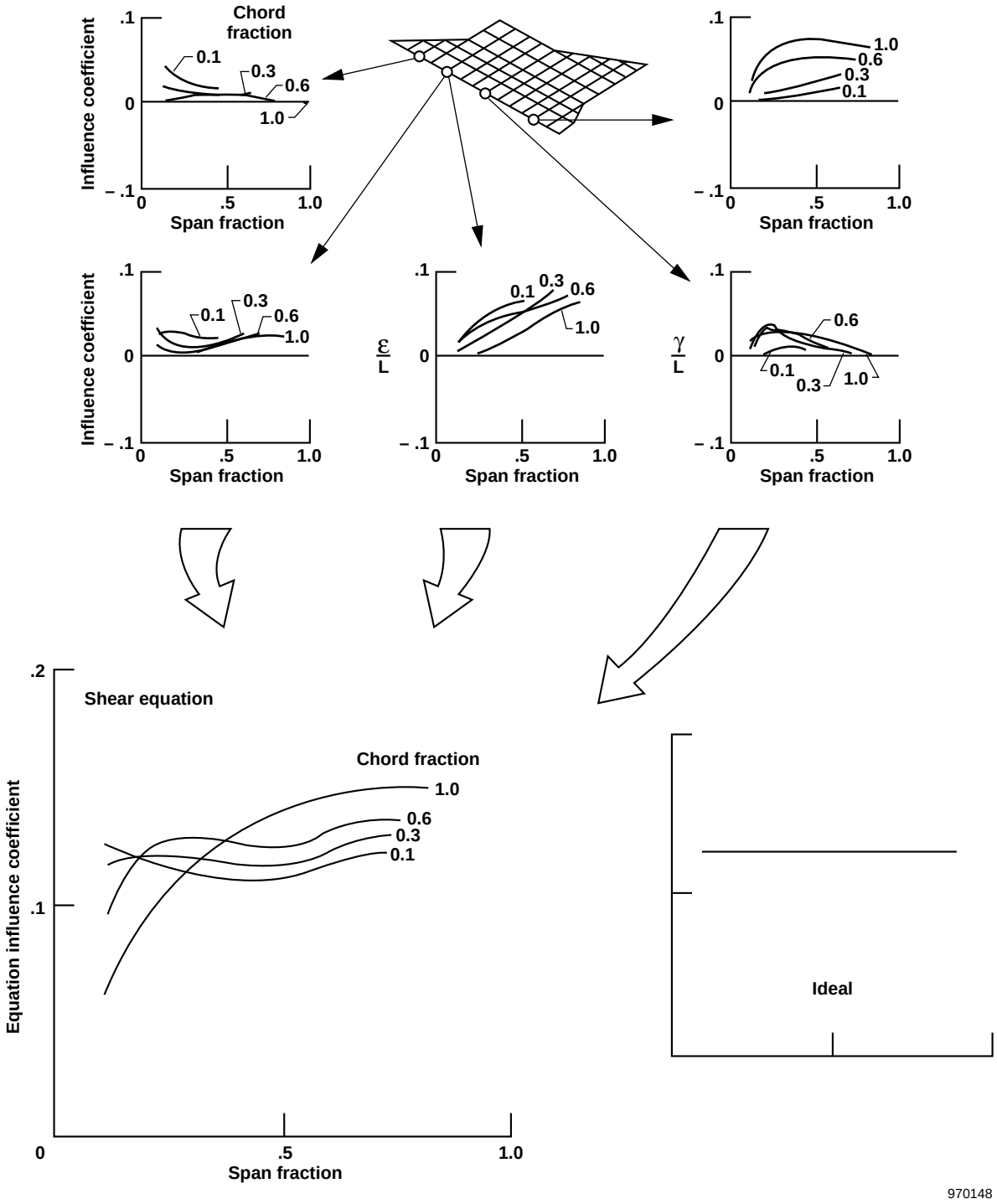

Figure 54. Properties of a shear equation as derived from constituents and compared with the ideal case for the YF-12A wing.[11]

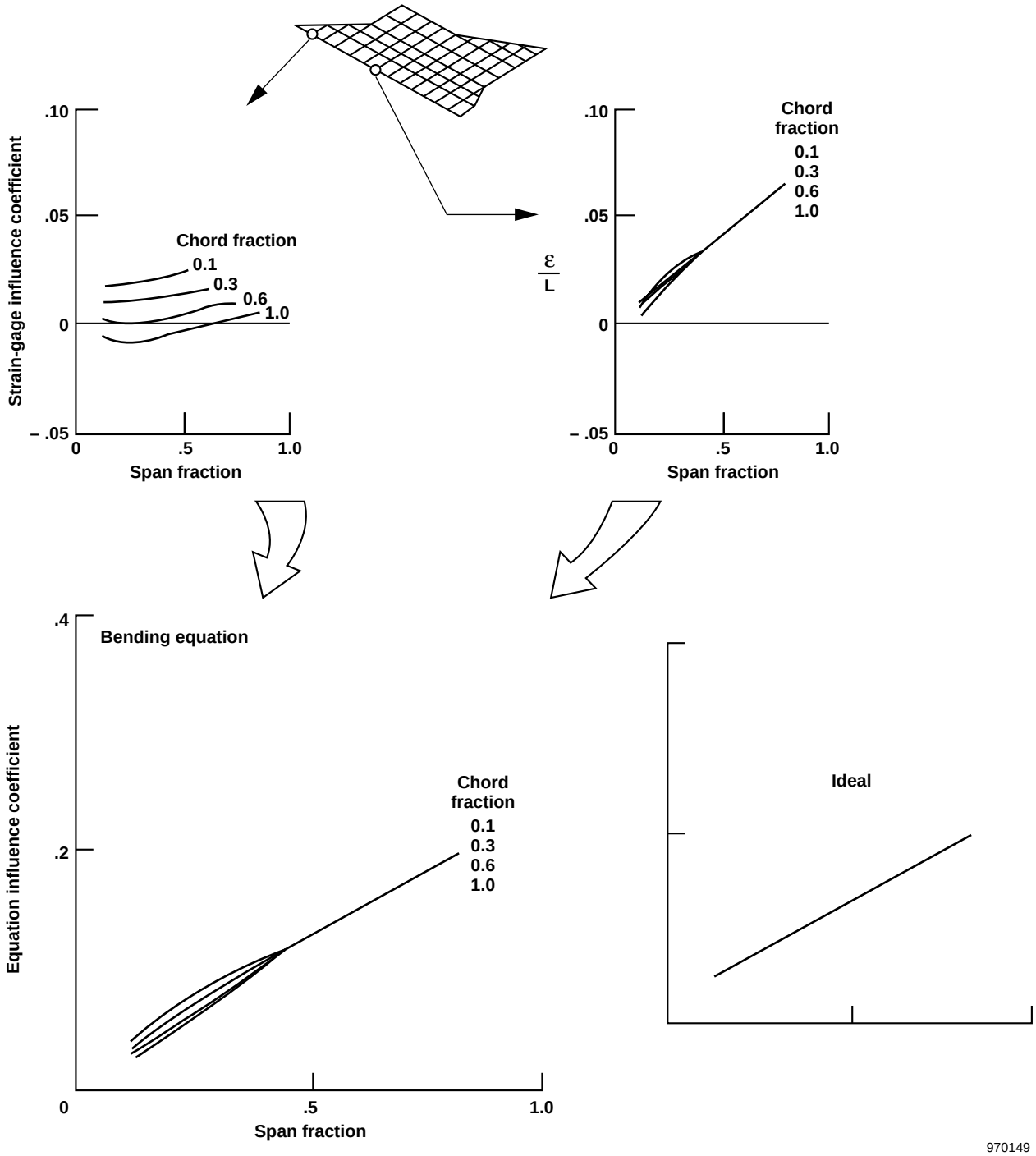

Figure 55. Properties of a bending equation as derived from constituents and compared to an ideal case for the YF-12A wing.[11]

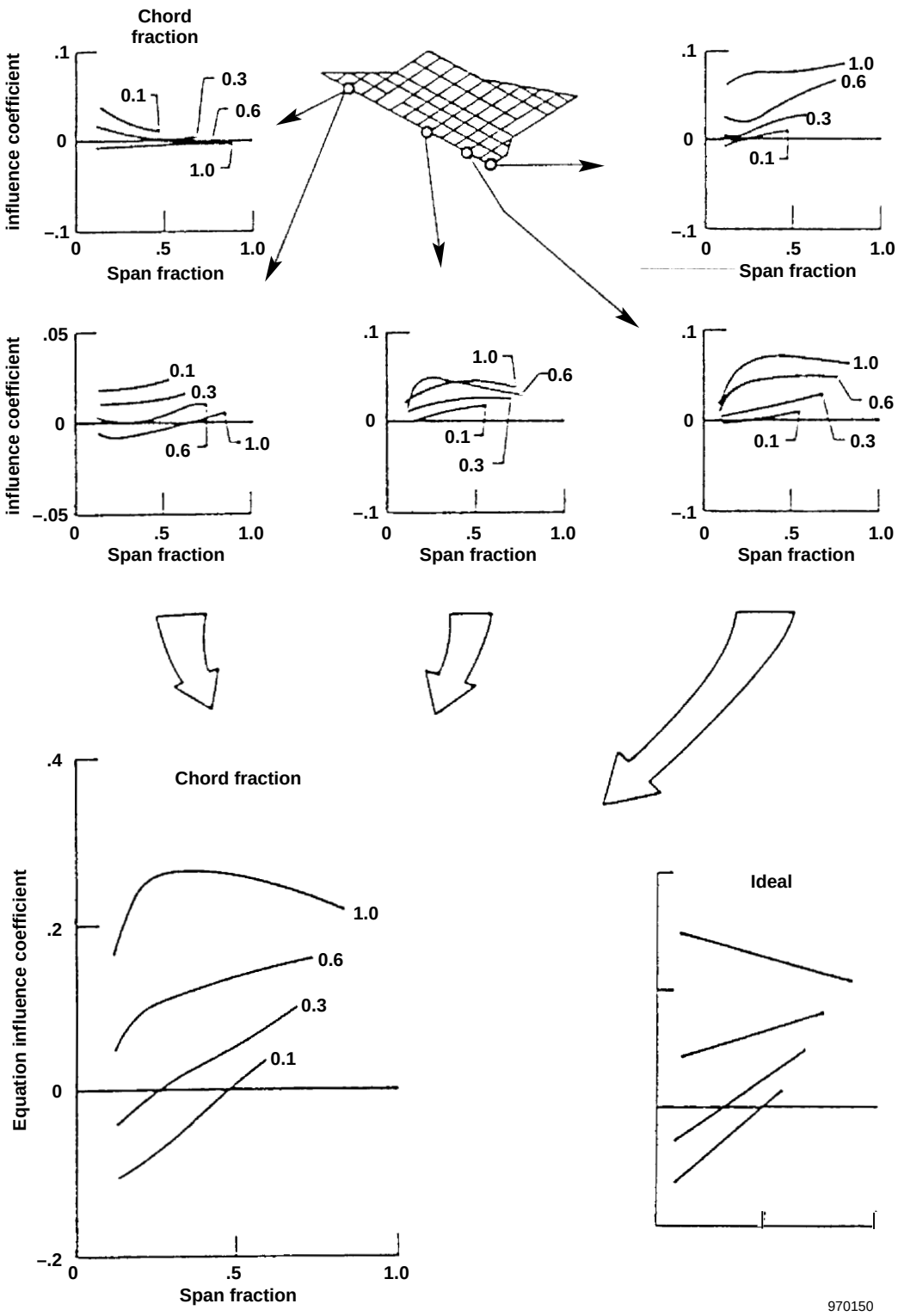

Figure 56. Properties of a torsion equation as derived from constituents and compared to an ideal case for the YF-12A wing.[11]

One of the primary reasons that the YF-12 loads program was so valuable is that finite-element models of the structure were developed to research the science of load measurement with strain gages. The simplified model (see appendix C) of the wing (fig. 57) is of particular interest because of the insight that can be gained from a relatively inexpensive and simple model. The individual calibration loads typically shown at the bottom right of figure 57 were applied to both the model and the airplane in a laboratory; therefore, both measured and calculated influence-coefficient plots are available for comparison. Direct strains can also be compared (figs. 58 and 59). Shear strains (fig. 58) from the model are compared to shear strains measured for the same single-point loading conditions in the laboratory. Figure 59 shows similar comparisons for bending strain. The overall comparison indicates promise in terms of being able to predict strain from computer models. The strain gages on the YF-12 wing were wired in four-active-arm bridges, and the methodology used to convert this information to discrete strains is given in appendix B.

Figures 60 and 61 show a comparison of measured and calculated influence-coefficient plots for several strain-gage bridges located at several points along the root of the wing. Considering the simplicity of the model, the comparison of calculated with measured influence-coefficient plots is amazingly good. This good comparison is attributed to the care with which the structural mechanics were input to formulate the elements of the NASTRAN model. The careful detail of the modeling is considered to be so important that appendix D has been included to explain how the structure was idealized. The comparison shown in figures 60 and 61 illustrates that the finite-element model can be effectively used to predict the nature of influence-coefficient plots for applied load points. The calculated values at the top right of figure 61 were somewhat larger than the measured values at the top left.

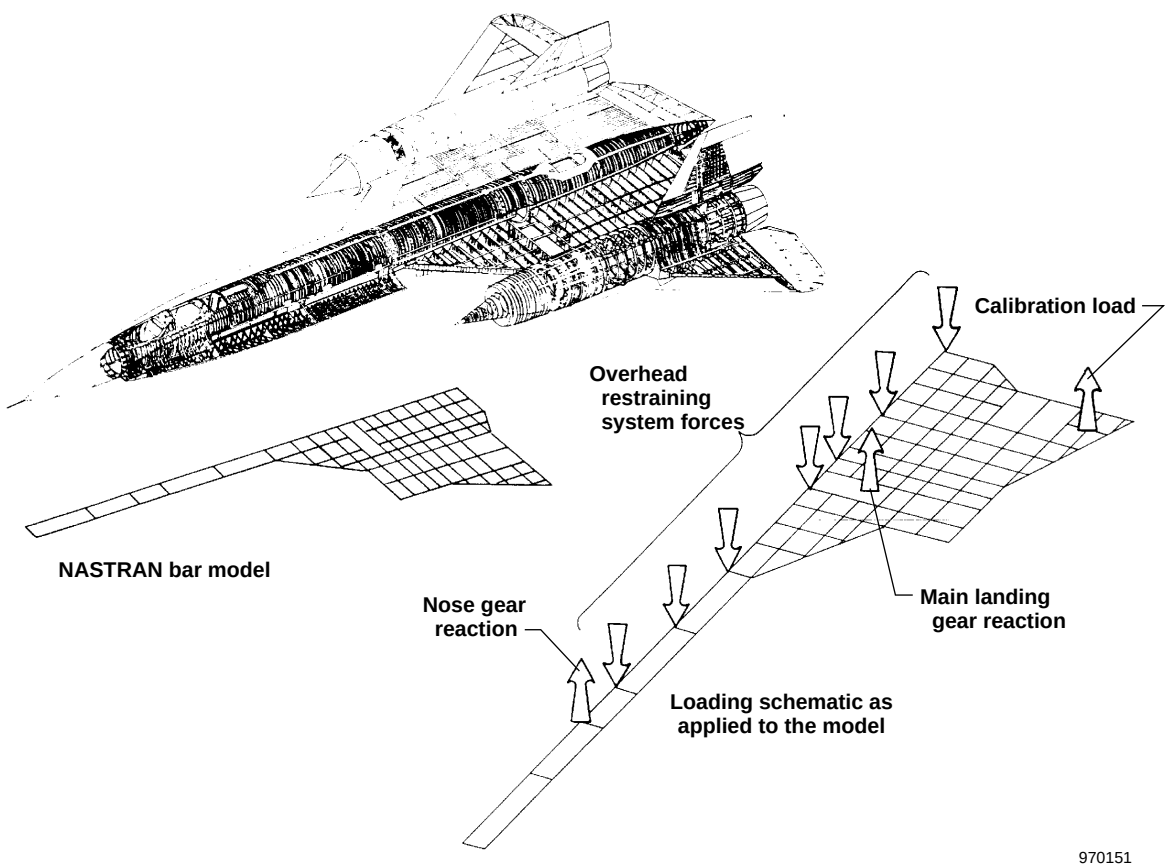

Figure 57. YF-12A structural skeleton with the model representation and a typical load calibration condition.

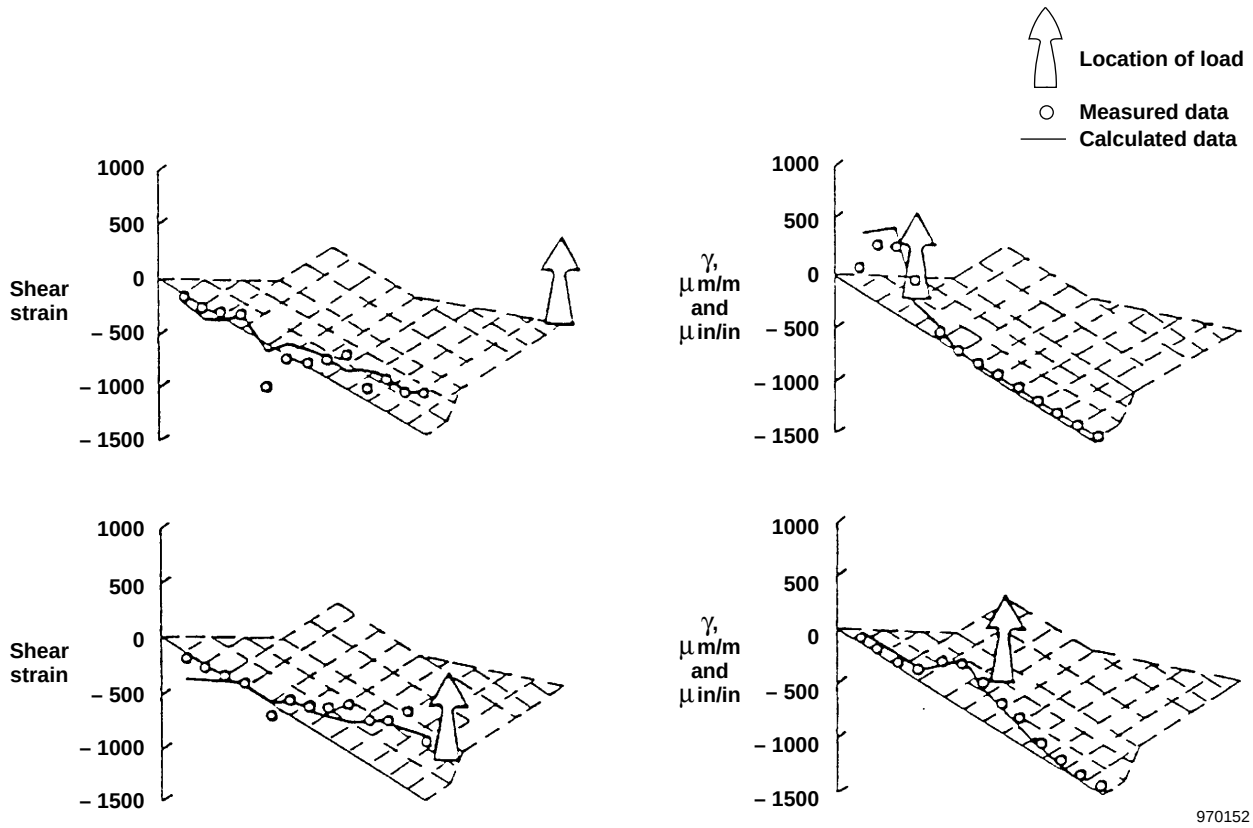

Figure 58. Comparison of measured and calculated shear strain response along the YF-12A wing root.[10]

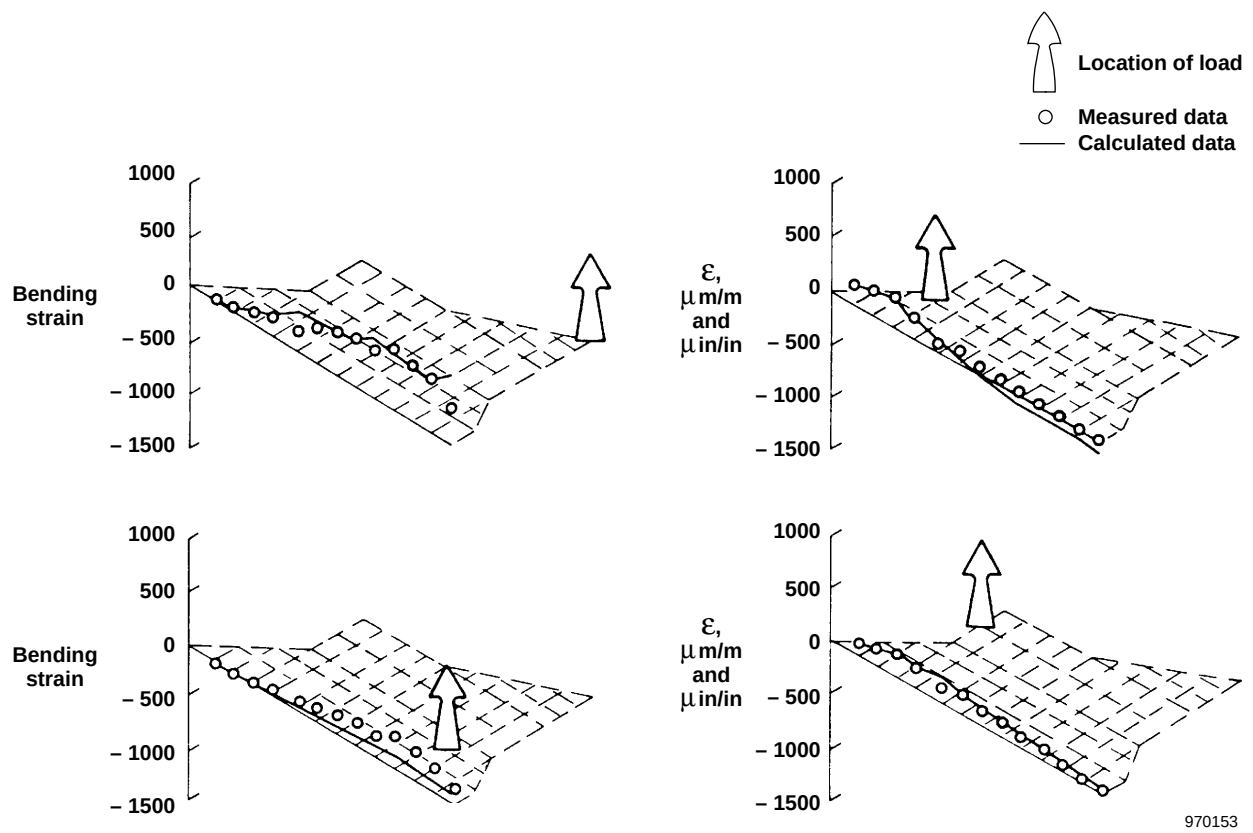

Figure 59. Comparison of measured and calculated bending strain response along the YF-12A wing root.[10]

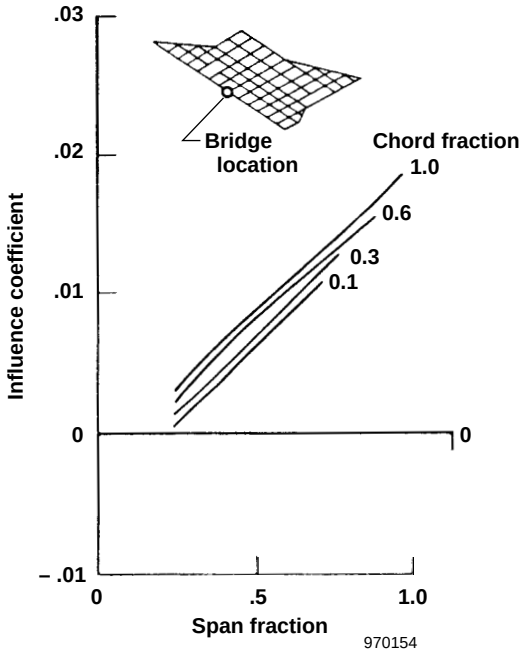

Figure 60(a).

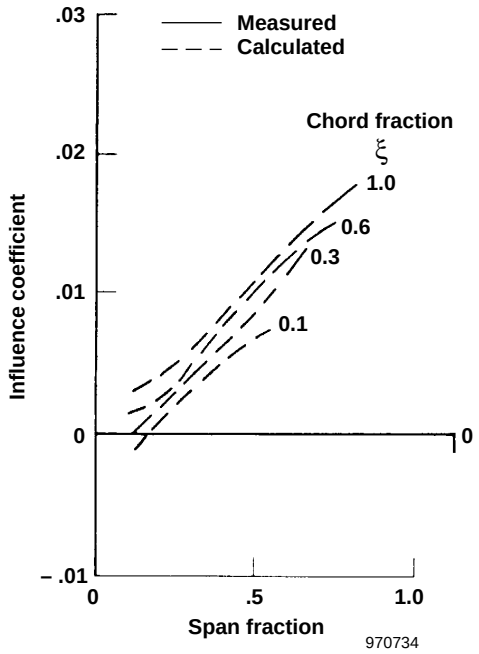

Figure 60(b).

Figure 60. Comparison of measured and calculated influence-coefficient plots for a bending strain-gage bridge for the YF-12A wing.[10]

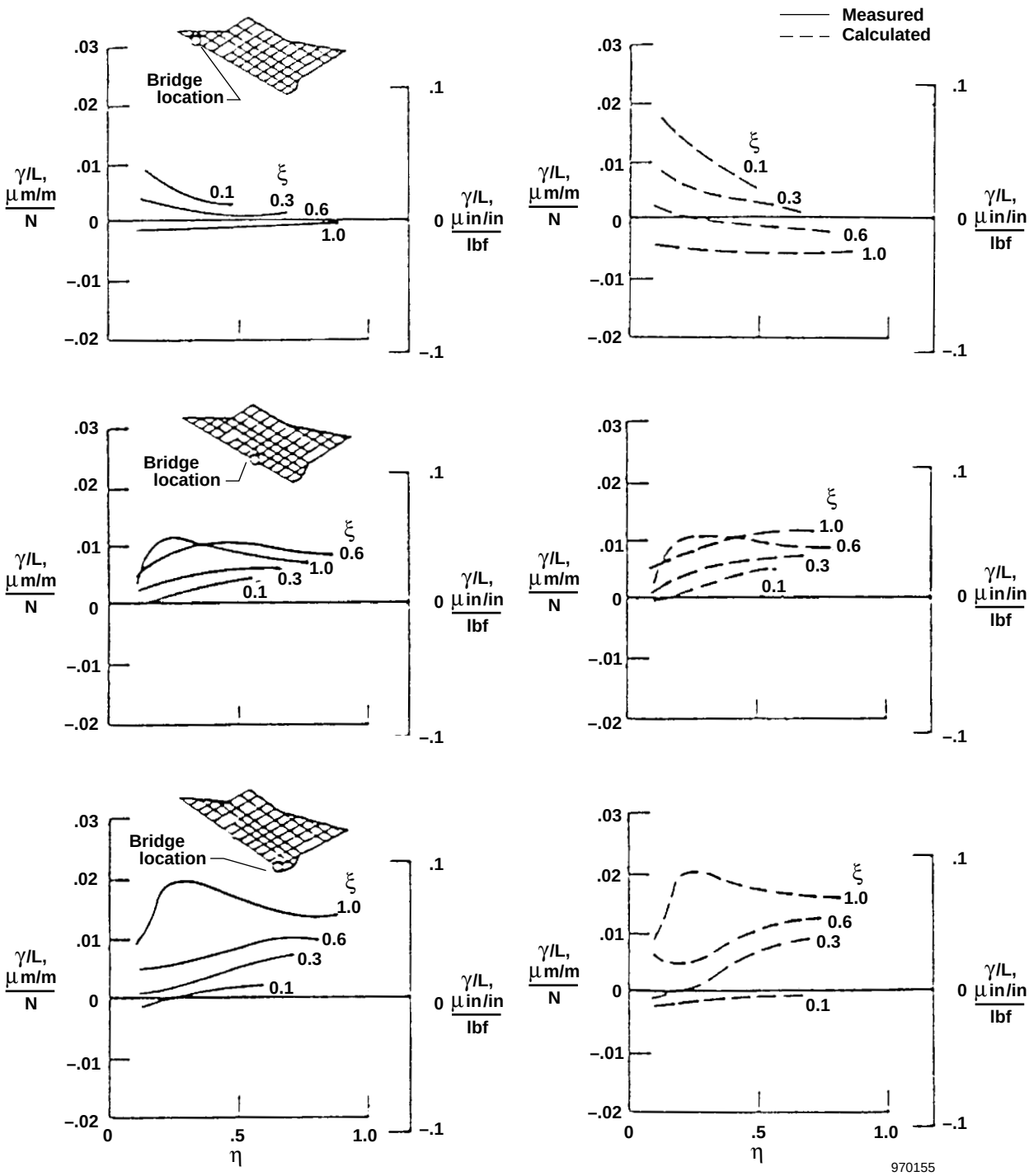

Figure 61. Comparison of measured and calculated influence-coefficient plots for shear strain-gage bridges on the YF-12A wing.[10]

The YF-12 wing was calibrated using 33 load points. Because the calibration was very extensive, the relevancy coefficient is a relatively large number:

$$C_R = 0.70$$

Figure 62 shows the distribution of calibration load jacks. Any apparent discrepancy in the number of load points is caused by the fact that some of the loading conditions involved two jacks applying the load in close proximity. The aggregate of the two jacks can be considered a single load point for some purposes (such as the derivation of equations and influence-coefficient plots) but can be considered two loadings for other purposes (such as summarizing the extent of the surface load distributions).

Highly Maneuverable Aircraft Technology Wing

Appendix A shows a plan view of the Highly Maneuverable Aircraft Technology (HiMAT) aircraft. Figure 1(j) shows the HiMAT wing in more detail and where the calibrated load points are located along with the strain-gage bridges. The wing is of a moderate aspect ratio with two main spars. Seventeen load points were used to calibrate the strain-gage bridges on the HiMAT wing. This wing is unique in that the skin is a composite with reinforcing layups tailored to the purpose of the wing. The sketch on the left side of figure 63 shows the principal direction of the ply lay-ups. When anisotropy is introduced to a wing, conventional influence-coefficient plots normally used to aid in bridge selection may not be valid. The validity depends on the degree and nature of the anisotropy. Appendix E gives a presentation of the physics of anisotropy with regard to the interpretation of influence coefficients with respect to strain-gage load calibrations.

The anisotropy associated with the skin does not appear to be significant enough to have a major effect on the traditional appearance of the influence-coefficient plot for the bending-moment bridge, B2. The plot shows a bending response that is characteristically the same as for other bending-moment plots (fig. 63). The only distinguishing difference is a larger-than-usual torsional spread. No clear reason exists to believe that this torsional spread is caused by the anisotropy.

The influence-coefficient plots shown in figure 64 exhibit characteristics that could be affected by the anisotropic skins. In the traditional sense, the plots do not appear to be favorable, particularly for sensing shear. The overall outputs are very low. Strain-gage bridges S1 and S2 both change sign in the span direction. This effect could be interpreted as not a traditionally favorable response. The basic difference between elasticity and anisotropic elasticity is addressed in some detail in appendix E, where the basic anisotropic equations are presented.

The 17 load points used to calibrate the HiMAT wing resulted in the following relevancy coefficient:

$$C_R = 0.51$$

Figure 65 shows the distribution of the calibration load points in terms of span and chord. Additional information regarding the HiMAT wing and the general program has previously been given.[12–14]

Supercritical Wing

Appendix A shows a three-view sketch of an F-8 aircraft modified to fly with a supercritical wing. Figure 1(k) shows where the calibration load points are located on the wing along with the strain-gage bridges. The supercritical wing is a high-aspect-ratio, high-degree-of-sweep wing with trailing-edge high-lift devices. Twenty-eight load points were used (fig. 66) to calibrate this wing panel. Figure 1(k) shows the general location of the strain-gage bridges. The information relating to the supercritical wing load calibration has been developed from unpublished, undocumented files and notebooks of Aerostructures Branch personnel at NASA Dryden. Some information regarding the program has been published.[15, 16] The strain-gage bridges are located on or about the three primary spars. This wing structure has the highest aspect ratio of any lifting surface included in this report.

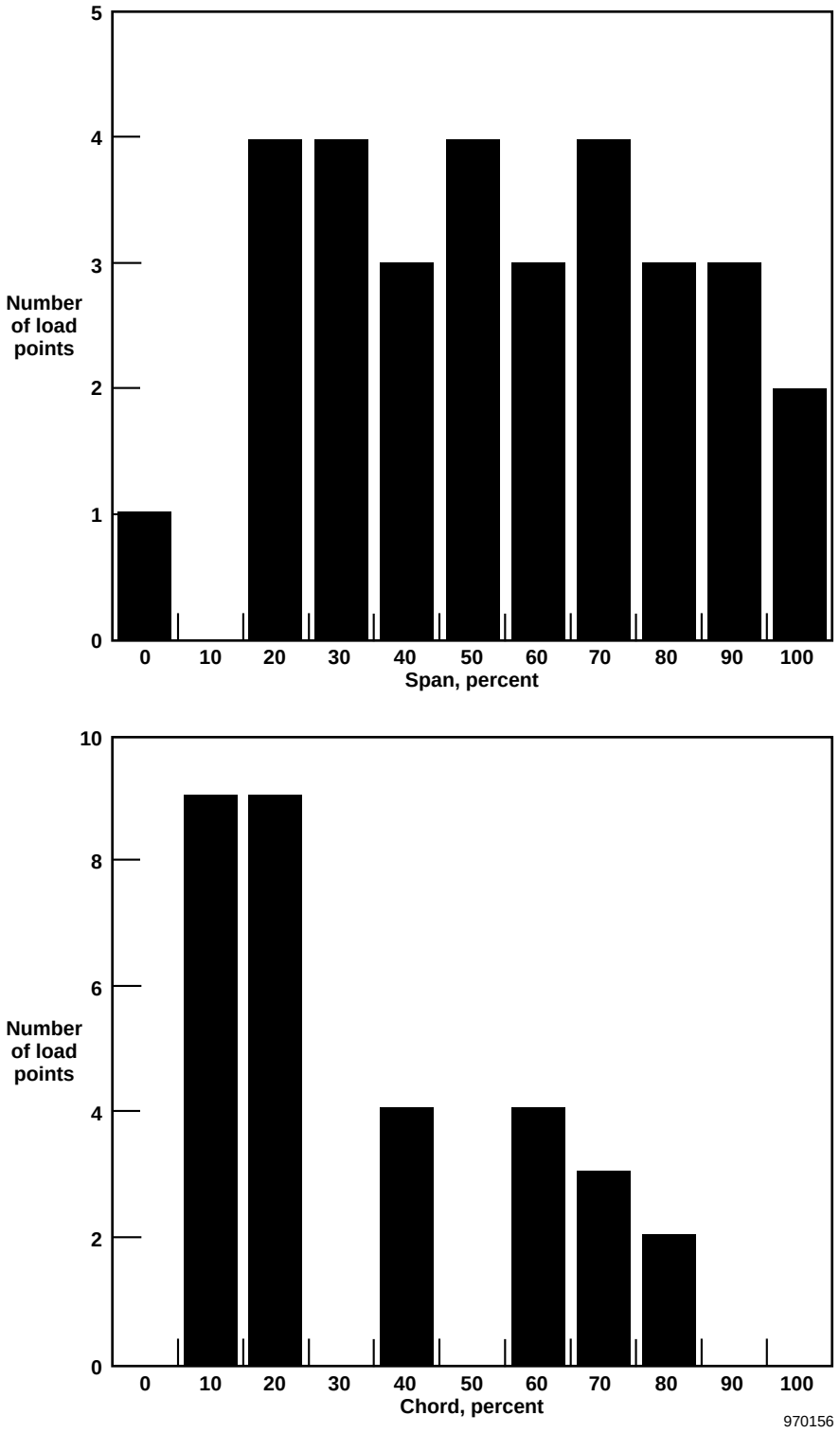

Figure 62. Span and chord distribution of calibration load points on the YF-12A wing.

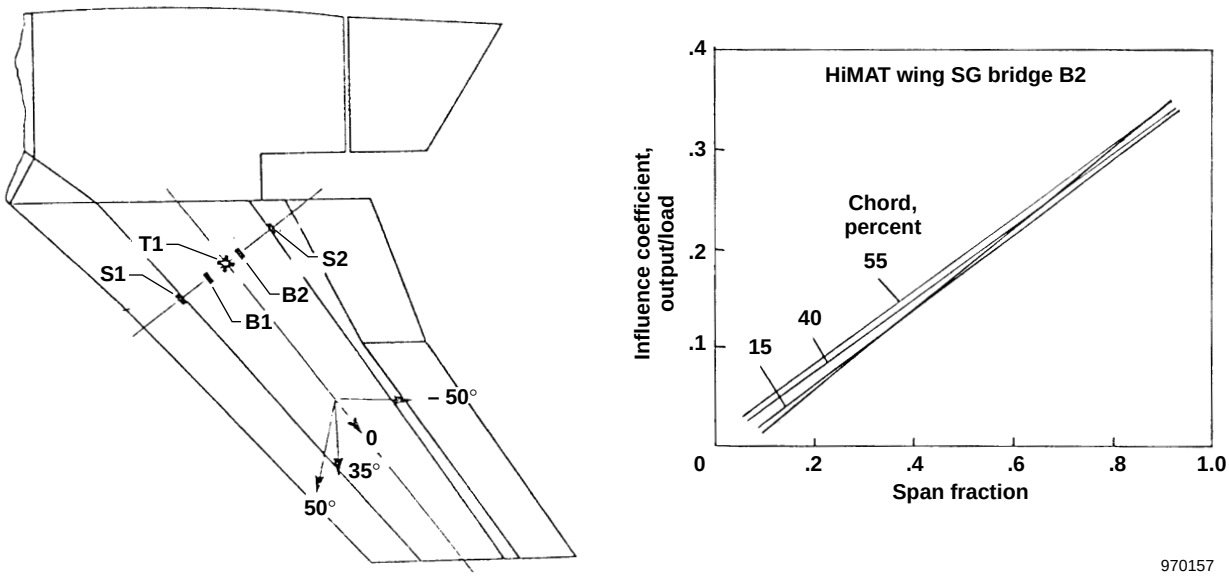

Figure 63. Influence-coefficient plot for a bending strain-gage bridge on the HiMAT aircraft wing.

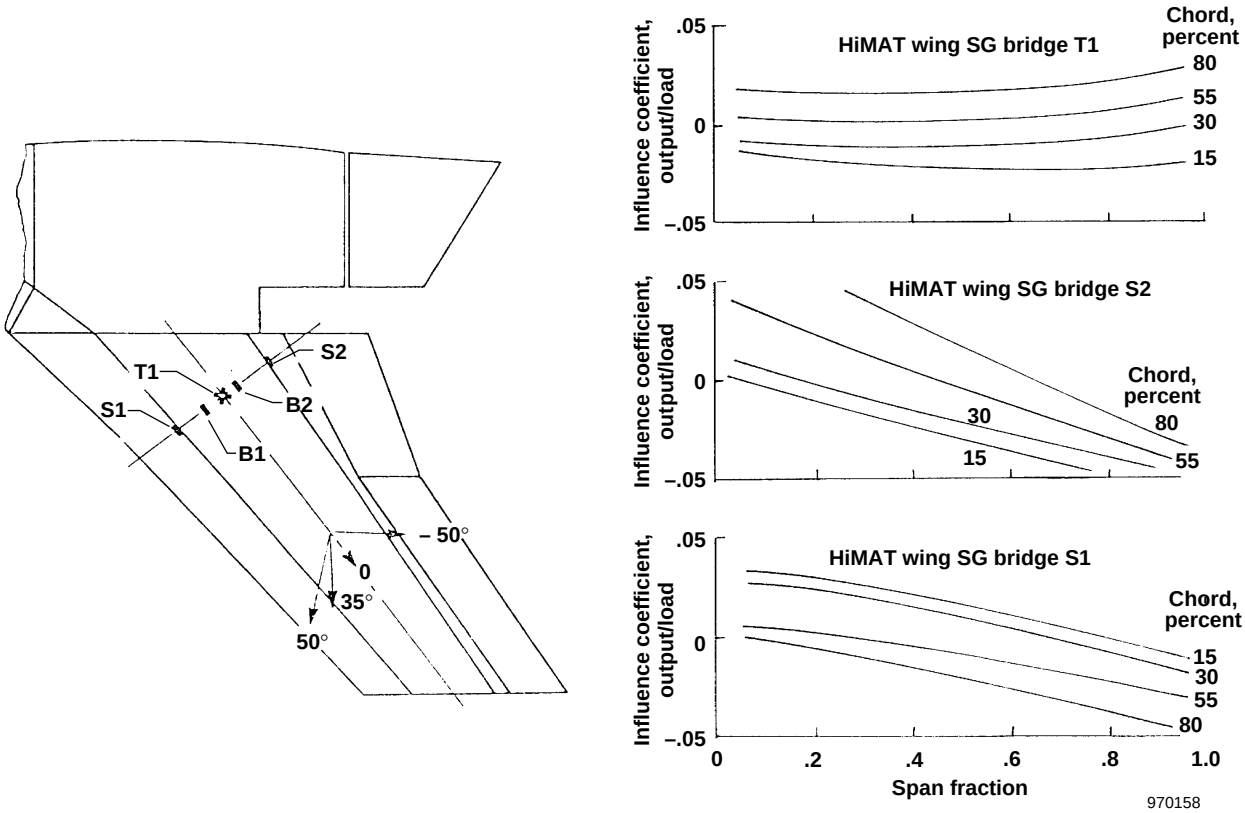

Figure 64. Influence-coefficient plots for strain-gage bridges configured for sensing shear on the HiMAT aircraft wing.

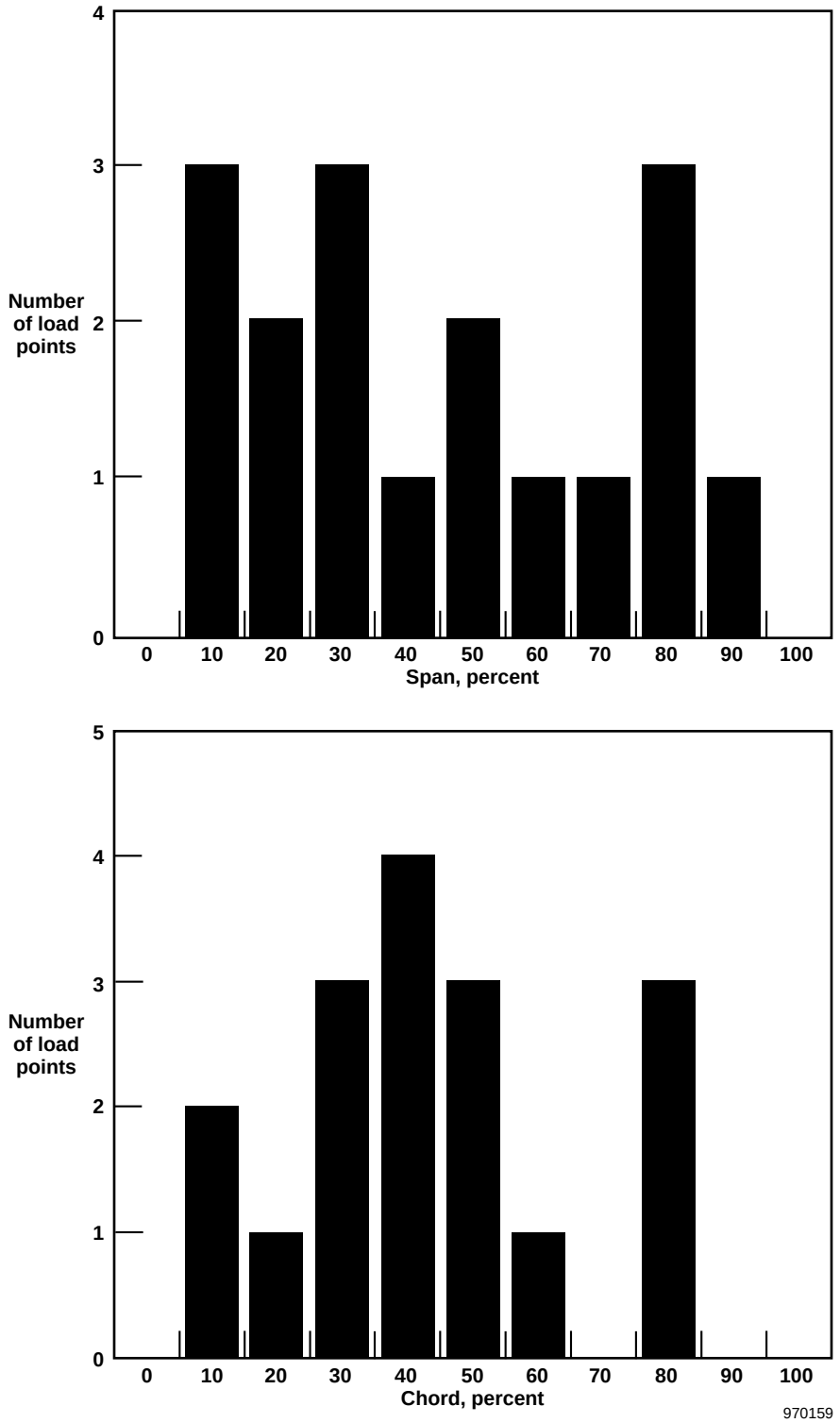

Figure 65. Distribution of load points in the span and chord directions for the HiMAT wing.

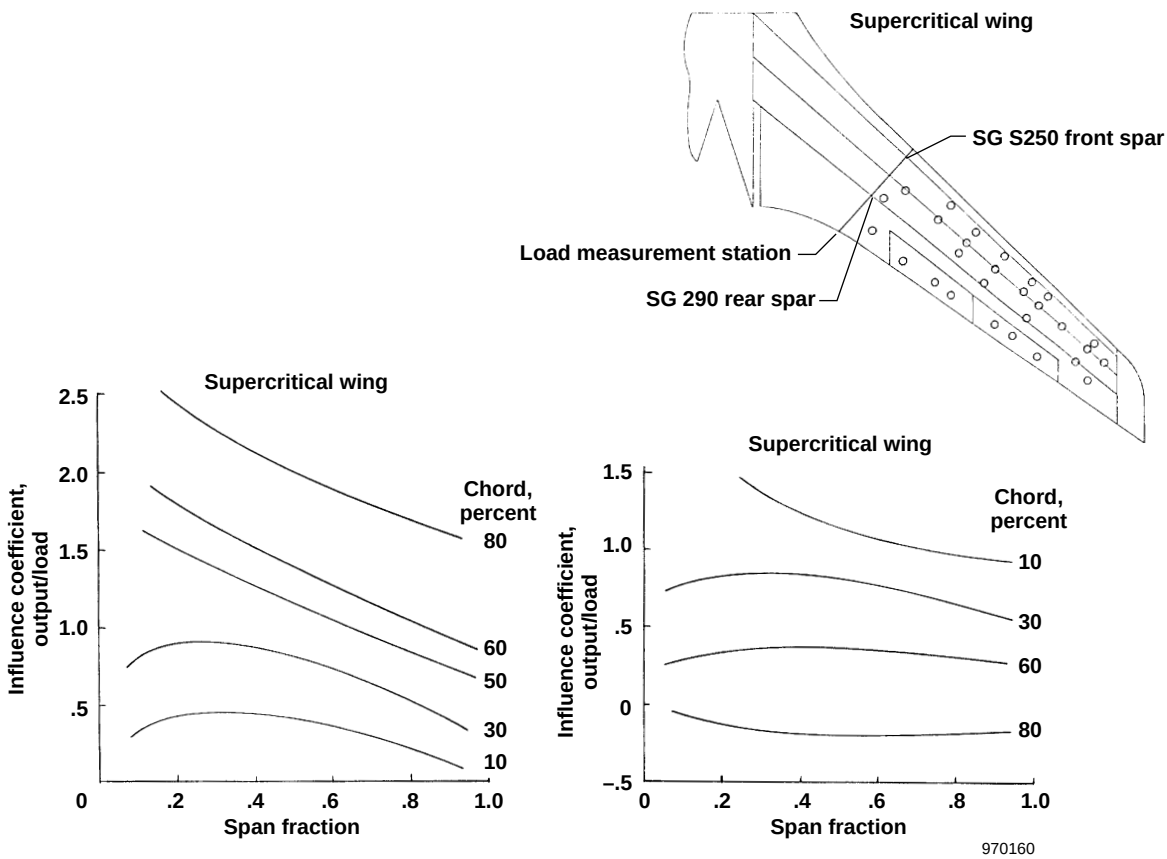

Figure 66. Typical influence-coefficient plots for two shear bridges on the Supercritical wing.

Figure 66 shows the influence-coefficient plots for two shear bridges. One bridge is located on the front spar, and the other is located on the rear spar. Neither bridge shows any characteristics that would make it suitable to directly sense any of the major loads without combination with other bridges in an equation. Both bridges are torsion sensitive. Strain-gage bridge 290 also shows a sensitivity to span location. Figure 67 shows influence-coefficient plots for several other strain-gage bridges. A bending bridge is shown in the lower left corner with a very favorable bending response. A shear-configured strain-gage bridge that is sensitive to torsion is shown in the upper right corner. The bridge has a relatively low response that detracts from its usefulness. The lower right plot (fig. 67) exhibits very unique characteristics that require a degree of speculation to explain. As the location of load moves from root to span on a wing or tail structure, the output normally remains constant or increases. The exception might be a torsion-sensing strain-gage bridge that may have certain chord lines that decrease in magnitude. What is seen on the strain-gage bridge numbered SG S270 (fig. 67) appears to be an exception. A root effect exists inboard of the 0.2 span fraction (20 percent); however, little torsion effect exists outboard from that fraction. The downward slope could be attributed to load path changes as the load gets farther away from the strain-gage bridge location. In this case, the load may be transferring to the front and rear spars as the load is moved toward the wing tip.

The supercritical wing was calibrated with 28 load points. The large number of load points resulted in a relevancy coefficient calculated to be:

$$C_R = 0.75$$

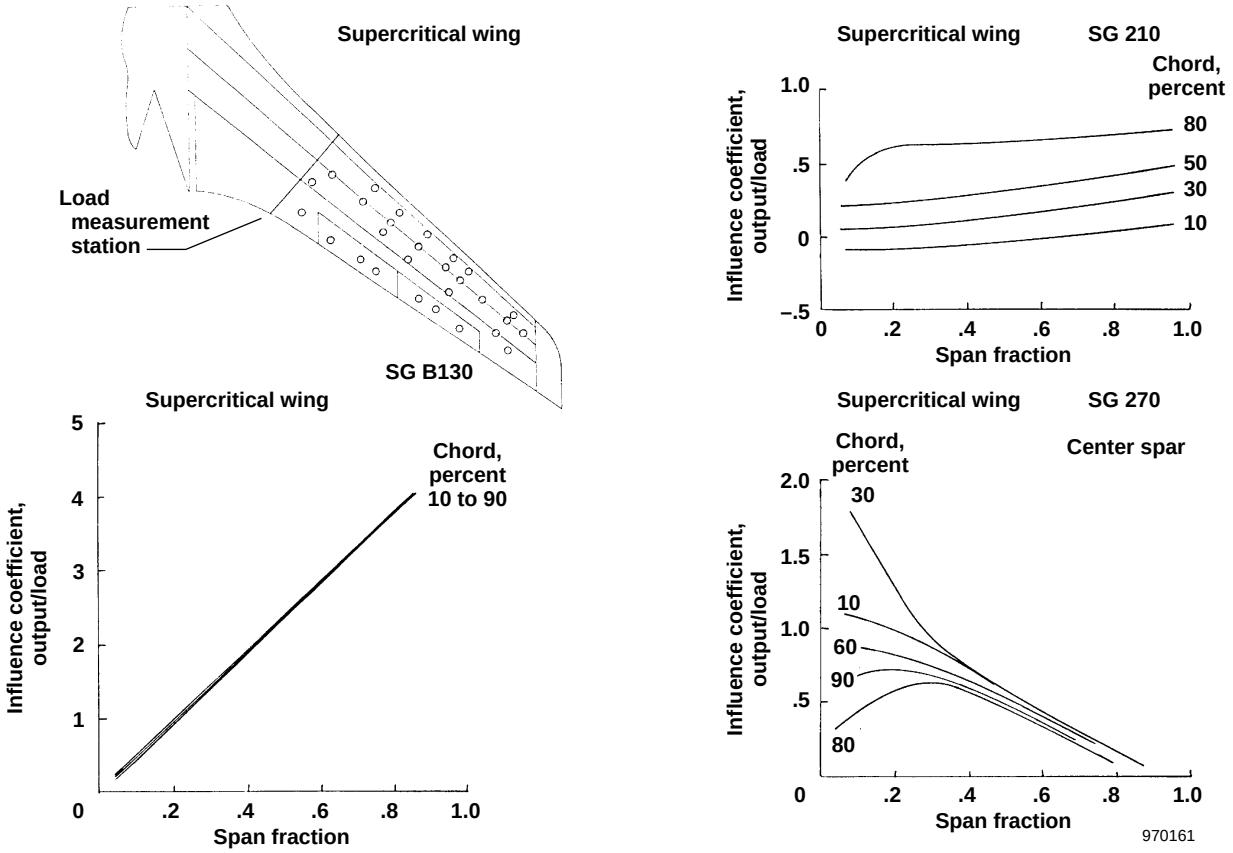

Figure 67. Influence-coefficient plots for several strain-gage bridges on the Supercritical wing.

Figure 68 shows the distribution of calibration load points in terms of span and chord for the calibration of the supercritical wing.

F-111 Transonic Aircraft Technology Wing

An F-111A aircraft was retrofitted with a research wing called the F-111 Transonic Aircraft Technology (TACT) Wing. Appendix A shows the difference between the planform of the regulation F-111A wing and the research wing. The TACT wing has a shorter wing span and a larger chord that results in a lower aspect ratio than the regulation wing. Figure 1(l) shows the location of strain-gage bridges and the calibration load points. The wing has a variable-sweep feature with a moderate-aspect-ratio planform. The wing is constructed with six spars with five cells and has very complete instrumentation. Thirteen load points were used to calibrate the strain gages. The data generated from the calibration of the F-111 TACT Wing were obtained from personal files of Aerostructures Branch personnel at NASA Dryden. Other information has also been published.[17, 18]

The calibration of this wing warrants being included in this report because of the numerous spars and the very complete instrumentation in the wing. Figure 69 shows influence-coefficient plots for six shear-oriented strain-gage bridges. One bridge is shown for each of the six spars, and the strain gages are located on the webs. The influence-coefficient plots are shown starting at the top left with strain-gage bridge 112 on the front spar and ending at the bottom left with strain-gage bridge 120 on the rear spar. At approximately the second auxiliary spar (strain-gage bridge 116), the chord lines tend to converge, which means that the shear center (for example, the axis along which a transverse force can be applied with no resulting torsion[19]) is near this location. Note that the bridges on the front spars of this wing have a torsional response with the 80-percent chord line at the top of the plot, and the bridges near the rear have a response with the 80-percent chord line near the bottom of the plot.

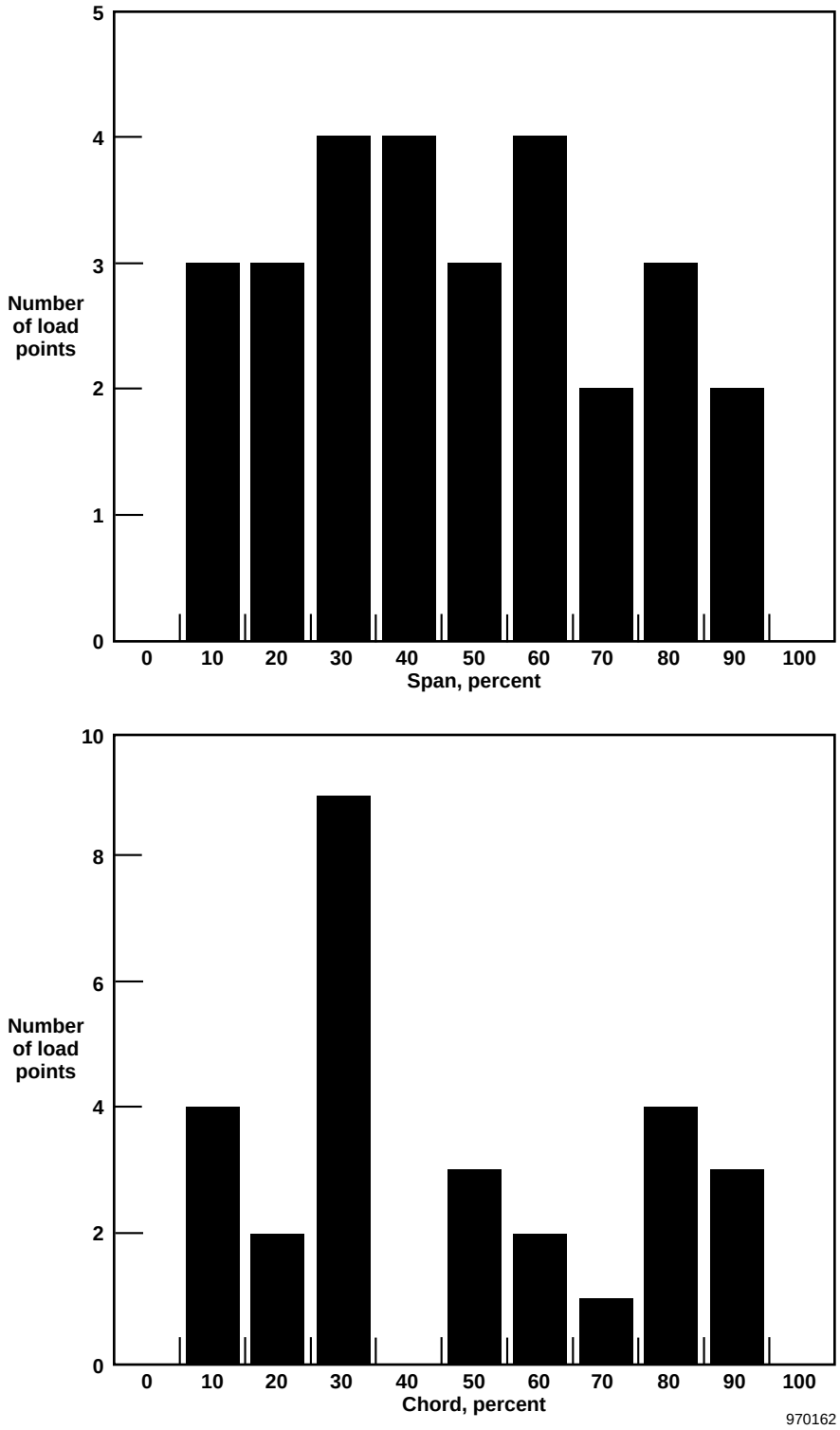

Figure 68. Distribution of load points in the span and chord directions for the Supercritical wing.

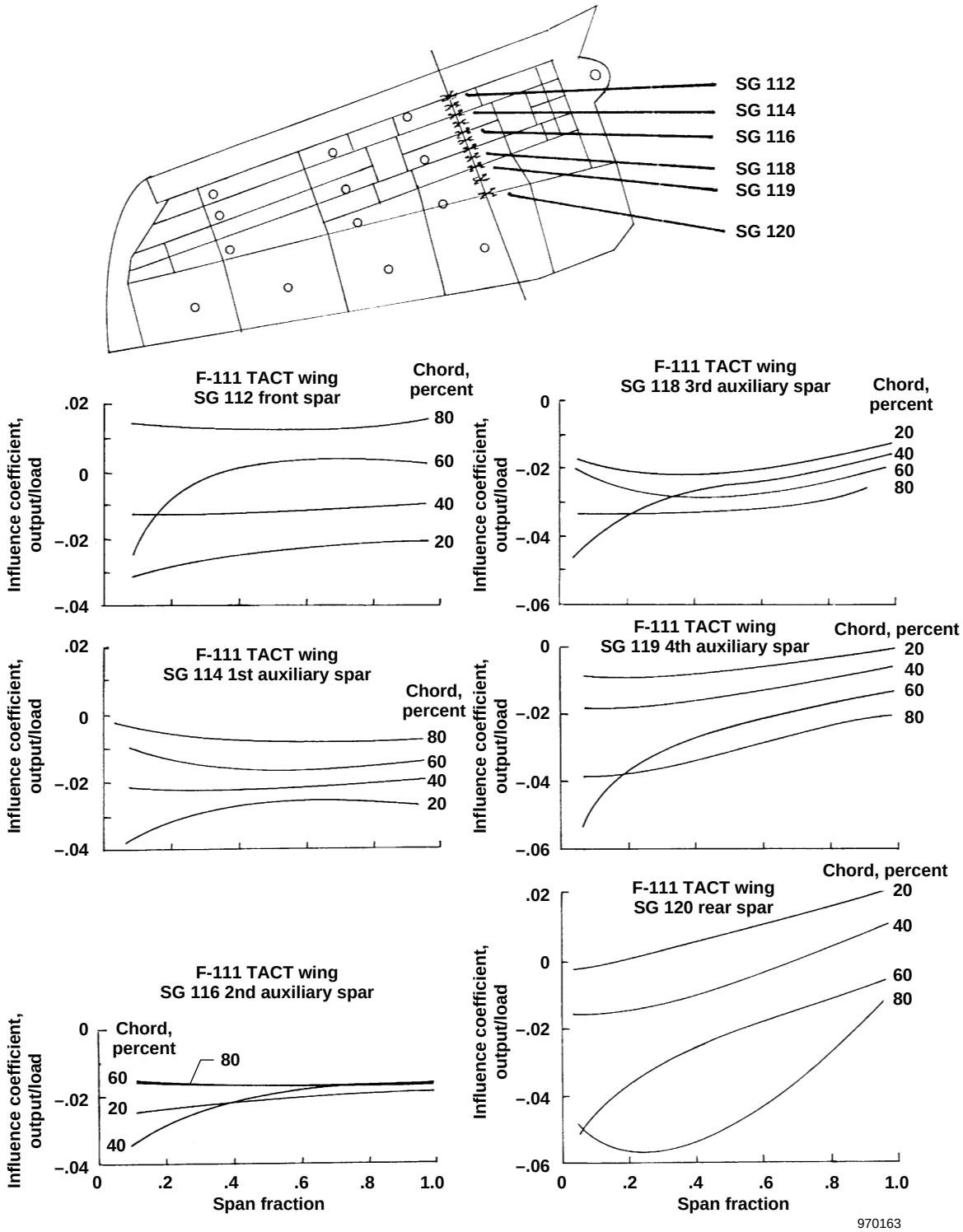

Figure 69. Typical shear strain-gage bridge influence-coefficient plots for the F-111 TACT wing.

It is obvious that if a strain-gage bridge with a pure shear response is sought, then a likely place to locate shear bridges is near the shear center. The influence-coefficient plot for strain-gage bridge 116 exemplifies a very good shear bridge. Locating shear bridges on spars near the shear center is probably a good rule to use on moderate- and high-aspect-ratio lifting-surface structures. Low-aspect-ratio lifting-surface structures are less likely to exhibit such a trait.

Figure 70 shows the influence-coefficient plots for two bridges located on the skin between spars. These bridges are configured and located to sense torsional loads. These two influence-coefficient plots are presented to illustrate the response of strain-gage bridges located on the skin of the structures. The strain-gage bridge responses for the influence-coefficient plots shown in figure 71 are typically bending in nature. Strain-gage bridge 102 is located on the spar caps near the shear center. The bridge appears to sense bending without contamination from shear or torsion. The influence-coefficient plot for strain-gage bridge 106 shows the bridge to be somewhat contaminated with torsion, particularly for the load points on the control surfaces. This strain-gage bridge is located considerably aft of the shear center.

The F-111 TACT Wing was calibrated with 13 load points that resulted in a relevancy coefficient of:

$$C_R = 0.50$$

Figure 72 shows the distribution of the calibration load points in terms of spar and chord location.

B-2 Wing

Most of the specific details of the calibration of the B-2 wing remain obscure because of classification considerations. Enough information is available, however, to extract some valuable information relative to the science of calibrated strain gages and to current characteristics of airplane load calibrations.

Appendix A shows a plan view of the B-2 aircraft. Figure 1(m) shows the B-2 wing in more detail and where the calibration load points are located along with the strain-gage bridges. The wing is extensively instrumented with strain gages. The structural arrangement is very complex, with spars and ribs intersecting obliquely. The load points are not widely distributed over the surface of the wing. Further, the loads were not applied individually as suggested[1] but were applied as a relatively small number of distributed loads with many individual jacks used simultaneously.

Figure 73 shows the distribution of jack points. A major portion of the wing obviously has no applied loads. Because of the nature of the outer surface of the wing, structure loads could only be applied to the forward and the rear parts of the wing surface, which raises several questions about the philosophy of the load calibration. If a major part of the surface of the wing cannot be loaded, then how can flight loads in that area be interpreted? In addition, a discrete load calibration was not conducted; a distributed load calibration was used instead. The basic philosophy behind the two contrasting approaches (discrete rather than distributed) to calibrating has really not been discussed. The method of calibration (calibration methods will be addressed in the Discussion section) is not as important as the significance of the large unloaded area that would similarly affect either load calibration approach. The casual observer would question the validity of a load calibration that has such a large portion of the problem missing.

Although the data cannot be presented in this report, the load calibration was considered to be satisfactory because the flight measurements correlated well with predicted loads. Figure 74 shows a possible explanation for this correlation. A classic subsonic load distribution[20] is shown at the top of the figure, and the distribution of the applied calibration loads is shown at the bottom of the figure. The primary distribution of this flight load is centered in the forward part of the chord of the wing. The application of calibration loads in the area where the flight loads are dominant provides an explanation of why the load calibration was thought to be valid.

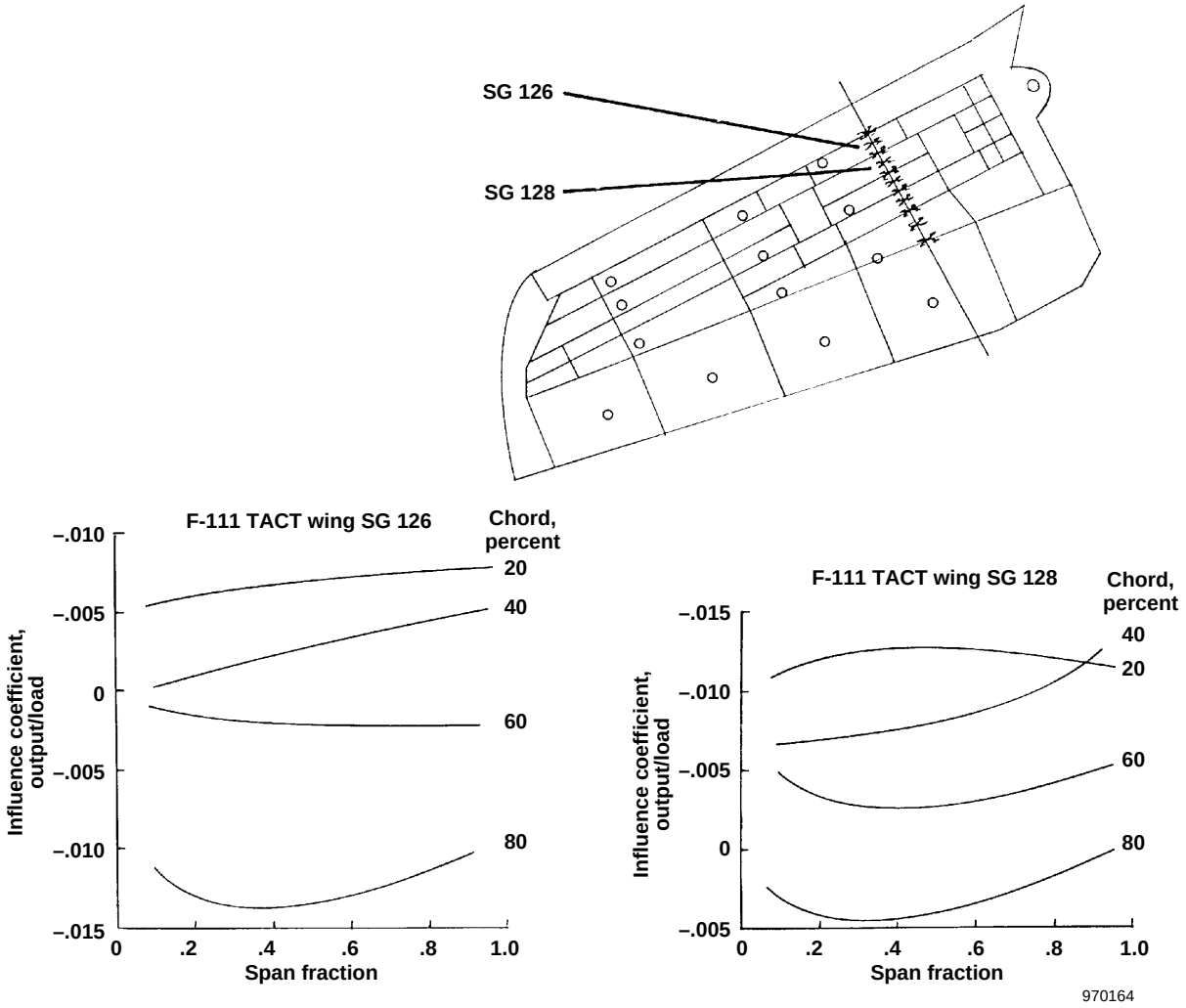

Figure 70. Typical torsional strain-gage bridge influence-coefficient plots for the F-111 TACT wing.

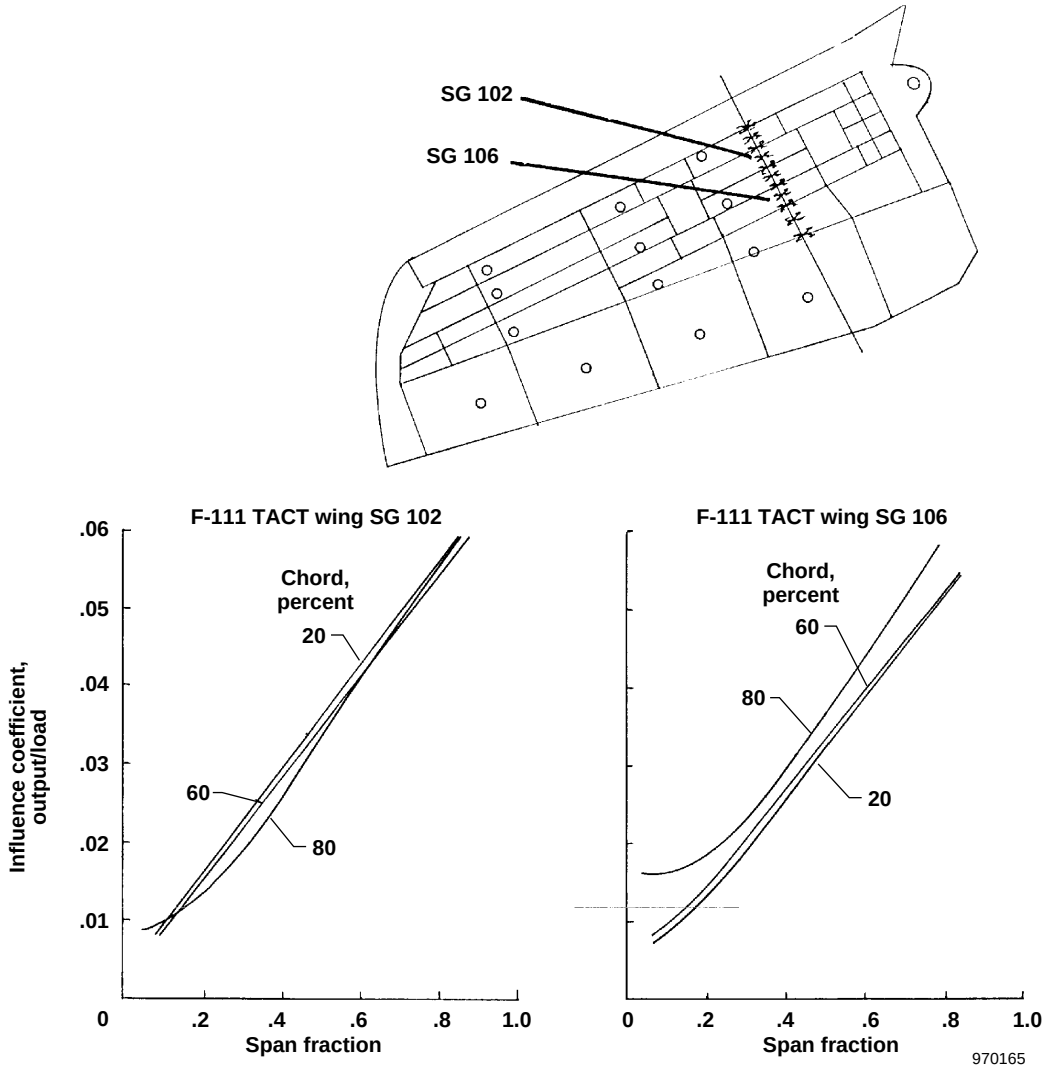

Figure 71. Typical bending strain-gage bridge influence-coefficient plots for the F-111 TACT wing.

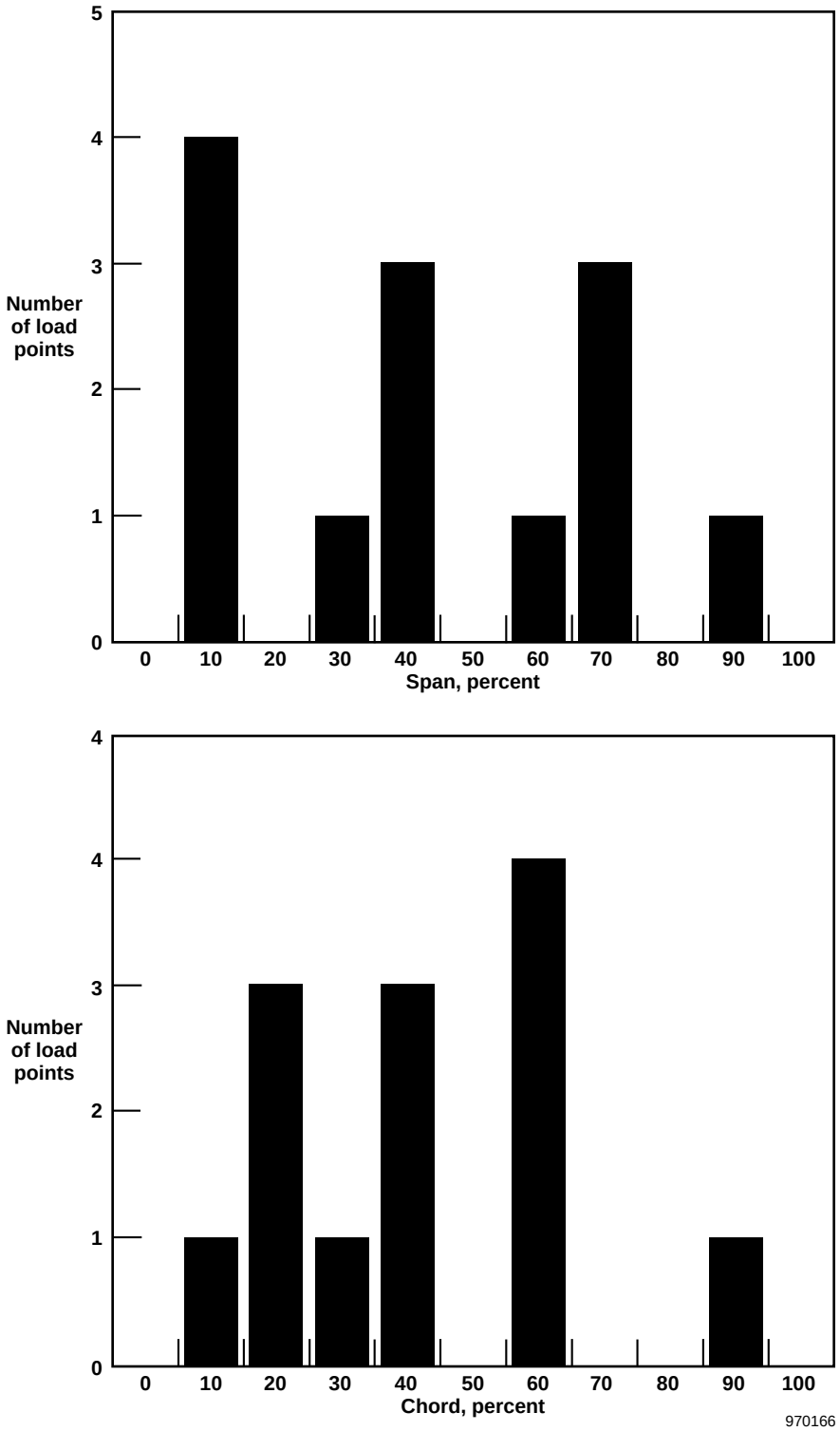

Figure 72. Distribution of load points in the span and chord directions for the F-111 TACT wing.

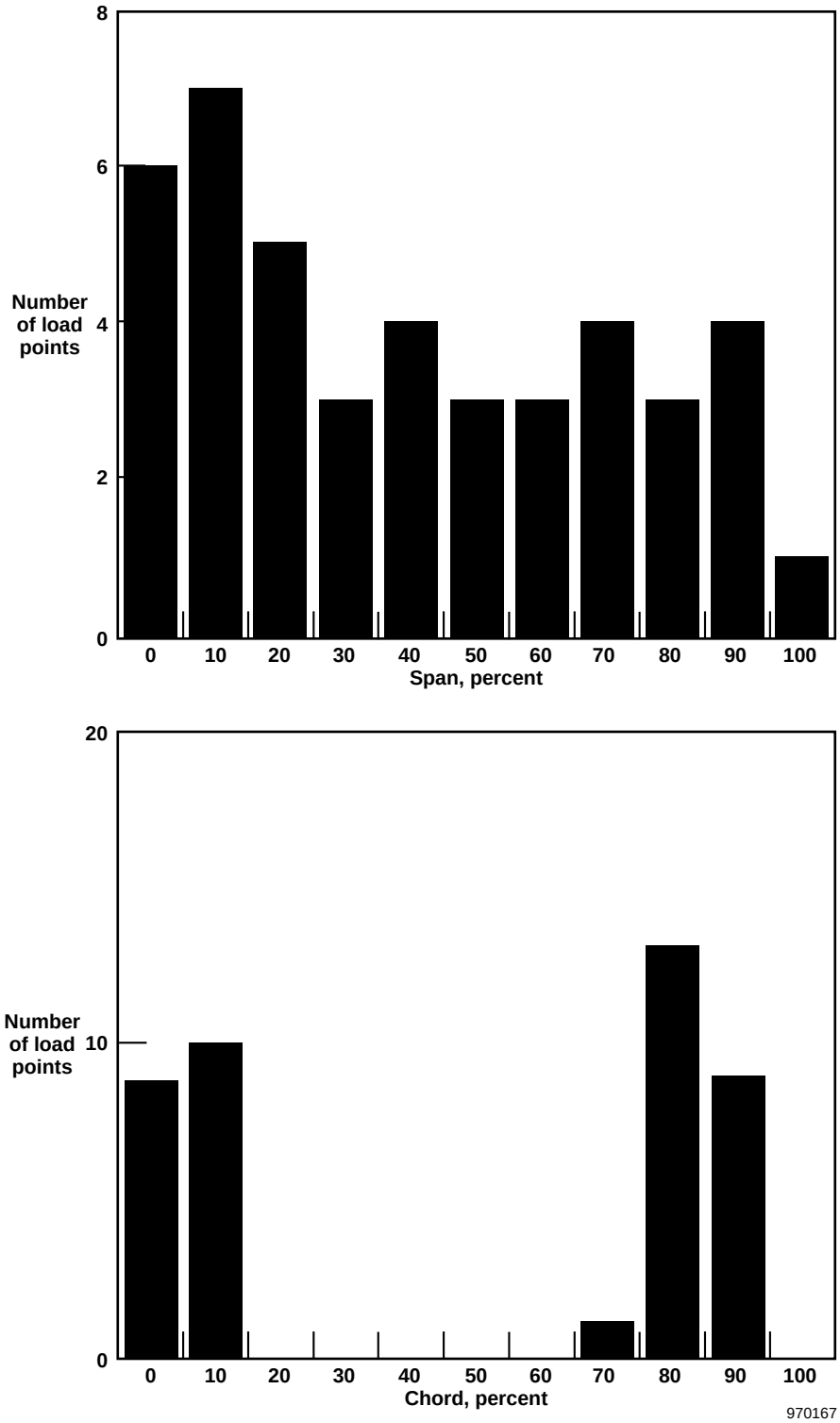

Figure 73. Span and chord distribution of load points on the B-2 wing.

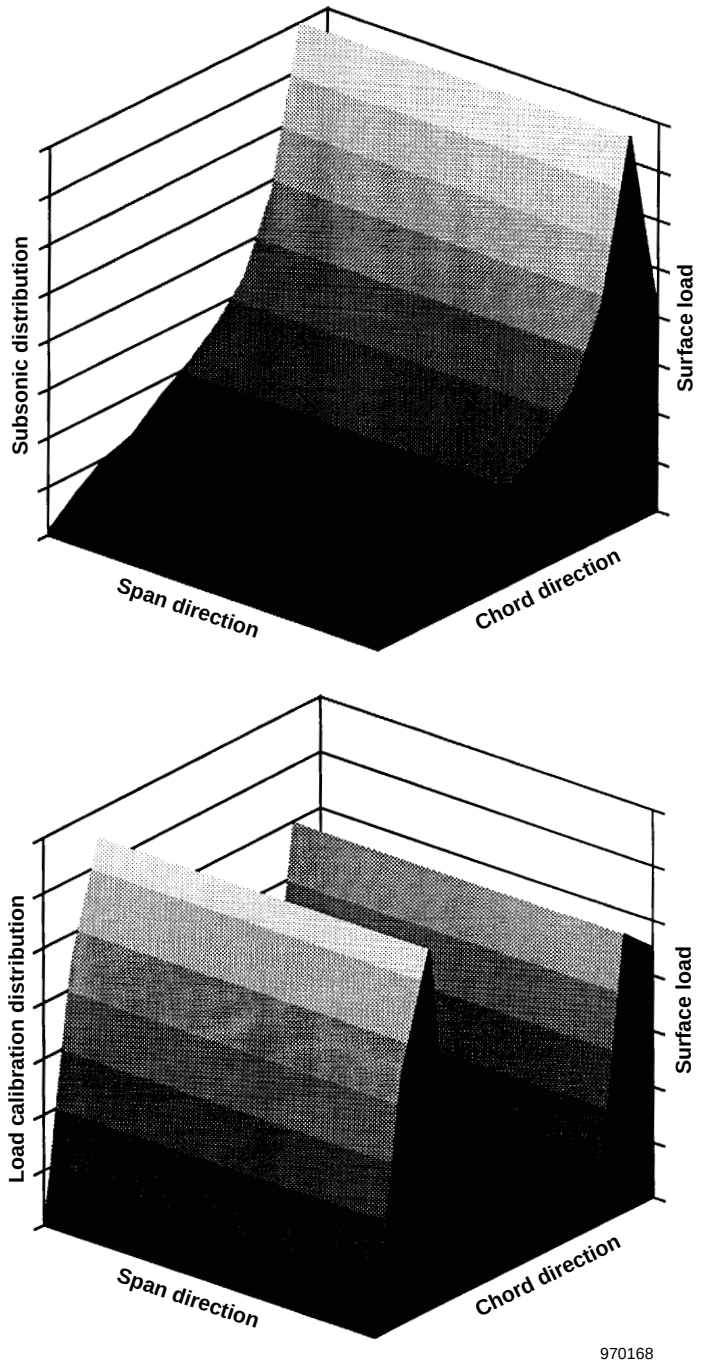

Figure 74. Comparison of a subsonic load distribution with the load calibration loads on the B-2 wing.

A second typical wing load distribution should be considered in evaluating the validity of the basic load calibration. A totally different load distribution occurs when the control surfaces are deflected. This difference is somewhat more difficult to identify in a classic sense; however, the primary result is to add load to the rear of the structure. Figure 74 shows that the spectrum of the load calibration also includes some large calibration loads in the rear of the wing. The two primary load distributions are safely assumed to be covered by the spectrum of loads used for the calibration. The two areas where flight load was concentrated largely corresponded to the two areas where large loads were applied during the load calibration.

The nature of the B-2 wing raises some very provocative thoughts relative to the strain-gage calibrations of future aircraft. If, in the future, large surface areas of wings cannot be physically loaded, then pursuing alternate approaches is logically prudent. Figure 75 shows two such approaches that are pertinent for both the B-2 wing and other aircraft. One approach involves using a finite-element structural model to develop a load calibration analytically. An incomplete loading such as the B-2 wing case could serve as a check load to verify the accuracy of the load equations developed from the analytical model. This idea is depicted in the right side of figure 75, where the square symbols represent analytical load points applied to the finite-element model from which load equations are developed. The accuracy of the analytically established load equations would then be verified by some type of physical loading such as is depicted as a check load by the circular symbols.

A second approach is shown in the left side of figure 75, where a hybrid load calibration is suggested. The idea in this approach is to apply physical loads to the structure where possible and augment these loads with analytical loadings using a finite-element structural model in the areas where load cannot be physically applied. Both of the approaches shown in figure 75 require a level of confidence in the accuracy of an analytical structural model. Structural modeling will be addressed in the Discussion section.

Eleven distributed-load calibration conditions were used to calibrate the structure. The aggregate of all load points resulted in a relevancy coefficient of:

$$C_R = 0.45$$

Figure 73 shows the distribution of these loads.

B-1 Wing

The strain-gage loads calibration of the B-1 wing provides one of the more unique aspects of all structures presented in this document. The strain-gage bridges were calibrated independently at different times using a distributed-load method in one case and a point-load method in another case. Equations were derived for both approaches using the same set of strain-gage bridges. This circumstance provides the opportunity to compare calculated flight loads using equations that have been derived with different calibration methods.

The B-1 wing is a high-aspect-ratio variable-sweep lifting surface with a configuration typical of this family of configurations that began with the F-111 airplane. Appendix A shows a three-view drawing of the B-1 aircraft. Figure 1(n) shows the B-1 wing in more detail and where the calibration load points and strain-gage bridges are located. The structural arrangement is relatively simple for a modern aircraft. Two primary spars (front and rear) exist from which leading- and trailing-edge control surfaces are cantilevered. The arrangements of the jack points for the point-load calibration is very straightforward, with the load points being applied at six span stations along three constant chord lines. The 18 load points provide a well-balanced distribution of applied loads. The distributed-load calibration was developed from static test loads that correspond to wing design conditions. Information concerning the distributed-load calibration has previously been published.[21] Information concerning the point-load calibration has been given.*

*Schuster, Lawrence S., “B-1 Point Load Calibration,” Memorandum to Aerostructures Branch Files, NASA Dryden Flight Research Center, July 1981.

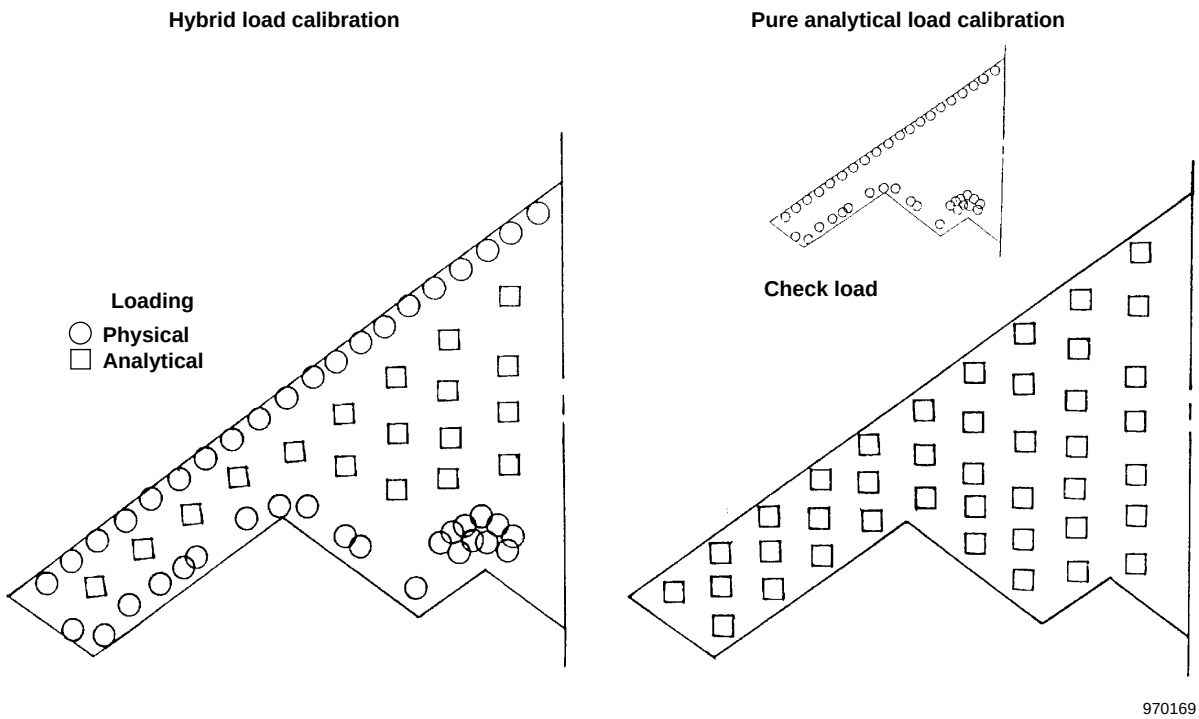

Figure 75. Two alternate methods for calibrating the strain gages of the B-2 wing.

The nature of the point-load calibration and the characteristics of the structure result in a set of influence-coefficient plots that are close to the ideal responses shown in figure 3. Figure 76 shows influence-coefficient plots for two strain-gage bridges located on the two primary spars of the B-1 wing. Both responses indicate shear sensitivity that is contaminated by torsion. This contamination is an expected result because both the spars are remote from the shear center of the wing. Figure 77 shows influence-coefficient plots for two strain-gage bridges located on the skin of the B-1 wing. The plot on the left indicates a torsion response that is sensitive to bending. The plot on the right is for a bending bridge that is well located. Figure 78 shows the distribution of applied loads for the 18 load points for the span and chord directions. This distribution of load points resulted in the following relevance coefficient:

$$C_R = 0.54$$

Because of the well-conditioned nature of the influence-coefficient plots, other approaches to influence-coefficient plot presentations were explored. Figure 79 shows the influence coefficients for spar strain-gage bridge 5307 in three different ways. The traditional two-dimensional plot is shown in the lower left corner of the figure. On the right side of the figure, the same information is presented as three-dimensional wire-frame and ribbon plots. The strain-gage and load-point locations are shown so that the observer can better grasp the relationship between the influence-coefficient magnitude and the location of load points and strain gages. Figure 80 shows a similar presentation for the strain-gage bending bridge 5310 that is located on the skin of the B-1 wing. The data presented in figures 79 and 80 represent near ideal structural responses in terms of classic influence-coefficient plots. These data allow the viewer to assess what approach encompasses the most meaningful information about the load calibration.

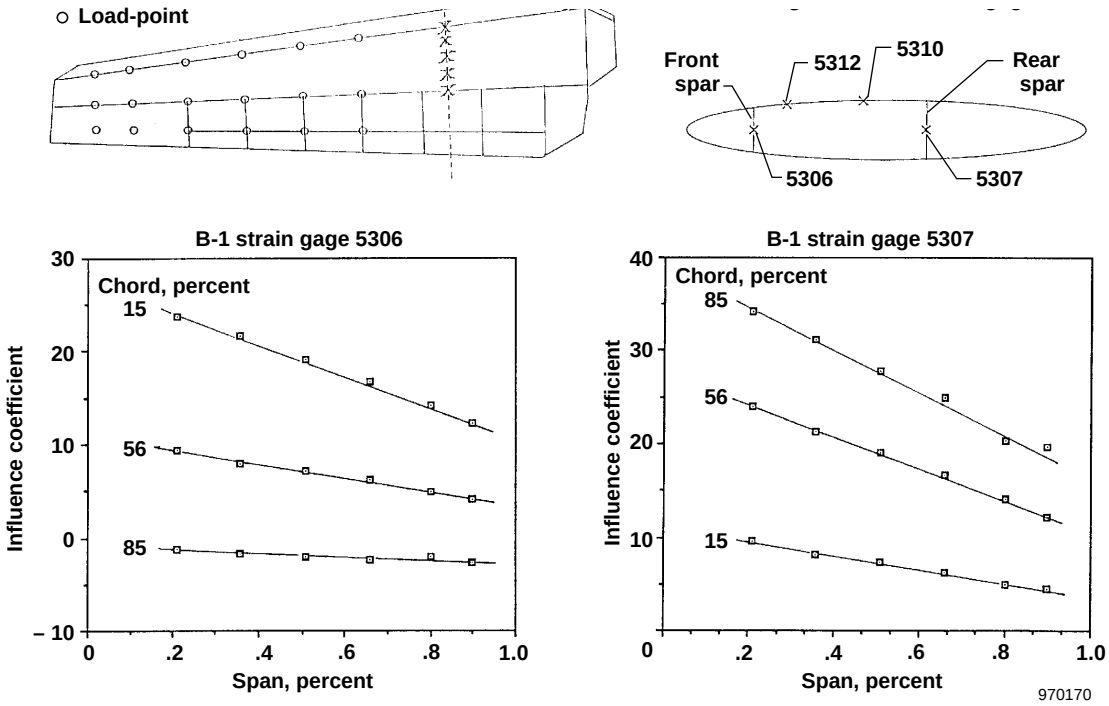

Figure 76. Typical influence-coefficient plots for strain-gage bridges located on the primary spars of the B-1 wing.

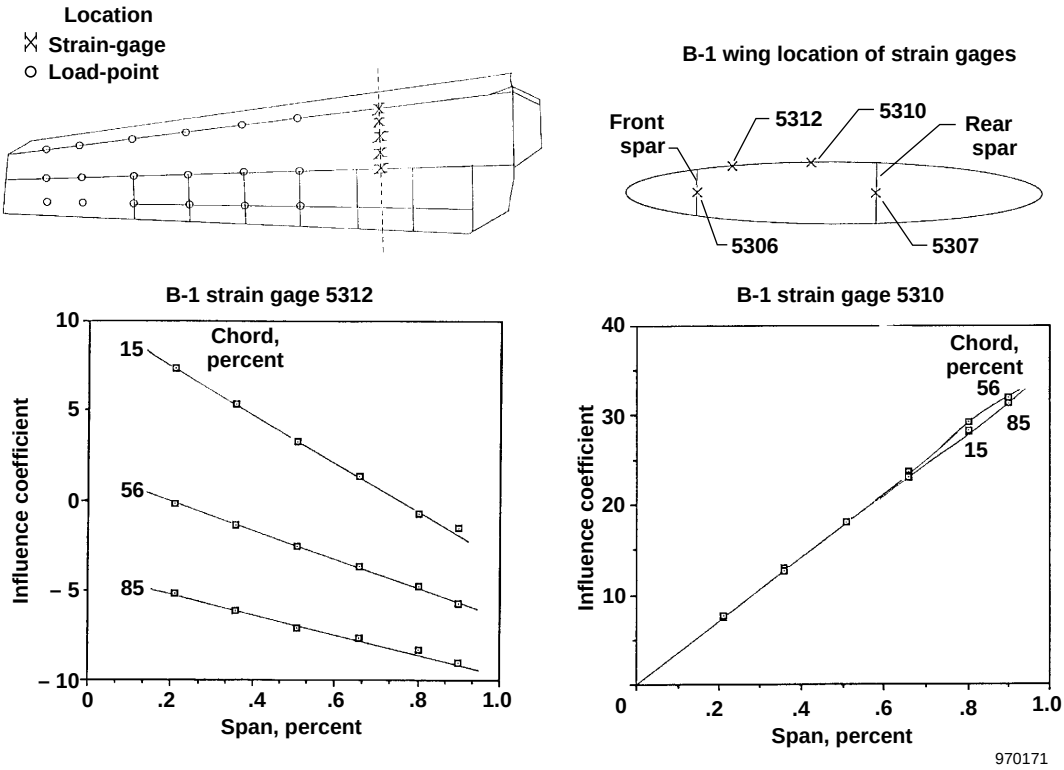

Figure 77. Typical influence-coefficient plots for strain-gage bridges located on the skin of the B-1 wing.

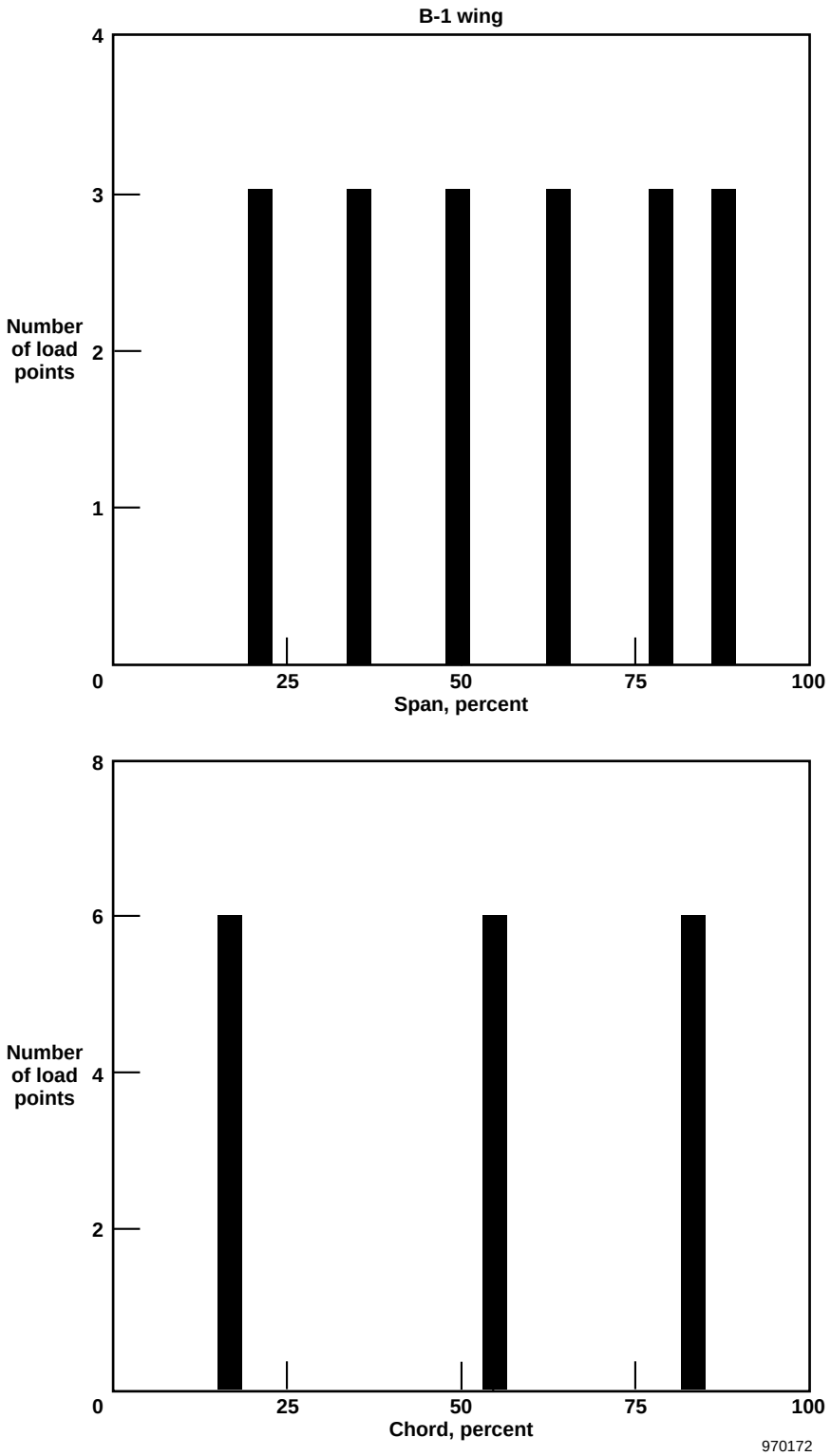

Figure 78. Distribution of load points in the span and chord directions for the B-1 wing.

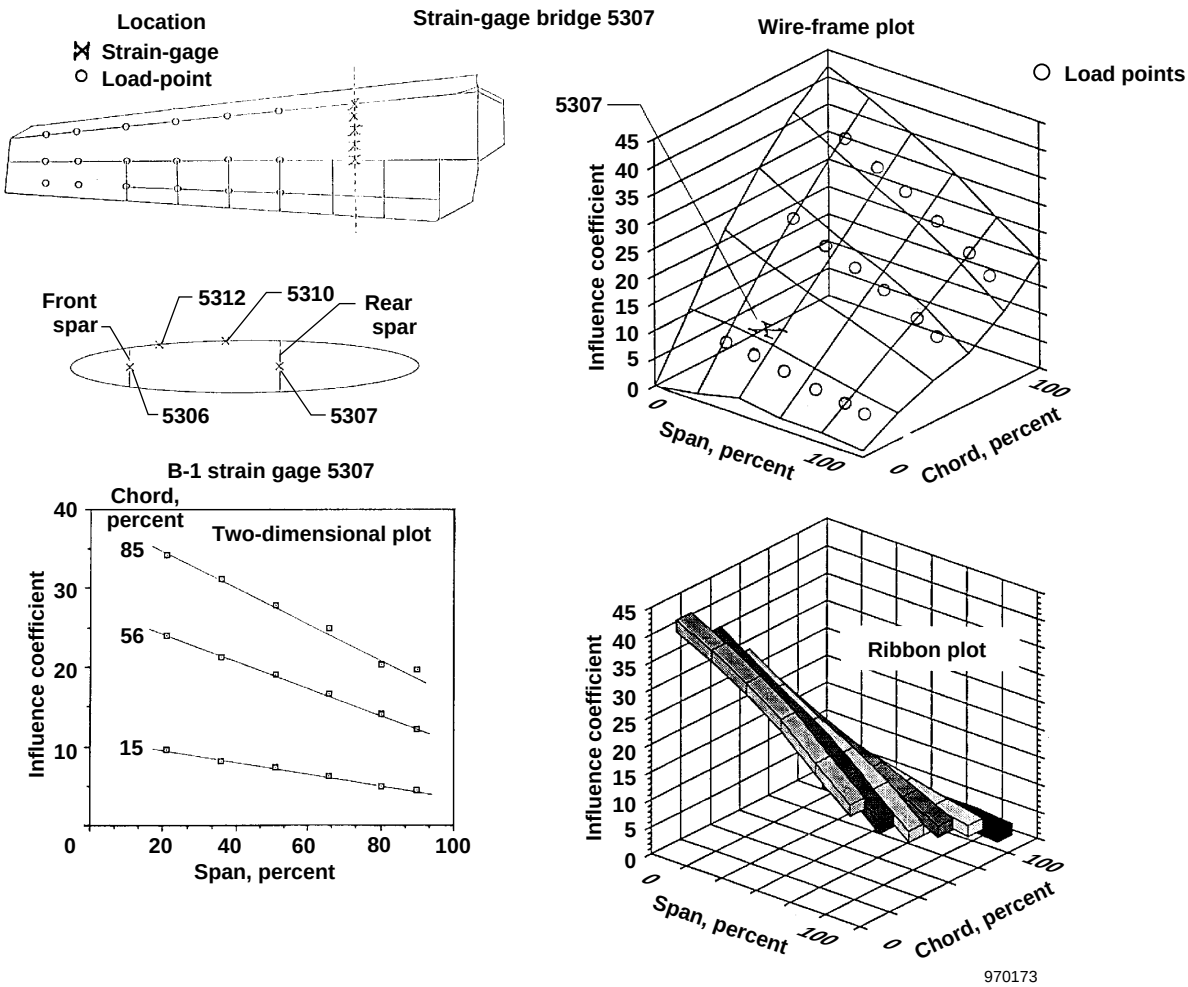

Figure 79. Comparison of methods of presenting influence-coefficient plots for a strain-gage bridge located on a B-1 wing spar.

Figure 81 shows the most unique aspect of the strain-gage calibration of the B-1 wing. Because the wing was calibrated using both a distributed-load and a point-load approach, the opportunity arises to compare the results obtained from the two methods. A spectrum of flight points is shown in the upper left corner of figure 81 in terms of load factor and Mach number. The five points selected represent a cross section of load distributions and magnitudes. The high- and low-load factors represent different magnitudes of loads, and the subsonic and supersonic Mach numbers provide a variation of load distribution in terms of forward and aft center of pressure. The remainder of the figure shows comparisons of computed shear, bending, and torsional loads from equations developed from both the distributed- and point-load calibrations. Very little difference exists in loads calculated from the two methods. The mean difference in loads calculated from the two methods is less than two percent for all the data shown.

Hypersonic Wing Test Structure

A significant laboratory test article representing part of a delta-wing structure (fig. 2) was fabricated approximately two decades ago.[22] The general area from which the test article was deduced is shown as the shaded area on the wing of a hypersonic airplane (fig. 82). Although the hypersonic wing test structure (HWTS) was primarily used for high-temperature structures research, studies associated with strain-gage load calibrations were

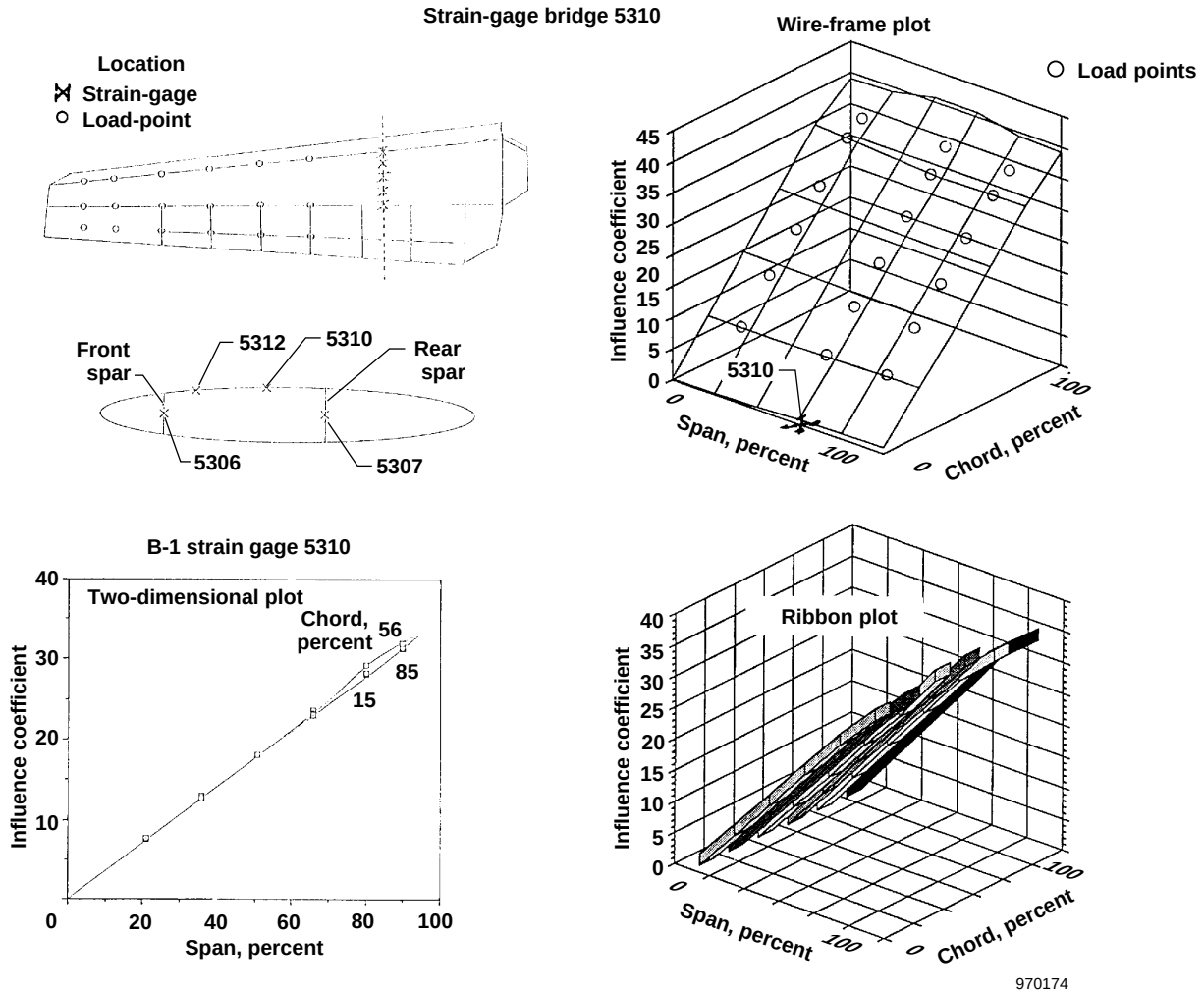

Figure 80. Comparison of methods of presenting influence-coefficient plots for a strain-gage bridge located on a B-1 wing skin.

also done. Figure 82 shows load-point application points and strain-gage bridge locations. The HWTS provided an excellent opportunity for a closely controlled laboratory study directed toward strain-gage load calibrations.

A NASTRAN finite-element model of the test article was also available, thus providing a comparison of an analytical measurement with a laboratory measurement. Figure 83 shows a comparison of measured influence coefficients with calculated influence coefficients for two shear bridges located along the root of the test structure. Figure 84 shows a similar comparison for a pair of bending bridges located similarly. The correlation between the experimental and the analytical data indicates a mixed result. Some of the information shown in figures 83 and 84 correlates well, but large deviations also exist.

Figures 85 and 86 show a comparison of computed-equation influence-coefficient plots with measured equations. The comparisons shown in figures 83 to 86 establish an additional component of the data base concerning how well structural computer models predict measured strain responses.

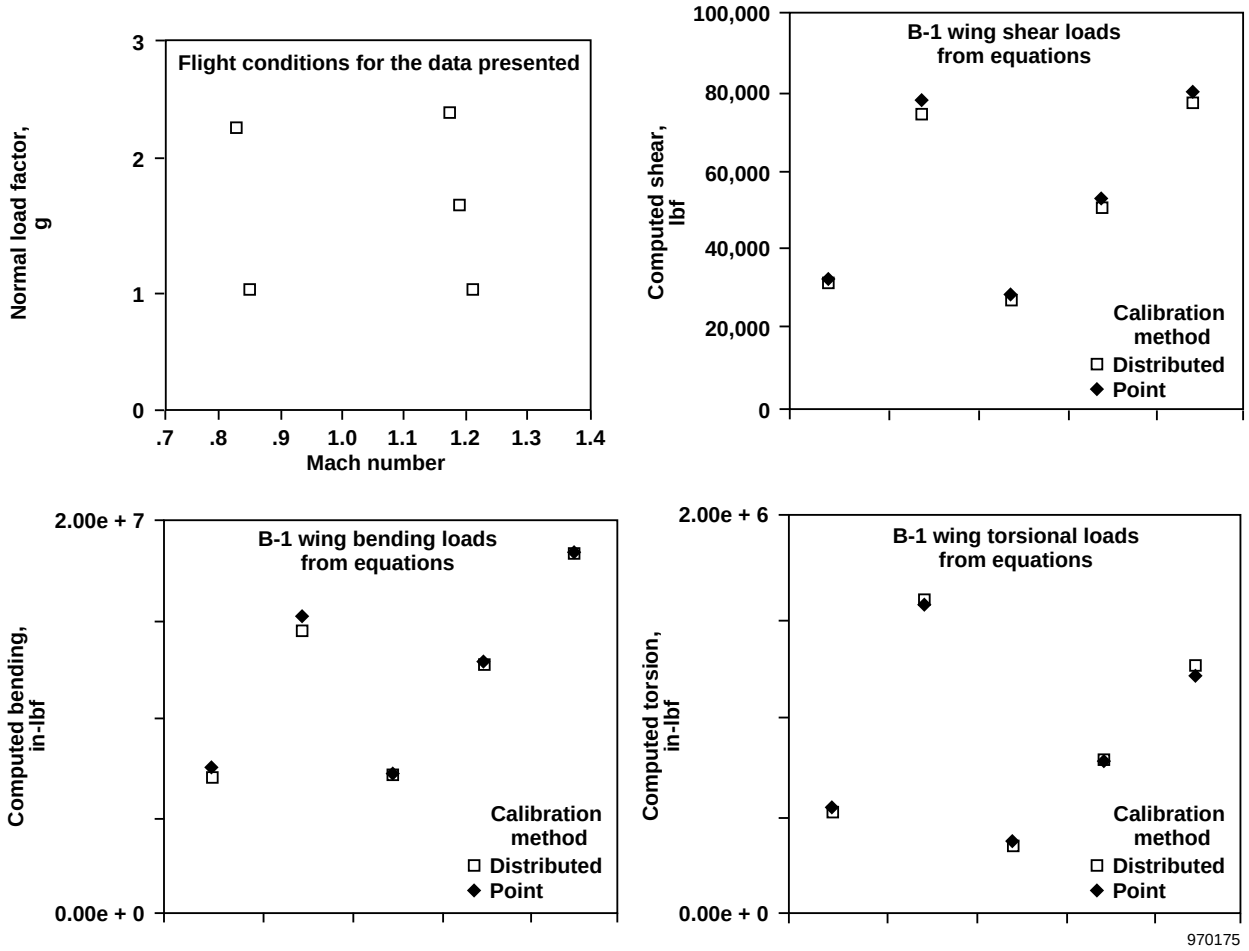

Figure 81. A comparison of equation-deduced flight loads data using both distributed- and point-load calibration methods for the B-1 wing.

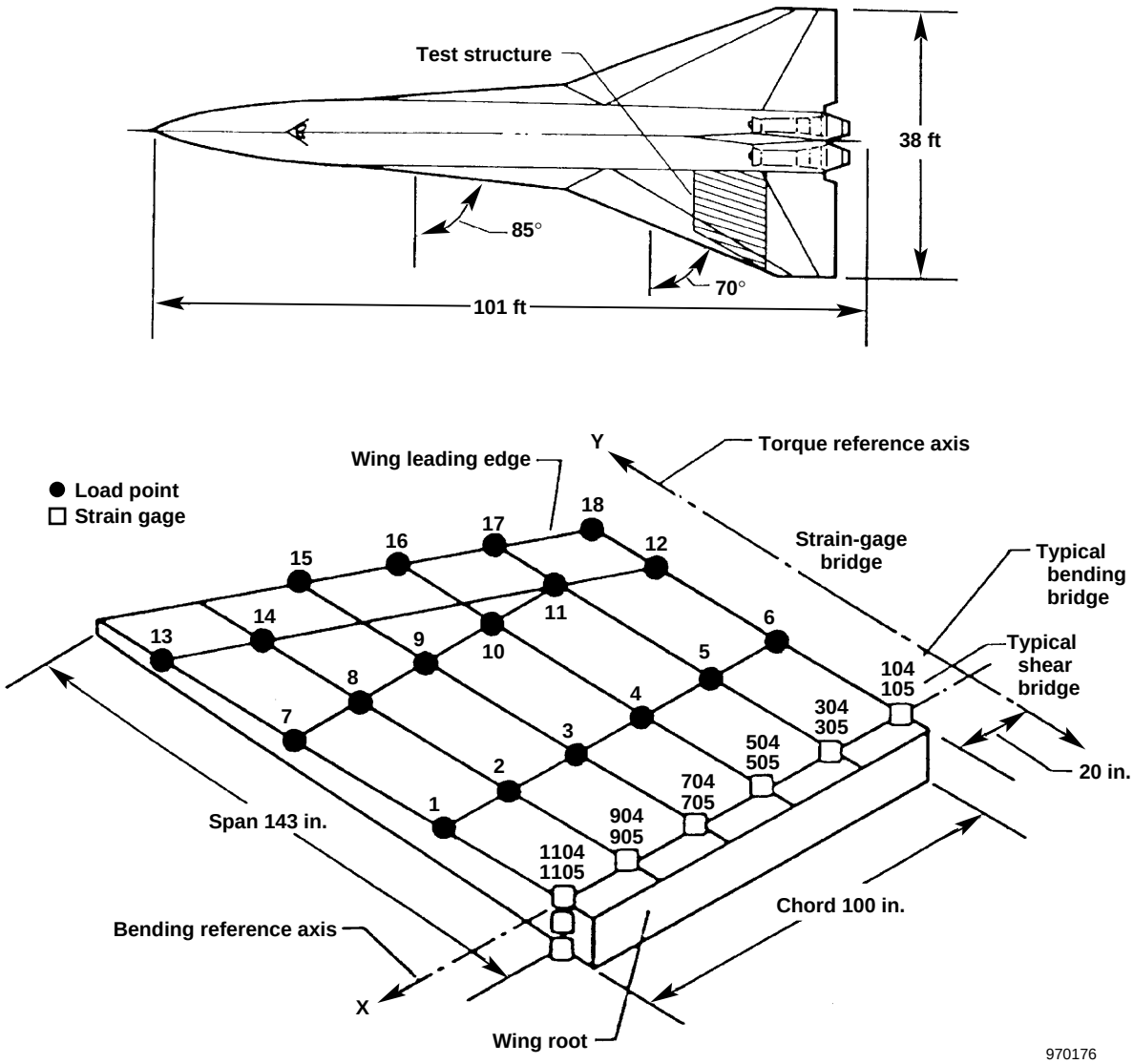

Figure 82. Location of strain gages and load points on the Hypersonic Wing Test Structure.[25]

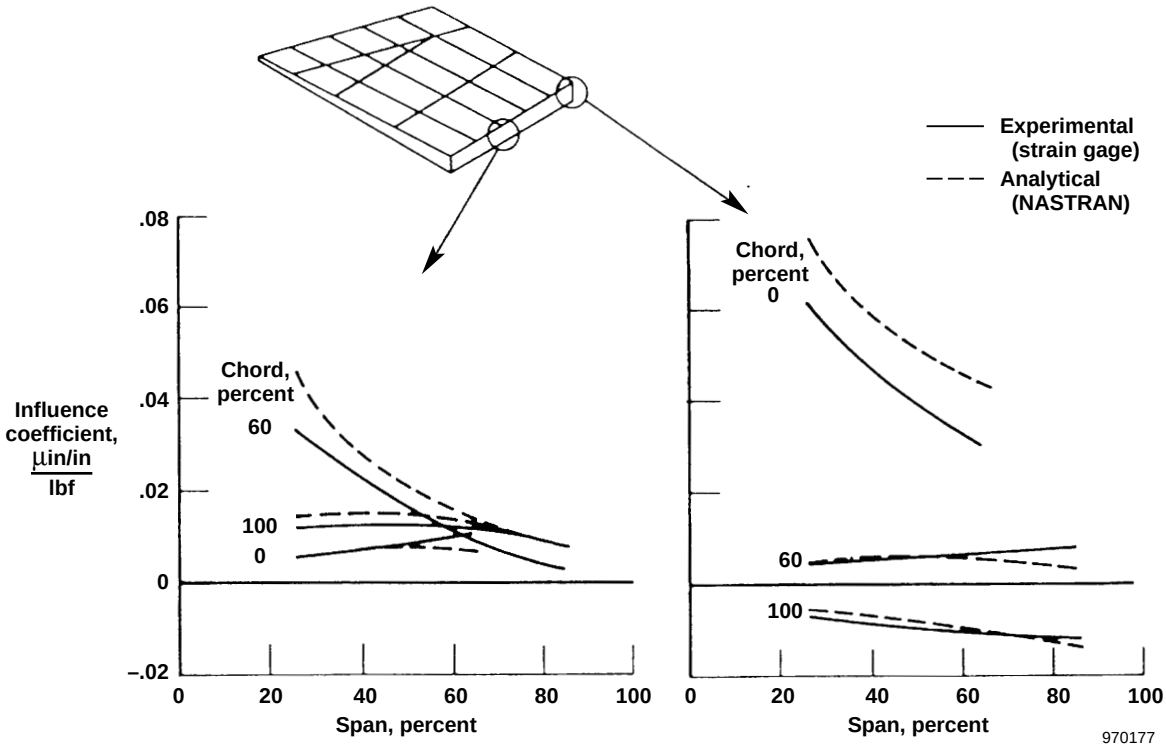

Figure 83. A comparison of the measured and calculated influence-coefficient plots for two shear bridges on the Hypersonic Wing Test Structure.[25]

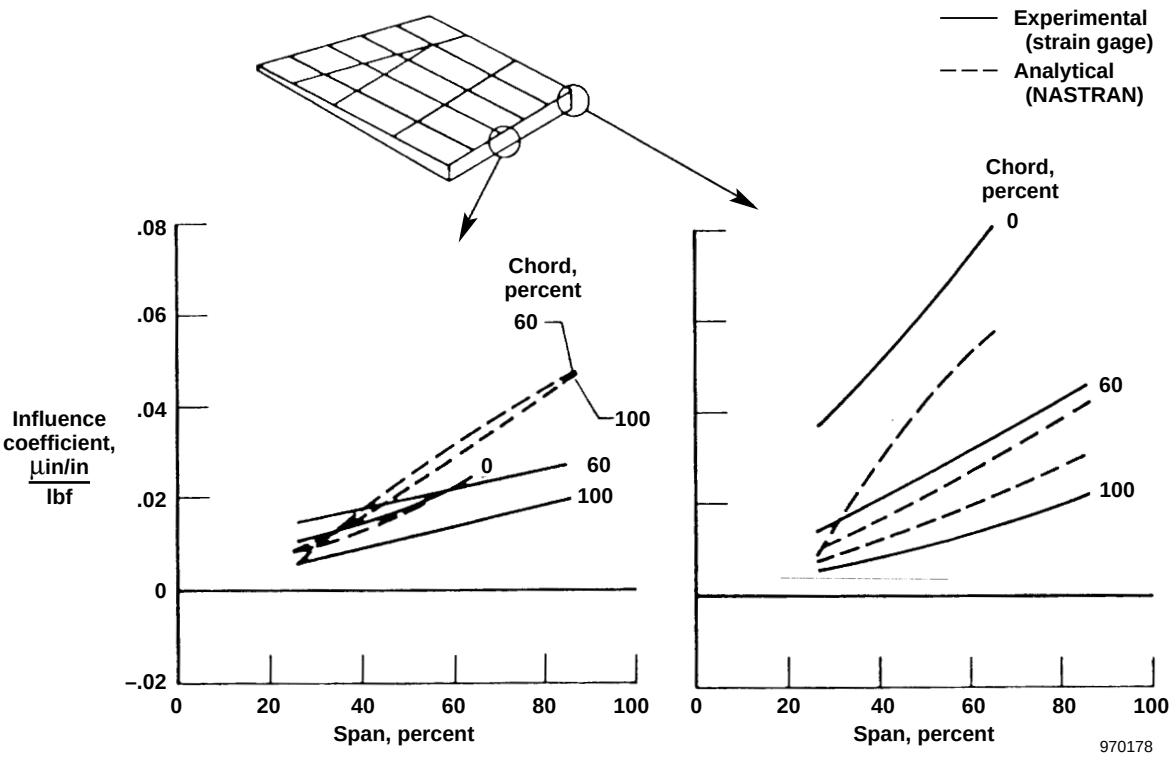

Figure 84. A comparison of the measured and calculated influence-coefficient plots for two bending bridges on the Hypersonic West Test Structure.[25]

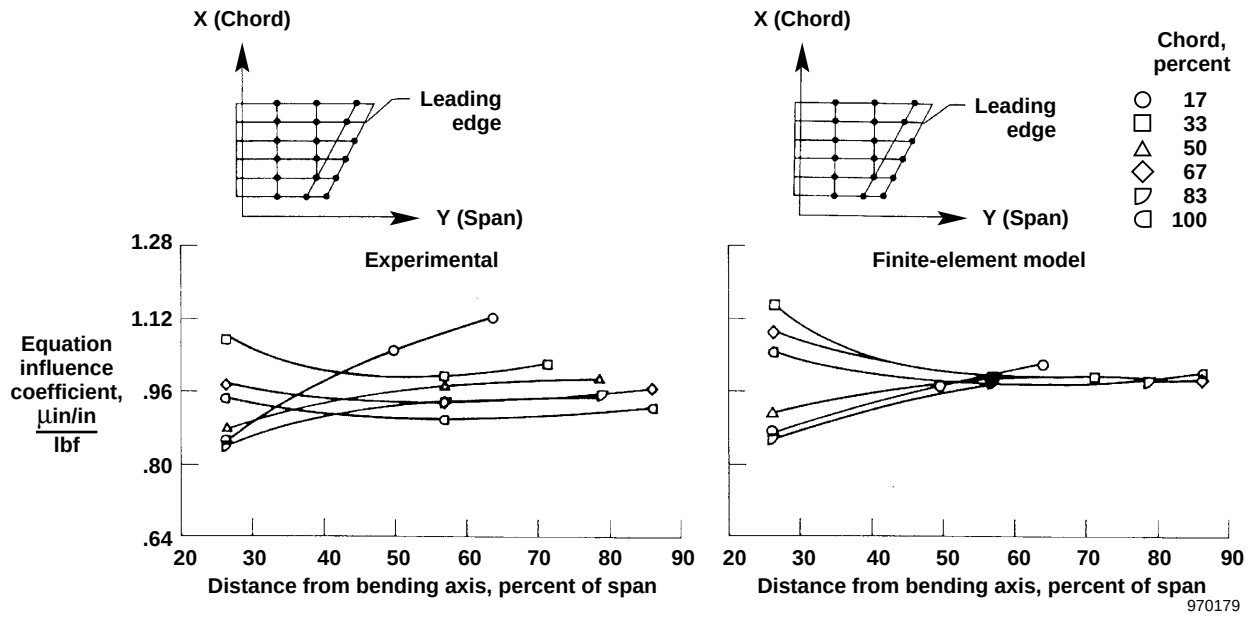

Figure 85. A comparison of the measured and calculated equation influence-coefficient plots for a shear equation on the Hypersonic West Test Structure.[25]

Several strain-gage bridges used in a load equation are known to provide a smaller equation error than two strain-gage bridges, for instance. Little exists in literature about the relationship between load equation error and the number of strain-gage bridges in the equation. Figure 87 shows that a region exists where adding additional strain-gage bridges to the equation does not improve the equation standard error. The issue of the number of strain gages goes beyond just the effect on the standard error. As figure 88 shows, the quality and nature of the equation influence-coefficient plot also improves by adding strain-gage bridges to the equation. Adding strain gages to the equation increases the total equation output and improves the character of the equation. The two examples shown in figure 88 substantiate these characteristics.

Because a large matrix of strain-gage bridges is usually available, pondering a method of selecting which strain gages are pertinent to the equation is logical. Selection processes have been previously discussed.[23–27] One selection process is to examine the ratio of the equation coefficient to its standard error. This process is suggested in reference 23, which notes that if any one bridge is linearly related to the response of any other bridge, then large standard errors ensue because of ill conditioning of the mathematics of the problem. Therefore, one by one, strain gages with large ratios of equation coefficient to standard errors are dropped from the equation until an appropriate or optimum number of terms are left. This method is sometimes referred to in reference literature as the T-value or modified T-value methods of selecting strain-gage bridges. The fact that an opportunity existed to study this method makes the HWTS an important part of documenting work pertinent to the science of strain-gage loads calibrations.

DISCUSSION

The data for the 15 strain-gage load calibrations have been selected for a variety of reasons. Finding older data that were still available in a complete and interpretable format was difficult; therefore, availability was a major factor. The specific data and the format of the data have been presented so that issues, lessons, rules, and problems pertinent to the science of flight loads measurement with calibrated strain gages can be examined. The remainder of this report will be directed toward arranging this information in a format that will be an aid to engineers who must conduct future strain-gage load calibrations. As much as possible, the report is intended to strengthen the basic science.

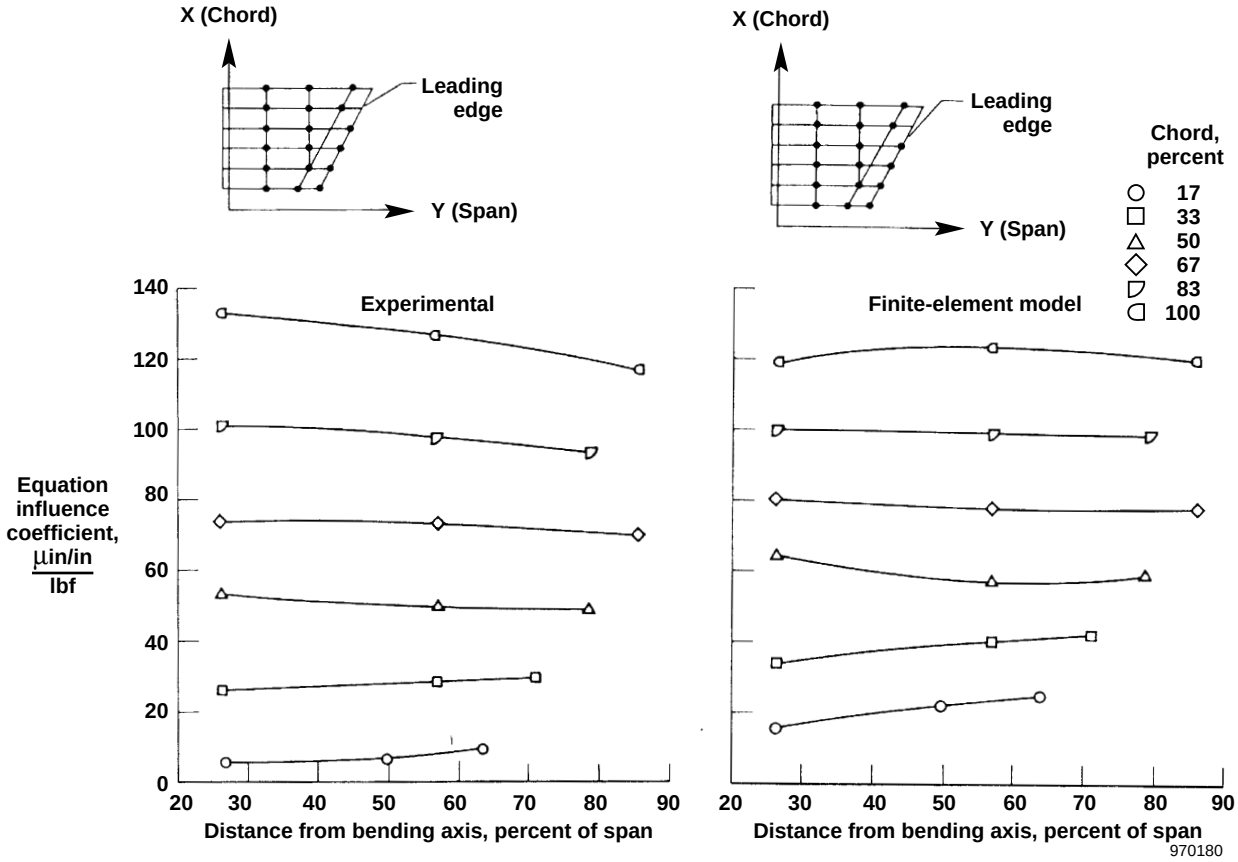

Figure 86. A comparison of the measured and calculated equation influence-coefficient plots for a torsion equation on the Hypersonic Wing Test Structure.[25]

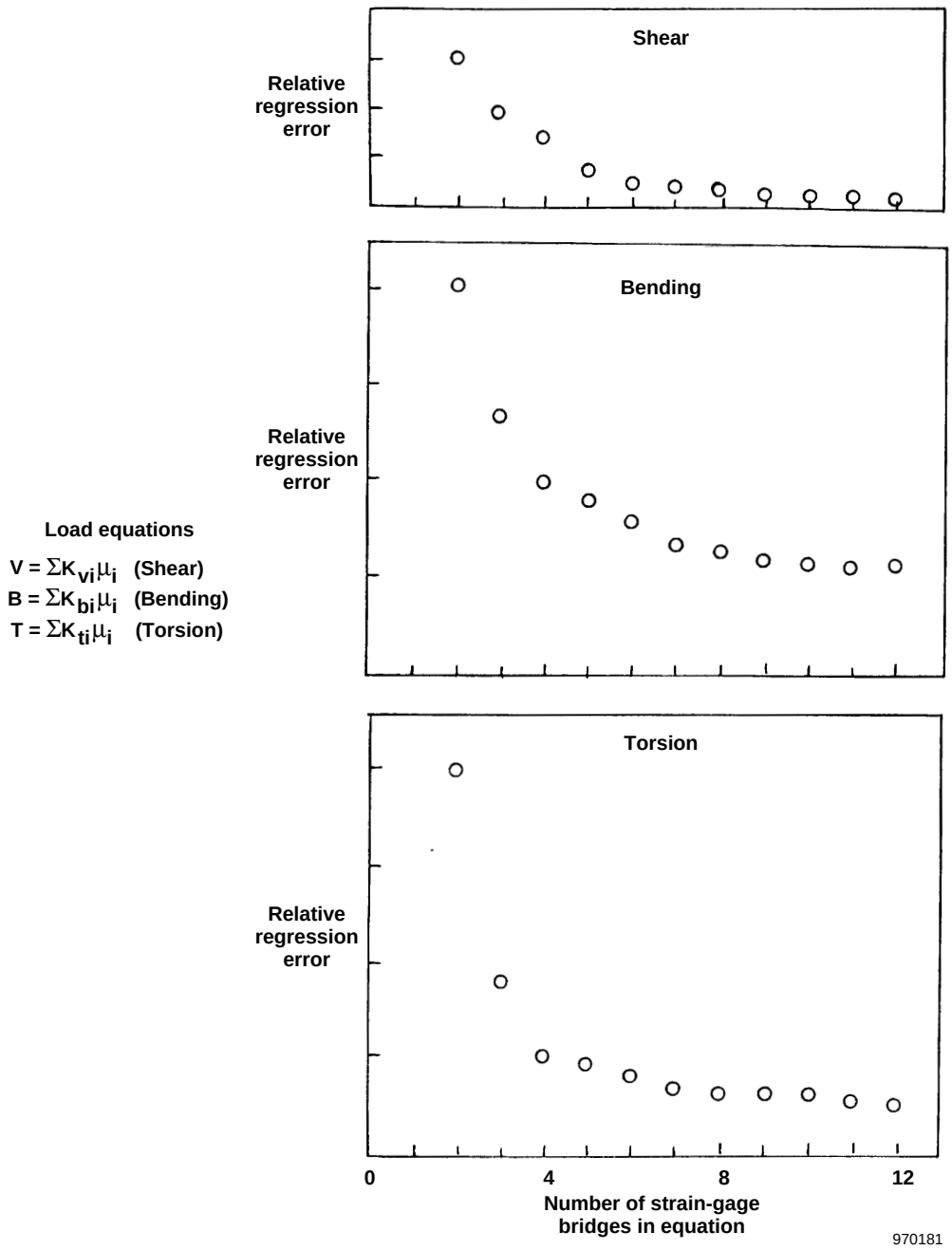

Figure 87. The effect of the number of strain gages in a typical loads equation on the standard error of the equation.[25]

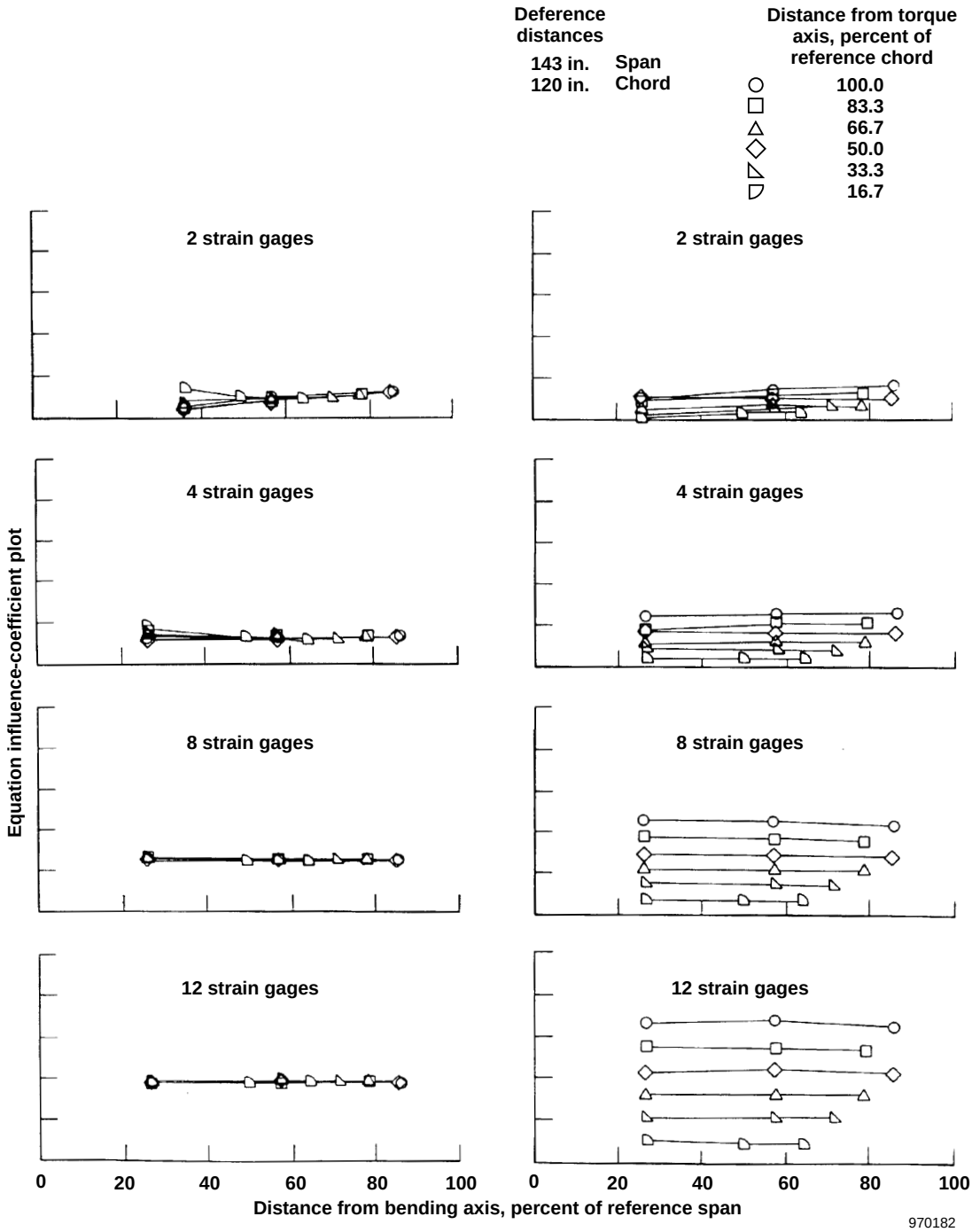

Figure 88. The effect of the number of strain-gage bridges on the character of two typical loads equation influence-coefficient plots.[25]

The basic science of measuring loads with calibrated strain gages is still evolving and somewhat fluid because the approaches must be constantly adapted to changing aircraft technology. The goal of this report is to provide more than just a catalog of information regarding the load calibrations of the various aircraft. Trends, rules, results, presumptions, and directions can be deduced from the data thus far presented that collectively are pertinent to developing a science. Although measuring loads with calibrated strain gages is not an exact, well-defined science, approaches certainly exist that are appropriate, and issues exist that should be examined on an individual basis. This section will therefore interpret the information that has thus far been presented with respect to individual aircraft strain-gage calibrations. The format will address specific critical issues in subjects that should form the basis of a check list for any scientist engaged in measuring loads with strain gages.

Location of Strain Gages

Load measurements are best taken if strain gages are wired in four-active-arm bridges so that the summing effect of the outputs of four strain gages can be used. Locating shear-sensing bridges on the webs near the shear center of the structure minimizes contamination from bending and torsion. Bending bridges should be located on skins or outer caps as far from the neutral axis as possible to maximize the bending outputs. Torsional bridges should be located on skins or webs as far from the shear center of the structure as possible, preferably near the plane of the neutral axis, to maximize the torsional response and minimize the bending response. If the location of the strain-gage bridge is subjected to temperature changes, the configuration of the strain-gage bridge can be used to provide temperature compensation. Appendix B provides more details concerning strain-gage bridge configurations. Figure 49 shows detailed locations for an actual strain-gage bridge installation for the T-37B wing.

Selection of Load Points

The point-load calibration of a set of strain gages on a wing- or tail-type structure should include point loadings in all areas where flight load occur. The spectrum of calibration loads should encompass as much of the span/chord area as is practical to result in a more complete statistical correlation between the actual flight load spectrum and the ground load calibration spectrum.

Limitations frequently exist on where loads can be applied to the surface of an aircraft structure. Because loads are normally applied in some concentrated manner, finding hard points such as spars or ribs that can withstand high local stress levels is necessary. The manner in which calibration load points is distributed is greatly influenced by where loads can or cannot be applied to the surface of a wing or tail or other structure. In many respects, the location and number of load points is determined more by practicality than by planning.

Number of Strain Gages in Loads Equations

The number of strain gages needed to successfully make a load measurement has always been a subject for much analysis and evaluation. For some measurements, particularly bending moment, a relatively small number of terms in the loads equation has yielded very good results. Measuring shear and torsion is clearly a different matter. In order to adequately describe the applied calibration loads, three, four, or even five strain-gage bridges may have to be included in the equation. Limitations in the number of flight data recording channels is a frequent problem when large numbers of strain-gage bridges must be used to acquire the load measurement. Data recording limitations may dictate a small number of strain-gage measurements, hence compromising the accuracy of the measurement. This subject was well covered in figures 87 and 88, where the general trends were studied on a laboratory test structure. Note that the trends and accuracies of the data shown in figures 87 and 88 apply only to the spectrum of the loads that were applied during the load calibration and that were also used in the derivation of the loads equations. Loading conditions outside the spectrum of the load calibration will be discussed in detail in a later section.

Derivation of Equations

The conventional approach associated with deriving loads equations has been identified,[1] and appendix F presents an example of the calculative process. Equations can also be derived using the singular-valued decomposition approach;[2] however, this approach is basically untried on strain-gage load calibrations. If an advantage to the method of reference 2 exists, it is neither apparent nor demonstrated. Regardless of how the equations are derived, it is important to recognize and be cognizant of the fact that the derivation process leads to an equation that is directed to define the applied loads and not necessarily anything else. Therefore, measuring loads that are not within the spectrum of the calibration loads must be approached with caution.

It is also worthwhile to note that reference 1 suggests two simplified approaches to obtaining loads equations. The first approach is to use n strain gages and apply n load points to the structure and then determine the equation coefficients exactly by merely solving a set of simultaneous equations of order n. These authors are unaware of documented applications of this method, so evaluating how well this method works is difficult. Another approach is to devise a group of n distributed loads pertinent to the character of the load to be measured. Again, a set of simultaneous equations of order n would be solved to obtain the equation coefficients. These authors are also unaware of any documented examples of this approach.

Automated Strain-Gage Selections

If the structure to be calibrated is complex or highly redundant and a large number of strain-gage bridges are available for use in the equations, then choosing the best three, four or five strain-gage bridges for the equation is a formidable task. Automatic selections processes were previously identified.[23–27] An additional approach has been developed recently.[28] This approach employs genetic algorithms to select an appropriate set of strain-gage bridges for the equation. These approaches certainly appear to save considerable work for the load measurement engineer.

In any case where automation is used, spot-checking to make certain that the result appears to correlate with the physical circumstance of the problem (for instance, the result appears logical) is prudent. In an automated process, a wise approach would be to examine the influence-coefficient plots of the strain-gage bridges that are finally selected to see if the bridges generally appear to be the combinations that would logically be selected by inspection.

Load Calibration Relevancy and Load Measurement Error

It is unfortunate that so much emphasis has been given to the handling of the load calibration data. The accuracies that are associated with the development of the load equations are only a part of the scenario that leads to a number that represents load measurement accuracy. Consider a wing in which a load calibration was done by applying loads to only 20 percent of the wing area, then equations were derived from this 20-percent load calibration, and the equation accuracies turned out to be quite good. Further consider the circumstance that in flight, no load occurred on the 20 percent that was calibrated, but the flight loads occurred on the remaining 80 percent. Figure 89 shows this extreme example. Although the equations derived from the 20-percent load calibration are calculated to be quite good, no reason exists to believe these numbers are relevant to measuring the flight load that occurs on the remaining 80 percent of the wing. Deducing an accuracy in this case would require some very far-reaching extrapolation.

This issue was somewhat addressed earlier in this report with the introduction of the relevancy coefficient. This attempt only related the coverage of the calibration loads to the total surface area of the wing or tail that was to be calibrated. As more load calibrations were introduced, this relevancy coefficient was obviously not that relevant, particularly with regard to the load to be measured. Other factors existed that should have been included in any relevancy measurement, such as aspect ratio, degree of structural redundancy, structural arrangement, and

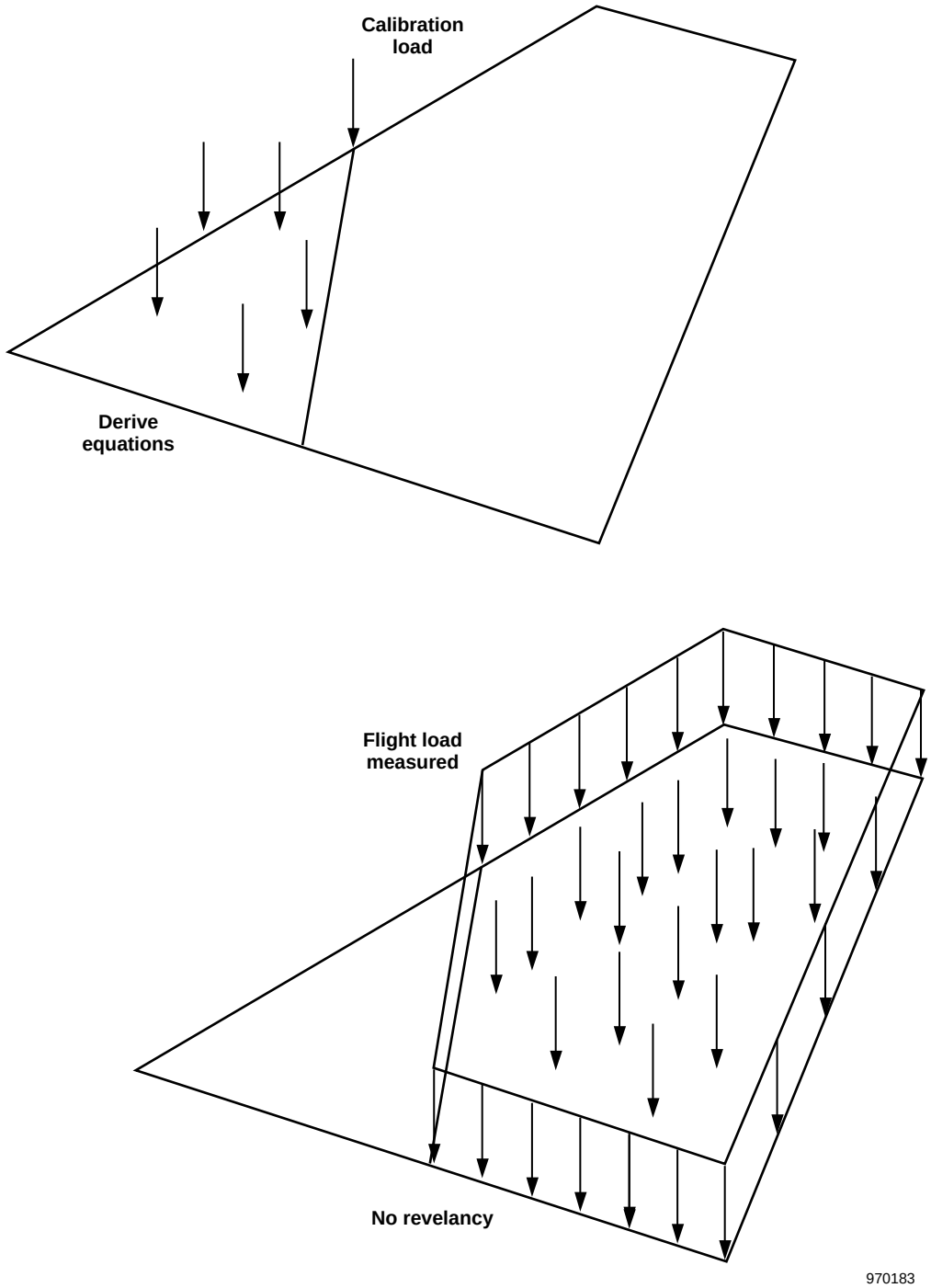

Figure 89. Depiction of a nonrelevant load calibration with regard to a load measurement.

the distribution of load. No clearly defined way of establishing a number that represents the accuracy of the load measurement exists. The closest approach to defining such a number would be the application of a distributed check load based on some pertinent knowledge of the actual flight load. A distributed check load provides some link between the equation determined by the load calibration and a relevant distributed check load. If the flight data recording system is used, then a reasonably good evaluation of the accuracy of the load measurement may result.

Point- and Distributed-Load Calibrations

Strain-gage load calibrations have been successfully accomplished using either point- or distributed-loading schemes. Other load calibrations have been accomplished using a combination of the two methods in a hybrid fashion. Some tendency exists to adopt an approach that is believed to be philosophically the best; however, the history of load calibrations indicates that success can be accomplished with any of the point-, distributed-, or hybrid-loading schemes. The approach is more one of applicability rather than philosophical superiority.

Many factors exist that determine the selection process associated with the calibration approach. In recent times, the cost of load calibrations has drastically inflated, raising the possibility that load measurements will not be done. Cost considerations might lead to combining the load calibration with some sort of proof test that might also dictate a distributed-load calibration. If the calibration has to be done on the airplane after it is ready to fly, the problem of reacting large calibration loads always exists. This factor tends to direct the effort toward a discrete point loading. Also, if the nature of the load to be measured is well known, then a distributed-load calibration with its more restrictive spectrum would seem more appropriate. If the spectrum of possible loads was quite large, however, then the more universal or global point-load approach would seem the most appropriate. In more recent years, the degree to which an airplane can be loaded has become more restrictive, hence complicating the load calibration process. Each strain-gage load calibration, however, must clearly be considered as a unique entity that requires an approach tailored to the circumstance.

The B-1 wing was calibrated with both distributed-load and point-load arrays, providing some insight into the issue. The insight is very narrow in perspective, however, because the B-1 wing is a two-cell, high-aspect-ratio structure that represents one end of the configuration spectrum. In the case of this particular structure, both calibration approaches essentially yielded the same results. It cannot be deduced that the same result might be obtained for a different configuration such as a low-aspect-ratio multispar wing. This issue requires additional information to establish generalizations.

Planform Aspect Ratio

Low-aspect-ratio planforms have generally been observed to be more difficult to calibrate than high-aspect-ratio planforms. This effect is likely more appropriately related to the redundancy of the structure than to the shape of the planform. Structures that have many spars have traditionally resulted in high error calibrations. These structures have also tended to be on the low end of the range of aspect ratios. Wings and tails on the high range of aspect ratios generally have fewer spars and have better-defined load paths that typically result in lower equation errors for each load calibration. The effect is most prominent in the measurement of shear. Bending-moment equation errors seem little affected by planform shape; torsion equations are somewhat more affected. One anomaly that is an exception to this generalization is the common high-aspect-ratio horizontal tail that frequently is attached to the fuselage with a spindle arrangement. Measuring shear on spindle-type structures has historically been very difficult, regardless of the planform shape.

The planform or aspect-ratio effect would not be as noticeable if the number of strain-gage bridges used in the equations were better correlated with the degree of redundancy of the individual structure. A lifting surface with many spars is usually low in aspect ratio, is highly redundant, and requires many strain-gage bridges in the loads equations. Therefore, if the number of strain gages in the equations is more closely representative of the degree of redundancy, then a planform (aspect-ratio) effect would probably not exist.

Influence-Coefficient Plots

The influence-coefficient plot is the single most important tool for evaluating the status of a load calibration and for comparing the character of the calibration with other strain-gage load calibrations. The variation of the influence coefficient must be plotted on the vertical axis, with the span plotted on the horizontal axis with constant chord lines in the field. This type of plot can be interpreted in the manner presented in the previous sections of this document.

Many calibrations are done without the benefit of influence-coefficient plots. With the capability to automate all parts of a strain-gage load calibration, the opportunity to separate the engineer from the physical problem is extensive. This automation creates the environment for very serious misinterpretations, presumptions, or oversights. Influence-coefficient plots are strongly recommended to be used, and the loads measurement engineer should remain very close to the physical load calibration so that it is apparent that the result is logical.

Because many computer graphics programs are available, influence-coefficient plots were examined from the three-dimensional point of view. Several cases were presented earlier in this report, and two-dimensional presentation was concluded to be more comprehensive than the three-dimensional presentation. This conclusion was reached because recognizing trends seemed more difficult when the viewer had to address three variables at one time. When addressing the two-dimensional presentation, the viewer could examine two of the variables and then note the effect of the third variable. This latter approach seemed to provide an easier method of reading the trends and also seemed more informative.

Local Root Effects

Almost all of the influence-coefficient plots presented in this document exhibit characteristics near the root that deviate from the trends that are seen outboard of the root area. These root trends might be characterized as irregularities, nonlinearities, or deviations from the general character of the influence-coefficient plots. The trends are, in reality, local effects caused by the close proximity of the load to the strain-gage bridges.

Figure 90 shows this effect, where loads A and B can be seen to cause elemental stresses that are different than those resulting from load C. What happens is that loads A and B predominately cause bending and shear responses in terms of the elemental stresses at the strain-gage locations. Load C results in bending, shear, and compressive responses at the elemental stress level at the strain-gage locations. For some load points, the strain-gage bridges respond to shear, bending, and torsion effects; and for a few other load points, the strain-gage bridges respond to shear, bending, torsion, and compression effects.

The knowledge of the nature of the problem and the knowledge of how to fix the problem can be widely separate issues. A calibration load is a very concentrated entity that may bear no resemblance to the way an air load in the same area is distributed to the structure. This lack of resemblance is a problem if the strain-gage bridge happens to be located in close proximity to the calibration loading jack. Load points that are located remote to the strain-gage bridge are not capable of causing the compression effect because of the St. Venant effect.[19] Therefore, the degree of similarity between the root load point and the air load must somehow be established if any problem-solving is to be accomplished. If the response of the structure to the air load is different from the response of the structure to the calibration load, then it may be better to discard the root load points from the equation derivation process. In other words, the loading at the root area may not be relevant to the measurement of the air loads; therefore, the root loading should not be included in the equation derivation. However, this case is only one scenario. In all probability, the root loading will not be totally irrelevant, in which case a major problem will need to be solved. Concentrated loads on the spars at the root may not be acceptable, in which case distributed loads that more closely simulate the actual flight loading at the root may be required. An analytical correction might also be applicable. The entire problem of local root effects is one in which considerable effort is required to effect a solution. The mechanics of the local root effects are presented in appendix G in terms of carryover expectations.

Nonlinear Approaches

Nonlinearities can occur at several stages in a strain-gage load calibration; however, a direct response to load that is really nonlinear is rare. The cause of the nonlinearity would more likely be traced to something like a partially detached strain gage or some other sensor problem. The primary nonlinearity problem (not withstanding the introduction of highly nonlinear materials) is associated with the problem discussed in the preceding section. Almost without exception, influence-coefficient plots tend to have a very consistent character in the outboard 80 percent of the span. The first 20 percent of the span is characterized by the root effects described in the previous section.

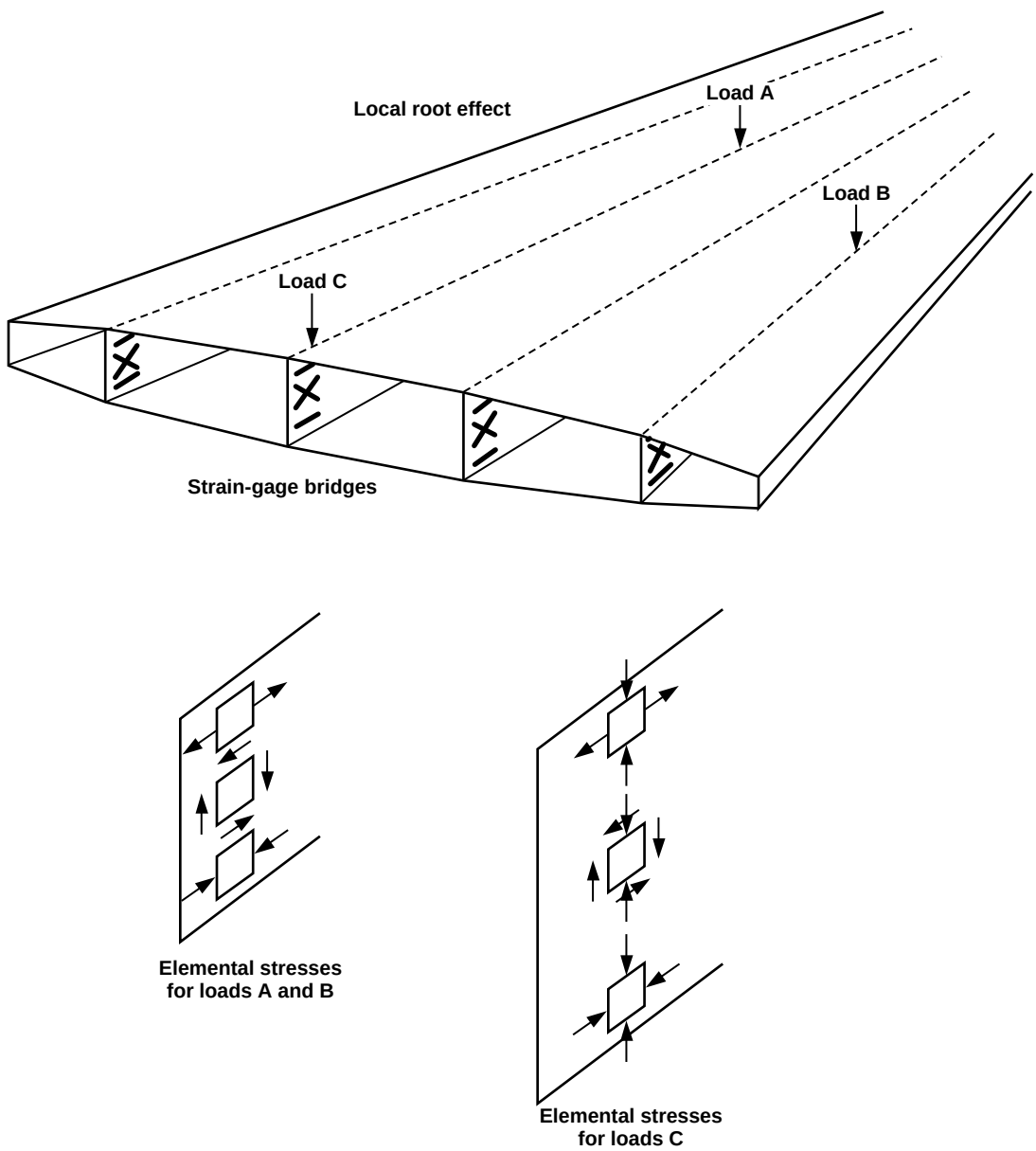

Figure 90. Effect of calibration loads located near the root strain-gage axis.

The difficulty of providing nonlinear definition of the influence-coefficient plots was illustrated quite well in figure 38, where a very severe nonlinearity was evident. The irregularity is so severe in the influence-coefficient plot (fig. 38) that the condition might be more appropriately referred to as a discontinuity, because some of the information appears asymptotic. Because applied loads and strain-gage bridge responses are definitely finite, asymptotic information in an influence-coefficient plot obviously cannot exist. Very irregular responses result in unusually complex requirements for any algorithm that would be used to define the influence-coefficient plot. Judgments would have to be made based on solid mechanics theories; hence, a nonlinear approach is thought to be imprudent. An algorithm that could generate the basic influence-coefficient plots from raw data would have to be very complex and have a large computational requirement.

Computational Strains

As early as 1970, when the YF-12A flight loads efforts were in progress, it became apparent that the powerful computational capabilities associated with evolving finite-element structures computer programs would have great impact on strain-gage load calibrations. What role these newly introduced computational capabilities might have was not clear at that time. In 1970, large structural models were not a realistic goal because of computer limitations. Small models were available but were not considered sufficiently sophisticated to provide detailed strains in discrete areas. However, the comparison of computed and measured strain patterns (as shown by the influence-coefficient plots and by strains reduced from bridge outputs by the method given in appendix B) was generally quite close for the YF-12A wing. This observation was made in approximately 1970, and at that time reliable computed influence-coefficient plots were recognized as a reality. This result could also be extrapolated to deduce that more could be done in terms of conducting or augmenting the actual load calibration than was possible at the time.

Later, computational data from the space shuttle and a laboratory test structure (the HWTS) contributed to the agglomerate associated with the ability to compute structural strains from computer models. The correlations of the computed influence-coefficient plots with the measured values indicate that, by using a finite-element model with sufficient elemental detail, a computational load calibration should be feasible. The primary correlation deficiency associated with computational efforts was shown to be in the magnitudes of influence-coefficient plots; the shape or character of the influence-coefficient plot correlated well with measurements. The cases where the measured and calculated values of strain did not correlate well were associated with shear-sensing strain gages. The shear strains associated with direct shear and shear flow are dependent on the thickness of the local structure. The thicknesses used for finite-element models are thought to be incompatible with the actual structure. This incompatibility exists because sufficient structural modeling detail does not exist in the areas where the strain gages were located.

Figure 91 shows this lack of detail. This figure shows that an actual spar may be a very complex built-up structure with many doublers. The more efficient the structural design is, the more probable this complexity will exist. The coarser finite element (typical of past models) may very well use one element having one thickness to represent the actual doublers/webs. This representation means the model does not have a correct thickness at the discrete location of the strain gage. This incorrect thickness results in the model generating an incorrect shear strain that obviously will not correlate well with the measurement. This problem can be fixed by using a finite-element model of sufficient detail to provide an accurate thickness at the location of the strain gage. This problem is believed to be resolvable because adequately modeling the local structure is easier with the powerful modeling and computational systems of today.

The need to use a finite-element structural model in association with a load calibration was graphically illustrated when the B-2 load calibration was discussed. Surface areas on airplanes that cannot be loaded frequently exist, such as in the case of the B-2 airplane. However, if a finite-element model of an airplane could be used to develop an analytical load calibration in lieu of a physical loading, the financial savings would be a major factor in the overall development cost. The degree to which augmentation, hybridization, and analytics are used in computational load calibrations is a scenario that has yet to be actualized. The important element is that the time for computational load calibrations has come.

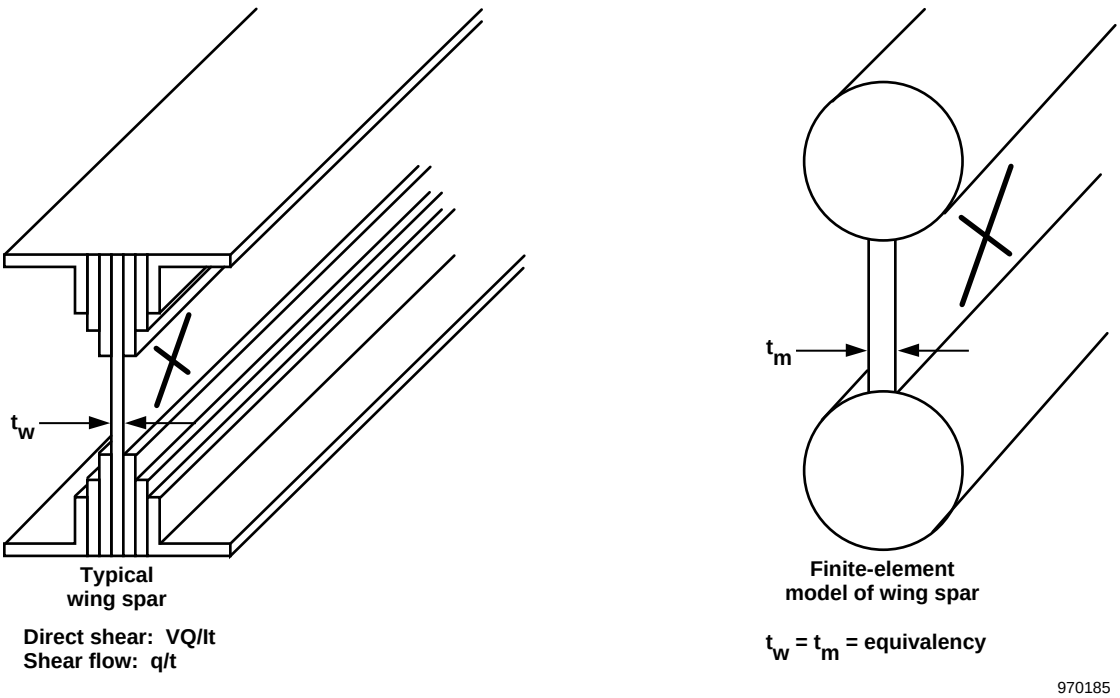

Figure 91. Wing and model thickness compatibility with respect to shear strain.

Anisotropic Structures

When an aircraft structure fabricated of anisotropic materials requires a strain-gage load calibration, some of the approaches presented in this report may not work. The strain response of an anisotropic material will be different from that of an isotropic material that is subjected to the same physically applied load. Much of this report has been directed toward interpreting what the influence-coefficient plots mean in terms of formulating the appropriate relationships pertinent to the strain-gage load calibration. A different avenue of thinking is therefore necessary for anisotropic structures.

Anisotropy impacts two areas in a major way. The influence-coefficient plots cannot be interpreted in the same manner as those previously shown in this report for isotropic structures; therefore, the strain-gage selection process for the equations will be less straightforward for anisotropic structure than for isotropic structures. Also, because the degree and nature of anisotropy include such a wide range of possibilities, traditional strain-gage bridge configurations may have to be tailored to the character of the particular anisotropic ply lay-up. Considerably more work will be involved in managing a strain-gage load calibration of a structure that is anisotropic. The loads engineer will have to use the science developed for isotropic structures as the baseline and create whatever additional science that is appropriate and necessary to do the job.

Relevance Coefficient

Figure 92 shows a distribution of all of the relevance coefficients for the structures presented in this document. A magnitude in the range of 0.6 to 0.7 appears to be the normal value, which means that the range of loads covered an average of approximately 60 to 70 percent of the effective structural lifting surface. The basic premise of the relevance coefficient was to establish a parameter that would relate to or result in an improved load-measurement

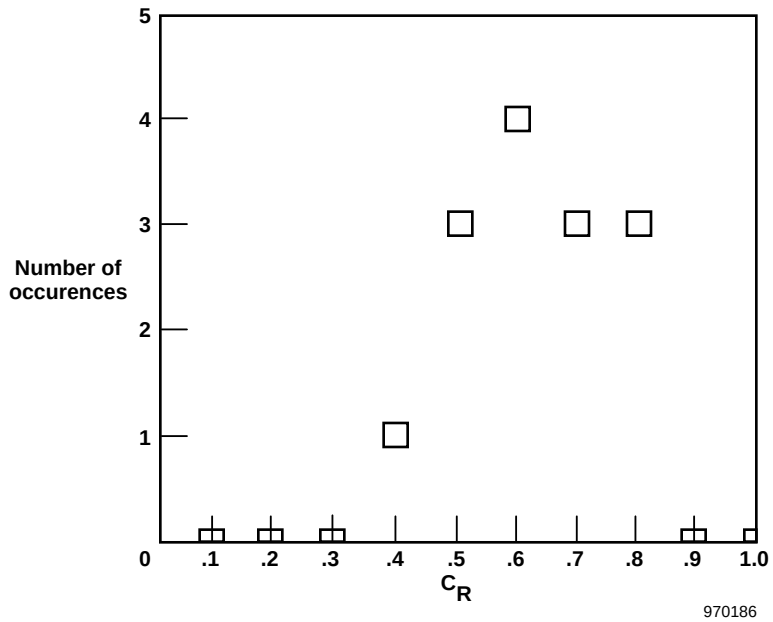

Figure 92. The distribution of relevance coefficients for the presented load calibrations.

accuracy. This premise is examined in figures 93, 94, and 95, where the error is plotted as a function of the value of relevance coefficients for shear, bending, and torsion measurements for those calibrated surfaces that have a stated error. No trend appears to exist in any of these three figures, which is disappointing. However, the previous discussion in the Load Calibration Relevancy and Load Measurement Error section should be referred to, where the basic difference between the load calibration error and the flight load measurement error is discussed. Some of the errors stated for the calibrated structures (figs. 93, 94, and 95) refer to load calibration error, and some refer to an estimate of the flight load measurement. If a national standard for stating these errors had been available, then the data presented in figures 93, 94, and 95 might show a meaningful result. Until a standard is established for the measurement error, the meaning and usefulness of the relevance coefficient will remain unknown.

Shear Flows

The majority of strain-gage bridges used for load measurements are configured to measure shear, because shear loads and torsional loads are primarily sensitive to shear flow. Loads that are eccentrically located with respect to the axis of a wing induce torsional moments that in turn create shear flow patterns around the webs and skins that form the individual cells of an airplane wing. The resulting torsional moments are an important load that is sought during flight test. The same loads also result in flexural shear flows in the webs of the same wing. In general, the shear flow in the webs of wings results from both torsional loads and direct shear loads. The shear flow in the skins of wings is primarily caused by the torsional loads. The relative proportions of shear flows in webs and skins is a function of several parameters. The configuration of the cells, the distribution of the structure, and the sweep angle are the primary parameters that affect the relative proportions of the shear flows.

The nature of the shear flows is such an important aspect of strain-gage load calibrations that it was decided to computationally study shear flows using a generic model. The straight-wing three-cell configuration shown in figure 96 was chosen as an initial subject. The basic approach was to examine shear strains at the center of the webs of inner and outer spars and at the center of the outer and middle skins. A grid of loads (fig. 96) was applied individually to the generic structure, and shear strains were analytically calculated. The three structural distributions shown in figure 97 were chosen so that a balanced structure, a skin-dominant structure, and a web-dominant structure could be examined parametrically.

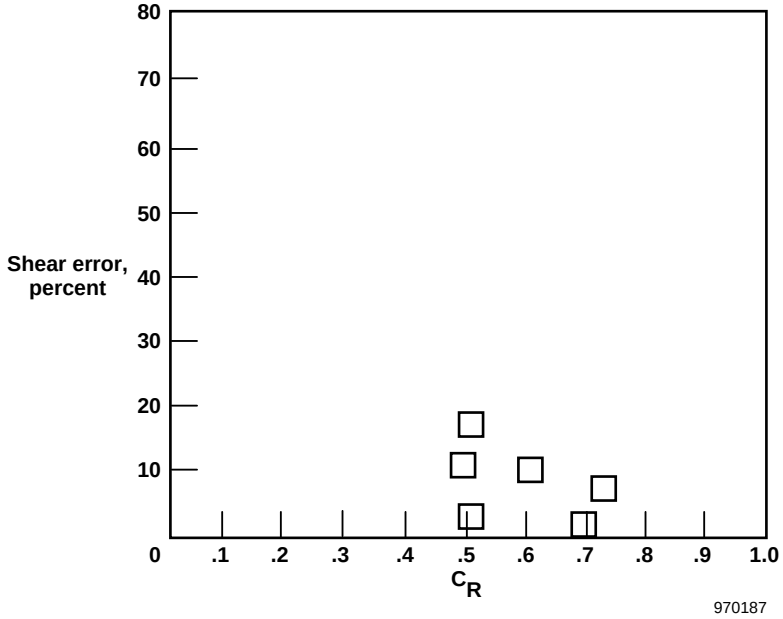

Figure 93. The variation of the shear equation error with the value of the relevancy coefficient.

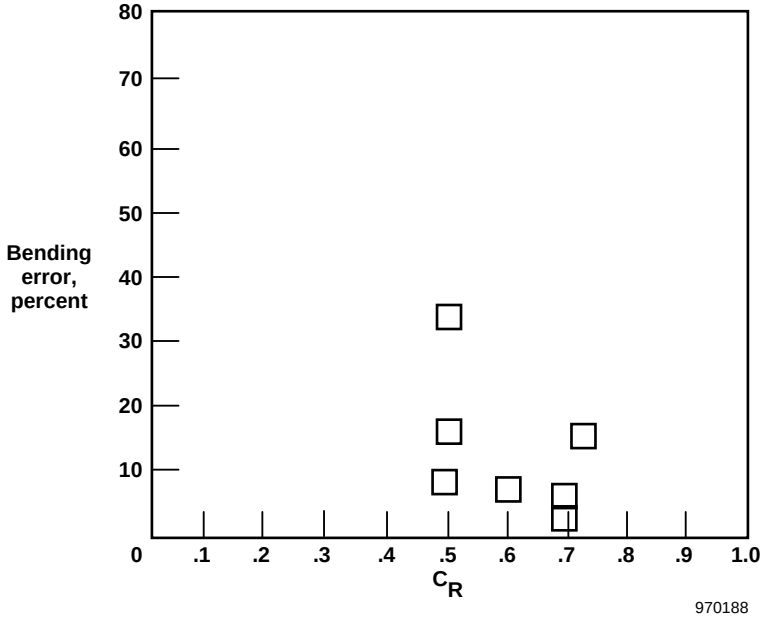

Figure 94. The variation of the bending-moment equation error with the value of the relevancy coefficient.

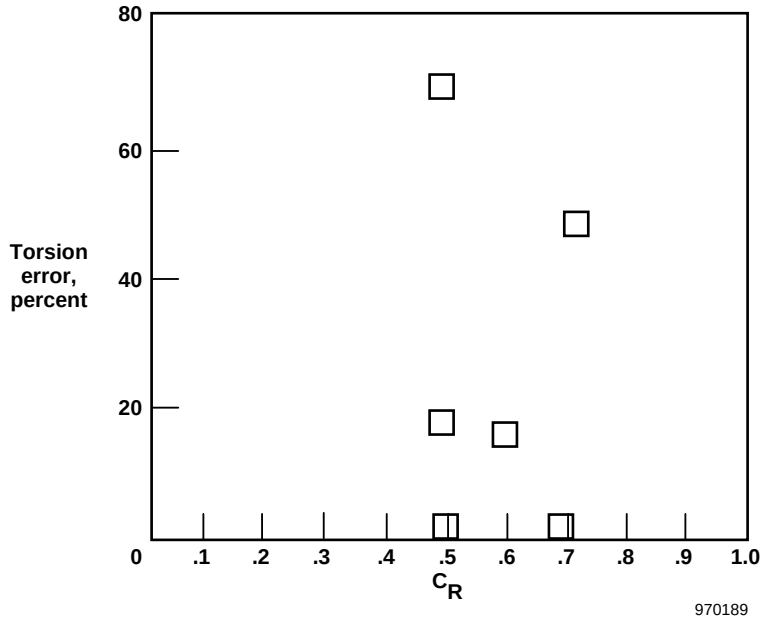

Figure 95. The variation of the torsion equation error with the value of the relevancy coefficient.

Figures 98 to 101 show basic information regarding shear-flow response to loads applied to the generic model. The characteristics are presented in influence-coefficient form so that the reader can project what trends may ensue for various parameters. The influence-coefficient plots shown in figure 98 are for a strain-gage bridge located on the outer web of the generic structure. The data indicates a strong torsion/shear complex when the skin is dominant and a good shear response when the web is dominant. The information presented in figure 99 is for a torsion bridge located on the outer skin. The dominant characteristic for this case is seen as a large torsional response when the web is dominant. Figure 100 shows the influence-coefficient plots for a shear bridge located on a center spar of the generic structure. A low-level but near perfect shear response results for the balanced structure case. A high-level response somewhat contaminated by torsion is seen for the skin-dominant case. Figure 101 shows results for a shear bridge located on the center skin of the generic structure. The influence-coefficient plots show very little response for the balanced and skin-dominant cases. A large torsional response exists for the web-dominant case.

The results for the generic wing structure provide insight, but the scope of the information is limited. Because the generic wing structure is a straight wing, varying other parameters such as the sweep angle results in influence-coefficient plots that exhibit considerably different characteristics than those shown in figures 98 to 101. The main reason for presenting this information is to encourage the loads engineer to study the mechanics of the strain-gage responses of each structure that is to be load calibrated.

CONCLUDING REMARKS

The issues, lessons, rules, problems, and observations associated with the strain-gage load calibration of 14 aircraft structures have been the focus of this document. The goal has been to consolidate the science as much as possible to facilitate future efforts directed toward measuring loads on aircraft with calibrated strain gages. The primary result has been to identify the issues rather than establish rules and laws. The matrix of variables has been concluded to be too large to constrain the options available to an engineer responsible for measuring loads. Therefore, most of the salient features of strain-gage load calibrations have been addressed, and the nature of most aircraft structures has been included.

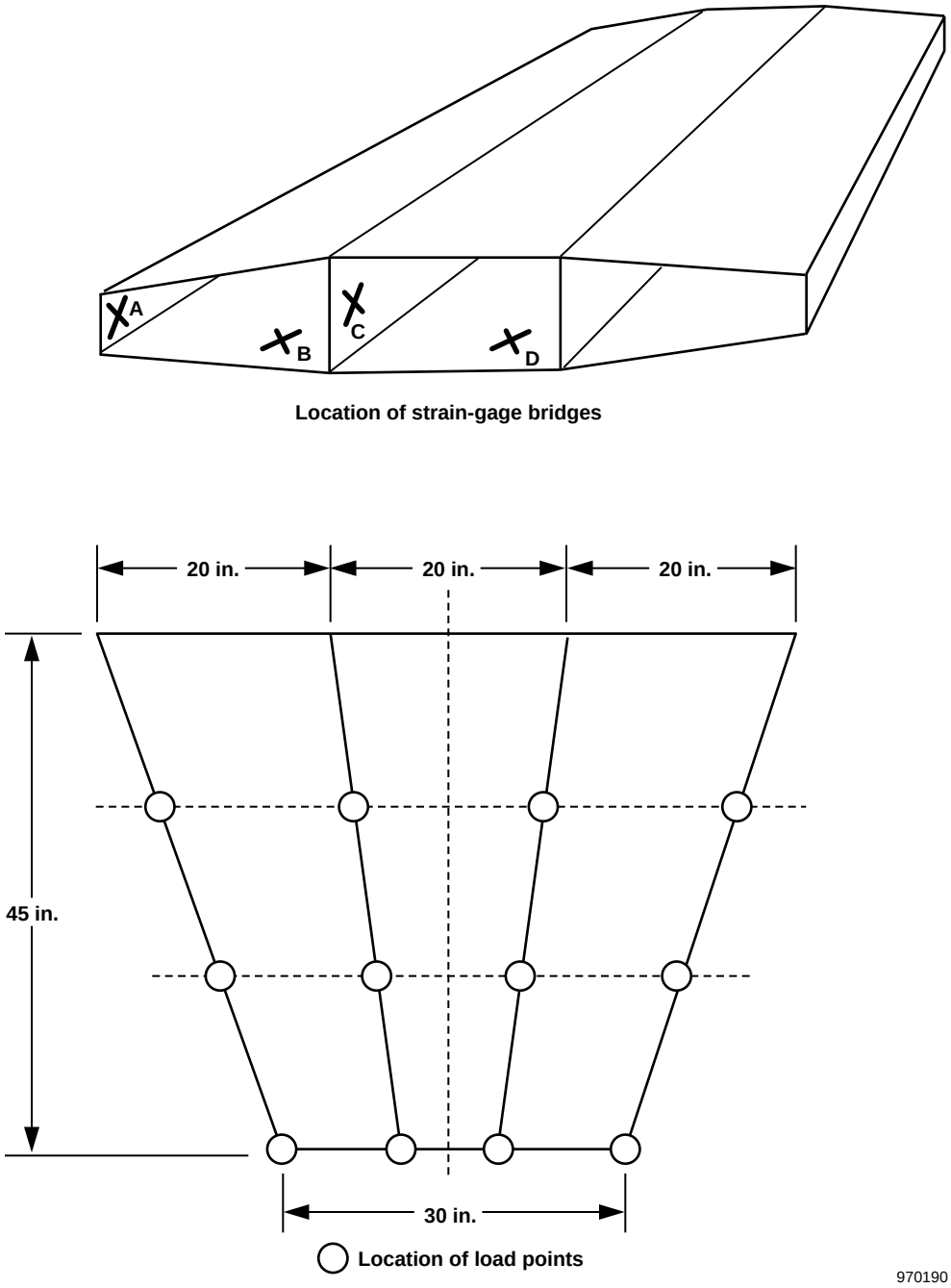

Figure 96. Physical description of generic wing used to study shear-flow patterns.

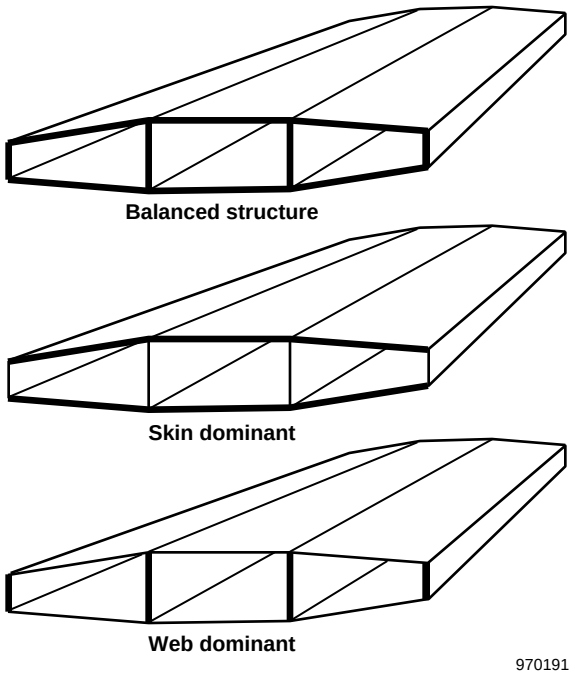

Figure 97. Illustration of three structural distributions used to study shear-flow patterns.

The configuration and location of strain-gage bridges have been examined and related to the nature of internal loads. The various factors affecting the number of strain-gage bridges required for valid load equations were discussed. Several methods of deriving loads equations have also been discussed, along with approaches used in automatic strain-gage bridge selection. Considerable discussion has been presented about the relevancy of the loading and the relationship to the error of the measurement.

The geometry of the planform of the structure to be calibrated has been discussed in terms of aspect ratio as the aspect ratio relates to measurement errors and equations. The basic methods of using influence-coefficient plots to select strain-gage bridges for the equations and to identify general load calibration integrity have been presented. The existence of local root effects associated with calibration loads that are close to the strain-gaged axis was identified and discussed. Nonlinearities associated with the influence-coefficient plots have also been discussed in terms of using nonlinear approaches. The state of the art of computing influence coefficients from finite-element models has been presented. The uniqueness of anisotropic situations has been presented and approaches have been discussed. The pertinence of the relevance coefficient with respect to the error of the load measurement has been presented. A generic, three-cell wing-type structure has been used to define the mechanics of shear flow as shear flow relates to various structural parameters.

The Discussion section has expounded upon the components of a check list that should be addressed subject-by-subject when any strain-gage load calibration is undertaken:

- location of strain gages
- selection of load points
- number of strain gages in loads equations
- derivation of equations

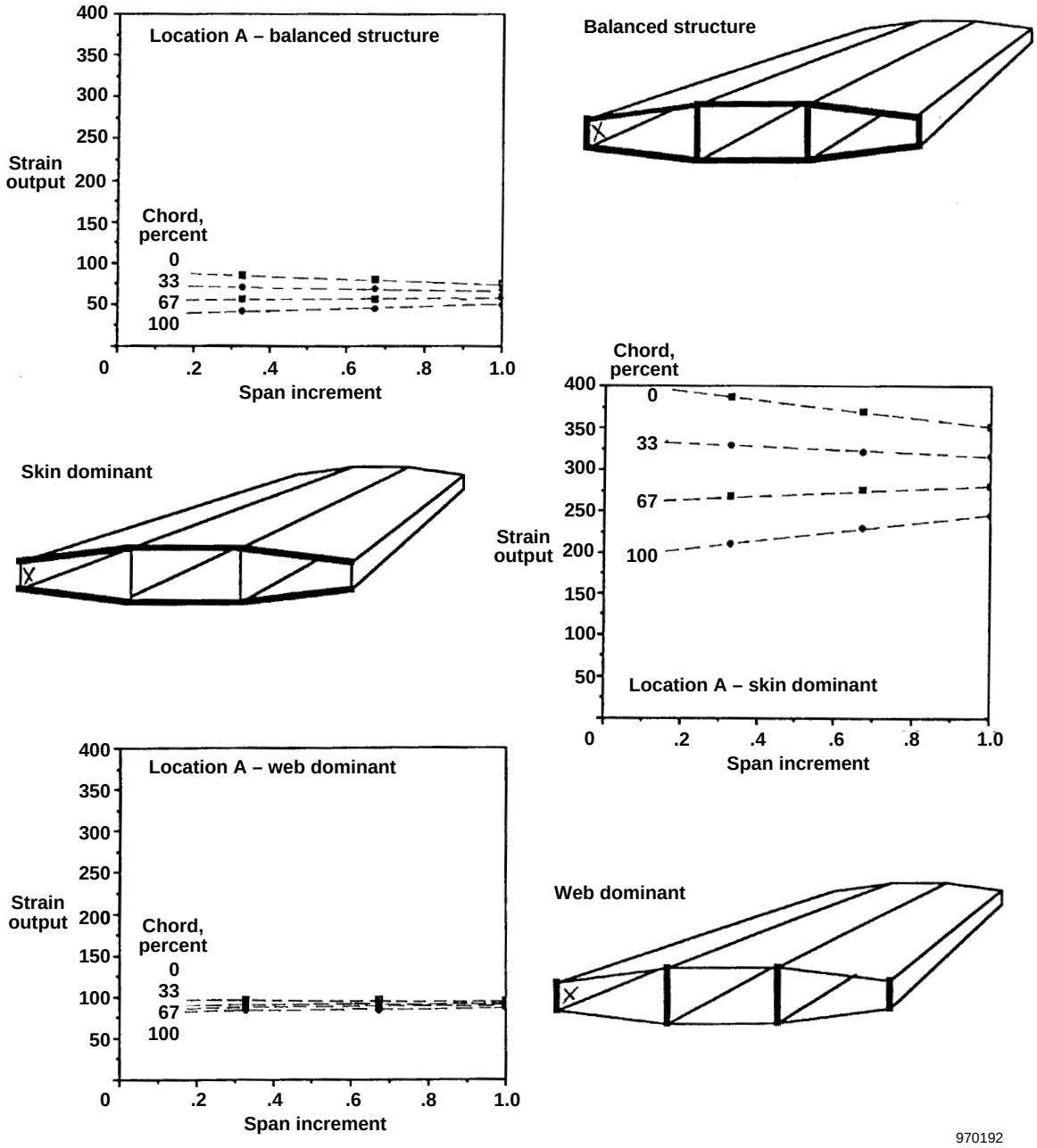

Figure 98. Influence-coefficient plots for three structural distributions used to study shear-flow patterns at location A.

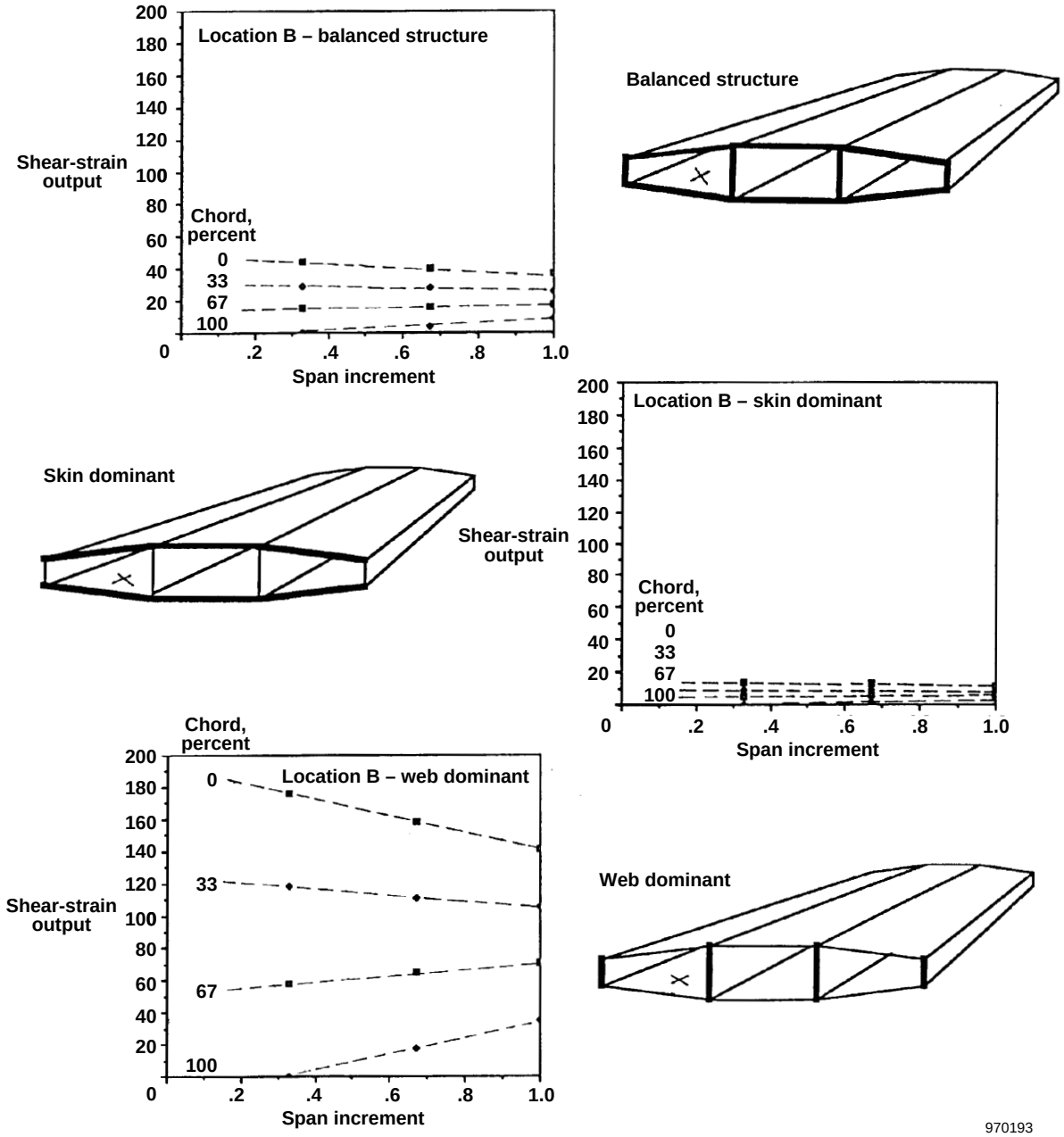

Figure 99. Influence-coefficient plots for three structural distributions used to study shear-flow patterns at location B.

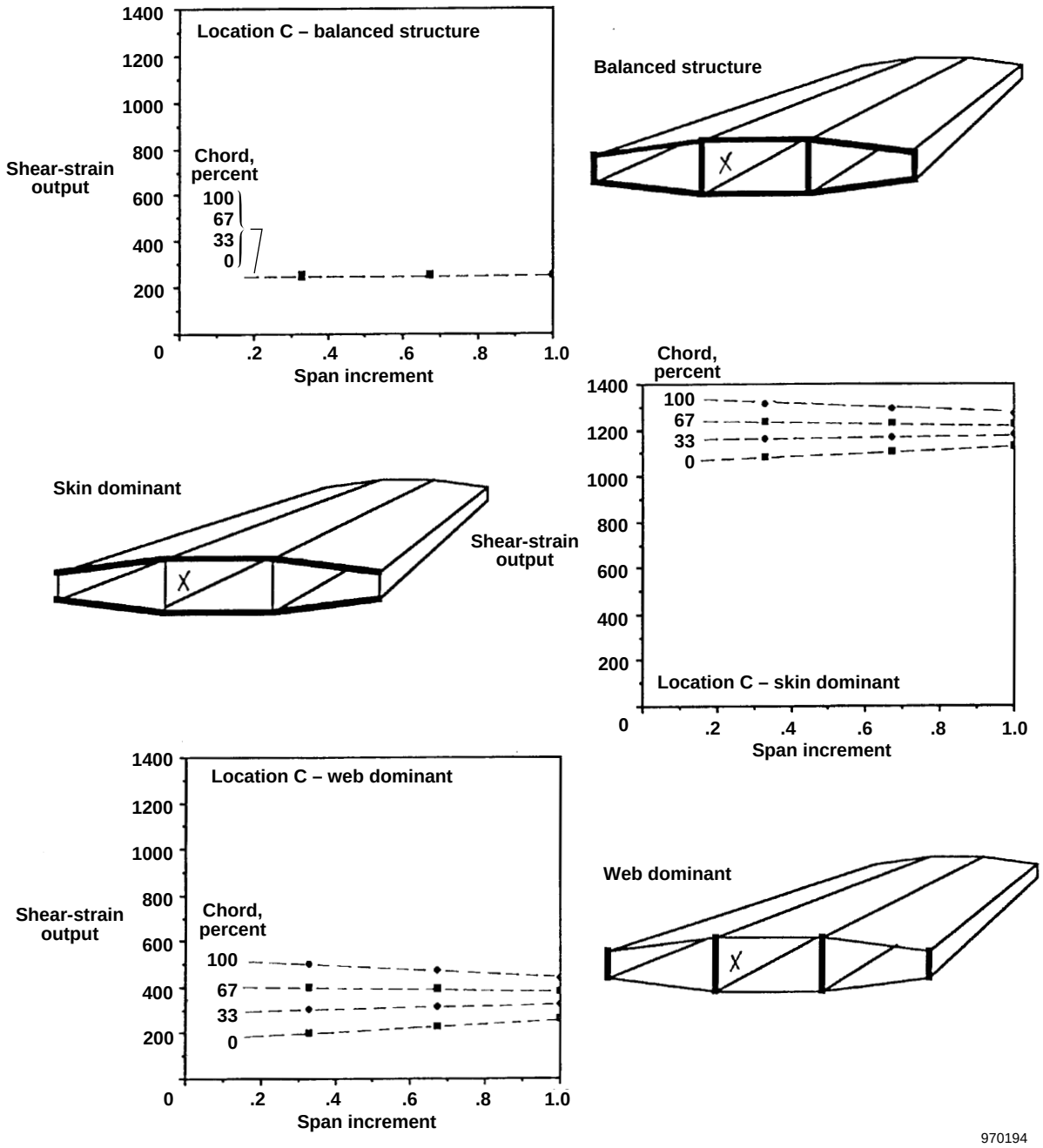

Figure 100. Influence-coefficient plots for three structural distributions used to study shear-flow patterns at location C.

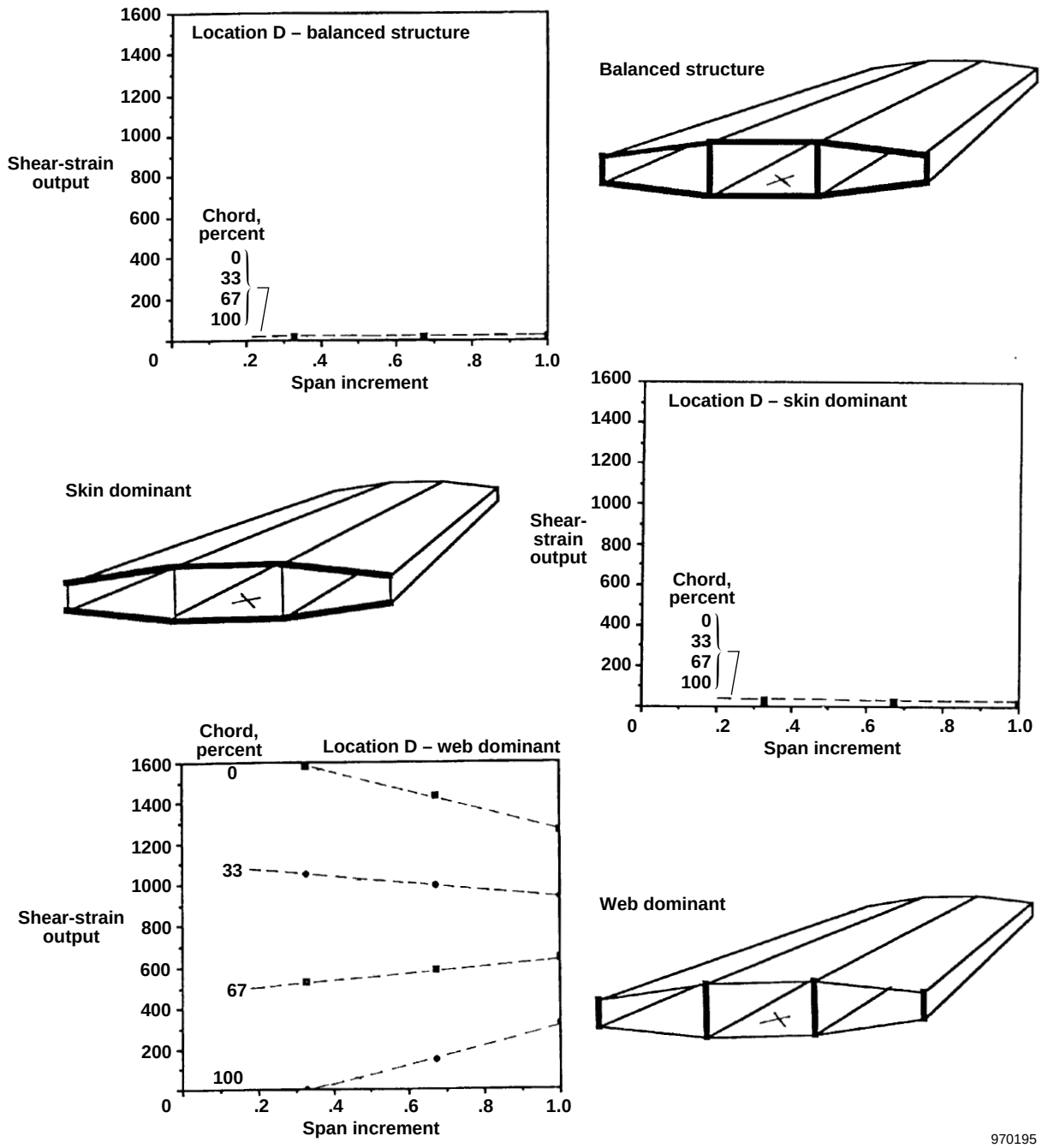

Figure 101. Influence-coefficient plots for three structural distributions used to study shear-flow patterns at location D.

- automated strain-gage selections
- load calibration relevancy and load measurement error
- point- and distributed-load calibrations
- planform aspect ratio
- influence-coefficient plots
- local root effects
- nonlinear approaches
- computational strains
- anisotropic structures
- relevance coefficient
- shear flows

Some of these subjects will obviously not be pertinent to specific cases. For those subjects that are applicable, however, all aspects of each subject should be considered for impact on the strains of the load calibration and ultimately the flight load measurement.

Dryden Flight Research Center
National Aeronautics and Space Administration
Edwards, California, January 27, 1997

APPENDIX A

SKETCHES OF AIRCRAFT

This appendix contains sketches of twelve aircraft that are subjects considered in the text of this report. Some of the sketches are three-view, and some are plan-view. The purpose of these sketches is to show how some of the structures interact with the rest of the aircraft.

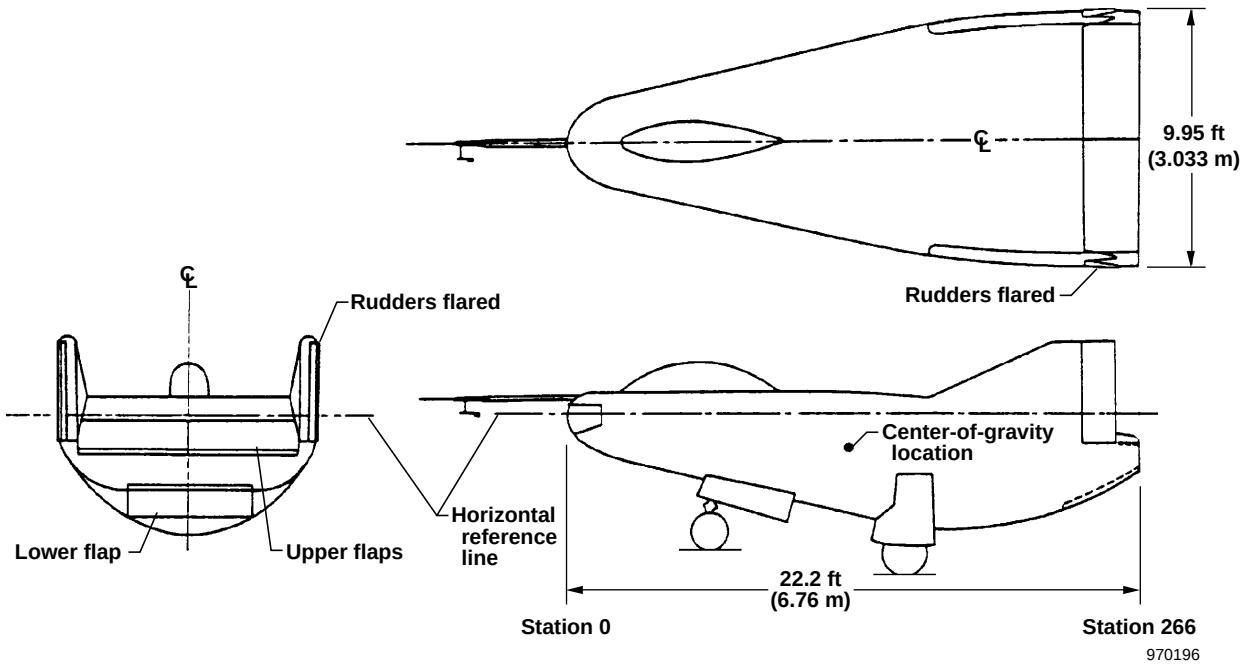

(a) M2-F2 lifting body.

Figure A-1. Description of aircraft presented in this document.

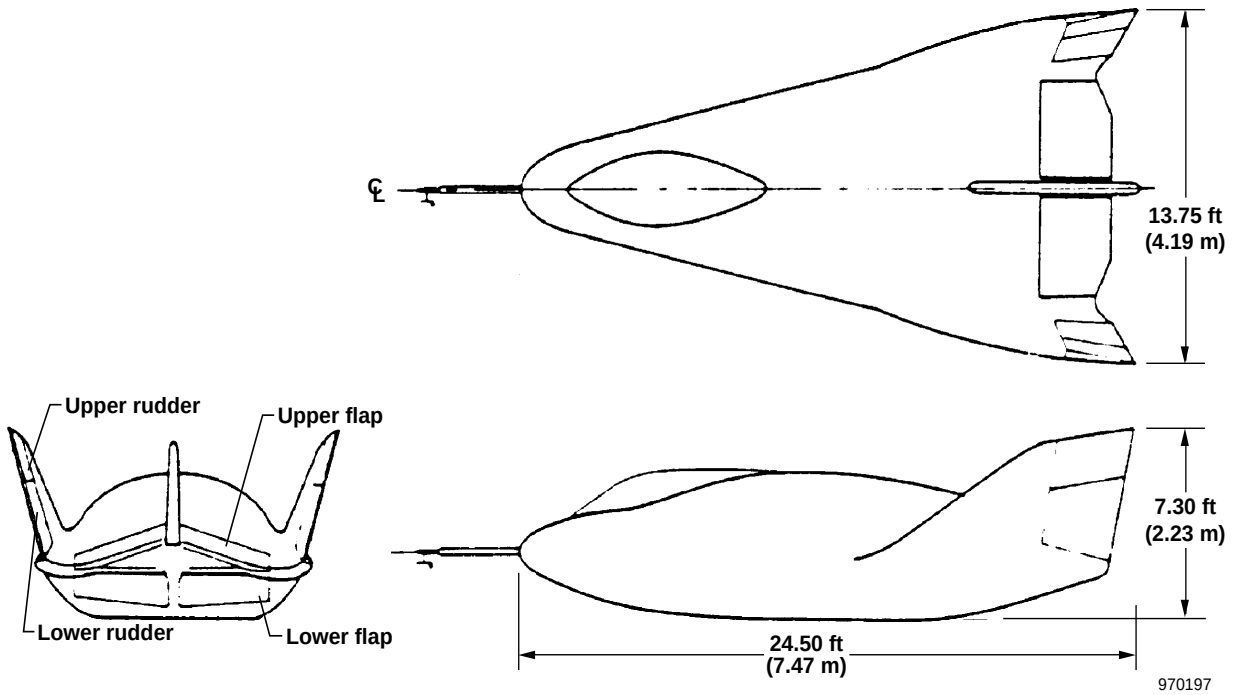

(b) X-24A lifting body.

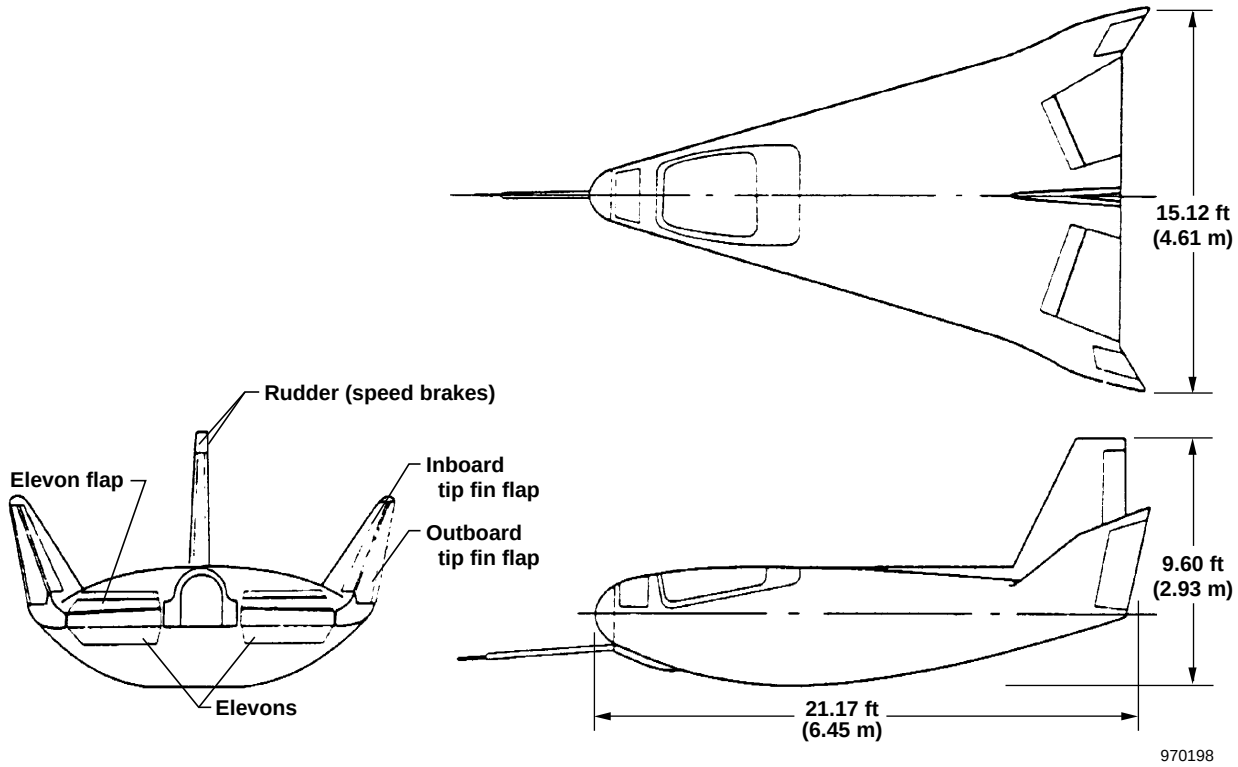

(c) HL-10 lifting body.

Figure A-1. Continued.

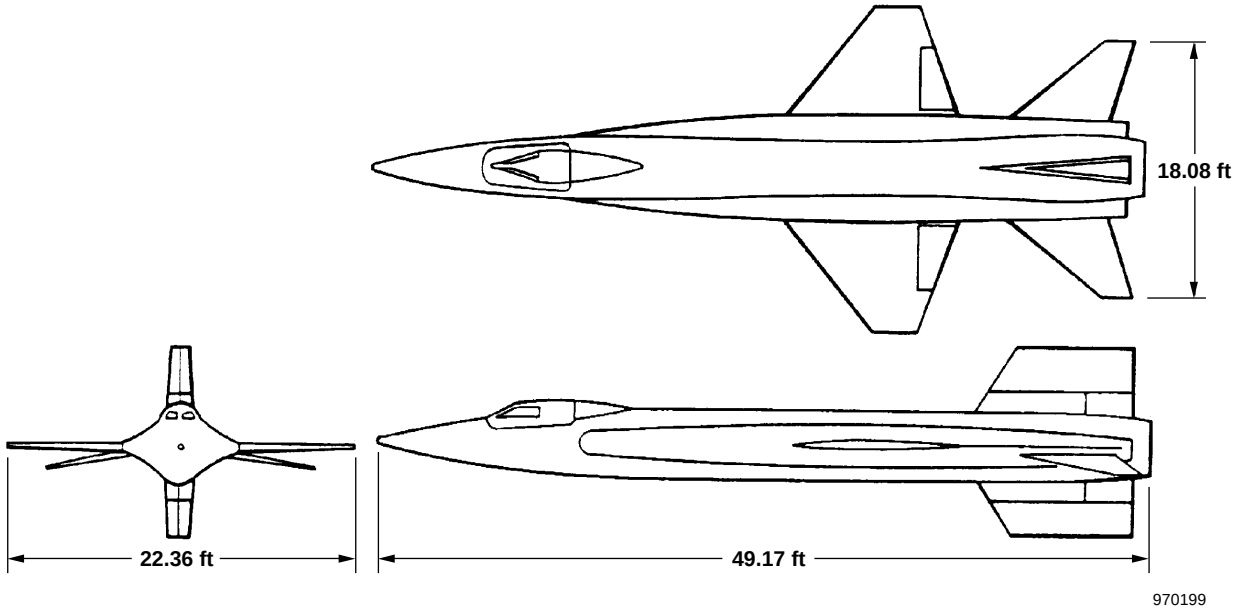

(d) X-15 aircraft.

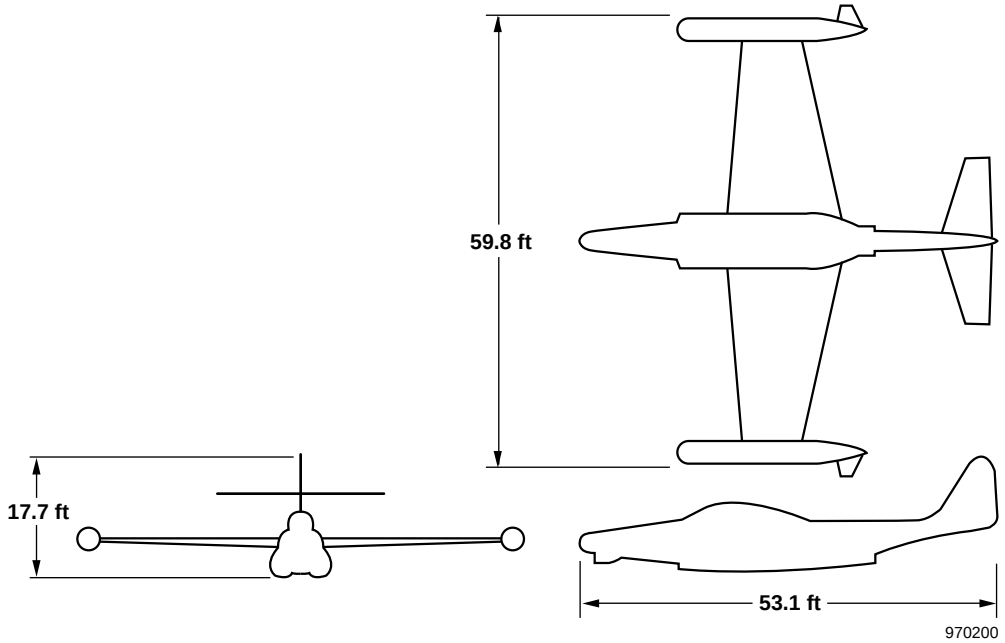

(e) F-89 aircraft.

Figure A-1. Continued.

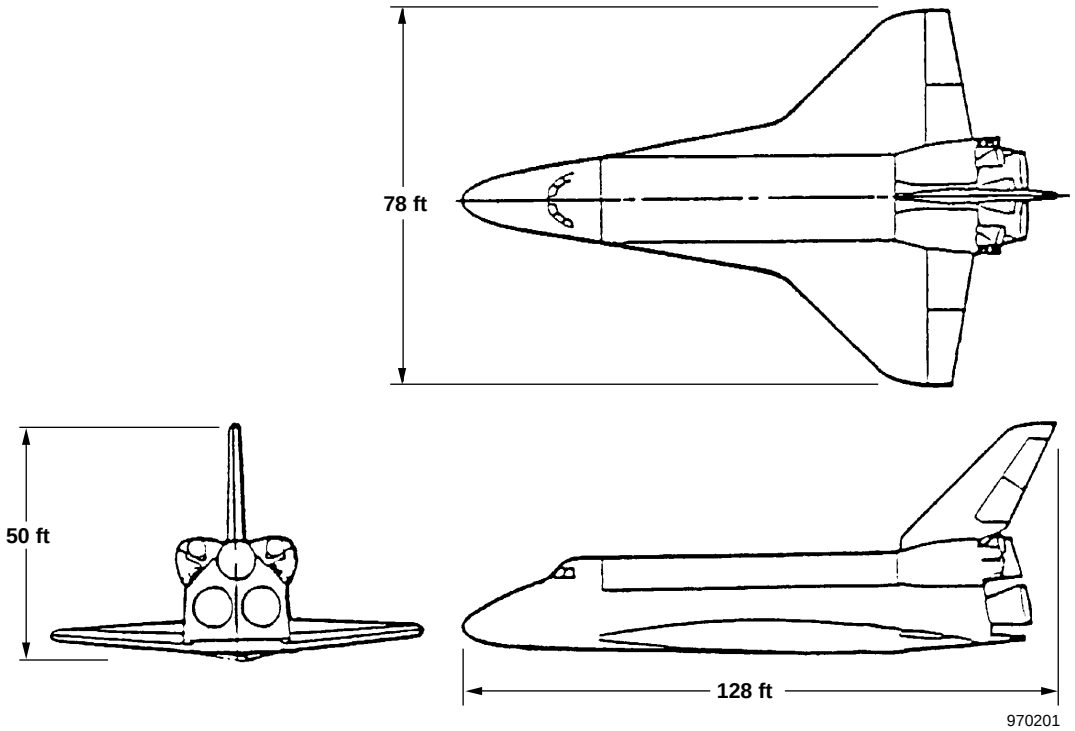

(f) Space Shuttle Orbiter.

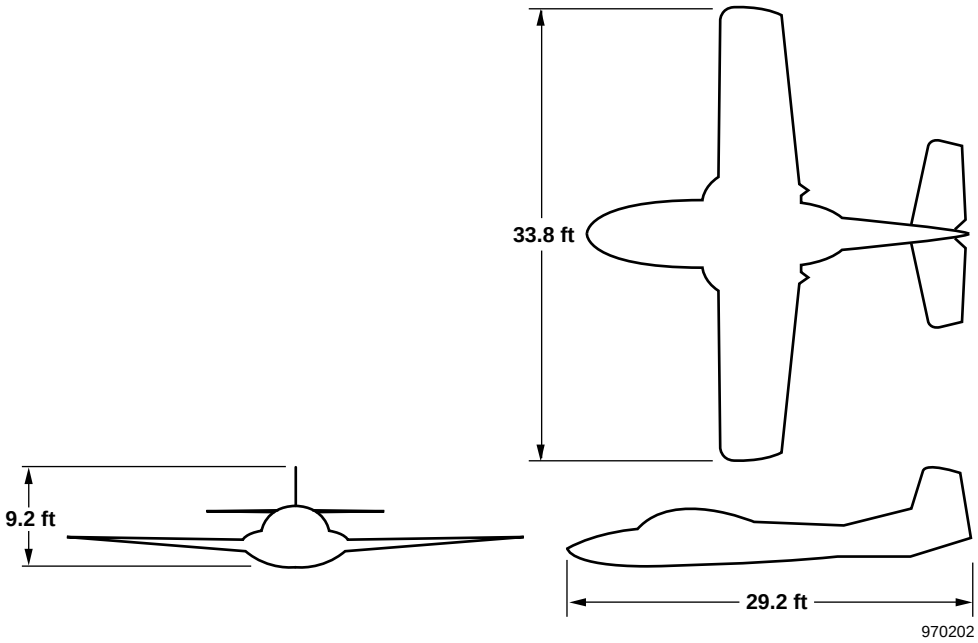

(g) T-37B aircraft.

Figure A-1. Continued.

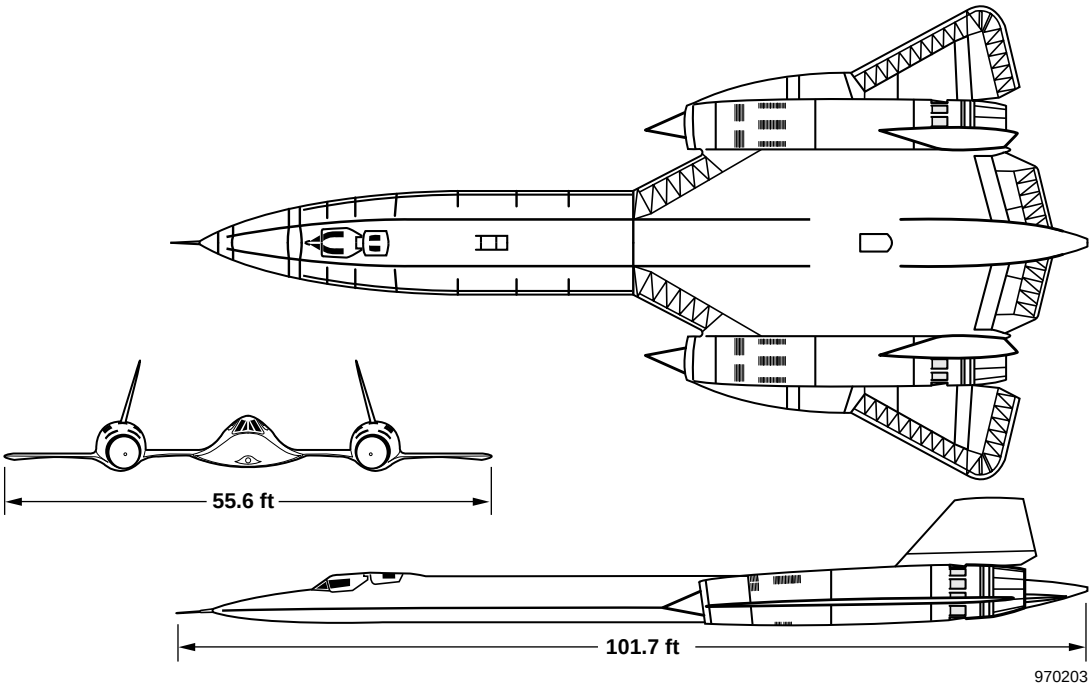

(h) YF-12A aircraft.

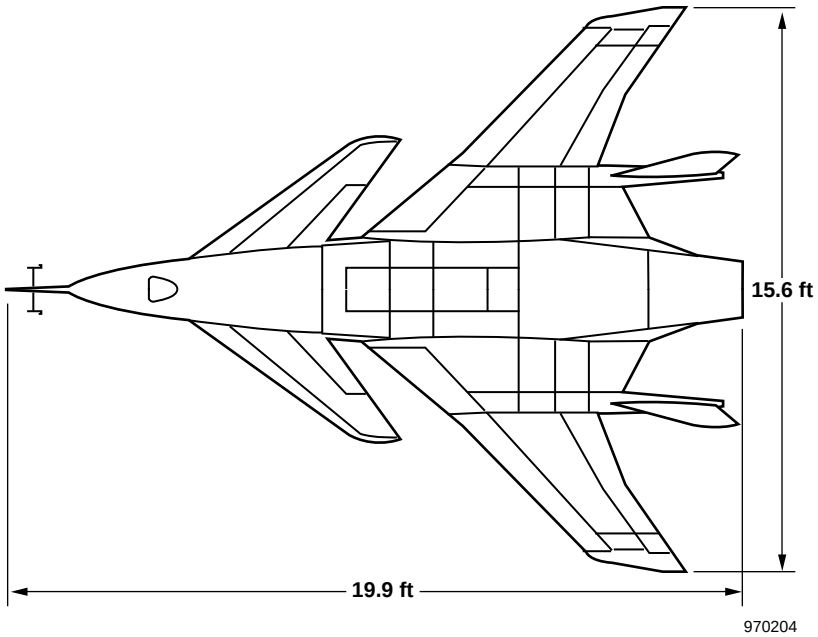

(i) HiMAT aircraft.

Figure A-1. Continued.

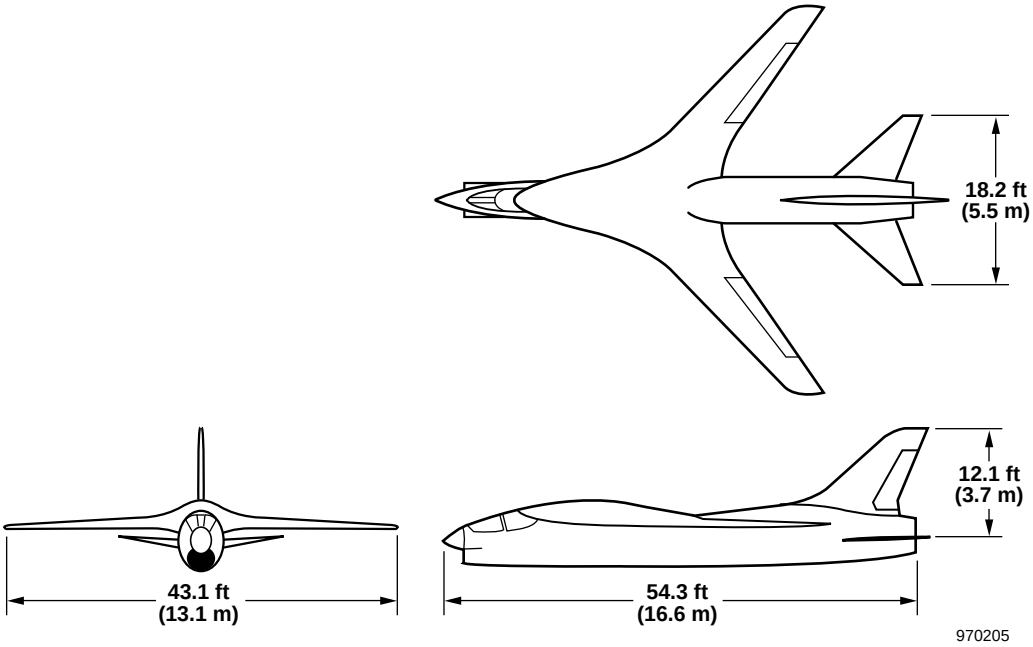

(j) Supercritical wing aircraft.

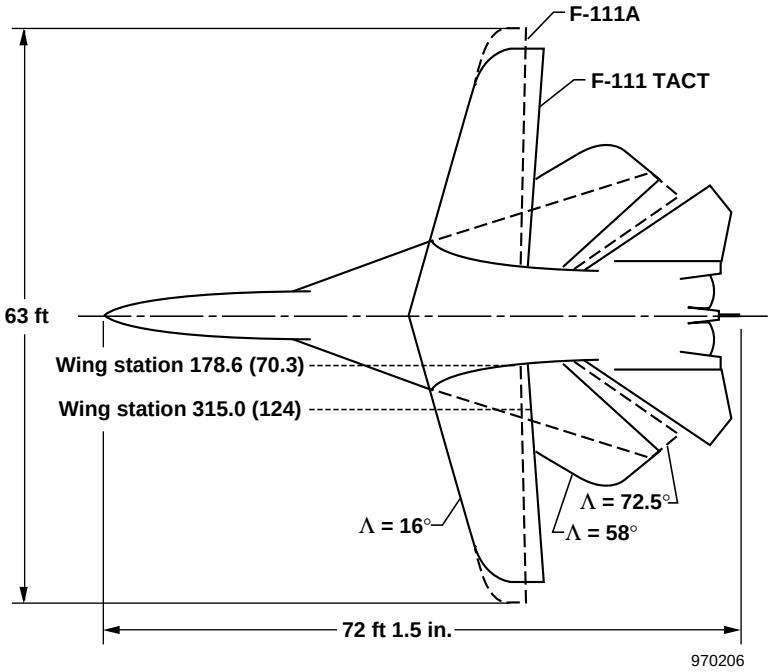

(k) F-111A/F-111 TACT aircraft.

Figure A-1. Continued.

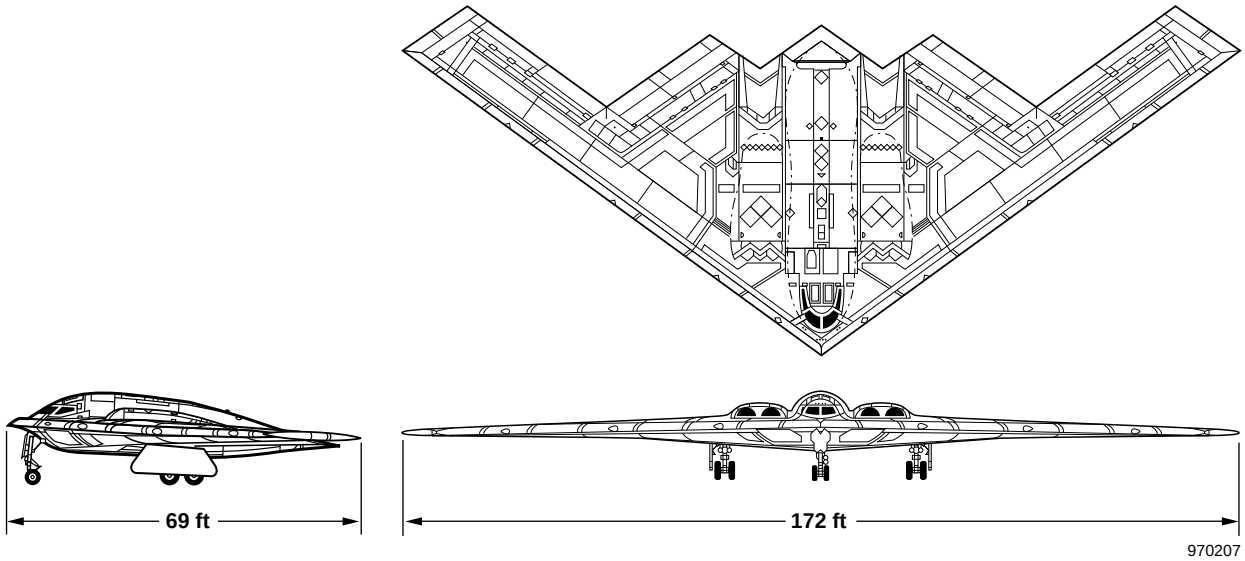

(l) B-2 aircraft.

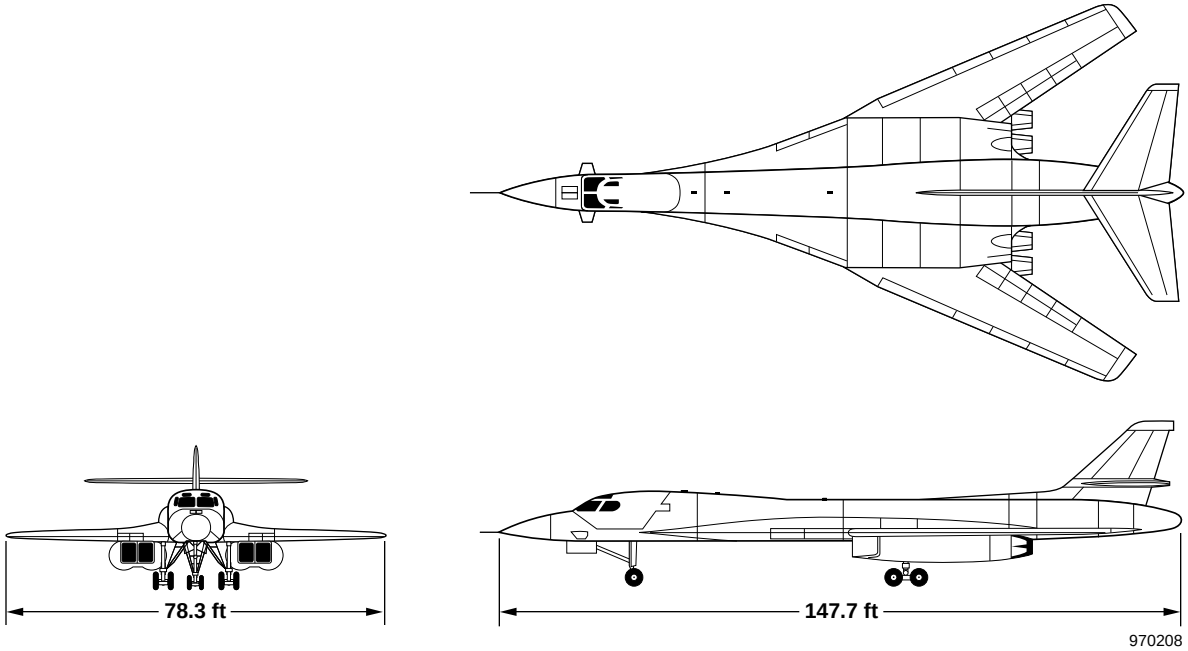

(m) B-1 aircraft.

Figure A-1. Concluded.

APPENDIX B

METHOD FOR CONVERTING LABORATORY STRAIN-GAGE BRIDGE DATA TO DISCRETE STRAINS

The basic equation relating strain-gage bridge electrical output with strain is

$$e_o = \left(\frac{\mathrm{N}}{4}\right)(\mathrm{GF})(\varepsilon)(E_X)$$

or

$$\varepsilon = \frac{4(e_o)}{(\mathrm{N})(\mathrm{GF})(E_X)}$$

where

e_o = output voltage

N = bridge factor (dependent upon the stress/strain relationship and the bridge configuration)

GF = gage factor

E_X = excitation voltage

The basic task that needs to be done in estimating the discrete strains is to determine the bridge factor N. The array of bending bridges shown at the right are usually wired in the bridge as shown at the left. Note that the signs would be reversed if the bending-moment direction were reversed.

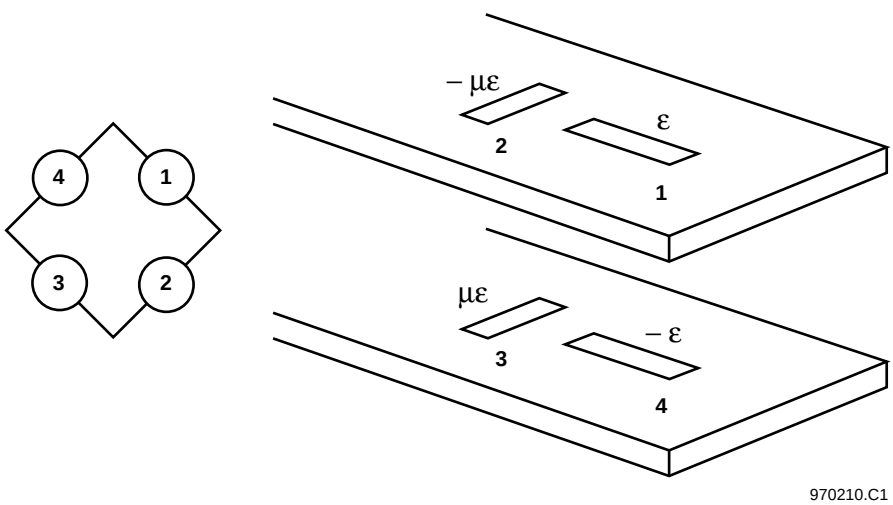

The total effectiveness or the bridge factor is as follows:

$$N = \text{Gage 1} + \text{Gage 3} - \text{Gage 2} - \text{Gage 4}$$
$$N = \varepsilon_1 + \mu\varepsilon_3 - \mu\varepsilon_2 - \varepsilon_4$$
$$N = 1.00 + 0.33 + 0.33 + 1.00$$
$$N = 2.67$$

Therefore, the discrete bending strain at location 1 is as follows:

$$\varepsilon = \frac{4(e_o)}{2.67(\mathrm{GF})(E_X)}$$

The array of strain gages shown at the right is usually wired in the bridge as shown at the left. Note that the signs of the individual strain gages would reverse if the direction of the shear were reversed.

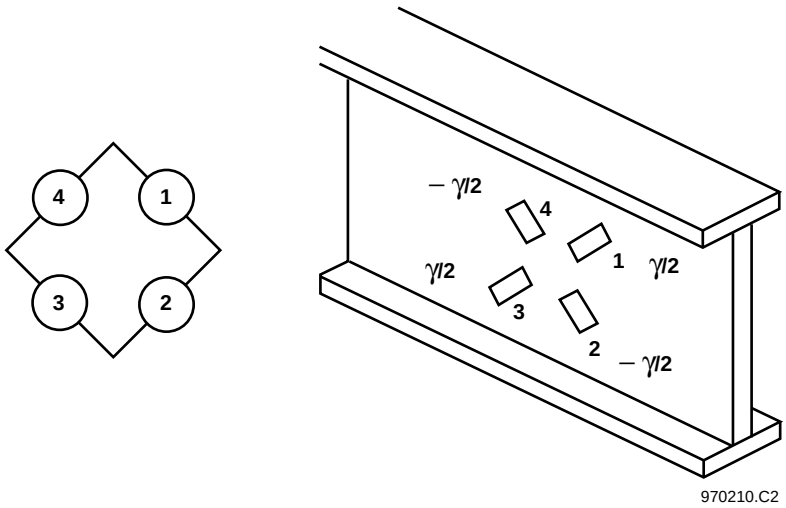

For a shear bridge, the total effectiveness or the bridge factor is as follows:

$$N = \frac{\gamma_1}{2} + \frac{\gamma_3}{2} - \frac{\gamma_2}{2} - \frac{\gamma_4}{2}$$

All shear strains are presumed to be the same and are considered to be discrete at the center of the strain-gage grouping. Therefore,

$$N = 2.0$$

Therefore, the discrete shear strain at the center of the bridge location is as follows:

$$\gamma = \frac{4(e_o)}{2.0(\mathrm{GF})(E_X)}$$

APPENDIX C

PHILOSOPHY OF THE YF-12A FINITE-ELEMENT MODEL

Each spar and rib is idealized as an upper and lower cap connected by a vertical shear web. For example:

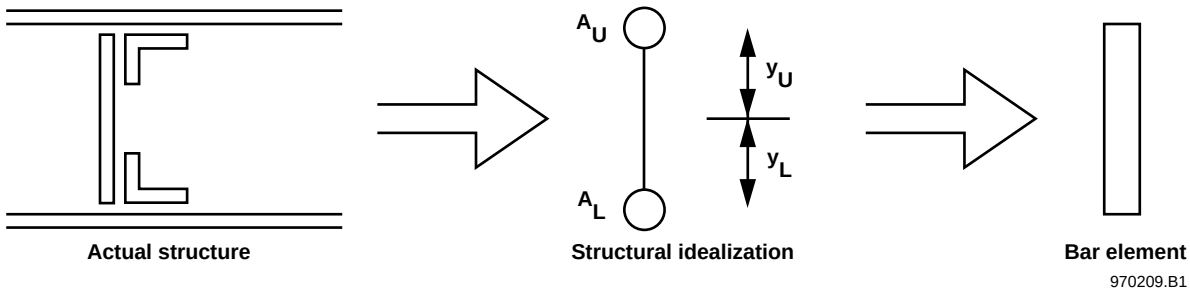

The cap area is considered to be the sum of the actual spar cap and a portion of the cover skin. For example:

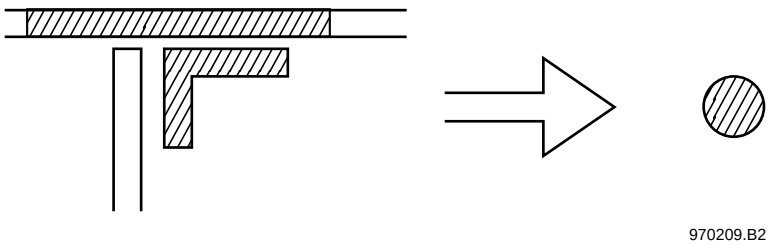

The amount of cover skin considered effective was determined from tests conducted by the manufacturer. The model beam inertias were computed from the magnitude and centroid location of these effective cap areas. For example:

$$I = A_U y_U^2 + A_L y_L^2$$

The nacelle spanwise bending was represented by equivalent beams that gave the same bending and shear stiffness as the actual nacelle rings:

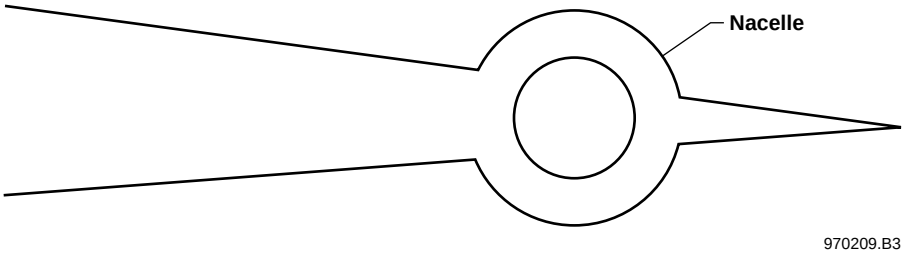

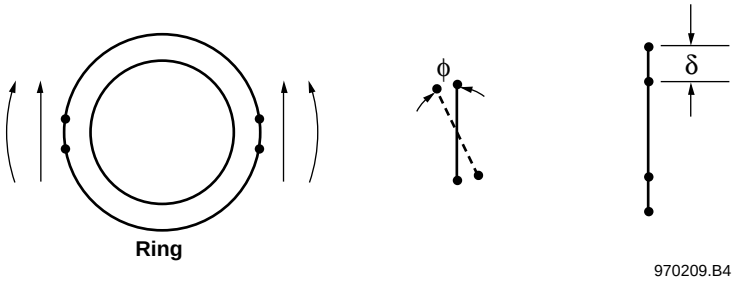

The nacelle ring was replaced with a beam of equivalent rotation and displacement for each unit of load.

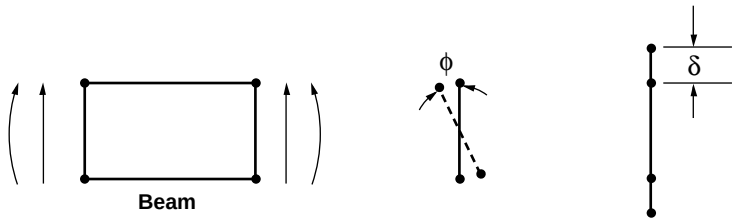

970209.B5

Hence, the model is represented as:

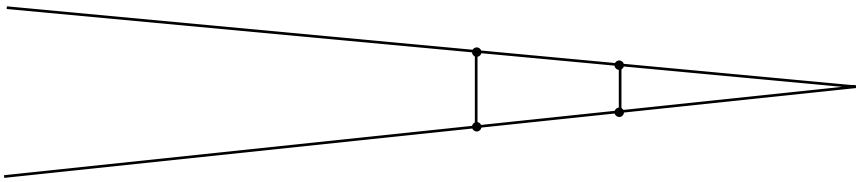

970209.B6

The wing beams are continuous across the fuselage for bending, and the wing shear loads are distributed to the fuselage through the wing root rib:

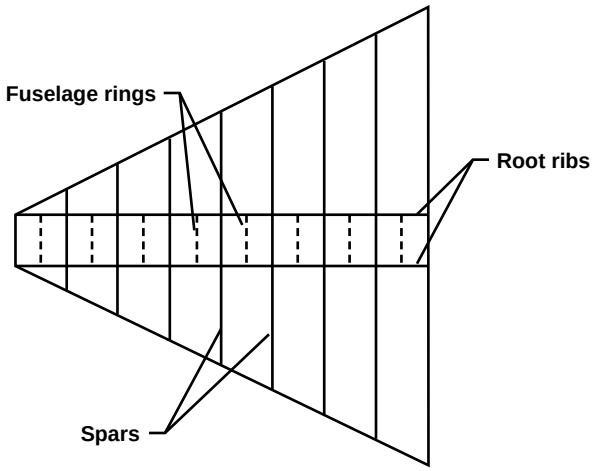

970209.B7

The model spanwise beams were carried into the centerline of the fuselage. The fuselage itself was represented by longitudinal beams simulating the bending stiffness of the fuselage shell and the shear stiffness of the wing by the root rib. Torsional stiffness of the wing was distributed to the spars and ribs (because no cover plates exist) by computing an equivalent polar moment of inertia for the model beams based on the torque box area and the effective skin thickness.

The structure basically looks like this:

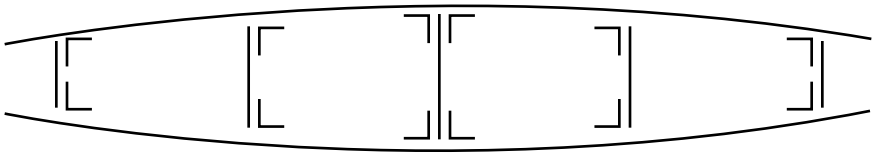

970209.B8

The model looks like this:

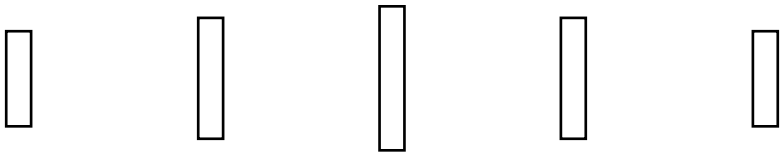

970209.B9

The stiffness is determined by:

$$J = 4 A^2 \frac{t}{p}$$

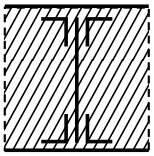

970209.B10

where

A = area of the cell formed by beams, webs, and upper and lower skins

t = average skin thickness

p = perimeter of the cell

Torsional stiffness of longitudinal beams representing the fuselage and nacelle was determined in a similar manner.

APPENDIX D

THE METHOD OF OBTAINING STRAINS FROM THE NASTRAN MODEL

The model is composed of BAR elements. A BAR element can be described by the following sketch:

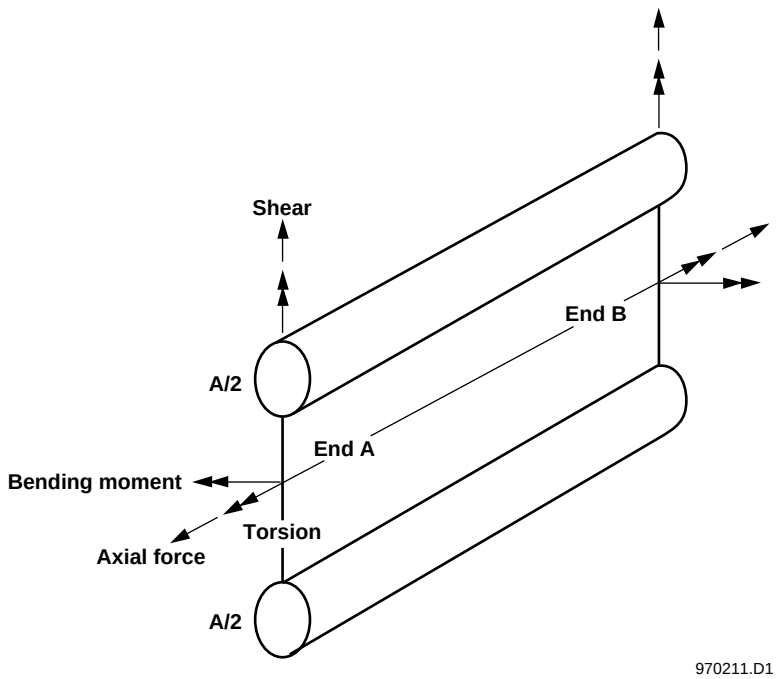

NASTRAN prints out the following for BAR elements:

- bending moments at both ends
- shears in two planes
- average axial force
- torque about the BAR axis

To decrease the number of elements, the following shortcut was used. If part of the actual structure has five spars, as shown below:

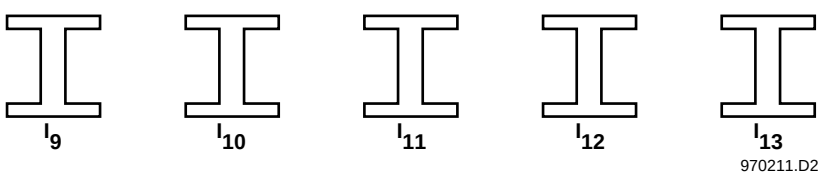

and if *I* represents the moment of inertia of spars 9, 10, 11, 12, and 13; then a single spar located at 11 can be represented by the moment of inertia of spar 11 plus one-half the moment of inertia of spars 10 and 12, as shown below:

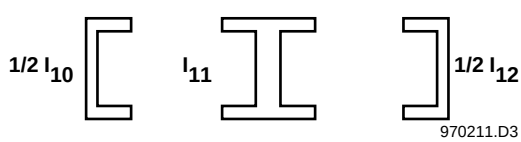

This combined structural member could be represented by the two lumped masses and the web to form a BAR element that includes the following:

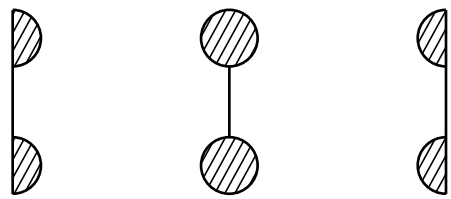

970211.D4

The moment of inertia of this combined element is

$$I_{BAR} = \frac{1}{2} I_{10} + I_{11} + \frac{1}{2} I_{12}$$

The torsional moment is found by the following method:

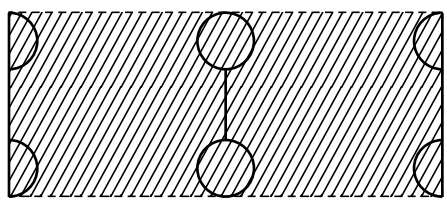

970211.D5

$$J = 4\,A^2\,\frac{t}{p}$$

where

A = Area of the cell formed by beams, webs, and upper and lower skins

t = Average skin thickness

p = Perimeter of the cell

To convert the shears and bending moments from the BAR elements to strains, the following procedure was used for bending moment:

$$\sigma = E\varepsilon = \frac{Mc}{I} = \frac{Mh}{2I}$$

$$\varepsilon = \frac{Mh}{2EI} = M\left(\frac{h}{2EI}\right)$$

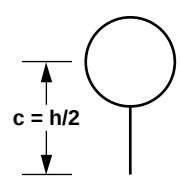

970211.D6

The following procedure was used for shear:

$$\tau = \gamma G = \frac{VQ}{It}$$

$$Q = \left(\frac{A}{2}\right)\left(\frac{h}{2}\right) = \frac{Ah}{4}$$

$$I = 2\left(\frac{A}{2}\right)\left(\frac{h}{2}\right)^2 = \frac{Ah^2}{4}$$

$$\tau = \gamma G = \frac{V\left(\frac{Ah}{4}\right)}{\left(\frac{Ah}{4}\right)^2 t}$$

$$\tau = \frac{V}{ht}$$

$$\gamma = \frac{V}{2Gth}$$

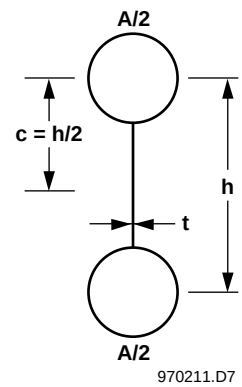

The shear printed out for the NASTRAN BAR elements represents the lumped element properties; hence, the shear strain is as follows:

$$\gamma = \frac{V}{2Ght}$$

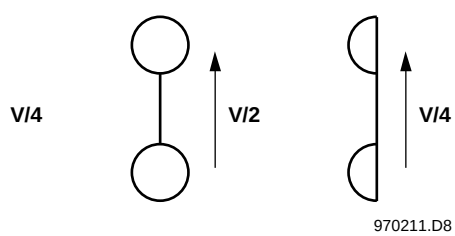

APPENDIX E

THE PHYSICS OF ANISOTROPY WITH RESPECT TO INFLUENCE-COEFFICIENT PLOTS

If the structure to be calibrated is a composite with anisotropic physical properties, then the rules and characteristics that have been presented in this document will probably not be applicable. The strain response of an anisotropic material is different than the strain response of an isotropic material to the same load-induced stress. When a force or moment is physically applied to two dimensionally equivalent aircraft structures, the same stress ensues at the surface traction. The nature of the strain response is drastically different if one of the two structures has anisotropic material characteristics. Therefore, it is unlikely that influence-coefficient plots for anisotropic structures can be interpreted in the manner shown in this report for isotropic structures.

If forces or moments that cause a given set of stresses are applied to an aircraft structure, then the following constitutive equations can be used to compute the resulting strains for the isotropic case:

$$\varepsilon_x = \frac{1}{E(\sigma_x - \upsilon\sigma_y)}$$

$$\varepsilon_y = \frac{1}{E(\sigma_y - \upsilon\sigma_x)}$$

$$\gamma_{xy} = \frac{\tau_{xy}}{G}$$

The resulting strain for the anisotropic case is as follows:

$$\varepsilon_x = \frac{1}{E_x(\sigma_x)} - \frac{\upsilon_{yx}}{E_y(\sigma_y)}$$

$$\varepsilon_y = \frac{\upsilon_{xy}}{E_x(\sigma_x)} - \frac{1}{E_y(\sigma_y)}$$

$$\gamma_{xy} = \frac{\tau_{xy}}{G_{xy}}$$

The class of fibrous composites being considered is presumed to have identical tensile and compressive elastic properties. This identity requires the compliance matrix[29] to be symmetric; hence, the following reciprocity relationship applies:

$$\frac{\upsilon_{yx}}{E_y} = \frac{\upsilon_{xy}}{E_x}$$

If rotating the applied stresses by an angle, θ, is desired so that the obliquely oriented strains can be examined, then the following equations can be used to rotate the applied stresses:

$$\begin{Bmatrix} \sigma'_x \\ \sigma'_y \\ \gamma'_{xy} \end{Bmatrix} = \begin{bmatrix} \cos^2\theta & \sin^2\theta & 2\cos\theta\sin\theta \\ \sin^2\theta & \cos^2\theta & -2\cos\theta\sin\theta \\ -\cos\theta\sin\theta & \cos\theta\sin\theta & \cos^2\theta - \sin^2\theta \end{bmatrix} \begin{Bmatrix} \sigma_x \\ \sigma_y \\ \gamma_{xy} \end{Bmatrix}$$

Table E-1 shows an example where two cases are considered. One case involves an arbitrary physical loading that results in a known normal stress oriented as shown on the element in the upper skin. The second case involves another physical loading that results in a known shear stress oriented also as shown on the upper skin. Strains were computed for the two loading cases for an isotropic and an anisotropic skin material. This computation results in a matrix of four sets of strains. The strains were also examined at a 45° oblique angle. This examination adds four items to the matrix so that the total is eight sets of strains (table E-1).

The strains that occur for the isotropic case illustrate patterns that are familiar to the experienced structures scientist. The symmetry that correlates to the Poisson's number is seen throughout the strain in the isotropic case. The strains that occur in the anisotropic structure are irregular with respect to major axes and did not illustrate the symmetry that normally occurs with an isotropic material. Table E-1 shows that for the same loading, the strain that occurs on an anisotropic structure is different from an isotropic structure. Therefore, the traditional formats in an influence-coefficient plot for an isotropic wing are not valid for a wing with anisotropy.

Table E-1. Comparison of isotropic and anisotropic strain responses in an aircraft structure.

	In-plane normal load σx = 1, σy = 0, σxy = 0 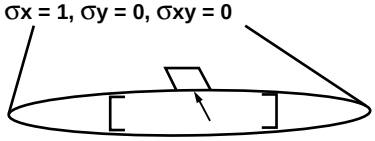 970212.E1.a		In-plane shear load σx = 0, σy = 0, σxy = 1 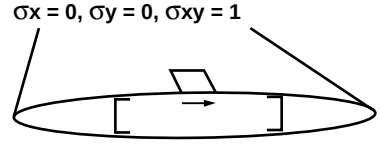 970212.E1.b	
	Isotropic material $\upsilon = \frac{1}{3}, E = 1$		Anisotropic material $E_x = 10, E_y = 5, \upsilon_{xy} = 4, \upsilon_{yx} = 2$	
	In-plane shear load	In-plane normal load	In-plane shear load	In-plane normal load
θ = 0 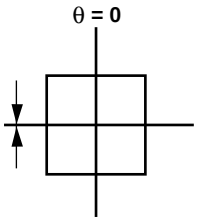 970212.E2	$\varepsilon_x = 0$ $\varepsilon_y = 0$ $\gamma_{xy} = \frac{8}{3}$	$\varepsilon_x = 1$ $\varepsilon_y = -\frac{1}{3}$ $\gamma_{xy} = 0$	$\varepsilon_x = 0$ $\varepsilon_y = 0$ $\gamma_{xy} = 1$	$\varepsilon_x = \frac{1}{10}$ $\varepsilon_y = -\frac{4}{10}$ $\gamma_{xy} = 0$
θ = 45 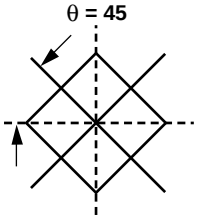 970212.E3	$\varepsilon'_x = \frac{4}{3}$ $\varepsilon'_y = -\frac{4}{3}$ $\gamma'_{xy} = 0$	$\varepsilon'_x = \frac{1}{3}$ $\varepsilon'_y = -\frac{1}{3}$ $\gamma'_{xy} = -\frac{4}{3}$	$\varepsilon'_x = \frac{5}{10}$ $\varepsilon'_y = -\frac{6}{10}$ $\gamma'_{xy} = 0$	$\varepsilon'_x = -\frac{3}{20}$ $\varepsilon'_y = -\frac{2}{20}$ $\gamma'_{xy} = -\frac{10}{20}$

σ denotes stress in the orthogonal axes, and σ' denotes stress at an angle, θ, to the orthogonal axes.

APPENDIX F

AN ILLUSTRATION OF THE PROCESS OF DERIVING A LOAD EQUATION

This section is included to illustrate how a loads equation can be derived manually. Consider the lifting surface shown in figure F-1. The load calibration involves three load points with two strain gages. Using both strain gages is desired in an equation to describe the applied shear load. For example:

$$V = \mu_{303}\beta_1 + \mu_{311}\beta_2$$

where V is the shear load, μ is the strain-gage output, and β is the equation coefficient to be determined.

The results of the calibration from the table in figure F-1 lead to the following equation:

$$\begin{aligned} 1000 &= 0.273\beta_1 + 0.285\beta_2 \\ 2000 &= 0.052\beta_1 + 0.946\beta_2 \\ 3000 &= 0.054\beta_1 + 0.909\beta_2 \end{aligned}$$

which can be written as

$$\begin{Bmatrix} 1000 \\ 2000 \\ 3000 \end{Bmatrix} = \begin{bmatrix} 0.273 & 0.285 \\ 0.052 & 0.946 \\ 0.054 & 0.909 \end{bmatrix} \begin{Bmatrix} \beta_1 \\ \beta_2 \end{Bmatrix}$$

or

$$\begin{Bmatrix} 1 \\ 2 \\ 3 \end{Bmatrix} = \begin{bmatrix} 273 & 285 \\ 52 & 946 \\ 54 & 909 \end{bmatrix} 10^{-6} \begin{Bmatrix} \beta_1 \\ \beta_2 \end{Bmatrix}$$

The matrix operations that lead to solving for the coefficients, β, are as follows:[1, 30]

$$\begin{aligned} \{V\} &= [\mu]\{\beta\} \\ [\mu]^T\{V\} &= [\mu]^T[\mu]\{\beta\} \\ [\mu]^T\{V\}\Big[[\mu]^T[\mu]\Big]^{-1} &= \{\beta\} \end{aligned}$$

The inverse of a matrix is the adjoint of the matrix divided by the determinant of the matrix:

$$[A]^{-1} = \frac{1}{[A]}\,[A_{ji}]$$

The transpose of the strain-gage output matrix, [μ], is found:

$$\begin{bmatrix} 273 & 285 \\ 52 & 946 \\ 54 & 909 \end{bmatrix}^{T} = \begin{bmatrix} 273 & 52 & 54 \\ 285 & 946 & 909 \end{bmatrix}$$

The quantity, $[\mu]^T [\mu]$, is as follows:

$$\begin{bmatrix} 273 & 52 & 54 \\ 285 & 946 & 909 \end{bmatrix} \begin{bmatrix} 273 & 285 \\ 52 & 946 \\ 54 & 909 \end{bmatrix} = \begin{bmatrix} 80149 & 176083 \\ 176083 & 1802422 \end{bmatrix}$$

A new matrix of the cofactors is constructed:

$$\begin{bmatrix} 1802422 & -176083 \\ -176083 & 80149 \end{bmatrix}$$

The transpose of the cofactor matrix is the adjoint:

$$\begin{bmatrix} 1802422 & -176083 \\ -176083 & 80149 \end{bmatrix}^{T} = \begin{bmatrix} 1802422 & -176083 \\ -176083 & 80149 \end{bmatrix}$$

The determinant of the matrix is as follows:

$$\left| \quad \right| = \begin{vmatrix} 80149 & 176083 \\ 176083 & 1802422 \end{vmatrix} = 113.4 \times 10^{9}$$

The inverse is the adjoint divided by the determinant:

$$\frac{1}{113.4 \times 10^{9}} \begin{bmatrix} 1802422 & -176100 \\ -176100 & 80200 \end{bmatrix} = \begin{bmatrix} 15885 & -1552 \\ -1552 & 707 \end{bmatrix} 10^{-9}$$

Therefore:

$$[\mu]^T \{V\} \left[[\mu]^T [\mu] \right]^{-1} = \{\beta\}$$

$$\begin{bmatrix} 273 & 52 & 54 \\ 285 & 946 & 909 \end{bmatrix} \begin{Bmatrix} 1 \\ 2 \\ 3 \end{Bmatrix} \begin{bmatrix} 15.885 & -1.552 \\ -1.552 & 0.707 \end{bmatrix} = \{\beta\}$$

$$\begin{matrix} 539 \\ 4904 \end{matrix} \begin{bmatrix} 15.885 & -1.552 \\ -1.552 & 0.707 \end{bmatrix} = \begin{Bmatrix} \beta_1 \\ \beta_2 \end{Bmatrix}$$

$$\begin{Bmatrix} 951 \\ 2630 \end{Bmatrix} = \begin{Bmatrix} \beta_1 \\ \beta_2 \end{Bmatrix}$$

Check the result:

$$V = 951 \ \mu_{303} + 2630 \ \mu_{311}$$
$$V = 951[0.000273] + 2630[0.000285] = 0.26 + 0.75 = 1.01$$
$$V = 951[0.000052] + 2630[0.000946] = 0.05 + 2.49 = 2.54$$
$$V = 951[0.000054] + 2630[0.000909] = 0.05 + 2.39 = 2.44$$

The applied loads are 1.00, 2.00, and 3.00; and the calculated loads are 1.01, 2.54, and 2.44, which is a result that reflects the fact that the problem is a created example.

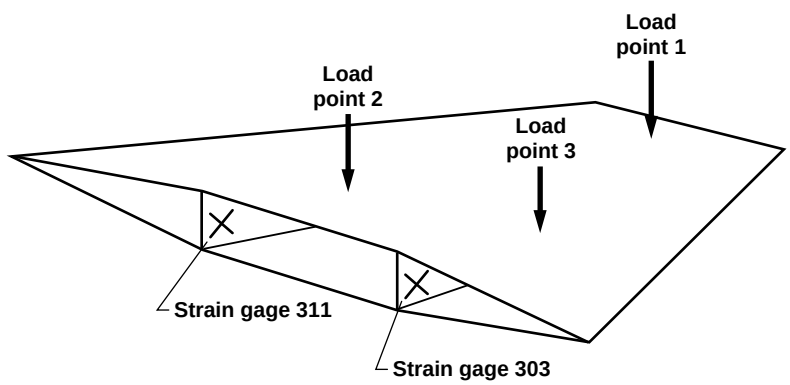

Loading schedule/strain-gage outputs

Strain-gage outputs

Point	Load	S/G 303	S/G 311
1	1000	0.273	0.285
2	2000	0.052	0.946
3	3000	0.054	0.909

970213

Figure F-1. Description of example load calibration.

APPENDIX G

CARRY-OVER EFFECTS

Many airplane lifting surfaces have structural arrangements in which the wing or tail is continuous through the fuselage. The net effect is that a load on one surface carries through to the support on the other lifting surface. This effect can be seen in the sketch below:

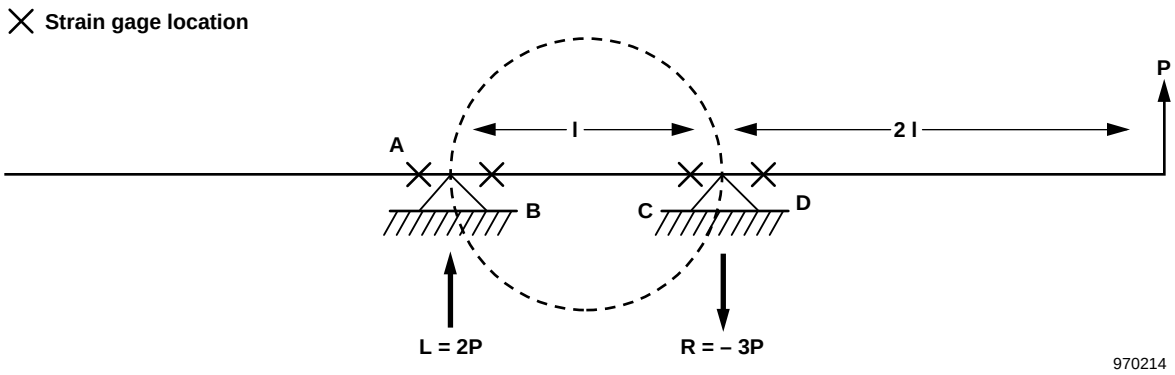

The effect of load, *P*, can be amplified several times because the geometry of the supports represents a mechanical advantage type of situation. Strain gages located at A, B, C, and D can be affected easily by the load, *P*. Although location A is outside the direct force system, a local crushing effect can easily exist. A load on both lifting surfaces normally exists that, at times, may be symmetrical. Therefore, if the structural arrangement is as depicted in the above sketch, then a strong possibility exists that a carry-over effect will have to be determined from the load calibrations.

REFERENCES

[1] Skopinski, T. H., Aiken, William S., Jr., and Huston, Wilber B., *Calibration of Strain-Gage Installations in Aircraft Structures for the Measurement of Flight Loads*, NACA Report 1178, 1954.

[2] Klema, Virginia C. and Laub, Alan J., "The Singular Value Decomposition: Its Computation and Some Applications," *IEEE Transactions on Automatic Control*, vol. AC-25, no. 2, Apr. 1980.

[3] DeAngelis, V. Michael, "Strain Gage Loads Measurement Techniques for Hot Structures," *Workshop on Correlation of Hot Structures Test Data With Analysis*, NASA CP-3065, vol. 1, Nov. 1988, pp. 15–XX.

[4] Jenkins, Jerald M., Tang, Ming H., and Pearson, George P. E., *Vertical-Tail Loads and Control-Surface Hinge-Moment Measurements on the M2-F2 Lifting Body During Initial Subsonic Flight Tests*, NASA TM-X-1712, Dec. 1968.

[5] Tang, Ming H., Sefic, Walter J., and Sheldon, Robert G., *Flight-Measured X-24B Fin Loads and Control Surface Hinge Moments and Correlation with Wind Tunnel Predictions*, NASA TM-X-56042, Jan. 1977.

[6] Fields, Roger A., *A Study of the Accuracy of a Flight-Heating Simulation and Its Effect on Load Measurement*, NASA TN-D-5741, Apr. 1970.

[7] McCormick, Caleb W., ed., *The NASTRAN User's Manual (Level 15)*, NASA SP-222(01), 1972.

[8] Sefic, Walter J. and Reardon, Lawrence F., "Loads Calibration of the Airplane," *NASA YF-12 Flight Loads Program*, NASA TM-X-3061, May 1974, pp. 61–107.

[9] Jenkins, Jerald M. and Kuhl, Albert E., *A Study of the Effect of Radical Load Distributions on Calibrated Strain Gage Load Equations*, NASA TM-56047, July 1977.

[10] Jenkins, Jerald M., Kuhl, Albert E., and Carter, Alan L., "Strain Gage Calibration of a Complex Wing," *Journal of Aircraft*, vol. 14, no. 12, Dec. 1977, pp. 1192–1196.

[11] National Aeronautics and Space Administration, *NASA YF-12 Flight Loads Program*, NASA TM-X-3061, May 1974.

[12] DeAngelis, V. Michael and Monaghan, Richard C., "HiMAT Strain Gage Loads Calibration and Flight Loads Measurement," *Highly Maneuverable Aircraft Technology (U)*, NASA CP-2412, May 1984, pp. 207–226.

[13] Monaghan, Richard C., *Description of the HiMAT Tailored Composite Structure and Laboratory Measured Vehicle Shape Under Load*, NASA TM-81354, Feb. 1981.

[14] Deets, Dwain A., DeAngelis, V. Michael, and Lux, David P., *HiMAT Flight Program: Test Results and Program Assessment Overview*, NASA TM-86725, June 1986.

[15] DeAngelis, V. Michael, *Wing Panel Loads and Aileron Hinge Moments Measured in Flight on the F-8 Supercritical Wing Airplane Including Correlations With Wind Tunnel Data*, NASA TM-X-3098, Aug. 1974.

[16] DeAngelis, V. Michael and Monaghan, Richard C., *Buffet Characteristics of the F-8 Supercritical Wing Airplane*, NASA TM-56049, Sept. 1977.

[17] Coe, Charles F. and Cunningham, Atlee M., Jr., *Predictions of F-111 TACT Aircraft Buffet Response and Correlations of Fluctuating Pressures Measured on Aluminum and Steel Models of the Aircraft*, NASA CR-4069, May 1987.

[18] Monaghan, Richard C., *Flight-Measured Buffet Characteristics of a Supercritical Wing and a Conventional Wing on a Variable-Sweep Airplane*, NASA TP-1244, May 1978.

[19] Popov, E. P., *Mechanics of Materials*, Prentice-Hall, Inc., New Jersey, 1952.

[20] Abbott, Ira H. and Van Doenhoff, Albert E., *Theory of Wing Sections: Including a Summary of Airfoil Data*, Dover Publications, Inc., New York, 1959.

[21] Mock, W. D., *Airloads Research Study: Distributed Load Calibration Data*, NASA CR-143845, Feb. 1978.

[22] Plank, P. P. and Penning, F. A., *Hypersonic Wing Test Structure Design, Analysis, and Fabrication*, NASA CR-127490, Aug. 1973.

[23] Hovell, P. B., Webber, D. A., and Roberts, T. A., "The Interpretation of Strain Measurements for Flight Load Determination," C.P. No. 839, Her Majesty's Stationery Office, London, 1966.

[24] Hovell, P. B., Webber, D. A., and Roberts, T. A., "The Use of Calibrated Strain Gauges for Flight Load Determination," C.P. No. 1041, Her Majesty's Stationery Office, London, 1969.

[25] Reardon, Lawrence F., *Evaluation of a Strain-Gage Load Calibration on a Low-Aspect-Ratio Wing Structure at Elevated Temperatures*, NASA TP-2921, June 1989.

[26] Tang, Ming H., "A Modified T-Value Method for Selection of Strain Gages for Measuring Loads," *SESA Western Regional Strain Gage Committee Fall Meeting*, Naval Weapons Center, California, Sept. 16–17, 1980.

[27] Tang, Ming H. and Sheldon, Robert G., *A Modified T-Value Method for Selection of Strain Gages for Measuring Loads on a Low Aspect Ratio Wing*, NASA TP-1748, Nov. 1980.

[28] Nelson, Sigurd A., II, *Strain Gage Selection in Loads Equations Using a Genetic Algorithm*, NASA CR-4597, Oct. 1994.

[29] Whitney, James M., Daniel, Isaac M., and Pipes, R. Byron, *Experimental Mechanics of Fiber Reinforced Composite Materials*, Society for Experimental Stress Analysis, Connecticut, 1982.

[30] Wylie, C. R., Jr., *Advanced Engineering Mathematics*, McGraw-Hill Book Company, Inc., New York, 1960.

REPORT DOCUMENTATION PAGE

Form Approved
OMB No. 0704-0188

Public reporting burden for this collection of information is estimated to average 1 hour per response, including the time for reviewing instructions, searching existing data sources, gathering and maintaining the data needed, and completing and reviewing the collection of information. Send comments regarding this burden estimate or any other aspect of this collection of information, including suggestions for reducing this burden, to Washington Headquarters Services, Directorate for Information Operations and Reports, 1215 Jefferson Davis Highway, Suite 1204, Arlington, VA 22202-4302, and to the Office of Management and Budget, Paperwork Reduction Project (0704-0188), Washington, DC 20503.

1. AGENCY USE ONLY (Leave blank)

2. REPORT DATE
July 1997

3. REPORT TYPE AND DATES COVERED
Technical Memorandum

4. TITLE AND SUBTITLE
A Summary of Numerous Strain-Gage Load Calibrations on Aircraft Wings and Tails in a Technological Format

5. FUNDING NUMBERS
WU 505-63-50

6. AUTHOR(S)
Jerald M. Jenkins and V. Michael DeAngelis

7. PERFORMING ORGANIZATION NAME(S) AND ADDRESS(ES)
NASA Dryden Flight Research Center
P.O. Box 273
Edwards, California 93523-0273

8. PERFORMING ORGANIZATION REPORT NUMBER
H-2154

9. SPONSORING/MONITORING AGENCY NAME(S) AND ADDRESS(ES)
National Aeronautics and Space Administration
Washington, DC 20546-0001

10. SPONSORING/MONITORING AGENCY REPORT NUMBER
NASA TM-4804

11. SUPPLEMENTARY NOTES

12a. DISTRIBUTION/AVAILABILITY STATEMENT
Unclassified—Unlimited
Subject Category 01

12b. DISTRIBUTION CODE

13. ABSTRACT (Maximum 200 words)

Fifteen aircraft structures that were calibrated for flight loads using strain gages are examined. The primary purpose of this paper is to document important examples of load calibrations on airplanes during the past four decades. The emphasis is placed on studying the physical procedures of calibrating strain-gaged structures and all the supporting analyses and computational techniques that have been used. The results and experiences obtained from actual data from 14 structures (on 13 airplanes and 1 laboratory test structure) are presented. This group of structures includes fins, tails, and wings with a wide variety of aspect ratios. Straight-wing, swept-wing, and delta-wing configurations are studied. Some of the structures have skin-dominant construction; others are spar-dominant. Anisotropic materials, heat shields, corrugated components, nonorthogonal primary structures, and truss-type structures are particular characteristics that are included.

14. SUBJECT TERMS
Anisotropic structure, Flight load, Isotropic structure, Load calibration, Loads measurement, Strain gage

15. NUMBER OF PAGES
147

16. PRICE CODE
A07

17. SECURITY CLASSIFICATION OF REPORT
Unclassified

18. SECURITY CLASSIFICATION OF THIS PAGE
Unclassified

19. SECURITY CLASSIFICATION OF ABSTRACT
Unclassified

20. LIMITATION OF ABSTRACT
Unlimited